UNIVERSIDAD DE SALAMANCA

INSTITUTO DE BIOLOGÍA MOLECULAR Y CELULAR DEL CÁNCER (CSIC-USAL)

Desmoplakin and Plakophilin-1a: Structure, Subcellular Distribution, and Interactions

MEMORIA PARA OPTAR AL GRADO DE DOCTOR

PRESENTADA POR

Ana María Carballido Vázquez

Bajo la dirección del Doctor

José M de Pereda Vega

Salamanca, 2015

Dr. JOSÉ MARÍA DE PEREDA VEGA, Científico Titular del Consejo Superior de Investigaciones Científicas (CSIC) en el Instituto de Biología Molecular y Celular del Cáncer (IBMCC, CSIC-Universidad de Salamanca).

CERTIFICA:

Que Dña. Ana María Carballido Vázquez, licenciada en Biología por la Universidad de Santiago de Compostela, ha realizado bajo su dirección el trabajo de Tesis Doctoral que lleva por título "***Desmoplakin and Plakophilin-1a: Structure, Subcellular Distribution, and Interactions***", y considera que éste reúne originalidad y contenidos suficientes para que sea presentada ante el Tribunal correspondiente y optar al Grado de Doctor por la Universidad de Salamanca.

Y para que así conste a los efectos oportunos, expide el presente certificado en Salamanca, 15 de Diciembre de 2014

Dr. José María de Pereda Vega

Director de la tesis

Ana M Carballido Vázquez ha realizado esta tesis doctoral siendo beneficiaria de una ayuda predoctoral del programa de Formación de Personal Investigador (BES-2010-038674) del Ministerio de Economía y Competitividad, durante el periodo de septiembre de 2010 a agosto de 2014.

Este trabajo se ha enmarcado dentro de los proyectos del Plan nacional I+D+i "*Bases estructurales de interacciones en hemidesmosomas: integrina α6β4, BPAG1e y tetraspanina CD151*" (BFU2009-08389) y "*Bases estructurales de la función de plakinas en adhesión celular, implicación en enfermedades*" (BFU2012-32847) financiados por el Ministerio de Ciencia e Innovación, el Ministerio de Economía y Competitividad y el Fondo Europeo de Desarrollo Regional; y del proyecto del Programa de apoyo a proyectos de investigación de la Consejería de Educación de la junta de Castilla y León titulado "Plakinas en complejos de adhesión: bases estructurales de su función e identificación de compuestos moduladores" (CSI181A12-1).

Ana M Carballido Vázquez realizó parte del trabajo de esta tesis durante una estancia de ocho meses en el laboratorio del Prof. Arnoud Sonnenberg en el Netherlands Cancer Institute (NKI) (Ámsterdam, Holanda). Parte de esa estancia estuvo financiada por una ayuda de Estancia Breve (referencia EEBB-I-13-06399) del Ministerio de Economía y Competitividad.

Acknowledgements

First, I would like to thank my mentor, Dr José M de Pereda for giving me the opportunity to learn in his lab during these years. I also want to extend my thanks to all the members of his lab.

A large part of this work would have not been possible without my stay at the Prof A. Sonneberg lab. I would like to express my most sincere thanks for the warmth of his welcoming and the helpful discussion and support during my time at the NKI. Again, I extend my acknowledgements to all the members of his lab, especially to Dr Pablo Secades and Dr Coert Margadant for their guidance and wise advice.

I also thank Dr Kees Jalink lab, in particular, Dr Marcel Raspe for providing me the opportunity to make FLIM experiments. I must also thank Dr Elisa Matas for her complete support at the NKI.

I am very grateful to Prof A. Sonneberg (NKI, Amsterdam), Dr AP. South (MRI, Dundee), and Dr C. Guerrero (CIC, Salamanca) for kindly providing me with the cell lines that I have used during my thesis and, in like manner, to everybody that in one way or another has contributed to this work.

On a personal note, I cannot miss this opportunity to thank all the people that have accompanied me through these years in Salamanca. It was fun to work and play with all of you!

List of Abbreviations

[θ]	Mean residue molar ellipticity
2θ	Scattering angle
A	Absorbance
a.u.	Arbitrary units
aa	Amino acid
AJs	Adherens Junctions
Akt2	RAC-beta serine/threonine-protein kinase
ARM	Armadillo
ARVCF	ARM-protein Deleted in Velo-Cardio-Facial Syndrome
AS	Ammonium Sulphate
BLAST	Basic Local Alignment Search Tool
BPAG1	Bullous Pemphigoid Antigen 1
BPE	Bovine Pituitary Extract
BSA	Bovine Serum Albumin
C-	Carboxyl-terminus
CD	Circular Dichroism
cDNA	Complementary DNA
CFP	Cyan Fluorescent Protein
CMV	Cytomegalovirus promoter
Co-IP	Co-immunoprecipitation
CT	C-terminal half
c-TAK1	CdC25C-associated Kinase 1
d	First derivative
DAPI	4', 6-diamidino-2-phenylindole
DESY	Deutsches Elektronen Synchrotron
Dmax	Maximun particle size/distance
DMEM	Dulbecco´s Modified Eagle´s Medium
DMs	Desmosomes
DMSO	Dimethyl sulfoxide
DNA	Deoxyribonucleic acid
DP	Desmoplakin
DP-PD	Desmoplakin Plakin Domain
Dr	Doctor
DSCs	Desmocollins
DSGs	Desmogleins
DTT	Dithiothreitol
E_{280}	Mass extinction coefficient
ε_{280}	Molar extinction coefficient
eCa	Extracellular calcium
EF1	Elongation Factor 1
EMBL	European Molecular Biology Laboratory
ETV1	ETS Translocation Variant 1
F	Fluorescence signal

FBS	Fetal Bovine Serum
FD-FLIM	Frequency domain FLIM
FIM	Fluorescence Imaging Microscopy
FLIM	Fluorescence lifetime imaging microscopy
FRET	Förster Resonance Energy Transfer
FXR1	Fragile X mental retardation syndrome-Related Protein 1
HA	Influenza hemagglutinin epitope
HMM	Profile Hidden Markov Models
HR2	Homology Region 2
HRP	Horseradish peroxidase
hv	Modulated light
I_0	Forward scattering intensity
iCa	Intracellular calcium
IDP	Inner Dense Plaque
IFs	Intermediate Filaments
IgG	Immunoglobulin G
IMAC	Immobilized Metal ion Affinity Chromatography
IP	Immunoprecipitation
IPTG	Isopropil-β-D-1-thiogalactopyranoside
JEB-PA	Junctional Epidermolysos Bullosa associated with Pyloric Atresia
KZ	Kozak consensus sequence
LB	Lysogeny Broth
LIFA	Lambert Instruments Fluorescence lifetime Attachment
MACF1	Microtubule Actin Cross-linking Factor 1
MCS	Multiple Cloning Site
MOM	Mitochondrial Outer Membrane
mRNA	Messenger RNA
Mw	Molecular weight
n	Number of values
N-	Amino-terminus
NES	Nuclear Exporting Signal
NHKs	Normal Human Keratinocytes
NLS	Nuclear Localization Signal
NPRAP	Neural Plakophilin-Related Armadillo Protein
NSD	Normalized Spatial Discrepancy
NT	N-terminal half
O/N	Overnight
ODP	Outer Dense Plaque
p	p-value
p-	Phosphorylated
P(r)	Pair-distribution probability function
p0071	p0071/PKP4
PBS	Phosphate Buffered Saline
PCR	Polymerase Chain Reaction
PD	Plakin Domain
PDB	Protein Data Bank entry

PEI	Polyethylenimine
PFA	Paraformaldehyde
pI	Isoelectric point
PI	Propidium Iodide
PKCα	Protein kinase C alpha
PKG	Plakoglobin
PKPs,1-3	Plakophilins, Isoforms 1 to 3
PM	Plasma Membrane
PRD	Plakin Repeat Domain
Prof	Professor
PTMs	Post-translational modifications
q	Scattering vector
qPCR	Quantitative PCR
rEGF	Recombinant Epidermal Growth Factor Receptor
rmsd	Root mean square deviation
RNA	Ribonucleic acid
RT	Room temperature
RT-PCR	Reverse transcription PCR
S_0	Electronic ground state
S_2	Electronic excited state
SAXS	Small Angle X-ray Scattering
SD	Standard Deviation
SDP-PAGE	SDS-PolyAcrylamide Gel Electrophoresis
SDS	Sodium Dodecyl Sulfate
SEM	Standard Error of the Mean
SFM	Serum Free Medium
SH3	SRC Homology 3 Domain
SR	Spectrin Repeat
ssDNA	Single-stranded DNA
T	Temperature
Ƭ	Lifetime
TCEP	Tris(2-carboxyethyl)phosphine
TEV	Tobacco Etch Virus
Tm	Melting Temperature
Tris-HCl	TRIS hydrochloride
UV	Ultraviolet
V	Hydrated particle volume
Vp	Porod volume
WT	Wild Type

Table of contents

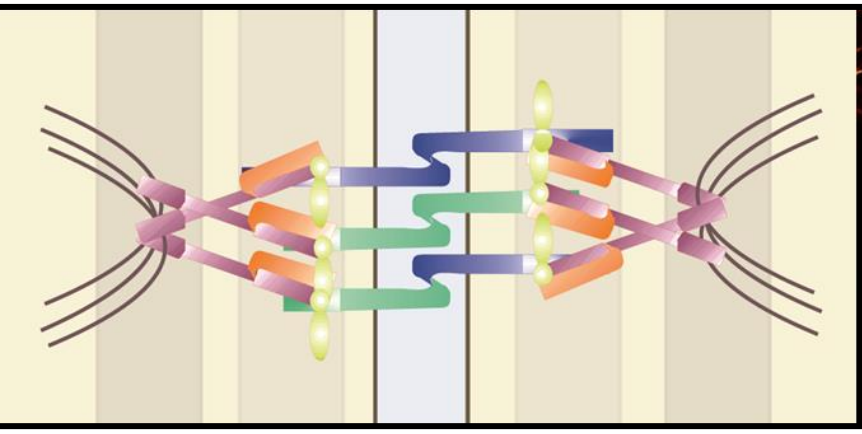

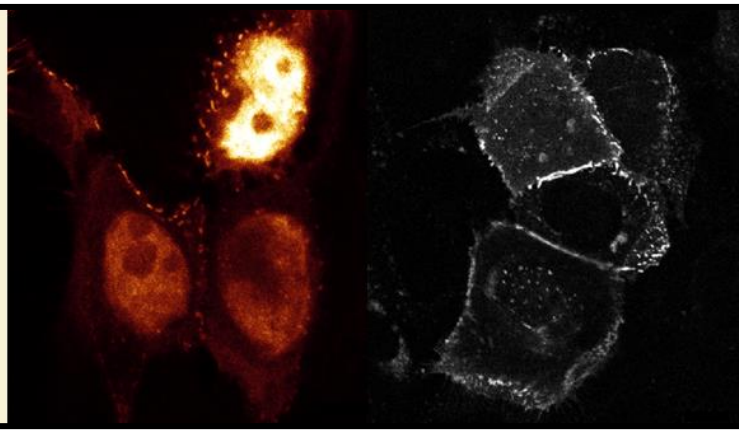

Chapter 1

INTRODUCTION

1. Desmosomes

Overview

Desmosomes (DMs) are specialized and highly organized intercellular junctions that indirectly couple cytoskeletal intermediate filaments of adjacent cells. Strong cell-cell adhesion between adjacent cells is achieved through a complex network of protein-protein interactions that distributes mechanical tension across all cells, maintaining the structural and functional integrity of tissues (Kowalczyk & Green 2013). DMs are present in all epithelial cells as well as in specific non-epithelial tissues such as the myocardium. Desmosome-mediated adhesion is particularly important in the skin and heart, which routinely undergo acute mechanical stress (Franke et al. 2006). They are especially predominant in these tissues, which are also the main targets in desmosome-related disorders. Desmosomal-diseases symptoms typically encompass epidermal fragility and blistering, palmoplantar keratoderma, and/or cardiomyopathy (Al-Jassar et al. 2013; Delmar & McKenna 2010; Ishida-Yamamoto & Igawa 2014).

Structure

Ultrastructurally, DMs appear as electron-dense discs symmetrically arranged in adjacent cells in a multi-layered manner. They are composed of three major protein families: desmosomal cadherins (desmogleins and desmocollins), armadillo proteins (plakoglobin and plakophilins) and plakins (desmoplakin) (Figure I1). Nonetheless, the precise molecular composition of DMs is variable, depending on tissue- and differentiation-specific expression of particular isoforms of the constituent proteins (Garrod & Chidgey 2008). The quite large number of desmosomal proteins isoforms, together with their complex expression patterns, suggests that specific isoforms make unique contributions to address the specific needs of different cell types or tissues.

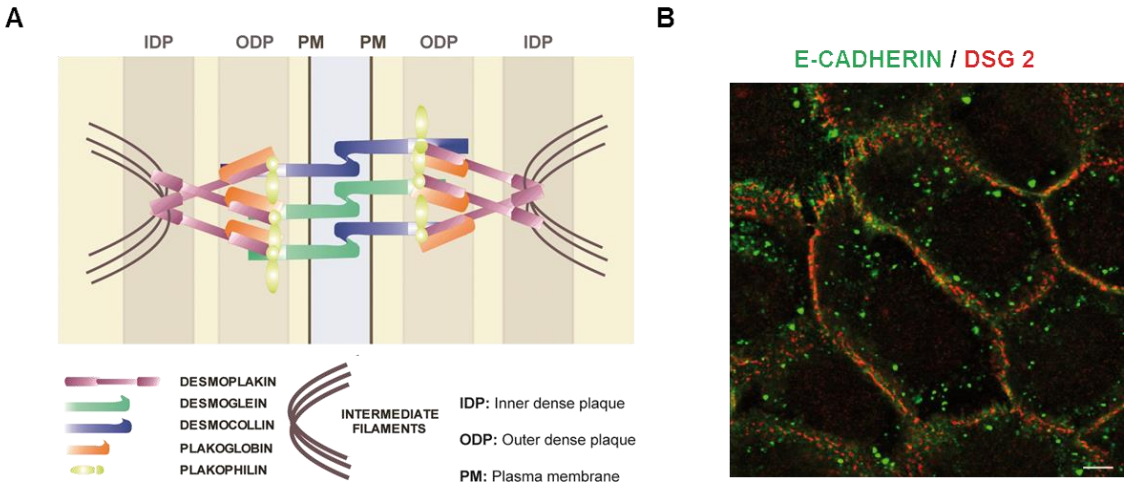

Figure I1. The desmosome. A) Schematic representation of the molecular composition of DMs and their organization. In brief, the desmosomal cadherins (desmocollins, green; desmogleins, blue) interact in the

extracellular space through their ectodomains. Intracellularly, desmosomal cadherins bind to armadillo-proteins (plakoglobin, orange; plakophilins, yellow) which mediate the connexion to the intermediate filaments (IFs, brown) throughout desmoplakin (DP, purple). The interactions between plaque proteins and the cytoplasmic tails of the desmosomal cadherins take part in the outer dense plaque (ODP), whereas DP binds IFs at the inner dense plaque (IDP). **B)** Immunofluorescence image of E-cadherin (adherens junctions, green) and DSG-2 (DMs, red) in HaCaT cells growing in DMEM. Notice that DSG-2 is located in a punctuate pattern over the plasma membrane, presumably, where DMs are formed. E-cadherin also shows a peripheral and punctuate distribution but does no co-localize with DSG-2.

Molecular composition

Desmosomal cadherins belong to the cadherin superfamily of transmembrane glycoproteins that mediate calcium-dependent cell–cell adhesion (Saito et al. 2012). Two different cadherins subtypes participate in DMs: desmogleins (DSGs 1-4) and desmocollins (DSCs 1-3). DSGs and DSCs form intercellular contacts by establishing homo- and hetero-philic interactions between their ectodomains (Chitaev & Troyanovsky 1997). Intracellularly, the cytoplasmic tails of the desmosomal cadherins scaffold the desmosomal plaque proteins.

Armadillo proteins (ARM-proteins) are characterized by the presence of a central domain containing repetitive units of ~42-amino acid that adopt an α-helical structure (ARM-repeats) (Choi & Weis 2005; Hatzfeld 1999). ARM-proteins do not necessarily show a high sequence identity but they share a similar structure where ARM-repeats are folded together in a superhelix that enables the interaction with many protein partners. Thus, ARM-proteins show very diverse cellular functions (Tewari et al. 2010). Within DMs, two different ARM-proteins tether desmoplakin (DP) and cluster the intracellular tails of DSGs and DSCs at the cytoplasmic plaque: plakoglobin (PKG) and plakophilins (PKPs).

PKG is the best characterized ARM-protein of DMs. It is also found at adherens junctions (AJs) (Knudsen & Wheelock 1992) and harbours the 12 ARM-repeats that characterize this family. In addition to this structural role at the DM, PKG also mediates important roles in signal transduction pathways (reviewed in Aktary & Pasdar 2012; see examples in Aktary et al. 2010, 2013; Todorović et al. 2010).

PKPs (in humans 1-3) belong to the p120-catenin subfamily, characterized by the presence of 9 ARM-repeats in the ARM-domain (Carnahan et al. 2010). They show complex tissue- and differentiation-specific expression patterns but at least one of the three PKPs is required for the formation of functional DMs. PKPs enhance the intercellular cohesion by recruiting desmosomal components to the cell junctions. Furthermore, they also play non-desmosomal roles in actin filament organization,

growth control, or protein synthesis (reviewed in Hatzfeld et al. 2014; see examples in Hatzfeld et al. 2000; Hofmann et al. 2006; Mertens et al. 2001).

DP is an obligate desmosomal component. It belongs to the plakin family of cytolinkers that place cytoskeletal elements together and connect them to junctional complexes (reviewed in Bouameur et al. 2014). At the DMs, DP interacts with PKG and PKPs by means of its N-terminal plakin domain and with the intermediate filaments (IFs) through its C-terminal region.

In addition, a variety of non-essential proteins are associated with DMs in specialized structures or differentiation-specific states. As an example, the armadillo protein p0071, also called PKP-4, has been identified in DMs of some cultured epithelial cells (Hatzfeld & Nachtsheim 1996). Despite of the name, p0071/PKP4 is more closely related to the AJs-protein p120-catenin than to PKPs. The dual localization of p0071 has been related with a possible function of this protein in the cross-talk between DMs and AJs (Hatzfeld 2003). According to that, p0071 is able to interact with some AJ-related cadherins as well as with DP (Calkins et al. 2003). Yet, its specific function has to be further investigated. Another example is Kazrin, which is up-regulated during keratinocyte terminal differentiation, and localizes to DMs where binds the epidermal cornified envelope protein periplakin (Groot et al. 2004; Sevilla et al. 2008).

Protein-protein interactions

The mechanical integration of adjacent cells provided by DMs is achieved through a complex network of protein-protein interactions. They have been described interactions between almost all desmosomal components but the main scaffold requires four types of associations: (i) outside cells, homo- and hetero-philic associations between DSGs and DSCs ectodomains form the extracellular interface; (ii) intracellularly, the cytoplasmic tails of the desmosomal cadherins bind the plaque proteins PKG and PKPs; (iii) PKG and the PKPs in turn associate with the N-terminal region of DP; and lastly, (iv) DP bridges all the previous associate proteins to the cytoskeleton through interactions of its C-terminus with the IFs.

Figure I2 shows the interactions between desmosomal proteins reported so far (Harmon & Green 2013). References for each interaction are specified in table I1. Most of the interactions have been proved through co-immunoprecipitation (co-IP), *in vitro* binding experiments, or yeast two hybrid assays.

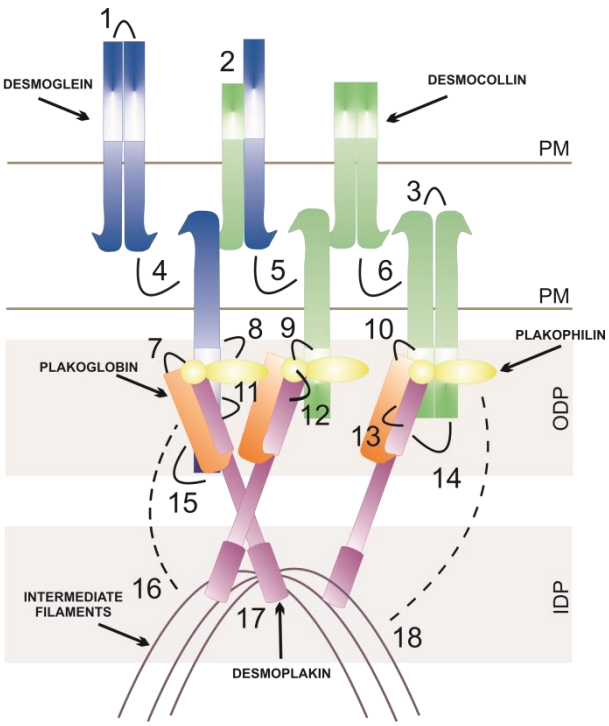

Figure I2. Protein-protein interactions within the DM. Schematic representation of the DM architecture showing the main interactions between desmosomal proteins reported so far. Interactions have been proved by using *in vitro* binding experiments, co-IP, and yeast two hybrid assays. Notice that binding-sites are not represented in the diagram, which just indicates which protein interacts with which other. For simplicity, isoforms and variants are omitted. Table I1 lists the references for each interaction. PM, plasma membrane; ODP, outer dense plaque; IDP, inner dense plaque.

Although the Figure I2 illustrates all of the reported interactions so far, some considerations must be taken. For instance, PKG-IFs and PKPs-IFs interactions have been widely reported *in vitro*; however, considering the accepted ultrastructural architecture of DMs where PKG and PKPs are in the outer dense plaque (ODP), whereas the IF-linkage occurs at the inner dense plaque (IDP), it seems that a spatial constraint would limit such interactions (North et al. 1999). In addition, there is also *in vitro* evidence of directly interaction between desmosomal cadherins and DP. However, it is though that adaptor proteins, such as PKG and PKPs, are required to link DP to desmosomal cadherins *in vivo*. Furthermore, the diagram does not consider the tissue- and differentiation-specific expression of different isoforms that may prevent some combinations.

Table I1. Reported desmosomal protein-protein interactions

Code	Interaction type	Reference
1	Interaction between DSGs cytoplasmic tails	(Chen et al. 2012)
2	DSGs – DSCs cytoplasmic tails associations	(Kami et al. 2009)
3	Homo-association between DSCs extracellular tails	(Syed et al. 2002)
4	Homophilic interactions between DSGs	(Waschke et al. 2007; Nie et al. 2011)
5	Heterophilic associations between DSGs and DSCs	(Chitaev & Troyanovsky 1997; Aoyama et al. 2009)
6	Homophilic interactions between DSCs	(Nie et al. 2011)
7	PKG – PKPs interactions	(Chen et al. 2002; Bonné et al. 2003)
8	PKPs – DSGs interactions	(Smith & Fuchs 1998; Hatzfeld et al. 2000; Chen et al. 2002; Bonné et al. 2003; Kami et al. 2009)
9	PKPs – DSCs interactions	(Smith & Fuchs 1998; Chen et al. 2002; Bonné et al. 2003)
10	PKG – DSCs interactions	(Smith & Fuchs 1998; Choi et al. 2009; Kowalczyk et al. 1996; Troyanovsky, et al. 1994; Witcher et al. 1996)
11	DP – DSGs interactions	(Bornslaeger et al. 2001; Kami et al. 2009)
12	PKPs – DP interactions	(Smith & Fuchs 1998; Hatzfeld et al. 2000; Hofmann, Mertens, et al. 2000; Chen et al. 2002; Bonné et al. 2003; Kowalczyk et al. 1999)
13	PKG – DP interactions	(Kowalczyk et al. 1997; Smith & Fuchs 1998; Bornslaeger et al. 2001)
14	DP – DSCs interactions	(Smith & Fuchs 1998)
15	PKG – DSGs interactions	(Mathur et al. 1994; Roh & Stanley 1995; Choi et al. 2009; Bornslaeger et al. 2001; Smith & Fuchs 1998; Kowalczyk et al. 1999; Kowalczyk et al. 1996; Stappenbeck & Green 1992; Witcher et al. 1996; Andl & Stanley 2001; Palka & Green 1997; Troyanovsky et al. 1994)
16	PKG – IFs interactions	(Smith & Fuchs 1998)
17	DP – IFs interactions	(Green, Stappenbeck, et al. 1992; Stappenbeck & Green 1992; Kouklis et al. 1994; Bornslaeger et al. 1996; Meng et al. 1997; Kowalczyk et al. 1997)
18	PKP – IFs interactions	(Kapprell 1988; Smith & Fuchs 1998; Hatzfeld et al. 2000; Hofmann, Mertens, et al. 2000; Bonné et al. 2003; Hatzfeld et al. 1994)

Desmosome functions and dynamics

During years, DMs have been considered simple spot-welds with the mere structural function of providing mechanical stability to a wide range of tissues. Today, in addition to maintenance cellular adhesion it is known to function in multiple processes through interactions with signalling pathways molecules important for cell polarity, cell shape or motility. In addition, they participate in the balance of proliferation versus differentiation. This multitasking role needs a strictly regulation of the DM dynamics, which depends on the proper synthesis, assembly, and turnover of the desmosomal components. DM remodelling is also essential in wound healing, development, and morphogenesis.

In cultured keratinocytes, DMs are assembled in response to cell–cell contact and raised levels of extracellular calcium (eCa) (Bikle et al. 2013; Kimura et al. 2007). DMs establishment upon increase of eCa in cell culture mimics the differentiation pattern of keratinocytes within the epidermis due to an ascending gradient of intracellular calcium (iCa) from the basal layer to the *stratum granulosum* (Kimutai et al. 2002), and has served as a tool to control DM formation *in vitro*. The importance of iCa homeostasis for desmosomal adhesion it is also revealed by diseases such as Darier's and Hailey–Hailey's diseases, which arise from mutations in calcium ATPases (Leinonen et al. 2009).

In brief, when calcium levels are low, newly synthesized desmosomal proteins are unstable. Only after DM assembly, desmosomal proteins are stabilized at the plasma membrane, probably due to the association with the IF-cytoskeleton. Desmosomal cadherins are thought to localize to the plasma membrane in association with PKG, whereas DP moves to cell-cell contacts in complexes with PKP2 (for detailed reviews see Kowalczyk & Green 2013; Nekrasova & Green 2013).

Interestingly, DMs have been reported to undergo a transition from a calcium-dependent state to an independent where they are hyper-adhesive. This conversion is appreciable in confluent culture sheets and intact epithelia *in vivo* and does not involve significant qualitative or quantitative changes in DMs composition (Kimura et al. 2007). Hyper-adhesion is considered the property that distinguishes DMs from the other cell junctions, providing the strong adhesion that contributes to tissue integrity (for a review see Garrod & Kimura 2008). *In vivo* the majority of the DMs are Ca^{+2}-independent and only revert to weaker adhesion after wounding. The regulation of the hyper-adhesiveness is mediated by PKCα phosphorylation (Garrod et al. 2005). Interestingly, it is thought to require structural changes in cadherins packaging (Garrod et al. 2005). Garrod and colleagues have suggested that changes in the interactions between cadherins ectodomains may accomplish a highly organized midline that has the ability to mediate stronger adhesion and to resist Ca^{2+} chelation because it is trapped by cis-interactions between cadherins tails.

2. Plakophilins

Overview

PKPs are vertebrate-specific proteins that, based on their primary sequence, have been classified as p120-catenin subfamily members. The p120-catenin subfamily comprises seven members, including δ-catenin/NPRAP (Neural Plakophilin-Related

Armadillo Protein), ARVCF (Armadillo Repeat Protein Deleted in Velo-Cardio-Facial Syndrome), p0071/PKP-4, and the more distantly related PKPs 1-3 (Carnahan et al. 2010). Like the others ARM-proteins, p120-catenin subfamily members mediate cell-cell adhesion. Based on their localization to the DMs instead of AJs and on the low degree of sequence similarity with the other p120-catenin subfamily members, PKPs are considered to form a separate group (Hatzfeld 2005).

Structure

The ARM-domain of PKPs is characterized by the presence of 9 ARM-repeats. The fifth and sixth domains are linked by a spacer sequence that results in a characteristic kink in the structure as shown by X-ray crystallography of the ARM-domain of PKP1 (PDB: 1XM9, Choi & Weis 2005). This domain is flanked by quite long N- and very short C-terminal domains. The head domain (N-terminal region) of the three PKPs is mostly devoid of any known secondary structure and is considered largely disordered. They do not exhibit homology to themselves or other proteins, only a small region near the amino-terminus, the so-called homology region 2 (HR2) (Bonné et al. 1999), shows some similarity between them (Figure I3). Interestingly, all the PKPs-binding partners reported so far interact with the head domain, although the ARM-domain contains the characteristic LxNL motifs along the groove that have been shown to bind a variety of proteins in the case of β-catenin (Huber et al. 1997; Choi & Weis 2005).

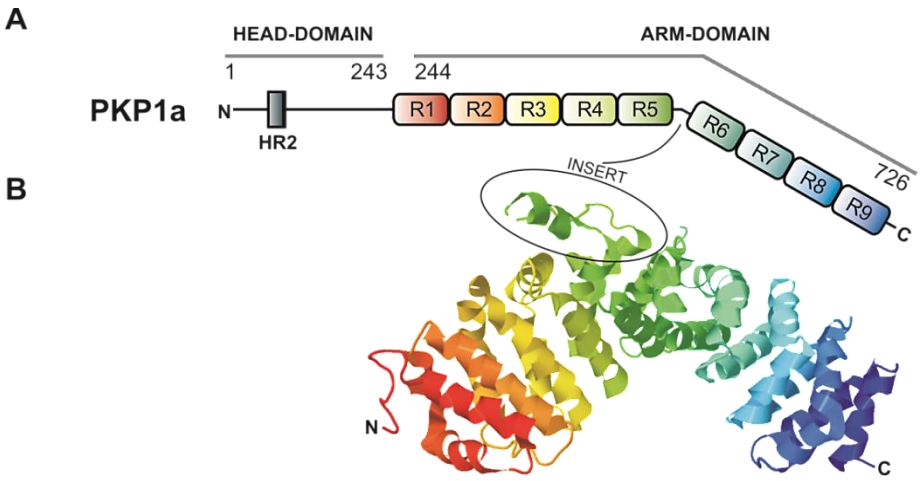

Figure I3. Multi-domain structure of plakophilin 1a. A) Schematic representation of the domain organization of PKP1a. **B)** Cartoon representation of the X-ray structure of the ARM-domain of PKP1 (PDB: 1XM9). ARM-repeats are shown in rainbow colours, starting in red in the N-terminus and ending in blue at the C-terminal region.

PKPs expression patterns

PKPs show complex but overlapping expression patterns in mammalian tissues. PKP2 shows the most widespread distribution, occurring in all proliferative epithelial cells and in non-epithelial tissues such as myocardium and arachnoid tissue (Rickelt 2012). PKP3 also presents a broad occurrence with the exception of hepatocytes and cardiomyocytes (Bonné et al. 2003). Conversely, PKP1 is localized in DMs of complex, stratified, and transitional epithelia but it is absent in simple epithelia (Moll et al. 1997). The three PKPs exist in two isoforms, a shorter “a” and a larger “b”, resulting from alternative splicing of the primary genes (Schmidt et al. 1997; Mertens et al. 1996; Mühmer et al. 2014). The “a” and “b” isoforms also show distinct subcellular localization. The different but overlapping expression patterns of the three PKPs suggests tissue- and/or differentiation-specific functions, but at the same time allow for some redundancy, smoothing PKPs-related diseases where more than one are present (McGrath & Mellerio 2010; Sklyarova et al. 2008), compared with scenarios where there is only one, such as heart (Grossmann et al. 2004).

PKPs functions

PKPs enhance intercellular cohesion by recruiting desmosomal components to cell junctions. Moreover, based on their interaction with many desmosomal proteins PKPs appear to act as scaffolds by linking desmosomal cadherins and PKG to DP and IFs (Chen et al. 2002; Bonné et al. 2003; Bornslaeger et al. 2001).

Although the three PKPs localise to DMs, only PKP1 enhances the number and/or size of junctions when overexpressed in cultured cells (Kowalczyk et al. 1999; Hatzfeld et al. 2000; South et al. 2003; South 2004; Tucker et al. 2014). This is in agreement with the *in vivo* situation where PKP1 is highly expressed in the suprabasal layer of the epidermis which contains numerous and large DMs. In addition, loss-of-function mutations in PKP1 produce epidermal-phenotypes with small and few DMs (McGrath et al. 1997).

PKPs also play non-desmosomal roles in actin filament organization, growth control, cell migration, and protein synthesis (reviewed in Hatzfeld et al. 2014; see examples in Godsel et al. 2010; Hatzfeld et al. 2000; Hofmann et al. 2006; Koetsier et al. 2014; Mertens et al. 2001; Wolf et al. 2010). Based on the phenotype of PKP3-deficient mice, it has also been suggested a contribution of PKP3 in limiting the inflammatory response via its interaction with the RNA binding protein FXR1 (Sklyarova et al. 2008). Interestingly, it has also been reported a main function of PKP1 in the transition of keratinocytes from a calcium-dependent to a calcium-independent, hyper-adhesive

state. In the latter conformation DMs are protected from *Pemphigus vulgaris* autoantibodies-induced loss of cell adhesion (Tucker et al. 2014).

PKPs in the nucleus

It has been demonstrated that both, endogenous and overexpressed PKPs prominently localise to the nucleus in DM-bearing and non-bearing cell lines (Schmidt et al. 1997; Mertens et al. 1996; Bonné et al. 1999). Although the nuclear localization has been reported for all PKPs (PKP1-3) the prevalence appears highly variable, being PKP1 the most nuclear-prominent. Likely, distinct mechanisms regulate nuclear localization of PKPs. One possible mechanism regulating PKP2 nuclear localization involves c-TAK1 mediated phosphorylation of the head domain of PKP2 to create binding sites for 14-3-3 proteins (Müller et al. 2003). This mechanism may be extended in the future to the whole family since: (i) PKP3 was recently shown to co-purify with the 14-3-3 family member stratifin (Roberts et al. 2013), and (ii) two of the PKP1-motifs phosphorylated by Akt2 are putative 14-3-3 binding sites (Wolf et al. 2013).

So far, it has been reported an interaction between PKP2 and the RNA polymerase III, PKP3 and the ETV1/ER81 transcription factor, as well as PKP1 binding to single-stranded DNA (ssDNA) (Mertens et al. 2001; Sobolik-Delmaire et al. 2010; Munoz et al. 2014). PKP1-head also binds ssDNA *in vitro* and is redistributed after induction of DNA damage, suggesting a putative function of PKP1 in DNA damage response. However, PKP1 nuclear binding partners have not been identified and there are no mechanistic insights about the PKP1 nuclear function. Thus, the identification of nuclear partners and functions of PKPs remain one future challenge.

3. Desmoplakin

Overview

DP belongs to the plakin family of cytolinkers. Plakins are huge proteins characterized by a multi-modular structure that provides an optimal architecture to interconnect elements of the cytoskeleton and tether them to membrane-associated junctions. Plakins cross-linking contributes to cell shape and polarity. They also participate in dynamic processes such as cell migration and differentiation, acting as scaffolds or adaptors for signalling proteins that modulate cytoskeletal dynamics (Bouameur et al. 2014; Sonnenberg & Liem 2007).

Mammalian plakins comprise 7 members: DP, plectin, bullous pemphigoid antigen 1 (BPAG1), microtubule actin cross-linking factor 1 (MACF1), periplakin, envoplakin, and epiplakin. Some plakins exist as tissue- and differentiation-specific variants (see

examples in Angst et al. 1990; Leung et al. 2001). Among plakins, only DP localizes to DMs, where it is an obligate plaque protein. DP also participates in specialised DM-like structures, such as the *area composita* of cardiomyocytes (Franke et al. 2006).

Structure

DP shares the typical tripartite domain organization of the plakins: (i) The N-terminus of DP is composed of a plakin domain (PD) characterized by a high α-helical content, (ii) the PD is followed by a central coiled-coil rod domain responsible for the formation of parallel dimers (O´Keefe et al. 1989), and (iii) a C-terminal region consisting of three homologous plakin repeat domains (PRDs), named A, B, and C, followed by regulatory regions that cooperate to facilitate the association with IFs (Sonnenberg & Liem 2007; Kouklis et al. 1994). Each domain is ~1000 residues long (Figure I4).

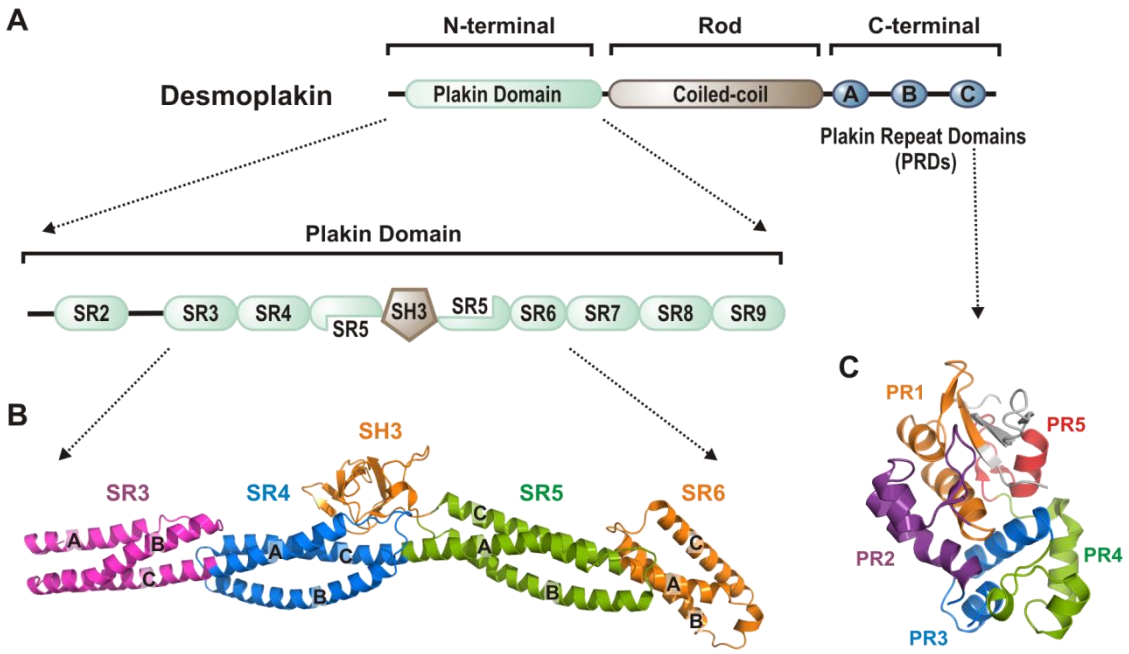

Figure I4. Structure of desmoplakin. A) Schematic representation of the domain organization of DP. Similarly to other plakins, DP has a tripartite organization: the N-terminal region contains the plakin domain; the middle region is occupied by a rod domain with coiled-coil structure involved in the dimerization of the molecule; lastly, the C-terminal region is composed of three plakin repeats domains (PRDs). The plakin domain is formed by an array of spectrin repeats. The presence of a SR2 domain upstream the SR3 is analysed in this work. **B)** Ribbon representation of the crystal structure of the SR3-SR6 region of DP (PDB entry 3R6N). Each SR consists of three α-helices (A, B, and C). **C)** Ribbon representation of the crystal structure of one PRD of DP (PDB entry 1LM5). Each PRD consists of 4.5 copies of a 38-amino acid plakin repeat (PR1 to PR5). Each PR is differentially coloured in the structure.

The plakin domain of DP

The plakin domain of DP (DP-PD) is formed by an array of seven spectrin repeats (SRs) termed SR3 to SR9 because of their correspondence to the SRs of plectin (Sonnenberg et al. 2007; Al-Jassar et al. 2011) (Figure I4-A). Each SR consists of three α-helices (A, B, and C) forming a helical bundle. As observed in the rest of the family, the DP-PD also contains a SH3 domain inserted between helices B and C of the SR5 (Jefferson et al. 2007; Ortega et al. 2011). The crystal structure of the SR3-SR6 segment of DP revealed a rod like structure in which, similarly to other SR tandem arrays, the helix C of a SR is fused to the helix A of the adjacent domain (Choi & Weis 2011) (Figure I4-B). This 3D structure is very similar to that observed for the SR3-SR5 segment of plectin (Ortega et al. 2011). In contrast with the roles of other SH3 domains involved in protein-protein interactions that regulate signal transduction pathways and trafficking (Li 2005), the SH3 domain of DP and plectin does not contain the canonical protein binding pocket. In these plakins, this area is occluded by hydrophobic interactions with the SR4, suggesting that the SH3 might have a main structural function in plakins, likely contributing to the stability of the PD (Ortega et al. 2011). It has been suggested that the region upstream of the SR3 was intrinsically disordered (Al-Jassar et al. 2011; Choi & Weis 2011). However, experiments performed in this thesis have suggested the presence of a SR2-like domain in this region.

The PD of DP is important for targeting DP to the desmosomal plaque through interactions with the armadillo proteins PKG and PKPs (Bornslaeger et al. 2001; Kowalczyk et al. 1997; Kowalczyk et al. 1999). Interestingly, phosphorylation events are thought to be involved in the regulation of these associations. For instance, the S299R mutation abolishes the PKG-DP interaction resulting in arrhythmogenic right ventricular cardiomyopathy (ARVC) (Rampazzo et al. 2002).

DP isoforms

In humans, DP exists in two splice variants, DPI (322 kDa) and DPII (259 kDa), resulting of alternative splicing of the same gene in the region of the rod domain. DPII lacks almost two thirds of the dimerization domain (O´Keefe et al. 1989). In addition, it has recently been reported a new minor isoform (DPIa) of intermediate size (Cabral et al. 2010). DPIa is expressed at lower levels but shows the same tissue distribution of DPI/II, usually expressed together. Based on the severe ARVC caused by complete ablation of DPI without affectation of DPII (Uzumcu et al. 2006), it is thought that DPI and DPII do not share all the functions.

DP functions

Mutations in the DP gene have been linked to devastating inherit diseases affecting skin, hair, nails, and teeth, as well as the heart (reviewed in Lai Cheong, Wessagowit, and McGrath 2005). DP-null mice (Gallicano et al. 2009) and epidermis-specific DP knockout mice (Vasioukhin et al. 2001) die early after bird. Ultrastructurally, DMs seem to be normal, indicating that DM-structure is not disrupted after DP ablation. However, a more detailed study of the DMs show a completely lack of IF attachments, resulting in the fatal outcome. Thus, although DP is not required for DM assembly, DP-null DMs are not functional, underlying the importance of DP in the intracellular scaffolding of desmosomal proteins and IF-tethering for maintaining tissue integrity.

One of the main roles proposed for DP in the DMs is promoting lateral associations through interactions with both PKG and PKPs. These lateral interactions drive clustering of desmosomal cadherins in the plasma membrane (reviewed in Hatsell & Cowin 2001). This idea is supported by biochemical (Kowalczyk et al. 1999) and cryoelectron microscopy tomography data (Al-Amoudi et al. 2011).

Beyond the DMs, DP has been reported to be important for microtubule organization, shape and size control of microvilli in the intestinal epithelium, and integrity of capillaries through its involvement in the formation and stabilization of microvasculature (Lechler & Fuchs 2007; Sumigray & Lechler 2012; Zhou et al. 2004; Gallicano et al. 2001).

4. Summary

There is a conventional understanding of the structure, functions, and protein interactions within the DM. However, the precise molecular mechanisms behind protein-protein interactions that orchestrate fully functional DMs are still not completely understood. Knowing how desmosomal proteins associate provides useful information about protein functions, interacting networks, and regulation (see an example in Garrod et al. 2005). In the case of desmosomal proteins, these insights are fundamental to understand how cells maintain their shape and polarity or regulate movement, adhesive potential, and strength.

The work presented here provides the first detailed examination of the molecular domains that mediate the formation of the DP-PKP1a complex. The precise mapping of the protein-protein interactions led us to determine the key interacting-regions in both molecules. In addition, the combined structural study of the PD of DP shed light on the

possible arrangement of this interaction. This work should assist in providing an understanding of how desmosomal proteins interplay their specific roles at DMs.

Non-desmosomal functions of ARM-proteins are becoming increasingly remarkable each day; however, the nuclear role of PKP1a is still largely unknown. Here, we presented the first comprehensive analysis of the major determinants of the PKP1a head domain, including the DP-binding region and the nuclear-targeting sequences. This study provides evidence of how PKP1a is able to combine DP-associated functions, with its prominent nuclear localization.

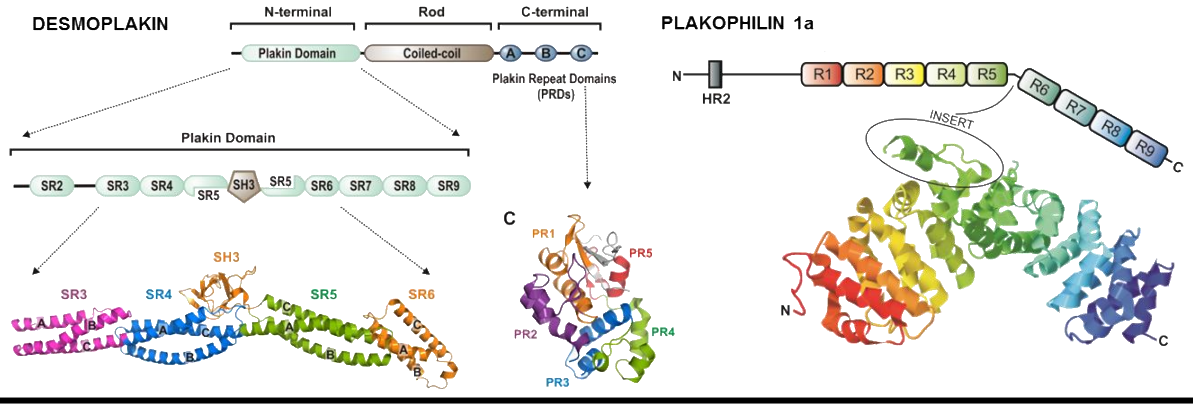

Chapter 2

SCOPE OF THE DISSERTATION

The overall scope of this work is to better understand the organization of the desmosome by characterizing two of its components, DP and PKP1a, as well as their interaction. To achieve this goal, the following specific objectives have been addressed:

i) To map in detail the interacting domains in the DP-PKP1a complex.

ii) To identify the regions implicated in the subcellular localization of DP and PKP1a

iii) To elucidate the structure of the plakin domain of DP.

By using a multi-methodological approach, we have narrowed the molecular definition of the DP-PKP1a recognition sites in both molecules. Moreover, we have identified the main regions implicated in the desmosome- versus nuclear-localization of PKP1a and we have obtained the big picture of the structural organization of the PD of DP.

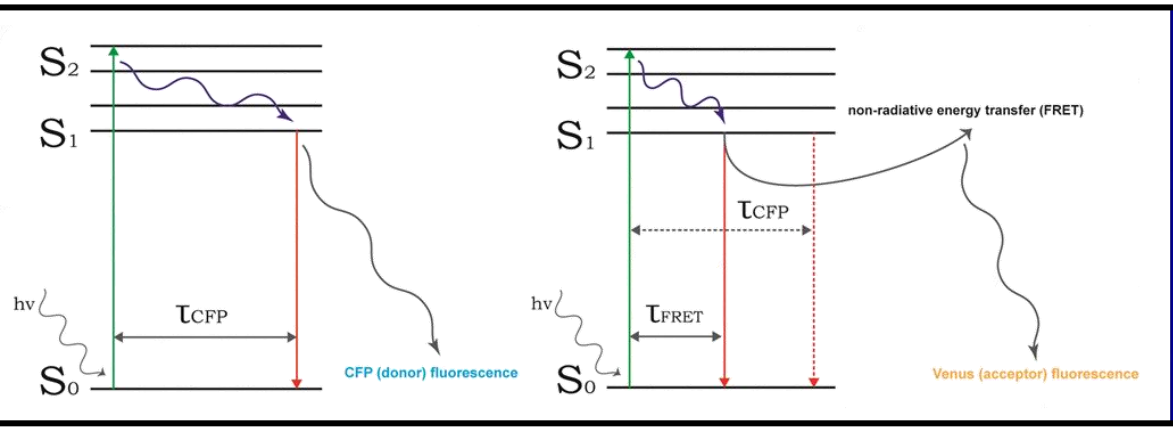

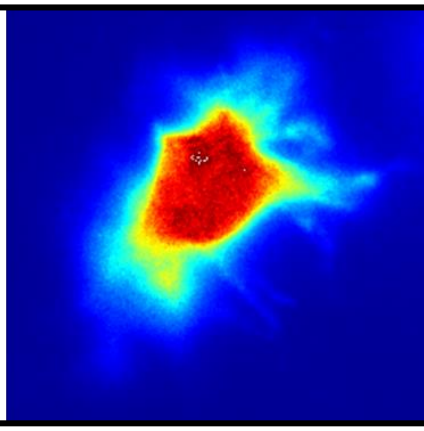

Chapter 3

MATERIALS & METHODS

1. cDNA

The cDNAs of human PKP1a, PKP2a, and PKG were obtained as I.M.A.G.E. clones from Imagenes GmbH (currently Source Bioscience) (Table M1).

Table M1. cDNA IMAGE clones used to create DNA constructs

Protein	UniProt Code	cDNA IMAGE clone	Vector	Description
Plakophilin 1a	Q13835-2	IRCMp5012B0632D	PCR-BluntII-TOPO	PKP1a cDNA full length
Plakophilin 2a	Q99959-2	IRATp970H11100D	pBluescriptR	PKP2a cDNA full length
Plakoglobin	P14923	IRAUp 969F061D	pOTB7	PKG cDNA full length

The cDNA coding for the PD of human DP (Uniprot entry P15924) was amplified by RT-PCR of mRNA extracted from Hek293T cells, kindly provided by Dr Carmen Guerrero (University of Salamanca, Spain). Total RNA was purified using the RNeasy Mini Kit (Qiagen) and mRNA was then isolated using the Poly(A)Purist MAG Kit (Ambion, Life Technologies). The cDNA coding for the DP-PD region (residues 1-1056) was amplified by two consecutive and nested PCRs using the primers shown in Table M2. The PCR product was cloned in the pETEV15b vector (see below) using NdeI and BamHI sites.

Table M2. Primers used to obtain DP-PD

A) Primers used to perform the first PCR reaction using as template DP cDNA obtained from mRNA	
DP-NEST-U001	5´ TTG CCC GCC GAC ATG AGC TGC 3´ M S C 1
DP-NEST-L1061	5´ G GTT CTG ATC CAG GAA TTT GTT CTT ATT ACA G 3´ N Q D L F K N K N C 1061 1056
B) Primers used to perform the second PCR reaction using as template DP DNA obtained in (A)	
DP-U001	5´ TGA GAA TTC CAT ATG AGC TGC AAC GGA GGC TCC C 3´ EcoR I Nde I S C N G G S 2
DP-L1056	5´ GAA TTC GGA TCC CTA CTA TTT GTT CTT ATT ACA GTT TTC CGA GTT G 3´ EcoR I BamH I *stop stop* K N K N C N E S N 1056

PKP1 and PKP2 exist as two isoforms, a shorter “a” and a longer “b”, due to alternative splicing of the primary genes products (Rickelt 2012). All of the work described here has been done with the shorter isoforms of both proteins, PKP1a and PKP2a. Nonetheless, most of the constructs names have been simplified and did not show the isoform specification “a”.

2. Modification of the PKP2a cDNA

The PKP2a sequence was modified to enable the use of specific restriction enzymes required for some cloning strategies (see below). Specifically, we eliminated from the PKP2a sequence one BamHI and two NotI restrictions sites. These sites were destroyed introducing silent mutations by site directed mutagenesis using the QuikChange method (Agilent Technologies). Briefly, the method consists of amplifying by PCR the whole vector containing the sequence of interest using two primers that hold the desired substitution. Then, the PCR product is digested with the endonuclease DpnI (Thermo Fisher Scientific) to eliminate the parental DNA. We used as template the cDNA of full length PKP2a (residues 1-838) cloned in the pBluescript SK- vector. The amplification was made by using the high fidelity polymerase *Pfu Turbo* (Agilent Technologies) and the primers reported in table M3.

Table M3. Mutagenesis primers for PKP2a

Primers for eliminating the BamHI site	
PKP2-BamX-F	5' CAAGAGCCTGCGGATCCAGGAGCAGGTG 3'
PKP2-BamX-R	5' GCTGCACCTGCTCCTGAATCCGCAGGC 3'
Primers for eliminating the NotI sites	
PKP2-Not325X-F	5' GTCGGCCAGGCGGCGGCAGGGGGAAG 3'
PKP2-Not325X-R	5' CTTCCCCCTGCCGCCGCCTGGCCGAC 3'
PKP2-Not45X-F	5' GGGGAGCAGCGGGCGCGGCGGCCAG 3'
PKP2-Not45X-R	5' CTGGCCGCCGCGCCCGCTGCTCCCC 3'

[1] *Notice that the amino acid exchanges maintain the residues in the protein sequence*

3. DNA constructs overview

DNA constructs were made by PCR amplification of the specific cDNA regions that were cloned in the appropriate vector according to their specific purpose using standard molecular biology techniques. All constructs were sequence verified before use. Tables M4, M5, and M6 summarize PKP1a, DP, and PKP2a constructs, respectively. They include given name, amino acid boundaries, restriction enzymes used to clone, vector cloned into and the main purpose of the constructs. These wide collections of PKP1a, PKP2a, and DP-PD fragments were generated based on different pieces of evidence such as, sequence analysis, structure predictions, and previously defined subdomains limits in the literature to ensure the structural integrity of all of them. Fragments design has been a continual and iterative process where the results contributed by the earliest directed the design of the upcoming ones.

Table M4. PKP1a constructs summary

Construct name	Boundaries	Vector name	Tag[Ŧ]	Restriction sites	Host	Purpose
PKP1-FLAG	1-726	pCEFLAG	FLAG	EcoRI-NotI	Mammalian	co-IP / FIM
PKP1-head-FLAG	1-243	pCEFLAG	FLAG	EcoRI-NotI	Mammalian	co-IP
PKP1-1-120	1-120	pCEFLAG	FLAG	EcoRI-NotI	Mammalian	co-IP
PKP1-1-51	1-51	pCEFLAG	FLAG	EcoRI-NotI	Mammalian	co-IP
PKP1-52-243	52-243	pCEFLAG	FLAG	EcoRI-NotI	Mammalian	co-IP
PKP1-121-243	121-243	pCEFLAG	FLAG	EcoRI-NotI	Mammalian	co-IP
PKP1-ARM-FLAG	244-726	pCEFLAG	FLAG	EcoRI-NotI	Mammalian	co-IP / FIM
PKP1-HA	1-726	pCEFLHA	HA	EcoRI-NotI	Mammalian	FIM
PKP1-ARM-HA	244-726	pCEFLHA	HA	EcoRI-NotI	Mammalian	FIM
PKP1-pcHA	1-726	pcDNA3-HA	HA	EcoRI-NotI	Mammalian	FIM
PKP1-ARM-pcHA	244-726	pcDNA3-HA	HA	EcoRI-NotI	Mammalian	FIM
PKP1	1-726	pcDNA3-CFP-C4	CFP	EcoRI-NotI	Mammalian	FIM
PKP1-head	1-243	pcDNA3-CFP-C4	CFP	EcoRI-NotI	Mammalian	FIM
PKP1-1-115	1-115	pcDNA3-CFP-C4	CFP	EcoRI-NotI	Mammalian	FIM
PKP1-1-132	1-132	pcDNA3-CFP-C4	CFP	EcoRI-NotI	Mammalian	FIM
PKP1-116-132	116-132	pcDNA3-CFP-C4	CFP	EcoRI-NotI	Mammalian	FIM
PKP1-52	52-726	pcDNA3-CFP-C4	CFP	EcoRI-NotI	Mammalian	FIM
PKP1-75	75-726	pcDNA3-CFP-C4	CFP	EcoRI-NotI	Mammalian	FIM
PKP1-98	98-726	pcDNA3-CFP-C4	CFP	EcoRI-NotI	Mammalian	FIM
PKP1-104	104-726	pcDNA3-CFP-C4	CFP	EcoRI-NotI	Mammalian	FIM
PKP1-110	110-726	pcDNA3-CFP-C4	CFP	EcoRI-NotI	Mammalian	FIM
PKP1-116	116-726	pcDNA3-CFP-C4	CFP	EcoRI-NotI	Mammalian	FIM
PKP1-121	121-726	pcDNA3-CFP-C4	CFP	EcoRI-NotI	Mammalian	FIM
PKP1-127	127-726	pcDNA3-CFP-C4	CFP	EcoRI-NotI	Mammalian	FIM
PKP1-133	133-726	pcDNA3-CFP-C4	CFP	EcoRI-NotI	Mammalian	FIM
PKP1-151	151-726	pcDNA3-CFP-C4	CFP	EcoRI-NotI	Mammalian	FIM
PKP1-181	181-726	pcDNA3-CFP-C4	CFP	EcoRI-NotI	Mammalian	FIM
PKP1-ARM	244-726	pcDNA3-CFP-C4	CFP	EcoRI-NotI	Mammalian	FIM
PKP1-Δ116-132	1-726(Δ116-132)	pcDNA3-CFP-C4	CFP	EcoRI-NotI	Mammalian	FIM
PKP1-Δ110-150	1-726(Δ110-150)	pcDNA3-CFP-C4	CFP	EcoRI-NotI	Mammalian	FIM
PKP1-head-Δ116-132	1-243(Δ116-132)	pcDNA3-CFP-C4	CFP	EcoRI-NotI	Mammalian	FIM
PKP1-head-Δ110-150	1-243(Δ110-150)	pcDNA3-CFP-C4	CFP	EcoRI-NotI	Mammalian	FIM

co-IP, co-immunoprecipitation; FIM, Fluorescence Imaging Microscopy
[Ŧ] All the tags are located at the N-terminus of PKP1a

Table M5. DP constructs summary

Construct name	Boundaries	Vector name	Tag[ǂ]	Restriction sites	Host	Purpose
DP-PD-HA	1-1056	pCEFLHA	N-HA	EcoRI-NotI	Mammalian	co-IP/ FIM
DP-NT-HA	1-545	pCEFLHA	N-HA	EcoRI-NotI	Mammalian	co-IP
DP-SR2-SR5-HA	64-545	pCEFLHA	N-HA	EcoRI-NotI	Mammalian	co-IP
DP-SR3-SR5-HA	180-545	pCEFLHA	N-HA	EcoRI-NotI	Mammalian	co-IP
DP-SR2-HA	1-170	pCEFLHA	N-HA	EcoRI-NotI	Mammalian	co-IP
DP-1-SR4-HA	1-376	pCEFLHA	N-HA	EcoRI-NotI	Mammalian	co-IP
DP-1-SR6	1-630	pCEFLHA	N-HA	EcoRI-NotI	Mammalian	co-IP
DP-SR3-SR6	180-630	pCEFLHA	N-HA	EcoRI-NotI	Mammalian	co-IP
DP-CT-HA	544-1056	pCEFLHA	N-HA	EcoRI-NotI	Mammalian	co-IP
DP-CT1025-HA	544-1025	pCEFLHA	N-HA	EcoRI-NotI	Mammalian	co-IP
DP-CT-FLAG	1-1056	pCEFLAG	N-FLAG	EcoRI-NotI	Mammalian	Dimerization
DP-PD	1-1056	pcDNA3-V-N3	N-Venus	EcoRI-NotI	Mammalian	FIM
DP-SR2-SR9	64-1056	pcDNA3-V-N3	N-Venus	EcoRI-NotI	Mammalian	FIM
DP-SR3-SR9	180-1056	pcDNA3-V-N3	N-Venus	EcoRI-NotI	Mammalian	FIM
DP-SR4-SR9	272-1056	pcDNA3-V-N3	N-Venus	EcoRI-NotI	Mammalian	FIM
DP-SR5-SR9	377-1056	pcDNA3-V-N3	N-Venus	EcoRI-NotI	Mammalian	FIM
DP-NT	1-545	pcDNA3-V-N3	N-Venus	EcoRI-NotI	Mammalian	FIM
DP-SR3-SR5	180-545	pcDNA3-V-N3	N-Venus	EcoRI-NotI	Mammalian	FIM
DP-SR2	1-170	pcDNA3-V-N3	N-Venus	EcoRI-NotI	Mammalian	FIM
DP-1-SR4	1-376	pcDNA3-V-N3	N-Venus	EcoRI-NotI	Mammalian	FIM
DP-CT	544-1056	pcDNA3-V-N3	N-Venus	EcoRI-NotI	Mammalian	FIM
DP-PD-N3	1-1056	pcDNA3-V-N3	C-Venus	KpnI-BamHI	Mammalian	FIM
DP-NT-N3	1-545	pcDNA3-V-N3	C-Venus	KpnI-BamHI	Mammalian	FIM
DP-CT-N3	544-1056	pcDNA3-V-N3	C-Venus	KpnI-BamHI	Mammalian	FIM
DP-SR2-L-pET	64-164	pETEV15b	N-octa-His	NdeI-BamHI	*E. coli*	Biophysics
DP-SR2-S-pET	64-155	pETEV15b	N-octa-His	NdeI-BamHI	*E. coli*	Biophysics
DP-1-SR6-pET	1-630	pETEV15b	N-octa-His	NdeI-BamHI	*E. coli*	Biophysics
DP-CT-pET	660-1056	pETEV15b	N-octa-His	NdeI-BamHI	*E. coli*	Biophysics
DP-CT-GCN4-22b	660-1060-GCN4	pET22b	---	NdeI-BamHI	*E. coli*	Biophysics

pcDNA3-V-C4/N3, pCDNA3-Venus-C4/N3; co-IP, co-immunoprecipitation; FIM, Fluorescence Imaging Microscopy

[ǂ] N-, refers to tags located in the N-terminus; C-, refers to tags located in the C-terminus

Table M6. PKP2a constructs summary

Construct name	Boundaries	Vector name	Tag[Ŧ]	Restriction sites	Host	Purpose
PKP2-pBSK	1-838	pBluescript SK (-)	---	EcoRI	*E. coli*	Mutagenesis
PKP2	1-838	pcDNA3-CFP-C4	CFP	EcoRI-NotI	Mammalian	FIM
PKP2-65	65-838	pcDNA3-CFP-C4	CFP	EcoRI-NotI	Mammalian	FIM
PKP2-151	151-838	pcDNA3-CFP-C4	CFP	EcoRI-NotI	Mammalian	FIM
PKP2-220	220-838	pcDNA3-CFP-C4	CFP	EcoRI-NotI	Mammalian	FIM
PKP2-ARM	349-838	pcDNA3-CFP-C4	CFP	EcoRI-NotI	Mammalian	FIM

FIM, Fluorescence Imaging Microscopy

[Ŧ] All the tags are located in the N-terminus of PKP2a

In addition, PKG full length (residues 1-745) was cloned in pcDNA3-CFP-C4 using EcoRI and NotI restriction sites. CFP-tagged PKG was used to analyse the subcellular distribution of desmosomal proteins in cell cultures of COS-7 cells and keratinocytes by confocal microscopy.

3. Primers

Primers used to generate PKP1a, PKP2a, PKG, and DP constructs were between 29 and 46 bases in length with a melting temperature (Tm) around 60ºC. They included at the 5' end sequences recognized by specific restriction enzymes. In addition, if necessary, reverse primers included a stop codon (TAG). Examples of primers used to clone PKP1a cDNA in different vectors are shown in table M7, similar primers were used to amplify and clone the other cDNAs.

Table M7. Examples of primers used to amplify the cDNA of PKP1a

Primer name	Sequence (5´ to 3´)[Ŧ]	Tm (ºC)[ǂ]	Vectors
PKP1-U001	TGA GAATTC CAT ATGAACCACTCGCCGCTCAAGACC EcoR I Nde I M N H S P L K T 1	60.8	pETEV15b, pBSK (-), pET22b
PKP1-L726	TGA GAATTC GGATCCCTACTAAGAATCGGGAGGTGAAGTTCCTG EcoR I BamH I *Stop Stop* F R S T F N R 726	58.8	pETEV15b, pBSK (-), pET22b
PKP1-U001-EcoRI	TGA GAATTC ATGAACCACTCGCCGCTCAAGACC EcoR I M N H S P L K T 1	60.8	pCEFLAG/HA, pcDNA3-C4/HA
PKP1a-L726-NotI	TGA GCGGCCGC CTA GAATCGGGAGGTGAAGTTCCTGAG Not I *Stop* F R S T F N R L 726	59.1	pCEFLAG/HA, pcDNA3-C4/HA

pBSK (-), pBluescript SK (-), pcDNA3-C4, pcDNA3-CFP-C4 and pcDNA3-Venus-C4

[Ŧ] Restriction sites and the encoded amino acids are shown under the DNA sequences

[ǂ] The Tm was calculated for the region matching the PKP1a cDNA

4. Vectors and cloning

Cloning in pBluescript SK (-)

pBluescript SK (-) (Agilent technologies) is a phagemid for bacterial expression used to general cloning. pBluescript harbours a versatile multi cloning site (MCS). PKP2a was subcloned in pBluescript SK (-) by using EcoRI as restriction enzyme to perform the mutagenesis reactions.

Cloning in pCEFL vectors

pCEFLAG and pCEFLHA vectors (Chiariello et al. 2000) encode for a Kozak consensus sequence (Kozak 1986) followed by the FLAG (Hopp et al. 1988) or the HA (Wilson et al. 1984) tags (Figure M1). Both vectors harbour equivalent MCS. Expression of the cDNA fragments is under the control of the elongation factor 1 promoter (EF1). PKP1a-constructs were subcloned in pCEFLAG and DP-constructs in pCEFLHA, unless otherwise indicated. In all cases, cDNAs were cloned using EcoRI and NotI restriction sites.

Figure M1. MCS of pCEFL vectors. DNA sequence of the coding strand of the MCS of the pCEFL vectors. Main characteristics such as Kozak sequence (KZ), tag (FLAG or HA) and restriction sites used to clone (EcoRI and NotI) are highlighted in bold.

Cloning in pcDNA3-CFP/Venus vectors

The pcDNA3 vector for mammalian expression (Invitrogen) was modified to create fusion proteins tagged with the cyan fluorescent protein (CFP) (Heim & Tsien 1996) or with Venus, which is an improved version of the yellow fluorescent protein (YFP) (Nagai et al. 2002). The cDNA of CFP and Venus was amplified using as templates the pCFP-N1 and pVenus-N1 vectors, kindly provided by Prof A. Sonnenberg (Netherlands Cancer Institute, Amsterdam; The Netherlands). We engineered two kinds of vectors, those coding for fusion proteins with CFP or Venus at the N-terminus (pcDNA3-CFP-C and pcDNA3-Venus-C) and those that code for C-terminal fluorescent proteins (pcDNA3-CFP-N and pcDNA3-Venus-N).

pcDNA3-CFP-C and pcDNA3-Venus-C vectors

Table M8 summarizes the pcDNA3-CFP-C and pcDNA3-Venus-C vectors that we engineered.

Table M8. pcDNA3-CFP-C and pcDNA3-Venus-C vectors

Vector name	Tag[Ŧ]	Sites for CFP/Venus	Modification
pcDNA3-CFP-C1	N-CFP	HindIII/BamHI	----
pcDNA3-CFP-C2	N-CFP	HindIII/BamHI	EcoRI in frame with BamHI
pcDNA3-CFP-C3	N-CFP	HindIII/BamHI	A206K, monomeric CFP
pcDNA3-CFP-C4	N-CFP	HindIII/BamHI	Intermediate flexible linker
pcDNA3-Venus-C1	N-Venus	HindIII/BamHI	----
pcDNA3-Venus-C2	N-Venus	HindIII/BamHI	EcoRI in frame with BamHI
pcDNA3-Venus-C3	N-Venus	HindIII/BamHI	A206K, monomeric CFP
pcDNA3-Venus-C4	N-Venus	HindIII/BamHI	Intermediate flexible linker

[Ŧ] N-, refers to tags located in the N-terminus

All the experiments reported here were performed with pcDNA3-CFP-C4 or pcDNA-Venus-C4 vectors. They were created as follows: first, the cDNA of CFP and Venus were amplified by PCR using forward primers that add a HindIII site and a Kozak sequence, and reverse primers that add a BamHI site (Table M9). PCR products were cloned in pcDNA3 using HindIII and BamHI sites. We named the resulting vectors pcDNA3-CFP-C1 and pcDNA3-Venus-C1.

Table M9. pcDNA3-C1 primers

CFP/Venus-Hind-For	5' TGA GAATTC AAGCTT GCC **GCC ACC ATG G**TG AGC AAG GGC 3' EcoRI HindIII **K Z** M V S K G
CFP/Venus-BamH-Rev	5' GCC GAATTC GGATCC CTT GTA CAG CTC GTC CAT GC 3' EcoRI BamHI K Y L E D M

KZ, Kozak consensus sequence

We intended to use the EcoRI site for cloning our cDNA of interest, yet the EcoRI site in the C1 vectors was not in the correct frame with the CFP and Venus sequences. Therefore, we deleted one base pair between the BamHI and EcoRI sites by site directed mutagenesis using the QuikChange method (Agilent Technologies) as explained before. Table M10 shows the parental sequence, the primers, and the resulting sequence of the vectors named pcDNA3-CFP-C2 and pcDNA3-Venus-C2.

Table M10. pcDNA3-C2 modifications

pcDNA3-C1 original MCS
TAGGGAGACCCAAGCTTGGTACCGAGCTCGGATCC ACT AGT AAC GGC CGC CAG TGT GCT G[ŦG]A ATT CTG HindIII BamHI EcoRI
Mutagenesis primers
pcDNA3-EcoRI-F 5' GC CGC CAG TGT GCT GAA TTC TGC AGA TAT CC 3'
pcDNA3-EcoRI-R 5' ATA TCT GCA GAA TTC AGC ACA CTG GCG GCC G 3'
pcDNA3-C2 resulting MCS
TAGGGAGACCCAAGCTTGGTACCGAGCTCGGATCC ACT AGT AAC GGC CGC CAG TGT GCT GAA TTC TG HindIII BamHI EcoRI

[Ŧ] Note the guanine eliminated to keep BamHI and EcoRI restriction sites in frame

In a third step, we introduced the A206K substitution in CFP and Venus by site directed mutagenesis (Table M11). The mutation A206K disrupts the dimerization interface resulting in monomeric forms of CFP and Venus (von Stetten et al. 2012), and prevents false positives in protein-protein interaction studies. Vectors carrying the A206K substitution were named pcDNA3-CFP-C3 and pcDNA3-Venus-C3.

Table M11. pcDNA3-C3 modification primers

CFP-A206K-F	5' CCTGAGCACCCAGTCC**AAG**CTGAGCAAAGACCCCAAC 3'
CFP-A206K-R	5' GTTGGGGTCTTTGCTCAG**CTT**GGACTGGGTGCTCAGG 3'
Venus-A206K-F	5' CCTGAGCTACCAGTCC**AAG**CTGAGCAAAGACCCCAAC 3'
Venus-A206K-R	5' GTTGGGGTCTTTGCTCAG**CTT**GGACTGGTAGCTCAGG 3'

Finally, we introduced a small linker comprising five repetitions of Gly-Ser between the fluorescent tag and the gene cloned after the EcoRI site. The combination of small (Gly) and polar (Ser) residues provides flexibility to the fusion protein (Argos 1990). The cDNA coding for the linker was created by annealing two complementary oligonucleotides that left single stranded tails that were complementary for the BamHI and EcoRI overhangs in the digested vector (Table M12). For annealing, a mixture 1 µM of each primer in annealing buffer (10 mM Tris, pH 7.5–8.0, 50 mM NaCl, 1 mM EDTA) was heated for 5 min at 95 °C and was slowly cooled down to 15 °C over a period of 90 min using a thermal cycler. The resulting cDNA was cloned using the BamHI and EcoRI sites to create the final pcDNA3-CFP-C4 and pcDNA3-Venus-C4 vectors.

Table M12. pcDNA3-C4 modification primers	
	G S G S G S G S G S 5’ gatccGGTAGCGGCTCGGGCAGTGGAAGTg 3’ 3’ GCCATCGCCGAGCCCGTCACCTTCACTTAA 5’
Link-BamEco-GS8-F	5’ gatccGGTAGCGGCTCGGGCAGTGGAAGTg 3’
Link-BamEco-GS8-R	5’ AATTCACTTCCACTGCCCGAGCCGCTACCG 3’

The cDNAs of PKP1a and DP were amplified using forward primers that add and EcoRI site, and reverse primers that add a stop codon and a NotI site. They were cloned in the pcDNA3-CFP-C4 and pcDNA3-Venus-C4 using EcoRI and NotI sites.

pcDNA3-CFP-N and pcDNA3-Venus-N vectors

pcDNA3-CFP-N and pcDNA3-Venus-N vectors produce fusion proteins with CFP or Venus in the C-terminus. Table M13 summarizes the variants of these vectors that we created.

Table M13. pcDNA3-CFP-N and pcDNA3-Venus-N vectors

Vector name	Tag	Sites for CFP/Venus	Modification
pcDNA3-CFP-N1	C-CFP	EcoRI/XhoI	----
pcDNA3-CFP-N2	C-CFP	EcoRI/XhoI	A206K, monomeric CFP
pcDNA3-CFP-N3	C-CFP	EcoRI/XhoI	Intermediate flexible linker
pcDNA3-Venus-N1	C-Venus	EcoRI/XhoI	----
pcDNA3-Venus-N2	C-Venus	EcoRI/XhoI	A206K, monomeric Venus
pcDNA3-Venus-N3	C-Venus	EcoRI/XhoI	Intermediate flexible linker

[Ŧ] C-, refers to tags located in the C-terminus

The cDNAs of CFP and Venus were amplified by PCR using forward primers that add an EcoRI site and reverse primers that included a termination codon and an XhoI site (Table M14). PCR products were digested with EcoRI and XhoI and were cloned in pcDNA3 using these sites. We named the resulting constructs pcDNA3-CFP-N1 and pcDNA3-Venus-N1.

Table M14. pcDNA3-CFP-N1 and pcDNA3-Venus-N1 primers

CFP/Venus-Eco-For	5’ GCC GAA TTC GCG GCC GC **T**[Ŧ] ATG GTG AGC AAG GGC GAG GAG 3’ EcoRI Not I M V S K G E E
CFP/Venus-Eco-Rev	5’ GCC GAT ATC CTC GAG **TTA** CTT GTA CAG CTC GTC CAT GCC 3’ EcoRV XhoI **stop** K Y L E D M G

[Ŧ] Note the extra-base added to keep CFP/Venus in frame

Next, we introduced by site directed mutagenesis as described above the A206K substitution to create pcDNA3-CFP-N2 and pcDNA3-Venus-N2. Finally, a cDNA encoding a Gly-Ser linker was introduced between the BamHI and EcoRI sites (see above) to create the pcDNA3-CFP-N3 and pcDNA3-Venus-N3.

DP cDNAs were subcloned in pcDNA3-Venus-N3. PCR amplification was made using forward primers that add a Kozak sequence and a KpnI site, and reverse primers that add a BamHI site and do not contain stop codons. The PCR products were digested with KpnI and BamHI and were cloned using the same sites in pcDNA3-Venus-N3.

Cloning in pETEV15b

pETEV15b is a derivative of the pET15b vector (Novagen) for expression of His-tagged fusion proteins in bacteria. pETEV15b had been engineered in our laboratory to code for an amino-terminal octa-Histidine tag followed by a sequence recognized by the tobacco etch virus (TEV) protease (Alonso-García et al. 2009) (Figure M2). The small MCS contains NdeI and BamHI sites that were used for cloning in this vector.

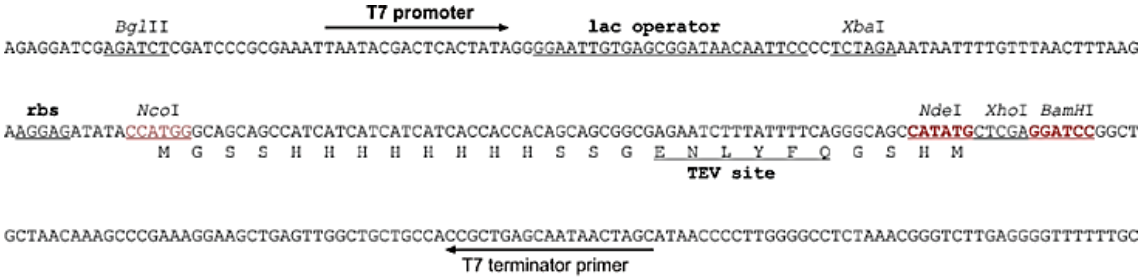

Figure M2. pETEV15b MCS. DNA sequence of the coding strand of the pETEV15b vector. The main characteristics of the vector have been highlighted. The TEV protease recognizes the ENLYFQ site (underlined) and digests right after it. cDNAs were cloned using the NdeI and BamHI sites (highlighted in red).

To clone in pETEV15b, fragments of cDNA of DP were amplified using forward primers that add an NdeI site and reverse primers that add a stop codon followed by a BamHI site (see Table M7 for examples of similar primers). PCR products were digested with NdeI and BamHI and cloned into pETEV15b using these sites.

Cloning in pET22b

The pET22b vector (Novagen) was used to express in bacteria the recombinant protein DP-CT-GCN4 without any additional sequence or tag (DP-CT-GCN4-22b). The expression region of pET22b codes for a pelB leader secretion sequence flanked by NdeI and NcoI sites, followed by a MCS that includes a BamHI site. The chimera DP-

SR7-SR9-GCN4 was made as follows. In a first round of PCR two cDNA fragments were produced. On one side the cDNA coding for the residues 660-1060 of DP was amplified using the forward primer DP-U660 (that adds an NdeI site) and the reverse primer DP-L1060-GCN4 (that adds 19 nucleotides of the GCN4 cDNA) (Table M15). In parallel, the GCN4 cDNA was amplified using the primers GCN4-U01 and GCN4-Bgl-L. A mix of the PCR products of the two previous reactions was used as template for a second PCR in which the DP-GCN4 chimera was amplified using the primers DP-U660 and GCN4-Bgl-L. The resulting DNA was digested with NdeI and BglII and was ligated to pET22b previously digested with NdeI and BamHI (the single strand produced by BglII matches that produced by BamHI resulting in the destruction of both sites after ligation). The coding cDNA included a stop codon upstream of the BglII-BamHI site; hence, the expressed protein did not contain any additional sequence.

Table M15. Primers used to create the DP-GCN4 chimeric constructs

Primer	Sequence (5' to 3')
DP-U660	TGA GAA TTC CAT ATG GAA AAT GAC AAG CAA GAA ACA TGG ATG CTG Nde I E N D K Q E T W M L 660
DP-L1060-GCN4	C TTC CAG CTG TTT CAT GCG CTG ATC CAG GAA TTT GTT CTT ATT ACA GTT TTC CGA GTT G E L Q K M R Q D L F K N K N C N E S N GCN4 1060 DP
GCN4-U01	CGC ATG AAA CAG CTG GAA GAC R M K Q L E D
GCN4-Bgl-L	TGA GAA TTC AGA TCT CTA CTA GCG TTC ACC AAC CAG TTT TTT CAG 3' BglII Stop Stop R E G V L K K L

5. Recombinant DNA maintenance and production

Recombinant DNA was maintained in the *E. coli* strain DH5α. Bacteria were grown either in solid media using LB agar plates or in the liquid media LB or 2xYT. In all cases, antibiotic selection was maintained by adding ampicillin (100 mg/l) to the medium. Recombinant DNA was isolated from bacterial cultures using the GeneJET™ Plasmid Miniprep or Maxiprep Kits (Thermo Fisher Scientific) according to the manufacturer's specifications.

6. Cell lines and culture conditions

Cell lines used through this work are specified in table M16. This table also summarizes the main cellular characteristics and culture conditions as well as the people who provide us with the different cell lines.

Table M16. Cell lines and culture conditions

Cell line	Organism	Tissue	Medium	Freeze medium	Provider	Selected references
COS-1	*C. aethiops*	kidney	DMEM	DMEM + 5-10% DMSO	C. Guerrero (CIC, Salamanca)	(Gluzman 1981)
COS-7	*C. aethiops*	kidney	DMEM	DMEM + 5-10% DMSO	A. Sonnenberg (NKI, Amsterdam)	(Gluzman 1981)
Hek293T	*H. sapiens*	kidney	DMEM	DMEM + 5-10% DMSO	A. Sonnenberg (NKI, Amsterdam)	(DuBridge et al. 1987)
NHK	*H. sapiens*	foreskin	SFM	50% SFM + 40% FBS + 10% DMSO	A. Sonnenberg (NKI, Amsterdam)	(Niessen et al. 1996)
HaCaT	*H. sapiens*	skin	DMEM	50% DMEM + 40% FBS + 10% DMSO	A. Sonnenberg (NKI, Amsterdam)	(Boukamp et al. 1988)
PA-JEB/β4	*H. sapiens*	skin	SFM	50% SFM + 40% FBS + 10% DMSO	A. Sonnenberg (NKI, Amsterdam)	(Niessen et al. 1996)
PKP1-null	*H. sapiens*	skin	SFM	50% SFM + 40% FBS + 10% DMSO	AP. South (MRI, Dundee)	(South et al. 2003)

NHK, Normal Human Keratinocytes; PKP1-null, PKP1-null keratinocytes; *C. aethiops, Cercopithecus aethiops; H. sapiens*, Homo sapiens; SFM, Keratinocyte Serum-Free Medium

Dulbecco´s modified Eagle´s medium (DMEM; Sigma-Aldrich or Life Technologies) was supplemented with 10 % fetal bovine serum (FBS; Life Technologies) and 1% penicillin/streptomycin (Life Technologies). Keratinocyte serum-free medium (SFM, Life Technologies) was supplemented with 50 µg/mL bovine pituitary extract (BPE), 5 ng/mL epidermal growth factor (rEGF), 100 U/mL penicillin, and 100 U/mL streptomycin (Life Technologies) providing a complete medium to grow keratinocytes at a low Ca^{2+} concentration (0.09 mM). Where necessary, cells were grown between 8-24 hours in DMEM, containing 1.2 mM Ca^{2+} concentration, to stimulate keratinocyte differentiation. All keratinocyte cell lines, with the exception of HaCaT cells, were seeded on collagen-coated (Advanced BioMatrix or Corning) dishes. Cell number was determined using either a Neubauer chamber or a cell counter (Beckman Coulter).

7. Transient transfections

The main purposes and conditions of the transient transfections of fusion proteins are summarized in table M17. Cells were processed 24-48 hours after transfection.

Table M17. Transient transfection conditions

Construct type	Cell line	Purpose	Reagent	Medium	Ratio‡	DNA (µg)	Dish type
FLAG/HA-tagged	COS-1	co-IP	JetPei (Polyplus transfection)	NaCl	1:2	5/10	60/100 mm
FLAG/HA-tagged	COS cells	FIM	X-tremeGENE 9 (Roche) / PEI (Polysciences inc.)	DMEM free∓	1:3	1/5	12-well plate
CFP/Venus-tagged	COS-7	FIM	PEI (Polysciences inc.)	DMEM free∓	1:2	1	6/12-well plate
CFP/Venus-tagged	Keratinocytes	FIM	X-tremeGENE HP (Roche)	Optimem	1:4	1	12-well plate

FIM, Fluorescence imaging microscopy (includes Immunofluorescence experiments, confocal microscopy, and FLIM)
∓ DMEM free, DMEM without any supplementation
‡ Ratio, DNA / Transfection reagent ratio

8. Cell lysis, co-immunoprecipitation (co-IP) and Western blotting

Total protein extracts were obtained from cells seeded at high density. Typically, cells were washed twice with ice-cold phosphate buffered saline (PBS) and subsequently lysed on ice in Triton X-100-based buffer consisting of 20 mM Tris-HCl (pH 7.5), 150 mM NaCl, 0.5 % Triton X-100, 1 mM Na_3VO_4, 25 mM NaF, 1 mM PMSF, 1x protease inhibitor cocktail (Roche). Cell lysates were cleared by centrifugation at 16000 xg (4ºC) and protein concentrations were determined with a Bradford assay using bovine serum albumin *(*BSA) as a standard. Equal amounts of total protein (30-40 µg) were loaded in SDS-polyacrylamide gels (9-20 %) after being heated at 95ºC in Laemmli buffer (2x: 125 mM Tris-HCl (pH 6.8), 4 % SDS, 55 % glycerol, 2 % β-mercaptoethanol, 0.02 % bromophenol blue; 4x: 250 mM Tris-HCl (pH 6.8), 8 % SDS, 40 % glycerol, 4 % β-mercaptoethanol, 0.04 % bromophenol blue), and separated by SDS-polyacrylamide gel electrophoresis (SDS-PAGE). Proteins were electrophoretically transferred to Immobilon-P membranes (Millipore) and analysed by Western blotting according to standard procedures. Inmmunoreactivity was detected using ECL reagents (Bio-rad, Thermo, or GE Healthcare) or the Odyssey Infrared Imaging System (LI-COR, Inc.). Primary and secondary antibodies used in Western blotting are summarized in tables M18 and M19, respectively.

Table M18. Primary antibodies used in Western blotting

Antibody	Species	Epitope	Supplier	Dilution
HA.11 Clone 16B12	Mouse	HA: influenza hemagglutinin epitope (YPYDVPDYA)	Covance (MMS-101R)	1:1000
HA-probe (Y-11)	Rabbit	Internal region of the influenza hemagglutinin (HA)	Santa Cruz (sc-805)	1:1000
Anti-FLAG M2	Mouse	FLAG tag (DYKDDDDK)	Sigma-Aldrich (F3165)	1 µg/mL
Anti-β-Actin Clone AC-15	Mouse	N-terminal end of the β-isoform of actin	Sigma-Aldrich (A5441)	1:10000

Table M19. Secondary antibodies used in Western blotting

Antibody	Type	Detection	Species	Target	Supplier
ECL Mouse IgG, HRP-linked	HRP-conjugated	ECL	Sheep	Mouse IgG	GE Healthcare (NA931)
Goat anti-rabbit IgG-HRP	HRP-conjugated	ECL	Goat	Rabbit IgG	Santa Cruz (sc-2004)
Goat anti-Mouse IgG, DyLight 680	Dye-conjugated	Odyssey	Goat	Mouse IgG	Thermo (35518)
Goat anti-Rabbit IgG, DyLight 680	Dye-conjugated	Odyssey	Goat	Rabbit IgG	Thermo (35568)

HRP, horseradish peroxidase, ECL, Chemiluminescent detection, Odyssey, Odyssey Infrared Imaging System.

[Ŧ] Subject to same case-by-case exceptions, secondary antibodies where applied using a dilution 1:5000

Co-immunoprecipitation assays (co-IP) were performed after transient transfection of FLAG- and HA-tagged proteins. FLAG-fusion proteins were purified by using the anti-FLAG M2 affinity gel (Sigma-Aldrich), which consists of a purified murine IgG monoclonal antibody covalently attached to agarose. The resin was used in the batch format following the indications of the manufacturer. Briefly, cleared lysates where fractionated in order to preserve ~20 % of the lysates for verification purposes of total lysates by Western blotting. The remaining lysates were incubated with the pre-equilibrated beads for 1 hour at 4ºC with rotation. During this time, FLAG-tag proteins bind to the resin and interacting partners become attached to FLAG-tag proteins. After washing 4 times, proteins were eluted by adding SDS-PAGE sample buffer. Co-IP were followed by Western blotting proved with a polyclonal α-HA antibody to identify the HA-tagged fragments that have interacted with the FLAG-fusion protein during the incubation step.

9. Immunostaining and fluorescent imaging acquisition

Generally, cells growing in glass coverslips were rinsed with PBS, fixed in 2-4 % paraformaldehyde (PFA), washed twice with PBS, permeabilized by treatment with 0.2 % Triton X-100, and washed again with PBS. Coverslips were subsequently blocked

with 2 % BSA in PBS for 1 hour, incubated with primary antibodies for 1 hour, washed three times with PBS, and incubated with secondary antibodies for 45 minutes; all these steps were run at room temperature (RT). After washing with PBS (3 times), coverslips were mounted in Mowiol supplemented with DABCO (Calbiochem). Cells transiently transfected with fluorescent tags were just fixed in 2-4 % PFA and mounted before fluorescent imaging acquisition.

Previous reports have shown different immunolocalization results of PKPs when using different experimental protocols (see Rickelt, 2012; Schmidt et al., 1997; South et al., 2003). In our hands, with the standard indirect immunofluorescence protocol (described above) we only saw PKP1a and PKP2a over the plasma membrane. Thus, for the experiments where we wanted to observe the possible nuclear localization of these proteins, cells were treated with 0.2 % Triton X-100 in PBS for five minutes before fixation. The following steps were the same than in the standard protocol.

Nuclear counterstaining was made by using different dyes depending on the needs. In standard indirect immunofluorescences we used DAPI (Invitrogen) as blue nuclear counterstain, whereas when we worked with CFP-transfected cells UV-excited dyes are not useful because of the bleed-through between channels. In these cases, we chose a red (propidium iodide (PI), Life Technologies) or far-red (TO-PRO-3, Life Technologies) counterstain. Fixed cells were label with 1 µg/mL DAPI or 1 µM TO-PRO-3 in PBS for 5-15 minutes just before mounting. PI also binds to RNA, requiring treatment of specimens fixed in PFA with RNase in order to eliminate such staining. Thus, fixed and permeabilized cells were incubated with 100 µg/mL RNase A (5 PRIME) in PBS for 30-60 minutes before adding 1 µg/mL PI for 5 minutes before fixation.

Images were obtained in a Leica TCS SP5 confocal microscope. Pictures were processed using LAS-AF software (Leica Microsystems). Antibodies used in indirect immunofluorescences are summarized in tables M20 and M21.

Table M20. Primary antibodies used in immunofluorescence

Antibody	Target	Species	Supplier	Dilution
Desmoplakin I/II C-20	C-terminus of human DP I/II	Goat	Santa Cruz (sc-18086)	1:50
Desmoglein I + II (clone DG3.10)	"Band 3" polypeptide of bovine DMs	Mouse	Acris Antibodies (BM370)	1:50
E-Cadherin Clone 36	Recombinant C-terminal human E-Cadherin	Mouse	BD Biosciences	1:50
Anti-FLAG M2	FLAG tag (DYKDDDDK)	Mouse	Sigma-Aldrich (F3165)	3 µg/mL
HA.11 Clone 16B12	HA epitope (YPYDVPDYA)	Mouse	Covance (MMS-101R)	1:100
γ-catenin C-20	C-terminus of human γ-catenin	Rabbit	Santa Cruz (sc-1497)	1:50
Plakophilin-1 (3G250)	N-terminal region of human PKP1	Mouse	Thermo (MA1-25786)	10 µg/mL
Plakophilin-2 (28)	residues 19-183 of human PKP2	Mouse	Santa Cruz (sc-136039)	1:50

Table M21. Secondary antibodies used in immunofluorescence

Antibody	Target	Species	Supplier	Dilution
Texas Red goat IgG (H+L)	mouse	Goat	Life Technologies (T-862)	1:200
Alexa Fluor 488 IgG (H+L)	goat	Donkey	Life Technologies (A-11055)	1:200
Cy3 IgG (H+L)	rabbit	goat	Abcam	1:200
Cy5-conjugated AffiniPure IgG (H+L)	mouse	Donkey	Jackson Immunoresearch	1:200

10. Fluorescence lifetime imaging microscopy

Fluorescence lifetime imaging microscopy (FLIM) is a quantitative tool to measure the lifetime (Ƭ) of molecular fluorescence. Fluorescence lifetime is the average time that a fluorophore remains in an excited state before returning to the ground state. This time is dependent of the environment of the fluorescent molecule providing an useful tool to investigate, among other purposes, the interaction between proteins in living cells (see examples in Danquah et al. 2012; Thomas et al. 2006; von Arnim et al. 2004).

FLIM was the method of choice for studying DP-PKP1a interactions because, unlike fluorescence intensity —the property measured in the most of the Förster resonance energy transfer (FRET)-based methods—, lifetime is independent of fluorophore concentration. This is a key point in the study of inter-molecular interactions, being FLIM the preferred method when donor-acceptor stoichiometry is variable. Among the different FLIM approaches, we have used frequency domain FLIM (FD-FLIM) which

uses periodically modulated light for the excitation and the generated fluorescent light is demodulated by using a micro-channel plate image intensifier (technical details can be reviewed in Zhao, Young, & de Jong, 2011).

Simplifying, a routine FLIM experiment requires co-transfection of cells with the proteins of interest tagged with an appropriate FRET-pair of fluorophores. In our case, we used CFP to tag PKP1a-fragments and the YFP variant Venus to tag DP-fragments. Twenty-four hours post-transfection, cells growing in 24 mm coverslips were mounted in slide holders and positioned in a wide-field microscope equipped with a fluorescence lifetime measuring system and a climate control chamber to keep sample temperature as stable as possible (37ºC degrees in our case). After calibration of the system with a fluorophore of known lifetime (e.g. rhodamine or fluorescein), the donor fluorophore (CFP) is excited; once in its electronic excited state (S_2), if the acceptor fluorophore (Venus) is close enough (<10 nm), CFP may transfer energy to it through non-radiative processes. This transfer will reduce CFP lifetime (Figure M3). Measuring the donor lifetime allows us to know whether CFP and Venus are coupled by dipole-dipole interactions and, therefore, whether the proteins of interest are interacting.

FLIM experiments were performed by using a LIFA (Lambert Instruments Fluorescence lifetime Attachment) system (Lambert Instruments BV) which includes a LI2CAM Intensified CCD camera (Lambert Instruments BV) as reference camera and a Leica DM IRE2 (Leica Microsystems) as inverted microscope. FD-FLIM system was controlled via the LI-FLIM software developed by Lambert Instruments. The fluorescent filter cube was comprised by a 472-nm single-band excitation filter, a 495-nm long pass dichroic mirror, and a 520-nm single-band emission filter (Semrock Inc.). We used a Zeiss oil objective with a magnification of 40x and a numerical aperture of 1.3 for the lifetime measurements. The calibration of the system was carry out using a 10 μM fluorescein solution (Sigma-Aldrich) in deionized water (τ=3.83 ns). During measurements cells were maintained in HBS buffer (10 mM HEPES, 140 mM NaCl, 5 mM KCl, 1mM MgCl2, 10 mM glucose, pH 7.20) (for further technical details see Qiaole Zhao et al., 2012).

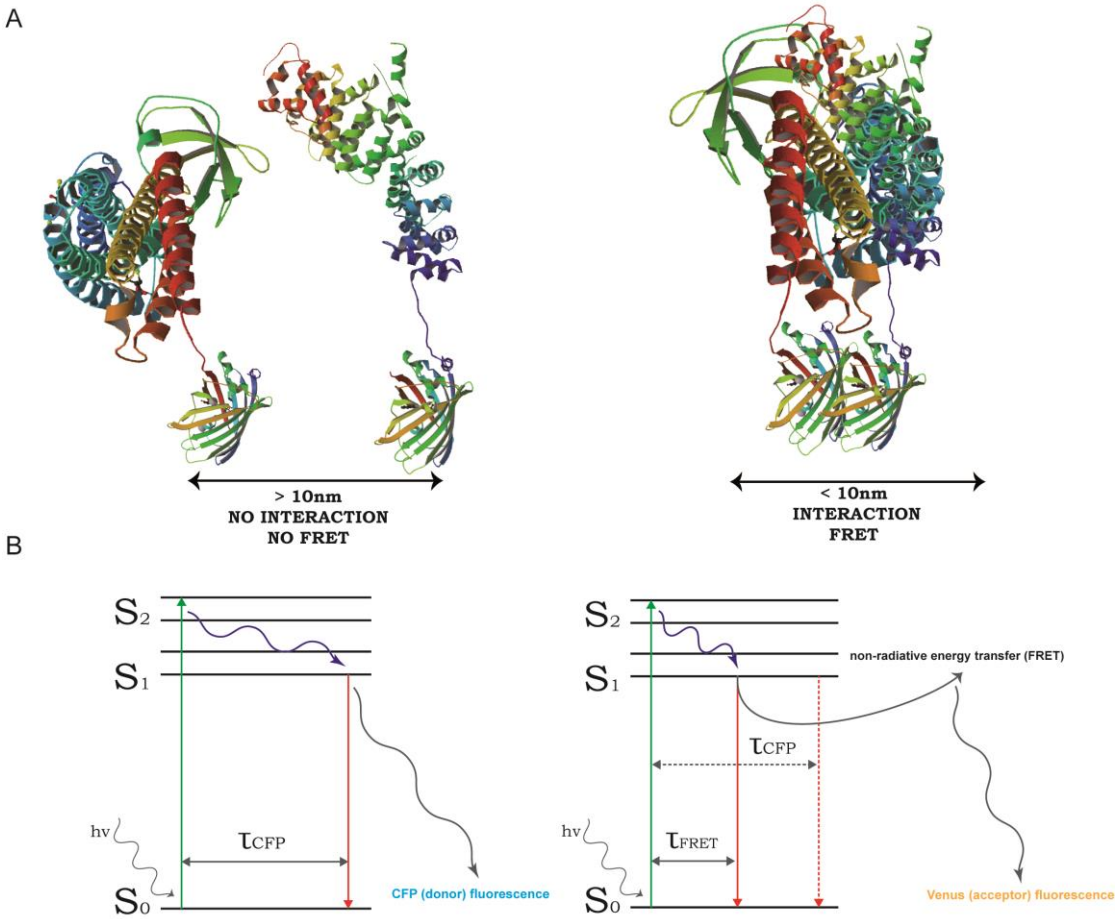

Figure M3. Simplified Jablonski diagrams illustrating the lifetime depletion due to non-radiative energy transfer between the CFP/Venus FRET-pair. **A)** Schematic drawing of the structure of the proteins of interest tagged with the fluorophores. On the left side, a situation of no interaction (distance > 10 nm) and, therefore, no FRET is represented. On the right side, proteins are interacting (distance < 10 nm) which allows the non-radiative energy transfer by means of dipole-dipole interactions between CFP and Venus. **B)** Simplified Jablonski diagrams illustrating the situations represented in A. On the left side, upon excitation of CFP by modulated light ($h\nu$), CFP goes into an excited state (S_2) (green arrow) for a certain characteristic time (CFP lifetime, τ_{CFP}) and then relaxes to the ground state (S_0) (red arrow) by emission of a less energetic photon (CFP fluorescence). On the right side, the closeness between CFP and Venus due to interaction between the fusion proteins, leads to resonance energy transfer from the donor to the acceptor, quenching the donor fluorescence. Note that CFP lifetime (τ_{FRET}) is reduced (red arrow) when an interaction exists in comparison of a situation with no interaction between tested proteins (τ_{CFP}, red dashed arrow).

Statistical analysis of FLIM data

Data analysis of FLIM experiments was performed by using GraphPad Prism 6.04 (GraphPad Software, Inc.). Statistical differences between the samples and the control group were evaluated using a 2-tailed t-test with the Welch´s correction in order to

avoid the necessity for equal variances in the samples (Ruxton 2006). A p-value ≤ 0.05 was used as indicative of statistical significance.

When mapping the PKP1a-interaction site in DP, the control group was the co-transfection of a PKP1a-fragment tagged with CFP with the fluorophore Venus cloned in the empty vector pcDNA3-Venus (coding for free-Venus). When mapping the DP-interaction site in PKP1a the control group was the co-transfection of both empty vectors pcDNA3-CFP and pcDNA3-Venus (coding for free-CFP and free-Venus). Average CFP lifetimes higher than the average CFP lifetime of the control group were considered not significant because only decreases in the CFP lifetime have biological relevance in FLIM experiments, being representative of protein-protein interaction. These higher values of CFP lifetime are often observed in samples where there is no interaction but the expression levels of the proteins are quite lower than the expression of the free fluorophores of the negative control.

11. Bacterial protein expression and purification

Bacterial protein expression was carried out using the *E. coli* strain BL21(DE3)T1 (Studier & Moffatt 1986) growing in 3 L of Terrific Broth (Tartof & Hobbs 1987) supplemented with 100 mg/L ampicillin. Protein expression was induced in log phase (A_{600}= 0.6-0.8) by addition of 0.2 mM IPTG. Bacteria were allowed to grow for 3-4 hours at 37 ºC or O/N at 15 ºC. Pelleted bacteria were resuspended in binding buffer containing 20 mM Tris-HCl (pH 7.9), 500 mM NaCl, 5 mM imidazole and 0.1 % (v/v) Triton X-100. Bacteria lysis was completed by one freezing-thawing cycle, followed by sonication. The soluble fraction was separated from the cell debris by centrifugation at 16,000 x*g* (30 min, 4ºC).

Fusion proteins were purified from bacteria supernatants by immobilized metal ion affinity chromatography (IMAC) using a 5 mL Ni^{2+} Hi-Trap chelating column (GE Healthcare) coupled to an ÄKTA Prime system (GE Healthcare). Protein elution was achieved by an imidazole gradient from 5 to 500 mM in 20 mM Tris-HCl (pH 7.9), 500 mM NaCl buffer. Fractions were analysed by SDS-PAGE followed by Coomassie Brilliant blue staining and those containing the protein were collected and dialyzed against 20 mM Tris-HCl (pH 7.5), 150 mM NaCl, 1 mM DTT, 0.5 mM EDTA in dialysis tubes (Spectra/por membranes, Spectrum Laboratories). During the dialysis the octa-His tag was exscinded by digestion with the recombinant TEV protease. A second purification step was performed to eliminate non-digested protein, the octa-His tail, and the recombinant protease, which contains a His-Tag. Collected fractions were extensively dialyzed against the buffer of choice depending on the purpose. A

concentration step was carried out by ultra-filtration in Amicon stirred cells (Millipore) using YM3 or YM10 membranes (Millipore). Once the desire volume and concentration were reached, possible aggregates were removed by high-speed centrifugation at 149,000 x*g* using a TLA 100.3 fixed-angle rotor (Beckman Coulter).

Under specific circumstances, the purification protocol was modified to add an additional purification step needed in some forthcoming procedures such as SAXS. In these cases, we used a Sephacryl S-300 HR 26/60 (GE Healthcare) gel filtration column for preparative separation of midsize proteins instead of the second standard IMAC. Subject to some case-by-case exception, the size exclusion chromatography was run in 20 mM NaPi (pH 7.5), 150 mM NaCl, 5 % Glycerol, 1-3 mM DTT.

Alternatively, the construct named DP-CT-GCN4-22b (DP residues 660-1060 fused with the C-terminus of the GCN4 coiled coil, in pET22b), which does not contain any additional tags, was purified by precipitation with ammonium sulphate (AS). Once the soluble fraction of the bacterial cultures was obtained as stated before, AS was added (119.5 g per 100 mL of protein solution) to get 21 % saturation. After 30 min at 4ºC, the protein solution was centrifuged at 43000 x*g* during 45 min at 4 °C. The pellet, that contains the DP protein, was resuspended in 5 mL of 20mM NaPi (pH 7.5), 150 mM NaCl, 5 % Glycerol, 1 mM DTT and the protein was purified by size exclusion chromatography using a Sephacryl S-300 HR 26/60 column equilibrated in the same buffer (GE Healthcare). Finally the protein was concentrated by ultra-filtration as described above.

12. Protein quantification

Protein concentration was determined by measuring the absorbance of the aromatic amino acids at 280 nm (A_{280}) in an U-2001 UV-Visible double beam spectrophotometer (Hitachi) using quartz absorption cuvettes with a 10 mm pathlength (Hellma GmbH). Molar (ε_{280}) and mass (E_{280}) extinction coefficients were calculated based on the amino acid sequence (Pace et al. 1995) using the Protparam tool implemented in ExPASy (http://web.expasy.org/protparam/) (Wilkins et al. 1999). Table M22 summarizes the molar and mass absorption coefficients used to calculate protein concentrations.

Table M22. Molecular weight (MW) and extinction coefficients of recombinant DP fragments

Construct name	aa boundaries[a]	$\varepsilon_{280}(M^{-1} cm^{-1})$ [b]	$E_{280}((mg mL^{-1})^{-1} cm^{-1})$ [b]	MW (Da)
DP-SR2-L-pET	64-164	4470	0.363	12307.1
DP-SR2-S-pET	64-155	4470	0.376	11271.8
DP-1-SR6-pET	1-630	102220	1.388	73640.1
DP-CT-pET	660-1056	44350	0.948	46772.4
DP-CT-GCN4-22b	660-1060-GCN4	45840	0.899	50973.3

[a] pET proteins contain an additional tetra-peptide GSHM in their N-terminus.

[b] ε_{280} and E_{280} are estimated in water, assuming all Cys residues are reduced.

13. Crystallization assays

Initial crystallization assays were performed by vapor diffusion methods in sitting-drop format using different commercial collections of crystallization solutions: Crystal Screen and SALT Rx (Hampton Research), Wizard I & II and Cryo I & II (Emerald Biosystems), and PACT (Newman et al. 2005) including a total of 432 crystallization conditions. All the conditions were assayed both at RT and a 4 ºC in 96-well plates (Swissci AG) and, if possible, two different protein concentrations were used. Additionally, DP-SR2-L (region 64-170) crystallization was also assayed in: Structure Screen 1 & 2, MIDAS, ProPlex, JCSG, Morpheus, and PGA-LM (all from Molecular Dimensions). Briefly, 1 µL of protein solution in 10 mM Tris-HCl (pH 7.5), 50 mM NaCl, 1 mM DTT (standard conditions) was mixed with an equal volume of mother liquor and equilibrated against 80 µL of mother liquor present in the reservoir.

Secondary fine screenings around conditions that yielded crystals in the initial screen were done using 24-well Cryschem sitting drop plates (Hampton Research). Parameters such as pH, precipitant or salt concentration, and volume of the drop were changed to attempt to improve the crystallization process.

14. Protein sequence analysis

Protein sequence analysis studies were performed by using different bioinformatics tools:

i) Protein sequences were obtained from the repository Uniprot (http://www.uniprot.org/). In several cases, domain limits were defined by sequence homology with other members of the protein families. In these cases, we searched for protein sequence homology by aligning and comparing the protein sequences with the BLAST (Basic Local Alignment Search Tool) algorithm implemented in the web page.

ii) Multiple sequence alignments were made with Clustal Omega (Sievers & Higgins 2014) that uses seeded guide trees and HMM profile comparisons to generate multiple alignments. Clustal Omega was run online at the web server of the European Bioinformatics Institute (EMBL-EBI) (http://www.ebi.ac.uk/Tools/msa/clustalo/).

iii) HMM profiles were built using the *hmmbuild* tool of the HHMER software (http://hmmer.janelia.org/) (Finn et al. 2011). Once we got the HMM profiles, they were used to search for homology against the human proteome database (ftp://ftp.uniprot.org/pub/databases/uniprot/), Pfam (Finn et al. 2014) or within sequences of specific proteins by using the *hmmsearch* tool of the same software.

iv) Secondary structure predictions were performed by using the online servers Jpred3 (http://www.compbio.dundee.ac.uk/jpred) (Cole et al. 2008) and PredictProtein (https://www.predictprotein.org/) (Yachdav et al. 2014).

15. Circular dichroism

Circular dichroism (CD) is a well-established low-resolution structural technique to determine the secondary structure content of chiral biomolecules based on the interaction of these molecules with polarized light (reviewed in Kelly, Jess, & Price, 2005 and Ranjbar & Gill, 2009). Optically active molecules exhibit circular dichroism because the absorption of light circularly polarized in one direction (right-handed) is different from that absorption in the opposite direction (left-handed). CD spectra are obtained when the dichroism is measured as a function of wavelength. The shape of the CD spectrum of proteins provides information about the structure. Protein secondary structure composition (content of helix, sheet, turns, etc.) can be quantitative estimated by CD spectroscopy in the far-UV spectral region (absorption in the range ~185 to 250 nm). At these wavelengths the chromophore of interest is the peptide bond; hence the CD signal is sensitive to the conformation of the polypeptide backbone. Furthermore, changes in the CD signals induced by denaturing agents (such as chemical denaturants or temperature) can be used to provide quantitative estimates of the conformational stability of a folded protein (Fasman 1996).

CD spectra were acquired with a Jasco J-720 dichrograph employing 1 mm and 0.1 mm optical path cells (Hellma GmbH) at 20 ºC. Four consecutive scans between 187 and 260 nm (bandwidth of 1 nm) were averaged from samples of purified protein in 20 mM NaPi (pH 7.5), 150 mM NaCl, 0.3 mM TCEP. Denaturation profiles were conducted by using as denaturant agent a temperature ramp from 20 to 90 ºC with a heating rate of 40 ºC/hour. A fixed wavelength of 222 nm was employed during thermal denaturation.

The secondary structure content of a protein can be estimated from its far-UV CD spectra using bioinformatic tools. Specifically, we used the methods SELCON (Sreerama et al. 1999), CONTIN (van Stokkum et al. 1990), and CDSSTR (Sreerama & Woody 2000) implemented in the online server DICHROWEB (Whitmore & Wallace 2004), and the K2D3 method (Louis-Jeune et al. 2012). When needed, the reference database number 6 was used for the analysis since it is optimized for a data range from 185 to 240 nm, and includes the broadest CD spectra in this range of data (Janes 2009).

CD denaturation profiles analysis

Changes induced by the temperature in the CD signal at 222 nm of the SR2-like fragments of DP were analysed using a two-state transition model that assumes an equilibrium between the folded and the unfolded state (Greenfield 2007). The following equation of a two-state transition was used for determining the midpoint temperature of the transition (melting temperature, Tm) (Koepf et al. 1999):

$$Y = \frac{(y_n + m_n T) + (y_d + m_d T)\exp\left(\Delta H_m / R(1/T_m - 1/T)\right)}{1 + \exp\left(\Delta H_m / R(1/T_m - 1/T)\right)}$$

Where: Y is the measured ellipticity at each temperature. ΔH_m is the enthalpy at the unfolding transition. T_m is the melting temperature (in Kelvin). T is the temperature (in Kelvin). R is the universal gas constant (1.987 cal K^{-1} mol^{-1}). m_n is the slope of the pre-transition (native) state. y_n is the intercept of the pre-transition (native) baseline. m_d is the slope of the post-transition (unfolded) state. y_d is the intercept of the post-transition (unfolded) baseline.

The equation assumes that the ellipticity of the pre-transition (native) and post-transition (unfolded) states changes linearly with the temperature. This model was fitted to the thermal denaturation CD curve using a nonlinear least-square fit running in Sigmaplot (Systat Software Inc).

16. Thermal shift assays using ThermoFluor

Thermal shift assays are fluorescence-based experiments useful to assess the thermal stability of proteins. Briefly, the method makes use of fluorescent probes that experience a large increase in the fluorescent intensity when they bound to hydrophobic regions of proteins. In native states proteins typically do not show large hydrophobic surfaces. However, hydrophobic patches are exposed upon unfolding.

Therefore, thermal induced unfolding transitions can be monitored as an increase in the fluorescence of the probe. The resultant fluorescence curve is used to determine the Tm of the protein (Pantoliano et al. 2001).

The fluorescence dye Sypro Orange (Life Technologies) was used to monitor the fluorescence changes in protein solutions at 0.25 - 1 mg/mL in buffer 50 mM HEPES or MES (depending on the pH, from 6 to 7.9), 150 mM NaCl. Experiments were carried out using 96-well Thermo-Fast PCR plates (ABgene, Thermo Scientific) in a quantitative PCR (qPCR) machine IQ5 (Biorad) settled for performing a heating ramp from 20 to 85 ºC with a heating rate of 1 ºC/min. Fluorescence measurements were conducted using an excitation filter of 480 nm with a 20 nm bandwidth and an emission filter of 530 nm with a 30 nm bandwidth. Data were collected every 0.5 ºC and samples were assayed in duplicate. The Tm, corresponding to the midpoint of the transition, was calculated as the maximum of the first derivative of the fluorescence signal (F) with respect to the temperature (T) (dF/dT).

17. Building atomic models of DP-PD fragments

Homology modelling of the SR2 and SR7-SR9 of DP

The atomic model of the SR2-like domain of DP was built by homology modelling with the JACKAL package (http://trantor.bioc.columbia.edu/jackal/index.html) running in FFAS03 (Jaroszewski et al. 2005). The crystal structure of the SR2 domain of BPAG1e (Gómez-Hernández and de Pereda, unpublished results) was used as template. Similarly, the structure of the SR7-SR9 region of DP was obtained by modelling using the crystal structure of the equivalent region of plectin (Ortega and de Pereda, unpublished results).

Composite model of the SR7-SR9-GCN4 of DP

The composite model of the dimer formed by the region 660-1060 of DP, which includes the SR7-SR9 and ~57 residues of the rod domain, fused to the coiled coil of GCN4 was built as follows. The SR7-SR9 region (660-1003) was modelled by homology as described above. The two protomers of the dimer were taken from the parallel arrangement of the two SR7-SR9 molecules in the asymmetric unit of the plectin structure. The N-terminal segment of the rod domain (region 1004-1060) was modelled by homology using as template the crystal structure of a dimeric N-terminal fragment of tropomyosin that forms a coiled coil (PDB entry 1IC2) (Brown et al. 2001). Finally, the dimeric crystal structure of the GCN4 coiled coil (PDB code 2ZTA) (O'Shea et al. 1991) was assembled at the C-terminus.

18. Small angle X-ray scattering

Small-angle X-ray scattering (SAXS) is a well-established method for structural characterization of biological macromolecules in solution. This technique provides three-dimensional low-resolution structures allowing the study of quaternary structure, domain organization, oligomeric state of proteins and protein complexes, kinetic processes, and responses to changes in conditions. Additionally, it is a powerful tool to complement and validate high resolution methods such as X-ray crystallography (see Mertens & Svergun, 2010 for a review about characterization of protein complexes by SAXS and Koch, Vachette, & Svergun, 2003 for a thorough explanation of the theory behind the technique).

Briefly, to extract structural information from non-crystalline samples by SAXS, proteins in solution are exposed to a collimated and focussed X-ray beam and the scattered intensity is recorded by a detector as a function of the scattering angle. The scattered intensity must be corrected by subtraction of the contribution of the solvent to assure that the intensity is proportional to the scattering of a single particle averaged over all orientations. Represented as one-dimensional curves, scattering patterns provide important information about size, oligomeric state, and overall shape of molecules based on parameters such as the molecular weight (Mw), radius of gyration (Rg), hydrated particle volume (V) or maximum particle distance (Dmax). Additionally, computational methods are available to determine reliable three-dimensional low-resolution models from scattering data by using *ab initio* methods or through the refinement of available high-resolution structures or homology models.

Sample preparation and data collection

Protein samples for SAXS analysis were additionally purified and equilibrated in 20 mM NaPi (pH 7.5), 150 mM NaCl, 5 % glycerol, 3 mM DTT by size exclusion chromatography using a Hi-Prep Sephacryl S300 26/60 column (GE Healthcare). Eventually, DP-CT-pET was equilibrated in 20 mM HEPES, 500 mM NaCl, 5% glycerol, 2.5 mM DTT (pH 7.9). High concentrations of DTT and glycerol are added to prevent radiation damage in SAXS samples (Kuwamoto et al. 2004). DP constructs studied by SAXS are summarized in table M23.

Table M23. DP fragments analysed by SAXS

Construct name	region	aa boundaries
DP-1-SR6-pET	N-SR6	1-630
DP-CT-pET	SR7-SR9	660-1056
DP-CT-GCN4-22b	SR7-SR9-GCN4	660-1060-GCN4

SAXS measurements were performed at the EMBL high brilliance synchrotron BioSAXS beamline P12 on the storage ring PETRA-III (Deutsches Elektronen Synchrotron - DESY, Hamburg, Germany) with a Pilatus 2M detector (Dectris) using radiation of wavelength 1.24 Å. Data were collected at a sample-detector distance of 4.1 m for a scattering vector (q) range from 0.01 to 0.35 $Å^{-1}$ (q= (4π sin θ)/λ, where 2θ is the scattering angle). Exceptionally, DP-SR6-pET fragment was measured using a detector distance of 3.1 m ($0.01 < q < 0.44$ $Å^{-1}$). Data collection was set to 10 °C for all the measurements. Data frames were recorded every 0.5 msec, for a total exposure time of 1 sec in a flow mode where the samples are moving through the capillary during the exposure time to reduce radiation damage. At least four different concentrations per sample were used to collet scattering data in a concentration range from ~0.90 to ~30 mg/mL. Samples were prepared by sequential dilution in the equilibration buffer.

SAXS data analysis

Data reduction and analysis was performed using the ATSAS package (Petoukhov et al. 2012) according to standard procedures. Briefly, after assessing the absence of radiation damage by comparing successive curves of the same sample, the non-damaged curves were averaged, the scattering from the buffer was subtracted and the curves were extrapolated to infinite dilution, unless otherwise indicated, using PRIMUS (Konarev et al. 2003). The Rg and the forward scattering intensity (I_0) were evaluated using the Guinier approximation (Guinier & Fournet 1955). The pair-distribution probability function ($P(r)$) was calculated by an indirect Fourier transform using the program GNOM (Svergun 1992) in the PRIMUS QT graphical interface. From the calculation of the P(r) distribution we also derived parameters such as the Rg, I_0, and Dmax.

Reconstruction of molecular envelopes of DP-PD fragments

The scattering profiles of those fragments with limited conformational variability were used to calculate low-resolution structures using two independent *ab initio* methods implemented in the programs DAMMIF (Franke & Svergun 2009) and DALAI_GA (Chacón et al. 2000). Typically, fifteen independent *ab initio* reconstructions were made with each program. The multiple models of a given protein were superimposed with the program SUPCOMB (Kozin & Svergun 2001) and an averaged model that represents the most populated volume was obtained with DAMAVER (Volkov & Svergun 2003). For illustration, volumetric representations of the low resolution structures were calculated with the SITUS package (Wriggers 2010). When available, atomic models were superimposed onto low resolution reconstructions with SUPCOMB.

Rigid body modelling

The structure of DP-1-SR6 was also modelled by rigid body fitting against SAXS data with the programs CORAL (COmplexes with RAndom Loops) (Petoukhov et al. 2012) and BUNCH (Petoukhov & Svergun 2005). The atomic model of the SR2 domain (see above) and the crystal structure of the SR3-SR6 region, residues 178-627 (PDB entry 3R6N, Choi & Weis 2011) were used as rigid bodies, whereas the N-terminal tail preceding the SR2 and the SR2-SR3 linker were modelled as flexible segments. Both methods start from arbitrary initial positions and orientations of the rigid domains linked by flexible regions made of dummy residues to build a final model where the positions of the rigid domains are defined.

Evaluation of theoretical scattering profiles against experimental data

The theoretical scattering profiles of atomic models were calculated and fitted to the experimental data by using CRYSOL (Svergun et al. 1995). The P(r) and Dmax of the atomic models were calculated with the program MOLEMAN 2 (Kleywegt et al. 2004).

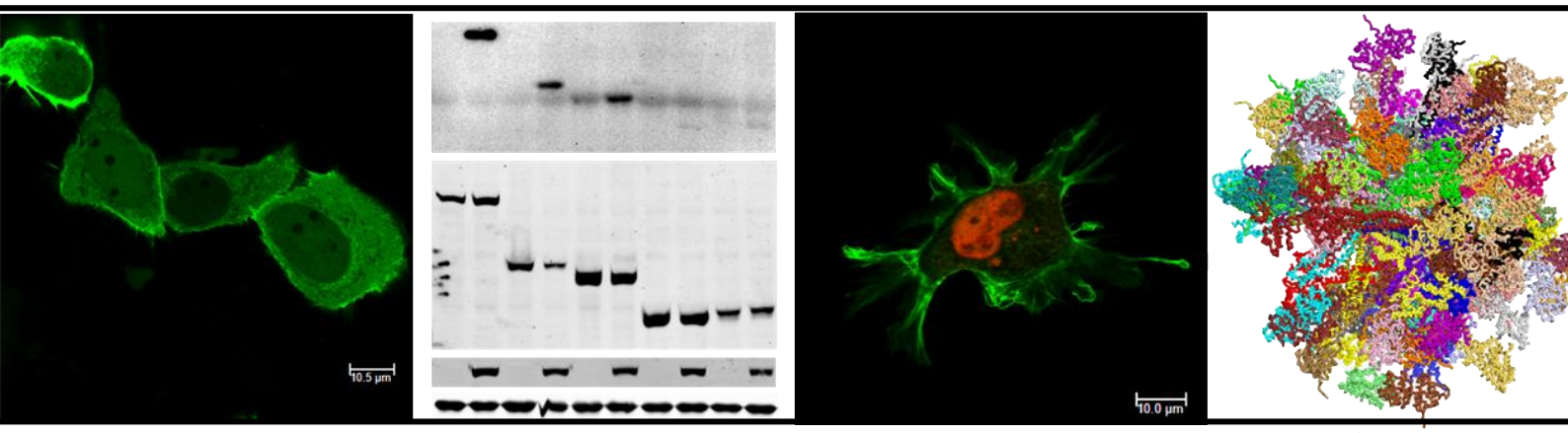

Chapter 4

RESULTS

Section A

Mapping of the interacting domains in the DP-PKP1a complex

1. Mapping of the PKP1a-interaction site in DP

Two regions of DP-PD interact with PKP1a in co-IP assays

The interaction between PKP1a and DP was analysed by co-IP in COS-1 cells transiently co-transfected with PKP1-FLAG and DP-PD-HA tagged constructs. Previous studies have shown that the N-terminal half of the DP-PD, region 1-584, interacts with desmosomal components such as plakoglobin or plakophilins (PKP1-3) (Bonné et al., 2003; Chen, Bonne, Hatzfeld, van Roy, & Green, 2002; Kowalczyk et al., 1997; Kowalczyk, 1999). Surprisingly, our results showed that, in addition to the complete DP-PD and the N-terminal half (DP-NT, SR2-SR5 domains), the non-overlapping C-terminal fragment corresponding to the SR6-SR9 domains (DP-CT) also interacted with PKP1a (Figure R1).

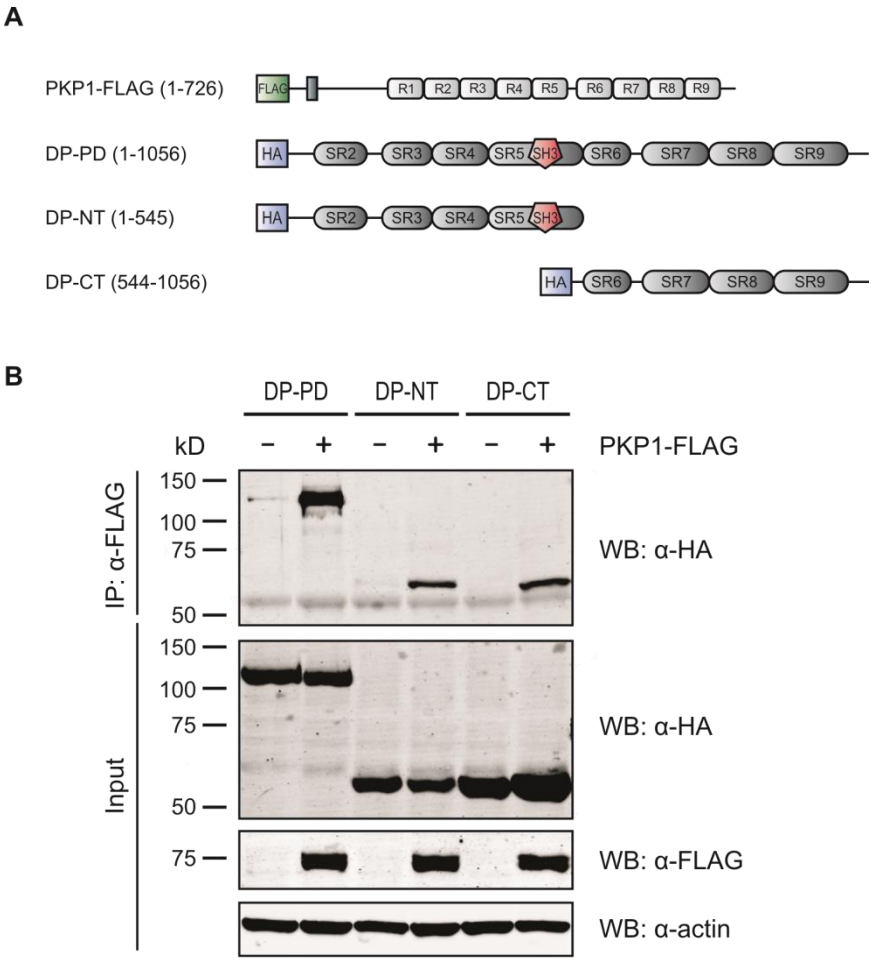

Figure R1. Analysis of the interaction between PKP1a and DP by co-IP. A) Schematic domain representation of FLAG-tagged PKP1a full length (pCEFLAG vector) and HA-tagged DP fragments (pCEFLHA vector) used in co-IP assays. **B)** The interaction between PKP1a and DP-PD was analysed by co-IP of DP fragments with PKP1a full length tagged with FLAG (PKP1-FLAG) and incubated with anti-FLAG agarose beads (+ lanes). Results were proved by western blotting using a polyclonal anti-HA antibody. In the negative control lanes (-) (COS-1 cells transfected with pCEFLAG empty vector instead of

PKP1-FLAG and incubated in the same conditions), no signal could be detected, suggesting a specific interaction between PKP1a and DP fragments (upper panel). Expression of PKP1-FLAG and DP-fragments in the co-IP input (total lysates) was detected by western blotting, using monoclonal anti-FLAG and anti-HA antibodies for detecting PKP1a and DP-fragments, respectively. β-actin detection was used as a loading control.

Co-IP assays suggested the existence of at least two PKP1a-binding sites within the DP-PD, each located on one half of the plakin domain. In order to validate the results obtained by co-IP and to confirm the novel second PKP1a-binding site located in the C-terminal half of DP-PD we used fluorescence imaging microscopy.

FLIM experiments only support one PKP1a-binding site in DP

As a complement to the analysis by co-IP we studied the interaction between PKP1a and DP by fluorescence lifetime imaging microscopy (FLIM). For doing so, we co-expressed CFP-tagged PKP1a constructs (made in our vector pcDNA3-CFP-C4) with Venus-tagged DP constructs (made in pcDNA3-Venus-C4 or pcDNA3-Venus-N3 vectors, see materials and methods) in COS-7 cells. These two fluorophores are a FRET pair in which CFP and Venus (YFP variant) act as donor and acceptor, respectively. CFP lifetime was measured in at least 30 cells per condition. Differences between transfected cells and the control group (cells transfected with one PKP1-CFP fragment and free-Venus) were analysed using an unequal variance t-test (Welch´s correction). P-values ≤ 0.05 were considered statistically significant.

Figure R2 shows one representative FLIM result of at least three independent experiments with the signification obtained in the unequal variance t-test. The CFP lifetime when the fluorophore was expressed alone in an empty vector was ~2.57 ns. When we co-transfected CFP and Venus in different vectors, CFP lifetime showed a slight decrease (~2.47 ns) that probably reflects intermolecular energy transfer between unlinked CFPs and YFPs (Grailhe et al. 2006). A new drop was observed when we co-transfected PKP1-CFP with free-Venus in a different and empty vector (~2.29 ns). Because Venus was not fused to any construct, the observed decrease in the CFP lifetime was just due to the higher overexpression of Venus in the surroundings of PKP1-CFP and might be considered the CFP lifetime drop as a result of the background. We considered that CFP lifetime as the reference value in a situation of non-specific interaction (negative control). Statistical significance is also referred to this value.

Table R1 shows the average CFP lifetime measured in more than 40 different cells per condition and the dispersion of this measure. DP-PD and DP-NT produced a significant decrease in the CFP lifetime from ~2.3 ns to around 2.2 ns ($p \leq 0.01$). On the other

hand, CFP lifetime was not reduced when PKP1-CFP was co-transfected with DP-CT ($p > 0.05$) suggesting that there is no interaction between them. Thus, in contrast to the co-IP results, FLIM experiments did not support an interaction between the C-terminal half of the DP-PD and PKP1a.

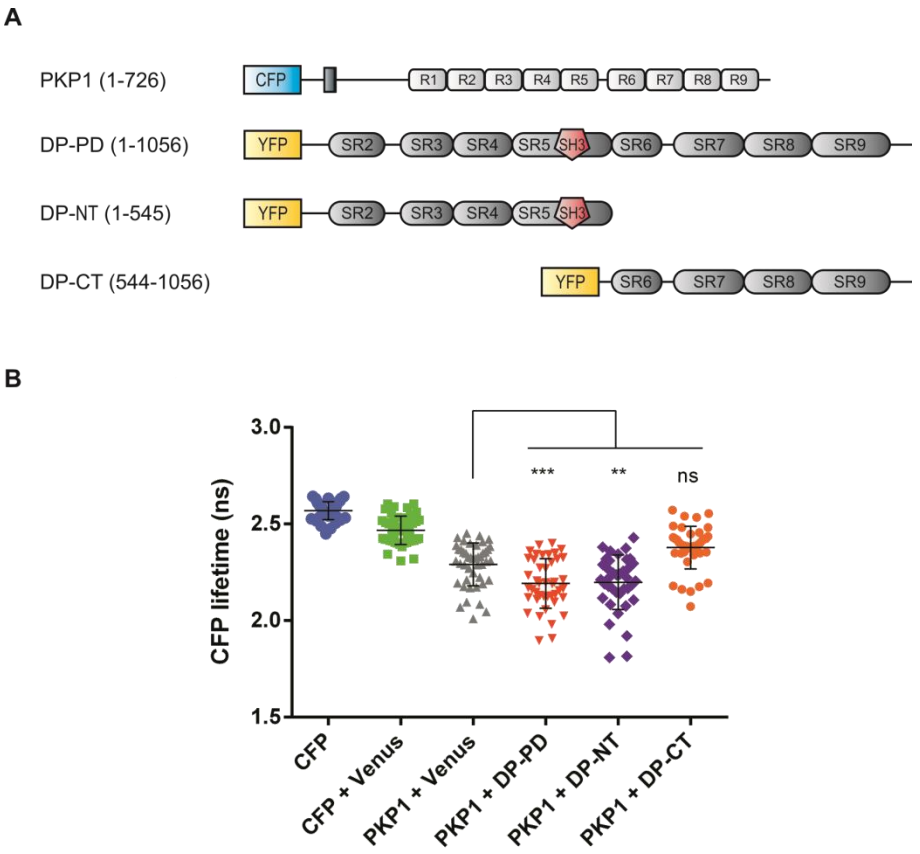

Figure R2. Analysis of the interaction between PKP1a and DP by FLIM. A) Schematic domain representation of CFP-tagged PKP1a full length and Venus-tagged DP fragments used in FLIM assays. In the scheme, the fluorophore Venus is represented by the general acronym YFP. **B)** The PKP1a-DP interaction was analysed by FLIM in COS-7 cells. Results of one representative experiment are shown in scatter dot plots of the CFP lifetime with the mean and the standard deviation. Statistically significant differences (unequal variance t-test) are indicated by *** ($p \leq 0.001$); ** ($p \leq 0.01$); ns, not significant ($p > 0.05$).

Table R1. Descriptive statistics of the data shown in figure R2

Donor	Acceptor	n	Mean lifetime (ns)	SD	SEM
CFP	-	40	2.570	0.047	0.007
CFP	Venus	47	2.467	0.074	0.011
PKP1-CFP	Venus	45	2.290	0.111	0.017
PKP1-CFP	DP-PD-Venus	43	2.193	0.129	0.020
PKP1-CFP	DP-NT-Venus	40	2.199	0.141	0.022
PKP1-CFP	DP-CT-Venus	42	2.378	0.110	0.017

n, number of values; SD, standard deviation; SEM, standard error of the mean

In order to gather more evidences about the interaction of PKP1a and DP-PD, we performed similar experiments but using the PKP1a-head domain as CFP-tagged fragment instead of PKP1a full length (Figure R3). It is well established that the region of PKP1a that interacts with DP is located within the head domain of PKP1a, which comprises the first 243 amino acids (Hofmann et al., 2000; Kowalczyk, 1999; Sobolik-Delmaire, Katafiasz, & Wahl, 2006).

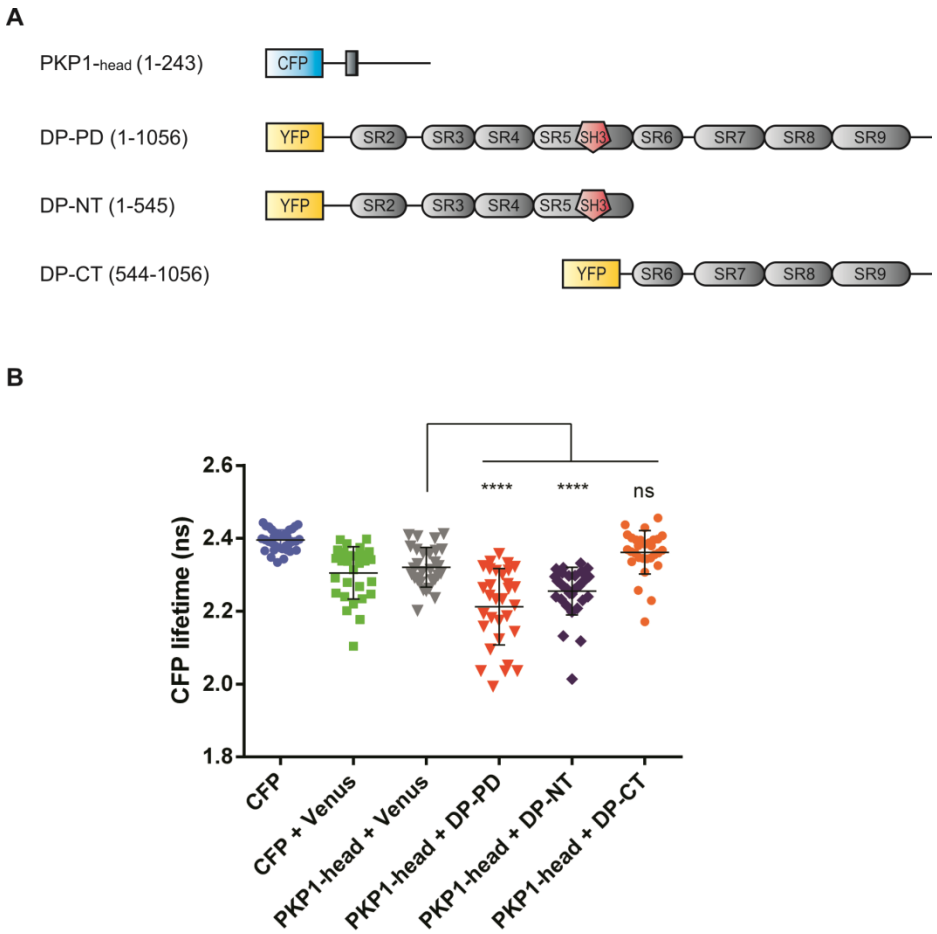

Figure R3. Analysis of the interaction between PKP1a-head domain and DP by FLIM. A) Schematic domain representation of CFP-tagged PKP1a head domain (PKP1-head, region 1-243) and Venus-tagged DP fragments used in FLIM assays. In the scheme, the fluorophore Venus is represented by the general acronym YFP. **B)** The PKP1a-head/DP interaction was analysed by FLIM in COS-7 cells. Results of one representative experiment are shown in scatter dot plots of the CFP lifetime with the mean and the standard deviation. Statistically significant differences (unpaired unequal variance t-test) are indicated by **** ($p \leq 0.0001$); ns, not significant ($p > 0.05$).

Table R2 shows the descriptive statistics of the representative experiment plotted in figure R3. Experimental conditions and data analysis were the same as those previously explained.

Table R2. Descriptive statistics of the data shown in figure R3

Donor	Acceptor	n	Mean lifetime (ns)	SD	SEM
CFP	-	35	2.395	0.028	0.005
CFP	Venus	29	2.305	0.072	0.013
PKP1head-CFP	Venus	29	2.321	0.055	0.010
PKP1head-CFP	DP-PD-Venus	31	2.212	0.105	0.019
PKP1head-CFP	DP-NT-Venus	32	2.263	0.049	0.009
PKP1head-CFP	DP-CT-Venus	28	2.373	0.041	0.008

n, number of values; SD, standard deviation; SEM, standard error of the mean

The head domain of PKP1a reproduced the DP-interaction results obtained with the full length PKP1a in FLIM experiments. Summarizing, by using FLIM we confirmed the interaction between the PKP1a head and DP-NT, but we did not detect association between PKP1a and DP-CT.

It may be possible that we did not detect the interaction between PKP1a and DP-CT because we were using DP-constructs with the fluorescent tag located in the N-terminal region of the fusion protein. To test whether the interaction that we observed between PKP1a and DP-NT was dependent on the location of the fluorescent tag we performed FLIM experiments using new DP-fragments with Venus linked to the C-terminal region by a flexible linker made of Gly-Ser repeats (pcDNA3-Venus-N3 vector). We did not change the N-terminal location of CFP in PKP1a because, as we stated before, it is well established that PKP1a interacts with DP by means of its N-terminal head domain. Moreover, we have not detected interaction of the ARM domain of PKP1a with DP in co-IP assays (see below, Figure R20). Results are summarized in figure R4 and table R3. They confirmed the interactions PKP1a-DP-PD and PKP1a-DP-NT, whereas interaction between PKP1a and DP-CT was not observed. So, the analysis of the interaction between PKP1a and DP by FLIM was not dependent on the location of the fluorescent tag.

Taking into account these results, the forthcoming FLIM experiments to map the PKP1a-DP interaction site were performed by using PKP1a and DP-fragments with CFP or Venus linked to the N-terminal region of the fusion proteins.

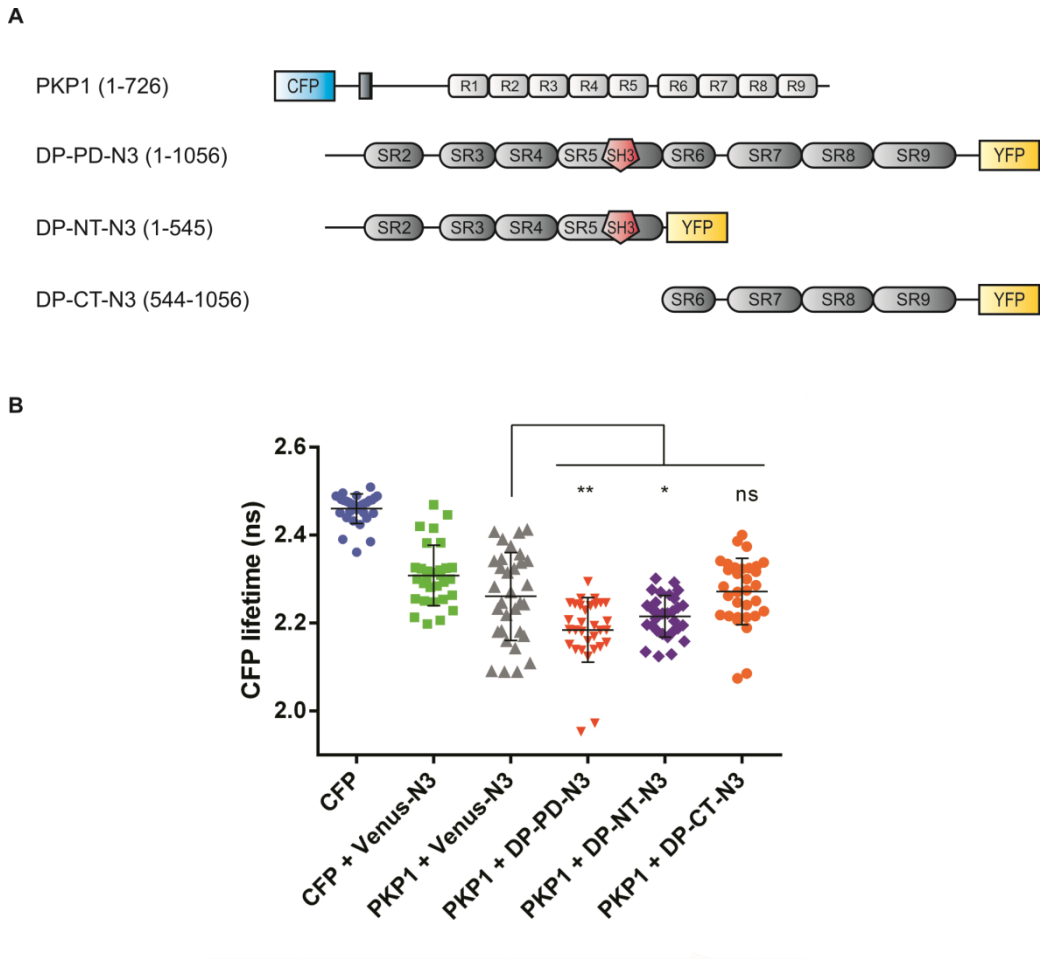

Figure R4. FLIM analysis of the interaction between PKP1a full length and DP-fragments tagged with C-terminal Venus. A) Schematic domain representation of CFP-tagged PKP1a full length and C-terminal Venus-tagged DP fragments used in FLIM experiments. In the scheme, the fluorophore Venus is represented by the general acronym YFP. **B)** The PKP1a-DP interaction was analysed by FLIM in COS-7 cells. Results of one representative experiment are shown in scatter dot plots of the CFP lifetime with the mean and the standard deviation. Statistically significant differences (unpaired unequal variance t-test) are indicated by ** ($p \leq 0.01$); * ($p \leq 0.05$); ns, not significant ($p > 0.05$). Notice that, although the statistical signification was lower using fusion proteins with the tag in the C-terminal end than when the tag was at the N-terminus, the overall result was the same, that is, PKP1a interacted with DP in a region located in the N-terminal half of the DP-PD.

Table R3. Descriptive statistics of the data shown in figure R4

Donor	Acceptor	n	Mean lifetime (ns)	SD	SEM
CFP	-	28	2.469	0.021	0.004
CFP	Venus-N3	30	2.308	0.069	0.013
PKP1-CFP	Venus-N3	32	2.261	0.100	0.018
PKP1-CFP	DP-PD-Venus-N3	29	2.199	0.045	0.008
PKP1-CFP	DP-NT-Venus-N3	30	2.215	0.047	0.009
PKP1-CFP	DP-CT-Venus-N3	32	2.272	0.076	0.013

n, number of values; SD, standard deviation; SEM, standard error of the mean

The subcellular localization of PKP1-CFP and DP-PD-Venus fragments evidences an interaction between PKP1a and DP-NT

In order to clarify whether an interaction between PKP1a and both halves of DP-PD was possible we decided to look at the subcellular localization of these fragments tagged with CFP or Venus. With this purpose we transiently transfected COS-7 cells with PKP1a or DP-fragments.

The PD of DP is known to target the protein to DMs (Bornslaeger et al. 1996; Smith & Fuchs 1998). When we transfected COS-7 cells with DP-PD, it appeared diffusely distributed throughout the cytoplasm, but also decorated the plasma membrane (Figure R5). DP-NT showed two different distributions in transfected cells. In some cells, it showed similar distribution with respect to the full plakin domain (DP-PD). On the contrary, other cells showed an aberrant distribution with DP-NT located only in prominent cytoplasmic aggregates. These aggregates were not positive for markers of lysosomes or the Golgi complex, nor co-localize with recycling endosome markers (data not shown). DP-PD and DP-NT were mostly excluded from the nucleus. On the other hand, DP-CT was clearly distributed over the plasma membrane, being excluded from the cytoplasm and nucleus. These results show clear domain dependence in the subcellular distribution of DP and suggest that the C-terminal half of DP-PD is required to target DP to the plasma membrane.

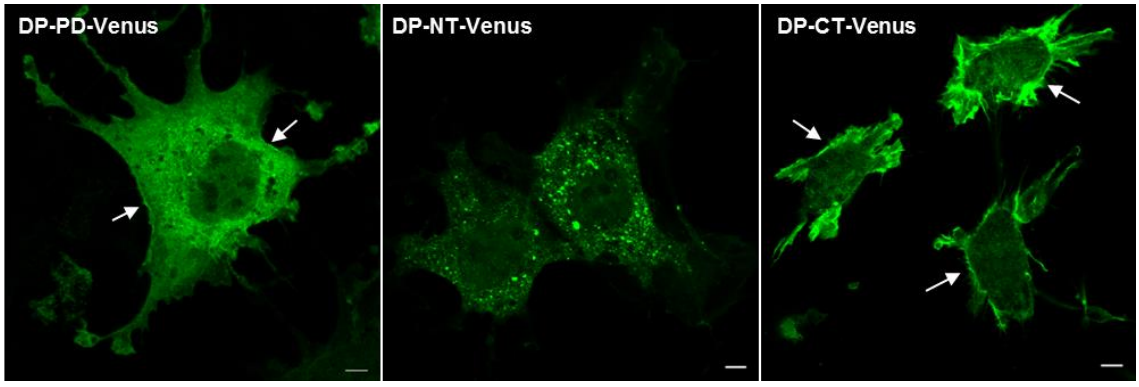

Figure R5. Subcellular localization of DP-fragments in COS-7 cells. The subcellular localization of Venus-tagged DP fragments was investigated in COS-7 cells transiently expressing these constructs by confocal microscopy. DP localization was detected by exciting Venus at 514 nm. Arrows highlight the presence of DP-fragments containing the C-terminal half of the PD over the plasma membrane. Bar, 5 µm. Images are representative of the overall subcellular distribution of the studied fragments.

COS-7 cells expressing PKP1-CFP showed an exclusively nuclear staining (Figure R6). PKP1a full length was localized to the nuclear karyoplasm and mostly excluded from nucleoli. PI counterstaining matched the PKP1-CFP signal, with exception of the PI nucleoli-staining. This subcellular distribution have been previously reported in

various cell types (Hatzfeld et al. 2000; Schmidt et al. 1997; Sobolik-Delmaire et al. 2010) being the expected in cell types not containing prominent DMs, such as COS cells which form only a small number of immature DMs (Stappenbeck & Green 1992).

Since PKP1-CFP by itself shows a very clear nuclear signal, from now on, nuclear counterstaining will not be shown in routine experiments where nuclei are brightly defined by PKP1-CFP signal.

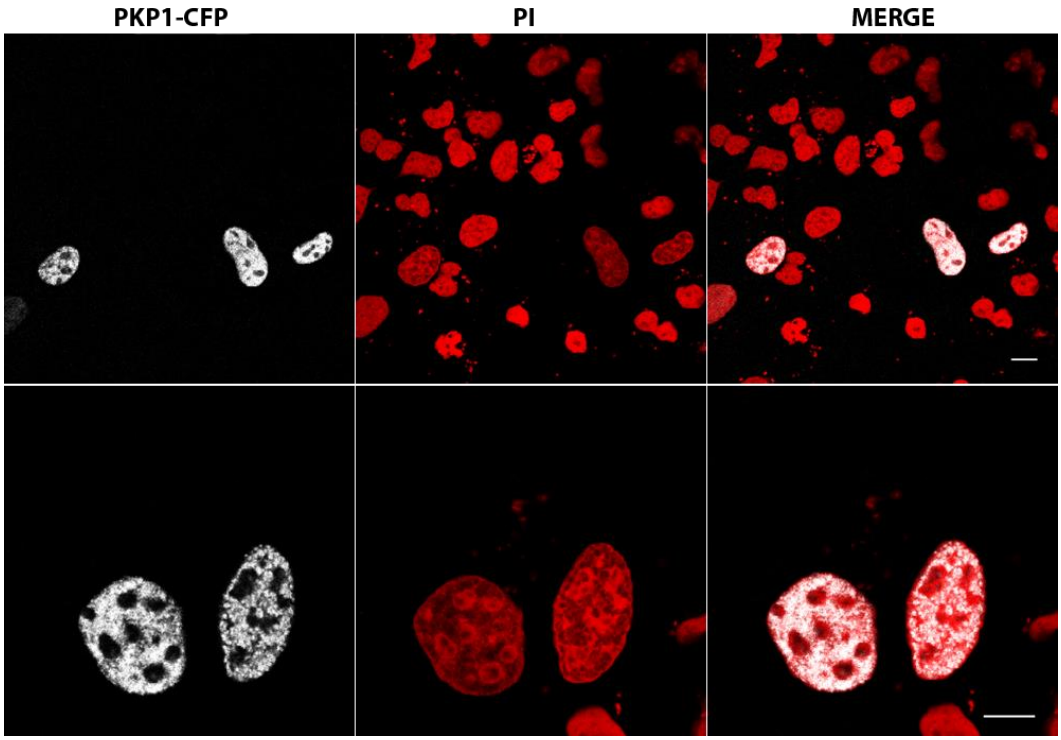

Figure R6. Subcellular localization of PKP1-CFP in COS-7 cells. Confocal microscopy images of COS-7 cells transiently expressing PKP1-CFP. Twenty-four hours after transfection, cells were PFA-fixed, permeabilized, treated with RNase A and incubated with PI to obtain a nuclear counterstain (red). CFP-tagged PKP1a full length was detected upon excitation of CFP at 442 nm (grey). PI and PKP1-CFP signals completely matched, demonstrating that PKP1-CFP has a specific and exclusive nuclear localization in COS-7 cells. Notice that PKP1-CFP was absent from nucleoli whereas PI staining was broadly distributed throughout the entire nucleus.

Once we knew the subcellular distribution of the fluorescent-tagged PKP1a and DP-fragments in COS-7 cells, we wanted to know whether the normal distribution of these constructs would be altered by the joint overexpression of PKP1a and DP. To assess this objective, we co-transfected COS-7 cells with PKP1a tagged with CFP (PKP1-CFP) and each of the DP-fragments tagged with Venus. We studied their distribution by confocal microscopy using the same conditions and settings as those used with the single transfections (Figure R7).

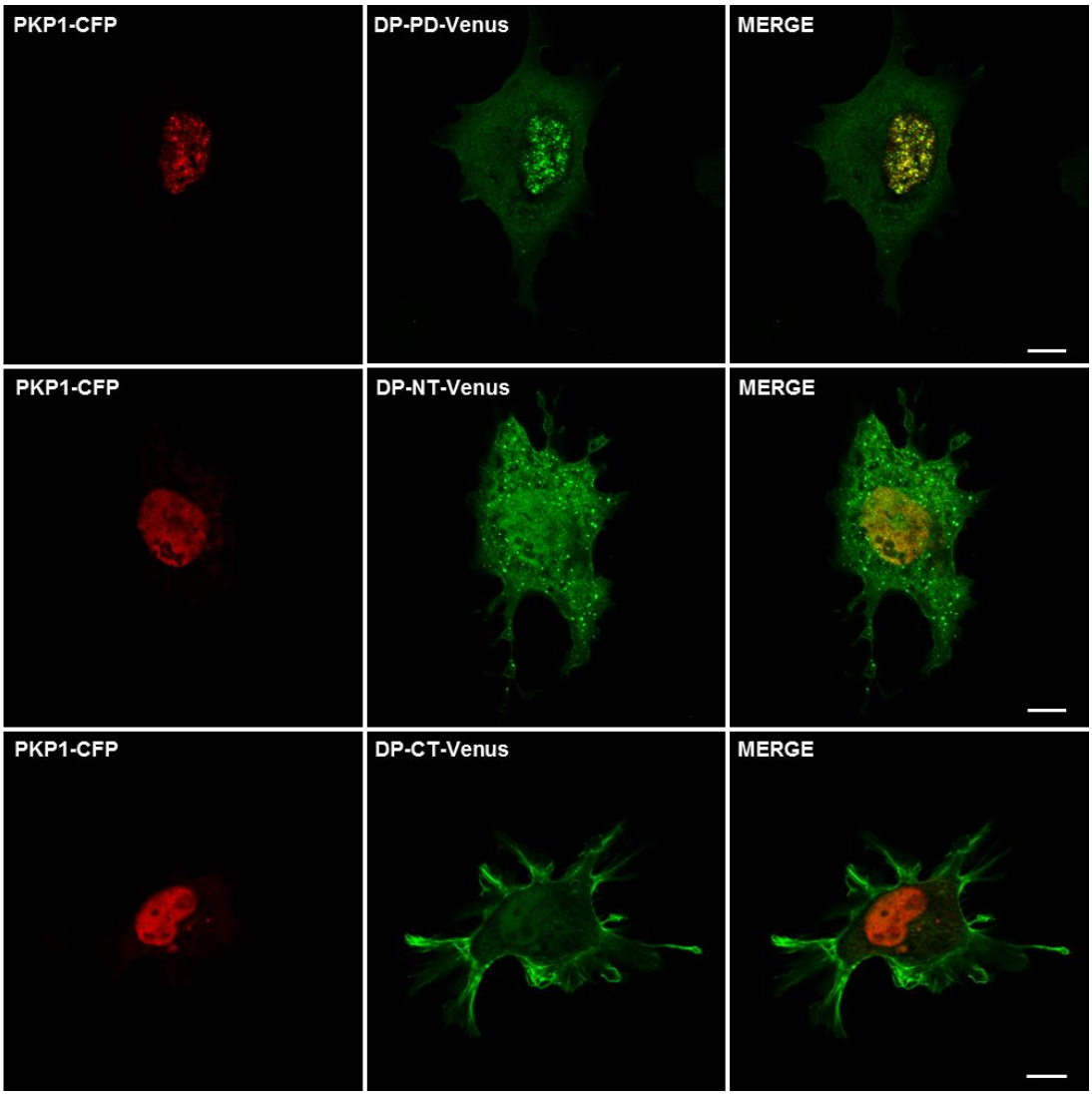

Figure R7. Subcellular localization of PKP1a and DP-fragments co-transfected in COS-7 cells. The co-localization of PKP1a full length and DP-fragments was investigated in COS-7 cells overexpressing both proteins by confocal microscopy. PKP1a full length was detected upon excitation of CFP (442 nm) and is represented in red (left images). Overexpression of DP-fragments (middle images) was detected by exciting Venus at 514 nm and is represented in green. The overlay images (on the right) show the co-localization of PKP1-CFP and DP-Venus fragments in yellow. Bar, 10 µm. Images are representative of the overall distribution of the studied fragments.

DP-PD (upper images) and DP-NT (middle images) experienced dramatic changes in their subcellular distribution when they were co-transfected with PKP1a. Both DP fragments were recruited to the nucleus showing notable co-localization with PKP1a-CFP (see yellow in merge images). Apparently PKP1a recruits more efficiently to the nucleus the complete PD than the N-terminal half (DP-NT), although it might be an effect of the abnormal expression of DP-NT-CFP explained before. Notice that in single transfections both DP constructs were mostly excluded from the nucleus. The fact that PKP1a promoted the recruitment of DP-PD and DP-NT to the nucleus demonstrated

that an interaction between PKP1a and DP was happening. On the other hand, co-expression with PKP1a did not have a significant effect on the subcellular distribution of DP-CT that remained at the plasma membrane. Hence, PKP1a and DP-CT did not interact in COS-7 cells.

Taken together, these results suggest that PKP1a interacts with DP by means of the N-terminal region of the PD. The C-terminal region of DP-PD does not participate in the interaction with PKP1a but it seems important for the localization of DP over the plasma membrane. These observations are consistent with our previous FLIM results showing the interaction of PKP1a with DP-PD and DP-NT but not with DP-CT.

Engineering fusion proteins carries the risk of affecting native proteins localization. We wanted to make certain that the observed subcellular distribution of PKP1a and DP-fragments was tag independent. Localization artefacts can be minimized by using two or more different tags and/or different tagging locations in each protein. Moreover, comparing the results with those obtained by indirect immunofluorescence of endogenous or untagged proteins may help to validate the results obtained by using fluorescent proteins (Stadler et al. 2013).

Good immunofluorescence images of endogenous proteins could not be obtained in COS cells, most likely due to the low expression levels of these proteins in this cell type (data not shown). Therefore, as an alternative, COS-7 cells were co-transfected with PKP1a full length and DP-PD tagged with FLAG and HA, respectively. Their localization was analysed by indirect immunofluorescence (Figure R8).

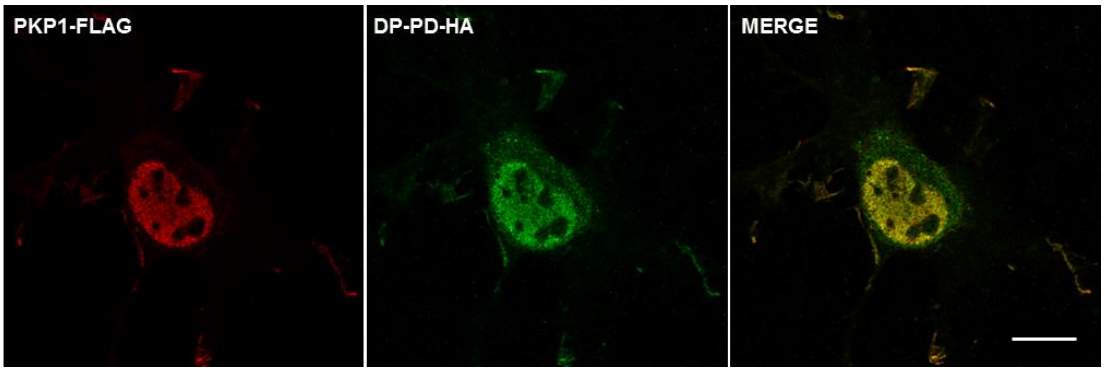

Figure R8. Subcellular localization of PKP1-FLAG and DP-PD-HA co-transfected in COS-7 cells. The co-localization of PKP1a full length tagged with FLAG (pCEFLAG vector) and DP-PD tagged with HA (pCEFLHA vector) was studied in COS-7 cells overexpressing both proteins by confocal microscopy. PKP1a full length was detected using a monoclonal antibody against the N-terminal region of PKP1a (3G250, Thermo) and a secondary antibody conjugated with Texas Red (red). DP-PD-HA was detected with a polyclonal antibody against the C-terminal region of DP-PD (sc-18086, Santa Cruz) and a secondary antibody conjugated to Alexa-488 (green). The overlay image (on the right) shows the co-

localization of PKP1-FLAG and DP-PD-HA in yellow. Bar, 15 µm. Images are representative of the overall distribution of the studied fragments.

The subcellular distribution of the fusion proteins with HA- or FLAG-tags was the same as that observed with fluorescent tags. That is, PKP1a was restricted to the nucleus, DP-PD alone was in the cytoplasm (data not shown) and it was recruited to the nucleus by PKP1a when they were expressed together. The overlay image showed co-localization of PKP1a and DP-PD in the nucleus, as observed with fluorescent fusion proteins. Thus, we can conclude that the subcellular distribution of PKP1a and DP-fragments was not affected by the tags used.

Analysis of the subcellular distribution of PKP1a and DP-fragments in keratinocytes

We wondered whether the previous results obtained in COS-7 cells would be reproducible in DMs-bearing cell lines such as keratinocytes. To assess this question we analysed by confocal microscopy the subcellular distribution and co-localization of the fluorophore-tagged constructs, cloned in the pcDNA3-CFP-C4 and pcDNA3-Venus-C4 vectors, in different keratinocyte cell lines. Results are summarized in Figures R9 and R10.

We used three different cell lines as keratinocytes models: Normal Human Keratinocytes (NHKs) (Niessen et al. 1996), the immortalized but highly differentiated HaCaT cell line (Boukamp et al. 1988), and a keratinocyte cell line obtained from a patient with junctional epidermolysis bullosa associated with pyloric atresia (JEB-PA), in which full-length integrin β4 was stably expressed by retroviral infection to generate PA-JEB/β4 (Niessen et al. 1996; Sterk et al. 2000). As before, we first made single transfections to analyse the subcellular distribution of the fusion proteins (Figure R9). The overall subcellular distribution of all the constructs was the same in the different keratinocytes cell lines and it was also very similar to the distribution in COS-7 cells. The main difference was observed for PKP1a that in differentiated keratinocytes (growing in medium with high calcium), in addition to the nucleus PKP1a was enriched laterally at cell-cell contact sites (see arrows), as expected due to the formation of DMs.

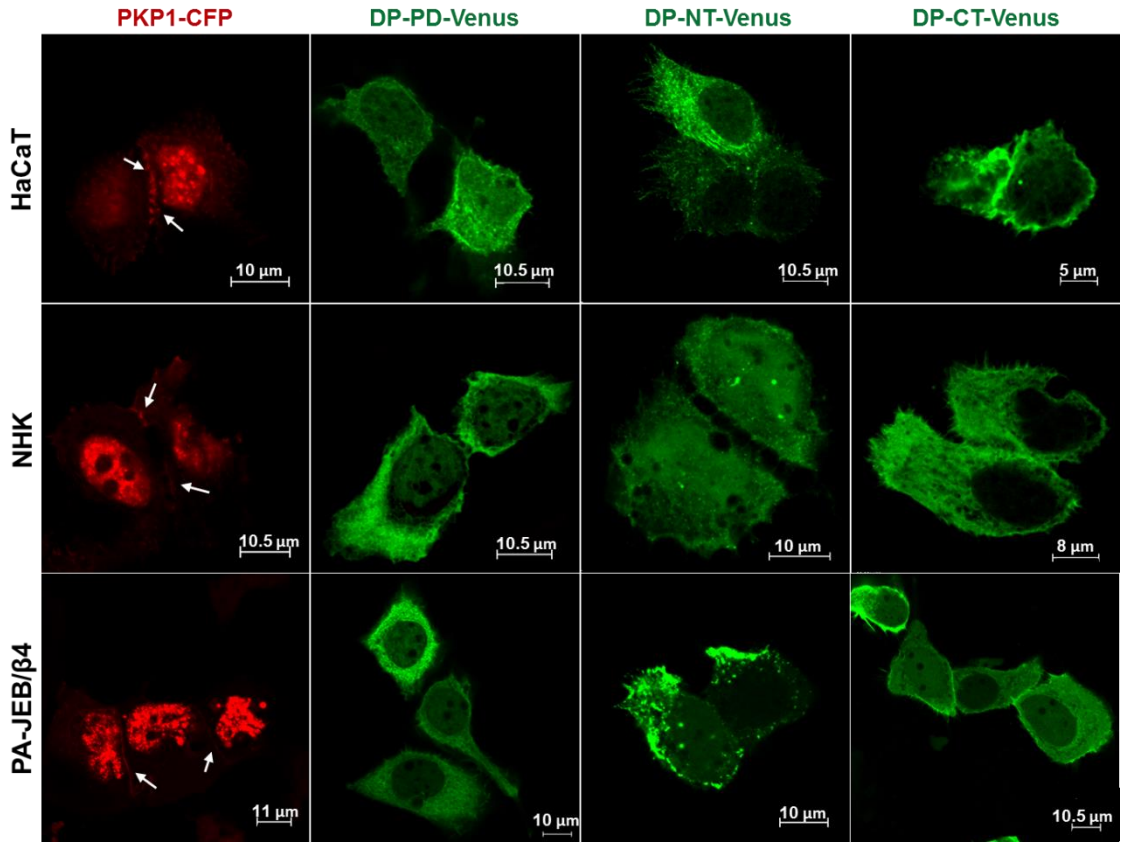

Figure R9. Subcellular localization of PKP1a and DP-fragments in keratinocyte cells lines. Confocal microscopy images of HaCaT (upper row), NHK (middle row), and PA-JEB/β4 (bottom row) ectopically expressing PKP1a full length and DP fragments tagged with CFP or Venus, respectively. PKP1a full length was detected upon excitation of CFP at 442 nm (red). DP-PD (second image of each row), DP-NT (third image of each row), and DP-CT (last image of each row) were detected by exciting Venus at 514 nm (green). Images are representative of the overall subcellular distribution of the studied fragments.

Next, we co-transfected PKP1-CFP full length with DP-fragments tagged with Venus to address whether the presence of one of them affected the distribution of the other (see an example with PA-JEB/β4 in Figure R10). As we had seen before in COS-7 cells, when DP-PD or DP-NT was co-transfected with PKP1a, the distribution of the DP fragments was changed by the presence of PKP1a. Specifically, these DP fragments were co-imported to the nucleus. This behaviour evidences an interaction of PKP1a with DP-PD and DP-NT. On the other hand, DP-CT did not show delocalization in the presence of PKP1a, but remained in the cytoplasm and was accumulated mainly at the plasma membrane.

Results obtained with NHK and HaCaT cells (data not shown) were very similar to those observed with PA-JEB/β4. Thus, we can conclude that the results regarding the localization of PKP1a and DP fragments in keratinocytes are consistent with the results obtained previously in COS cells.

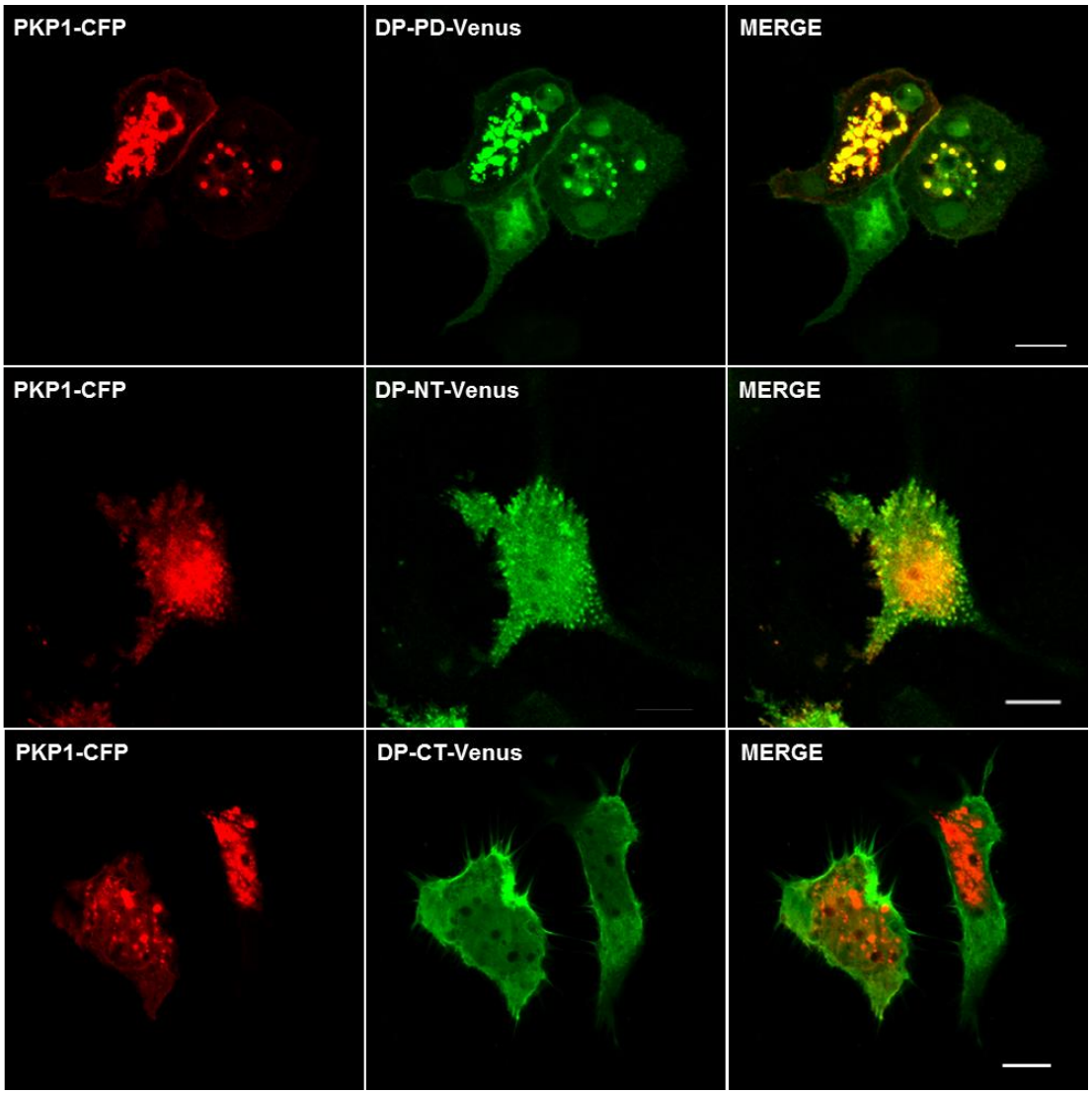

Figure R10. Subcellular localization of PKP1a and DP-fragments co-transfected in PA-JEB/β4. Confocal microscopy images of PA-JEB/β4 co-expressing PKP1a full length and one DP fragment tagged with CFP or Venus, respectively. PKP1-CFP was detected upon excitation of CFP (red). Venus-tagged DP-PD (first row), DP-NT (second row), and DP-CT (third row) were detected by exciting Venus at 514 nm (green). The overlay images (on the right) show the co-localization of PKP1-CFP and DP-fragments-Venus in yellow. Bar, 10 µm. Images are representative of the overall subcellular distribution of the studied fragments in the three keratinocyte cell lines used (NHK, HaCaT, and PA-JEB/β4).

Taken together the results of co-IP, FLIM, and co-localization analysis in COS cells and keratinocytes, they suggest that DP interacts with PKP1a through the N-terminal half of the plakin domain. DP and PKP1a are closer than 10 nm when they interact with each other, suggesting a direct binding. Furthermore, such interaction does not require the formation of DMs.

Mapping of the PKP1a-binding site in the N-terminal region of the PD of DP, role of the SR2

Once the interaction between PKP1a and the N-terminal half of the PD of DP (DP-NT) was confirmed by using different approaches, we wanted to further map the PKP1a-binding site within this region. For this purpose, we made several N-terminal deletion mutants of DP and assayed their interaction with PKP1a full length by co-IP (Figure R11). The DP-SR2-SR5 fragment, which lacks the N-terminal first 63 residues, interacted with PKP1a. On the other hand, removing the SR2, as in the DP-SR3-SR5 fragment (region 180-545), compromised the association with PKP1a. Yet a faint band in the co-IP sample suggested that the SR3-SR5 might have a marginal contribution to the interaction. These results indicate that the SR2-like domain of DP-PD is necessary for the interaction with PKP1a.

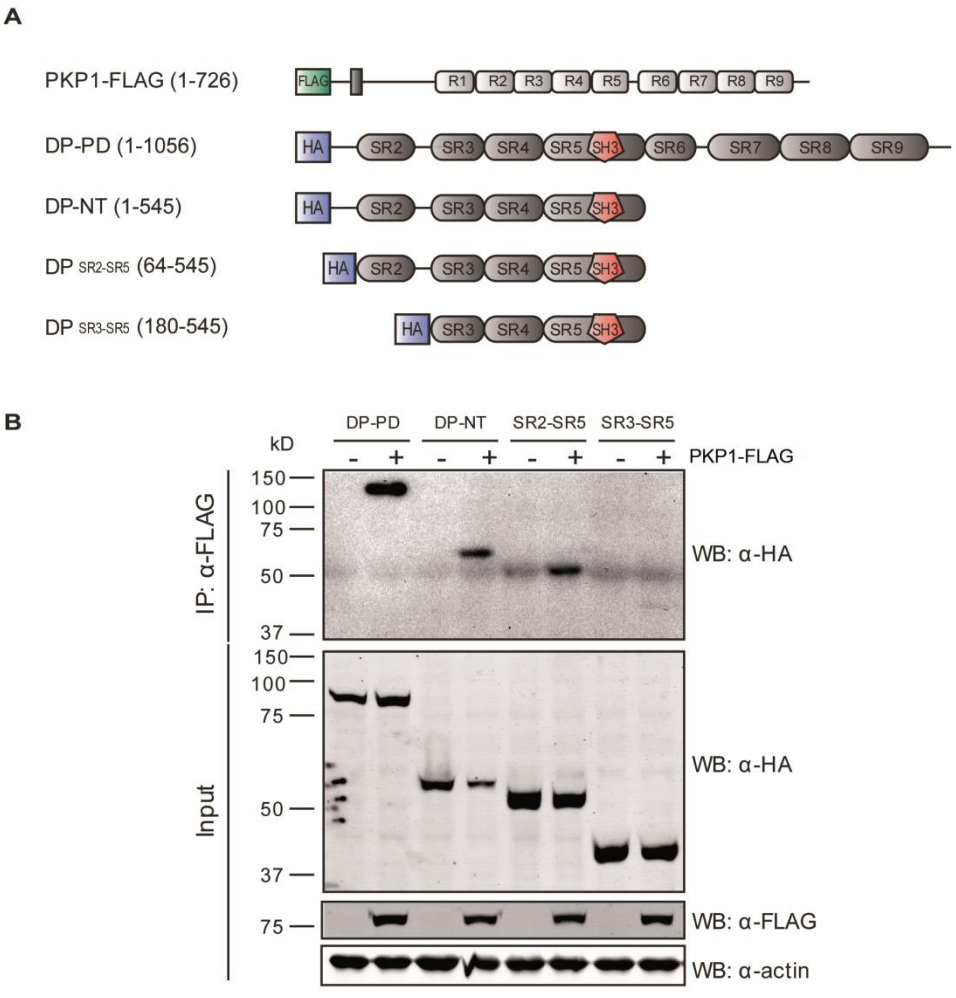

Figure R11. Analysis of the interaction between PKP1a and N-terminal fragments of DP by co-IP. A) Schematic domain representation of FLAG-tagged PKP1a full length and HA-tagged N-terminal DP fragments used in co-IP assays. **B)** The interaction of PKP1a with fragments of the N-terminal region of DP was analysed by co-IP. COS-1 cells were co-transfected with DP-HA fragments and PKP1-FLAG (+ lanes) or the empty pCEFLAG vector (- lanes). Lysates were immunoprecipitated with anti-FLAG agarose beads.

The presence of DP proteins in the immunoprecipitate was detected with an anti-HA polyclonal antibody. Fragments that were co-immunoprecipitated with PKP1a were not detected in its absence (- lanes), indicating a specific interaction. The expression of PKP1-FLAG and the DP fragments in the total lysates (input) was detected by western blotting using monoclonal anti-FLAG and anti-HA antibodies, respectively. β-actin detection was used as a loading control.

Next, we investigated the contribution of the different regions within the DP-NT to the interaction with PKP1a. Since the SR6 domain is part of a structural element that includes the SR3-SR4-SR5(SH3)-SR6 region (Choi & Weis 2011), we assayed whether it could contribute to the interaction. We created two fragments that extend to the SR6, one of them starts in the first residue, region 1-630 (DP-1-SR6), whereas the other lacks the SR2 domain, region 180-630 (DP-SR3-SR6). DP-1-SR6 interacted with PKP1-FLAG in co-IP assays, whereas the construct that lacks the SR2 failed to interact with PKP1a (Figure R12-B). Thus, we can conclude that the SR6 domain is not necessary for the establishment of the DP/PKP1a complex.

In order to assess the contribution of the SR5(SH3) region to the interaction with PKP1a, we created a C-terminal deletion mutant of DP-NT that lacks the SR5(SH3) domain, residues 1-376 (DP-1-SR4). This fragment interacted with PKP1a in co-IP assays (Figure R12-C). The intensity of the DP-1-SR4 band in the immunoprecipitated sample was weaker than the intensity of other fragments that interacted with PKP1a. Nonetheless, it should be noted that this fragment was expressed to significant lower levels than the other fragments of the DP-NT region. Since the SH3 domain makes contact with the SR4 as seen in crystal structures of desmoplakin and plectin (Ortega et al. 2011; Choi & Weis 2011), the low expression levels of the fragment 1-SR4 could be related to a reduced stability of this protein caused by the loss of the SH3-SR4 intramolecular contacts.

To further narrow down the PKP1a-interacting region in DP, we studied whether the SR2-like domain was sufficient to mediate the DP-PKP1a interaction. DP-SR2-HA, which contains the SR2-like domain and the preceding N-terminal sequence, interacted with PKP1-FLAG to a similar extent than DP-NT did (Figure R12-D).

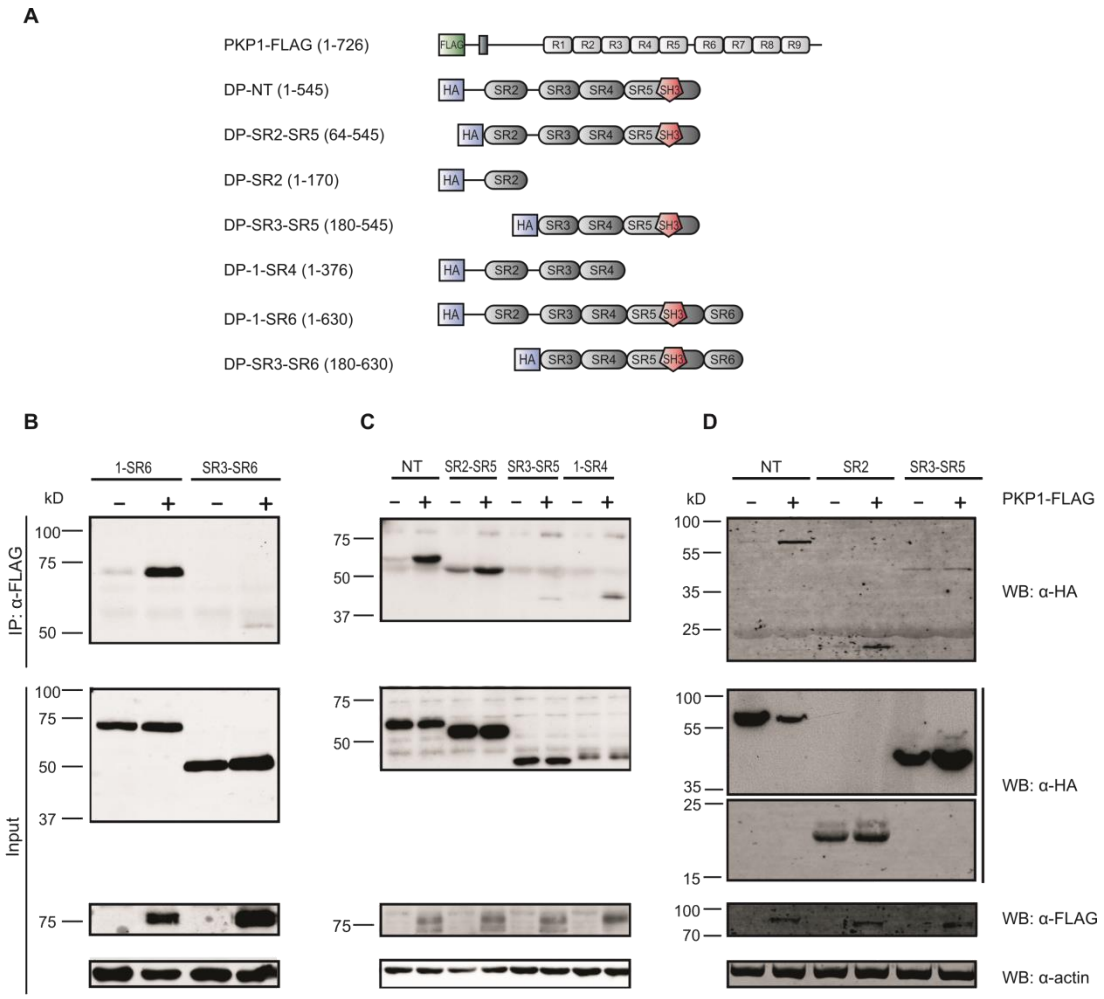

Figure R12. Analysis of the contribution of different regions of DP-PD to the interaction with PKP1. **A)** Schematic domain representation of FLAG-tagged PKP1a full length and HA-tagged N-terminal DP fragments used in co-IP assays. HA-tagged DP fragments were co-transfected with a plasmid coding for PKP1-FLAG (+ lanes) or the empty pCEFLAG vector (- lanes). Cell lysates were incubated with anti-FLAG agarose beads and the presence of HA-DP fragments in the immunoprecipitates was analysed by western blotting using a polyclonal antibody anti-HA. Expression of PKP1-FLAG and DP-HA fragments in the co-IP input (total lysates) was detected with monoclonal anti-FLAG and anti-HA antibodies, respectively. β-actin detection was used as a loading control. **B)** Analysis of the contribution of the SR6 domain of DP to the interaction of PKP1/DP-PD. **C)** Analysis of the contribution of the SR5(SH3) domain of DP to the interaction of PKP1/DP-PD. **D)** Analysis of the contribution of the SR2-like domain to the interaction of PKP1/DP-PD. Notice that the expression of HA-tagged DP fragments is shown by using two different detection methods due to the differences in the expression of the fragments. DP-NT and DP-SR3-SR5 were detected with a peroxidase-tagged secondary antibody (upper membrane, ECL) whereas DP-SR2 was detected with a 680-Dylight secondary antibody (bottom membrane, Odyssey).

As before, we validated the results obtained in co-IP assays by using FLIM. For this purpose, we co-transfected COS-7 cells with one DP N-terminal fragment tagged with Venus and PKP1a full length tagged with CFP. Figure R13 summarizes the mapping of the PKP1a interaction site in DP-NT by FLIM. Table R4 depicts the descriptive

statistics of the plotted experiments, including the number of measurements, the average CFP lifetime, and the dispersion measures (SD and SEM).

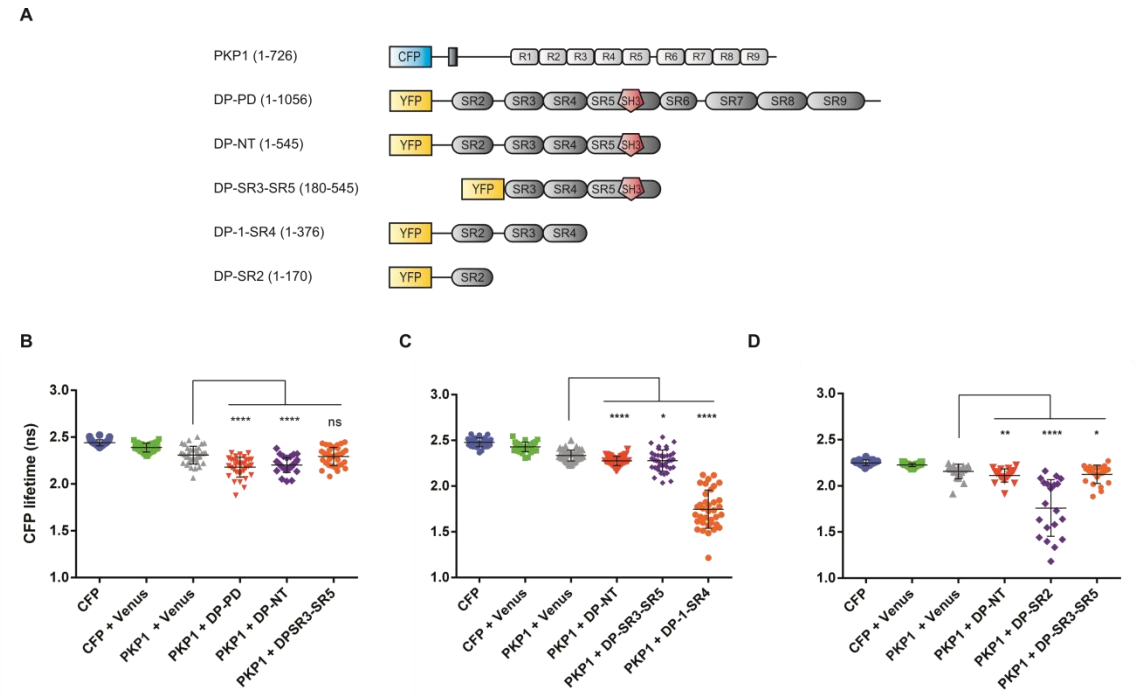

Figure R13. Analysis of the interaction between PKP1a and DP-NT by FLIM. A) Schematic domain representation of CFP-tagged PKP1a full length and Venus-tagged N-terminal DP fragments used in FLIM experiments. Venus is represented as YFP. **B, C, D)** PKP1a-DP interaction was analysed by FLIM in COS-7 cells. Results of three independent representative experiments are shown in scatter dot plots of the CFP lifetime with the mean and the standard deviation. Statistically significant differences (unpaired unequal variance t-test) are indicated by **** ($p \leq 0.0001$); ** ($p \leq 0.01$); * ($p \leq 0.05$); ns, not significant ($p > 0.05$).

DP-PD and DP-NT produced a highly significant decrease in the CFP lifetime of PKP1-CFP from ~2.31 ns to ~2.18 and ~2.20 ns, respectively ($p \leq 0.0001$) (Figure R13-B). On the other hand, CFP lifetime was not significantly reduced when PKP1-CFP was co-transfected with DP-SR3-SR5 ($p > 0.05$). Thus, FLIM experiments supported the importance of the SR2-like domain (region 1-170) in the DP/PKP1a interaction.

Next, we analysed the possible role of the SR5(SH3) region of the plakin domain of DP in the interaction with PKP1a. For doing so, we used DP-NT (1-545) that contains the N-terminal tail and the region SR2-SR5, DP-1-SR4 (1-376), and DP-SR3-SR5 (180-545). CFP lifetime was severely reduced in cells co-transfected with PKP1a and DP-1-SR4 (1-376), indicating that this region interacts efficiently with PKP1a ($p \leq 0.0001$) (Figure R13-C).

The severe drop observed in the CFP lifetime of the cells co-transfected with PKP1a and DP-1-SR4 suggests that the region 1-376 of DP is able to interact with PKP1a full length and that the SR5(SH3) region of the DP-PD is not necessary for such

interaction. These results are in accordance with the previous ones obtained by co-IP (Figure R12-C) and support the idea that the region SR5(SH3) is not directly involved in the interaction between DP and PKP1a. Before, we hypothesised about the possibility that the quite ineffective expression of HA-DP-1-SR4 might be related with the stability loss caused by the lack of the SH3 domain. Nonetheless, in the FLIM experiments the Venus-DP-1-SR4 construct was expressed at high levels, similarly to other small DP fragments tagged with Venus. This may be explained by the different tag, HA or Venus, that the recombinant DP-1-SR4 had in the constructs used in each experiment.

In this case, DP-SR3-SR5 reduced CFP lifetime from ~2.33 ns to ~2.28 ns ($p \leq 0.05$). This slight decrease is in agreement with the faint band observed in co-IP assays (see Figure R11).

Table R4. Descriptive statistics of the data shown in figure R13

Figure	Donor	Acceptor	n	Mean lifetime (ns)	SD	SEM
R13-B	CFP	-	34	2.440	0.032	0.005
	CFP	Venus	36	2.388	0.048	0.008
	PKP1-CFP	Venus	36	2.309	0.095	0.016
	PKP1-CFP	DP-PD-Venus	34	2.181	0.107	0.018
	PKP1-CFP	DP-NT-Venus	35	2.203	0.078	0.013
	PKP1-CFP	DP-SR3-SR5	35	2.294	0.097	0.016
R13-C	CFP	-	34	2.479	0.048	0.008
	CFP	Venus	35	2.429	0.052	0.009
	PKP1-CFP	Venus	39	2.334	0.059	0.009
	PKP1-CFP	DP-NT-Venus	39	2.275	0.050	0.008
	PKP1-CFP	DP-SR3-SR5-Venus	39	2.278	0.116	0.019
	PKP1-CFP	DP-1-SR4-Venus	36	1.748	0.208	0.035
R13-D	CFP	-	21	2.250	0.030	0.007
	CFP	Venus	21	2.226	0.019	0.004
	PKP1-CFP	Venus	18	2.176	0.045	0.01
	PKP1-CFP	DP-NT-Venus	20	2.112	0.071	0.016
	PKP1-CFP	DP-SR2-Venus	20	1.759	0.306	0.068
	PKP1-CFP	DP-SR3-SR5-Venus	22	2.124	0.099	0.021

n, number of values; SD, standard deviation; SEM, standard error of the mean.

We also studied by FLIM whether the SR2-like domain of DP was sufficient to interact with PKP1a. For this purpose we made a small DP fragment that comprehends the region 1-170 (DP-SR2). This fragment produced a decrease in the CFP lifetime from ~2.18 ns to ~1.76 ns ($p \leq 0.0001$) (Figure R13-D). DP-SR2 includes the SR2-like domain (region ~64-170) and the N-terminal segment that we have previously shown

that it is not required for the interaction with PKP1a (see examples in Figures R11 and R12). On the other hand, DP-SR3-SR5 (region 180-630) produced a slight decrease in the CFP lifetime (from ~2.18 ns to ~2.12ns). Thus, we can conclude that the SR2-like domain of DP is necessary and sufficient for the interaction with PKP1a. In addition, since the fragment SR3-SR5 caused a statistically significant small reduction in the CFP lifetime in two out of three experiments, it is likely that this region has an accessory contribution to the interaction with PKP1a.

Both DP-1-SR4 and DP-SR2 produced a large reduction in the CFP lifetime when they were co-transfected with PKP1-CFP. Moreover, both showed high variability in the CFP lifetime measurements (SDs of 0.208 and 0.306, respectively). We wondered whether it might be related to the much higher expression levels of these small fragments, compared to larger constructs. High expression levels of one of the fragments in co-transfection experiments may cause a significant imbalance in the donor-acceptor ratio that might affect the CFP-lifetimes determined by FLIM. Specifically, high concentrations of the acceptor may cause quenching of the donor due to proximity of the Venus-tagged protein to the CFP, within the Försters distance, in the absence of a molecular interaction (Grailhe et al. 2006).

Thus, we analysed whether the CFP lifetime was affected by the expression levels of the fragments tagged with Venus. Since it was not possible to directly measure the concentration of the Venus-tagged fragments we measured the intensity of Venus that presumably reflects the intracellular content in recombinant protein, although not necessarily linearly (Gaigalas et al. 2001), and studied the correlation with the CFP lifetime (Figure R14).

When PKP1-CFP was co-expressed with isolated Venus, DP-PD-Venus, DP-NT-Venus or DP-SR3-SR5-Venus, the lifetime of CFP showed a very small dependence with the intensity of Venus (Figure R14-A, B, C, D). On the other hand, when PKP1-CFP was co-expressed with DP-1-SR4-Venus or with DP-SR2-Venus, the CFP lifetime decreased at high values of Venus fluorescence intensity (Figure R14-E, F). Nonetheless, even at low Venus fluorescence intensity DP-SR2-Venus and DP-1-SR4-Venus already caused a reduction in the CFP lifetime with respect to the isolated Venus. Since variation in the fluorescence lifetime of PKP1-CFP as a function of the intensity of isolated Venus, which is typically expressed in high levels, is negligible the concentration-dependent effect observed for the DP-SR2-Venus and DP-1-SR4-Venus constructs might be related to an increase in the association of these DP fragments to PKP1a.

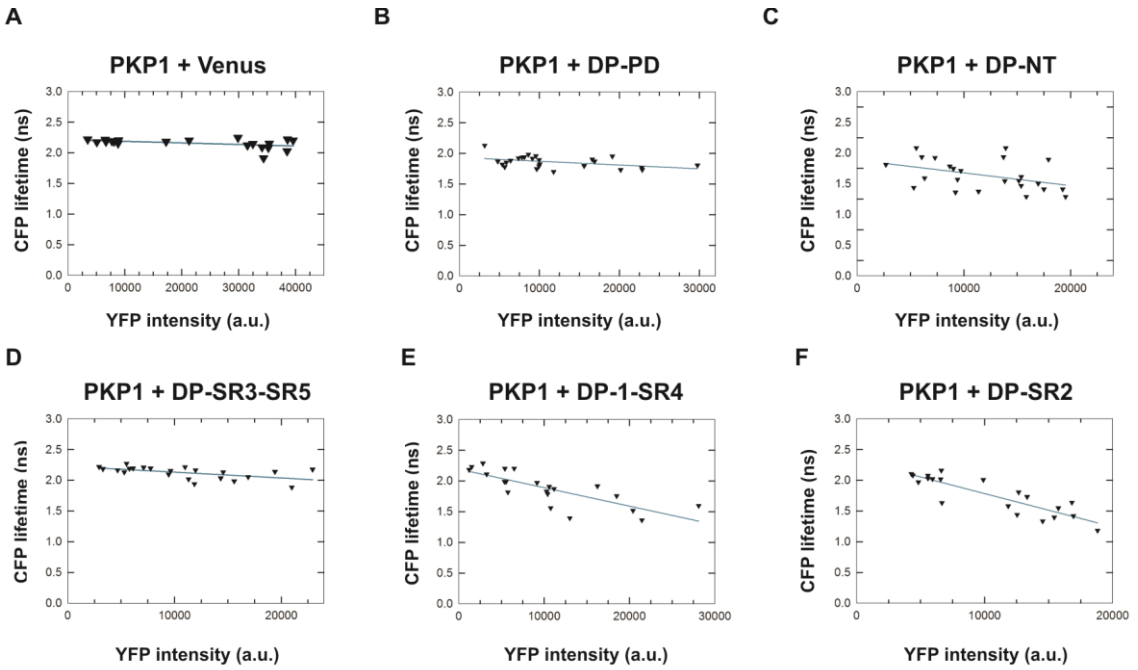

Figure R14. Dependence of the CFP lifetime on the intensity of Venus fluorescence in FLIM experiments. CFP lifetime and Venus fluorescence intensity were measured in COS-7 cells co-transfected with CFP-tagged PKP1a full length and different Venus-tagged DP fragments (see above each graph). For each DP construct, the Venus fluorescence intensity is approximately related to the protein levels in the cells (a.u., arbitrary units). Yet, the ranges of expression levels are not comparable between different constructs.

In conclusion, the results obtained by using FLIM are in accordance with those obtained by co-IP, and support that the SR2-like domain of DP is necessary and sufficient to mediate the interaction with PKP1a.

To complement the analysis made by co-IP and FLIM, we investigated by confocal microscopy the subcellular distribution of fragments of the N-terminal half of the plakin domain of DP. Initially, we made single transfections of DP-SR2 (region 1-170), DP-SR3-SR5 (region 180-545), and DP 1-SR4 (region 1-376) tagged with Venus in COS-7 cells. These three constructs showed a homogeneous distribution throughout the cell in most of the cells, and exhibited certain nuclear staining in cells expressing high levels of the fusion proteins (Figure R15).

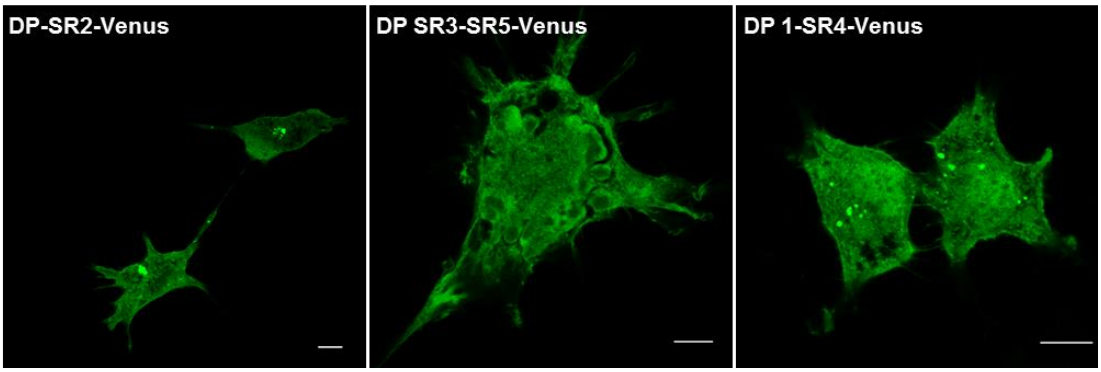

Figure R15. Subcellular localization of DP N-terminal fragments in COS-7 cells. The subcellular localization of Venus-tagged DP N-terminal fragments was investigated by confocal microscopy in COS-7 cells overexpressing these constructs. DP-Venus fragments were detected by using an Argon laser line at 514 nm. Bar, 10 μm. Images are representative of the overall subcellular distribution of the studied fragments.

Next, we analysed the effect of the co-expression of PKP1a on the distribution of these DP constructs. COS-7 cell were co-transfected with PKP1-CFP and one Venus-tagged DP N-terminal fragment, and their co-localization was studied by confocal microscopy (Figure R16). We used the nuclear recruitment or enrichment of DP fragments as an indication of the interaction with PKP1a.

In the presence of PKP1a, a nuclear enrichment of the DP fragments DP-SR2 (1-170) and DP-1-SR4 (1-376) was observed compared to the distribution showed when they were expressed in the absence of PKP1a in single transfection experiments (see above).

The construct DP-SR3-SR5 showed a dual pattern when co-expressed with PKP1-CFP. In some cells, DP-SR3-SR5 was not recruited to the nucleus by PKP1a (Figure R16, second row). Yet, in other cells DP-SR3-SR5 was clearly enriched at the nucleus where it co-localized with PKP1a (Figure R16, third row). This dual behaviour might be explained if the interaction between DP-SR3-SR5 and PKP1a had only moderate or weak affinity, so that small differences in the expression levels could result in large differences in the association, not always being possible to detect it.

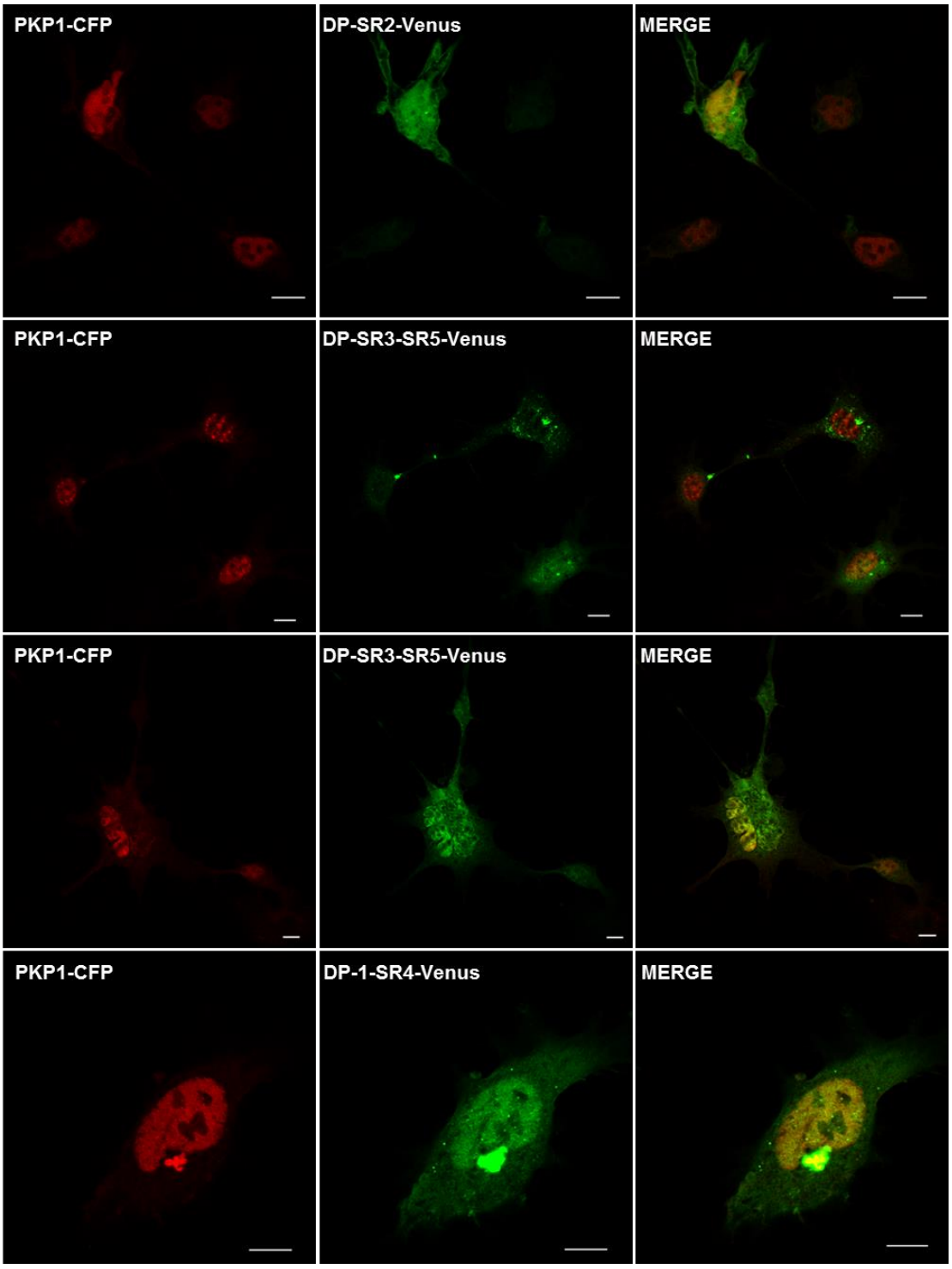

Figure R16. Subcellular localization of PKP1a and DP N-terminal fragments co-transfected in COS-7 cells. Confocal microscopy images of COS-7 cells overexpressing PKP1a full length and one DP N-terminal fragment tagged with CFP or Venus, respectively. PKP1-CFP was detected upon excitation of CFP at 442 nm and is represented in red. DP-SR2 (first row), DP-SR3-SR5 (second and third rows), and DP-1-SR4 (last row) were detected by using an Argon laser line at 514 nm (green). The overlay images (on the right) show the co-localization of PKP1-CFP and DP-Venus fragments in yellow. Bar, 10 µm. Images are representative of the overall subcellular distribution of the studied fragments.

Analysis of secondary PKP1a-interaction sites outside the SR2-like domain of DP

Previous experiments suggested that the region SR3-SR5 of DP might have an accessory contribution to the interaction with PKP1a. In co-IP assays, a faint band was visible in the position of DP-SR3-SR5. Moreover, in FLIM experiments the DP-SR3-SR5 fragment showed statistically significant results in some experiments, and co-localization assays showed a dual distribution pattern of DP-SR3-SR5 when it was expressed in COS cells in the presence of PKP1a. Collectively, these results invited us to think that, in addition to the primary site in the SR2-like domain, secondary sites through the DP-NT domain might be taking part in the interaction with PKP1a.

To further study this possibility, we made additional N-terminal deletion mutants of the PD of DP tagged with Venus and assayed their interaction with PKP1-CFP by FLIM (Table R5 and Figure R17). These DP mutants contain the SR6-SR9 region. Furthermore, they presented similar expression levels in COS cells, which avoided the potential complexity caused by the imbalance between PKP1-CFP and small DP Venus-tagged fragments.

DP-PD and the construct SR2-SR9, which lacks the N-terminal 63 residues that precede the SR2, produced a marked reduction in the CFP-lifetime of PKP1-CFP, ~2.14 ns and ~2.17 ns, respectively, compared to the reference value in the presence of Venus (~2.31 ns) ($p \leq 0.0001$). Interestingly, the CFP lifetime in the presence of the fragment DP-SR3-SR9 (residues 272-1056), ~2.26 ns, was also significantly shorter ($p \leq 0.001$) than that of the control. On the contrary, fragments beginning at the SR4, SR5, and SR6 domains did not show any significant decrease in the CFP lifetime with respect to the control ($p > 0.5$).

Table R5. Descriptive statistics of the data shown in figure R17

Donor	Acceptor	n	Mean lifetime (ns)	SD	SEM
CFP	-	41	2.471	0.063	0.010
CFP	Venus	39	2.314	0.097	0.016
PKP1-CFP	Venus	42	2.310	0.062	0.010
PKP1-CFP	DP-PD-Venus	42	2.139	0.077	0.012
PKP1-CFP	DP-SR2-SR9-Venus	32	2.169	0.054	0.010
PKP1-CFP	DP-SR3-SR9-Venus	38	2.267	0.027	0.004
PKP1-CFP	DP-SR4-SR9-Venus	38	2.335	0.078	0.013
PKP1-CFP	DP-SR5-SR9-Venus	34	2.320	0.073	0.013
PKP1-CFP	DP-CT-Venus	34	2.342	0.069	0.012

n, number of values; SD, standard deviation; SEM, standard error of the mean

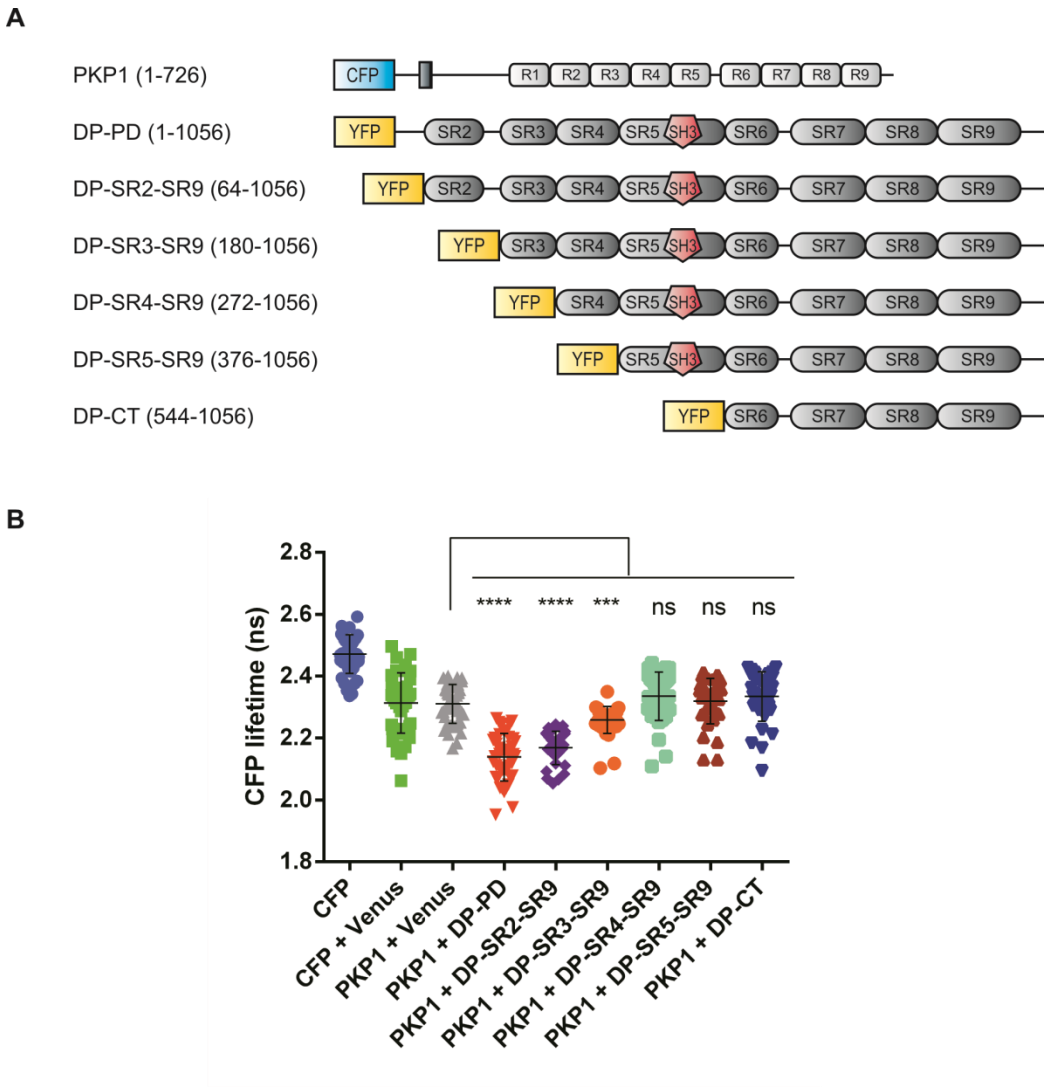

Figure R17. Analysis of the interaction between PKP1a and DP N-terminal deletion mutants by FLIM. A) Schematic domain representation of CFP-tagged PKP1a full length and Venus-tagged DP N-terminal deletion mutants used in FLIM assays. Venus is represented by the acronym YFP. **B)** The PKP1a-DP interaction was analysed by FLIM in COS-7 cells. Results of one representative experiment are shown in scatter dot plots of the CFP lifetime with the mean and the standard deviation. Statistically significant differences (unpaired unequal variance t-test) are indicated by **** ($p \leq 0.0001$); *** ($p \leq 0.001$); ns, not significant ($p > 0.05$).

Taken together, these results indicate that in addition to the SR2-like domain, DP-PD possibly interacts with PKP1a by means of secondary sites that most likely involve the SR3 sub-domain.

To complement the analysis by FLIM, we studied the subcellular distribution of PKP1-CFP and the DP-Venus N-terminal mutants transiently transfected in COS-7 cells. First, we made single transfections of the DP fragments described in figure R17-A (Figure R18).

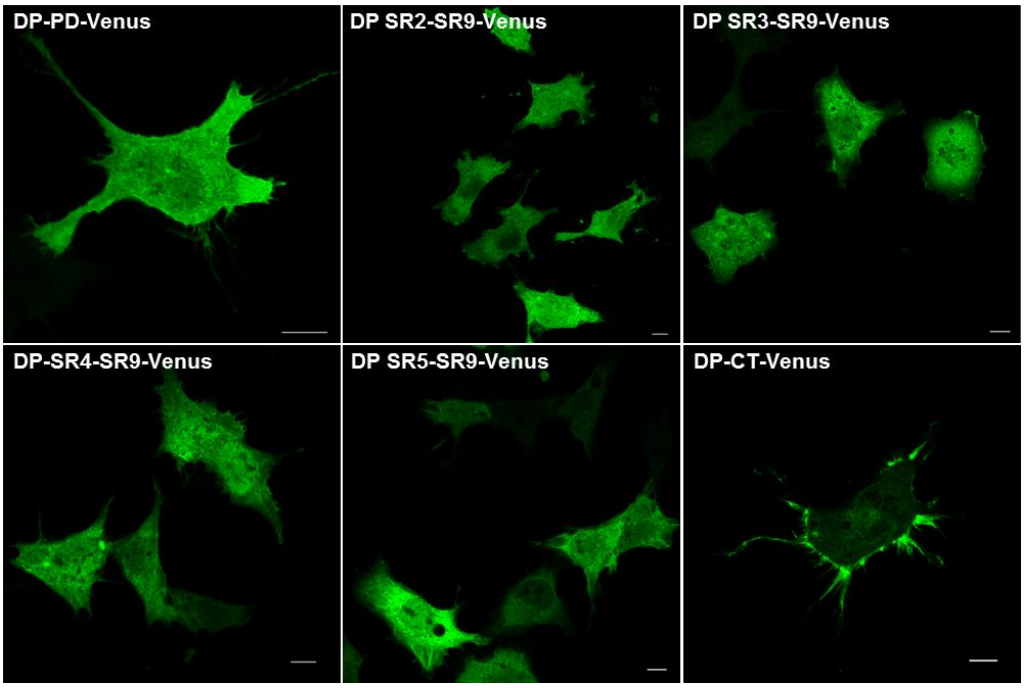

Figure R18. Subcellular distribution of DP N-terminal deletion mutants transfected in COS-7 cells. The subcellular localization of ectopically expressed Venus-tagged DP N-terminal fragments (described in figure R17-A) was investigated in COS-7 cells by confocal microscopy. DP fragments were detected by exciting Venus at 514 nm. Bar, 10 μm. Images are representative of the overall subcellular distribution of the studied fragments.

Except for DP-CT (region 544-1056), all the fragments of the plakin domain of DP showed similar distribution. They were diffusely distributed throughout the cytoplasm and appeared mostly excluded from the nucleus though not in every cell. They were also present at the plasma membrane. DP-CT was mainly enriched at the cell borders as we had observed before (see Figure R5).

Next, we analysed the subcellular distribution of these DP fragments when they were co-expressed with CFP-tagged PKP1a, which shows an exclusively nuclear localization (Figure R19). The complete plakin domain of DP (DP-PD-Venus, residues 1-1056) and a similar construct that lacks the first 63 residues upstream of the SR2 (DP-SR2-SR9-Venus, residues 64-1056) were markedly recruited to the nucleus in the presence of PKP1a (see white arrows). On the contrary, DP-SR4-SR9-Venus (region 272-1056), DP-SR5-SR9-Venus (region 376-1056), and DP-CT-Venus (region 544-1056) were completely excluded from the nucleus (see grey arrows), suggesting that an interaction of PKP1a with these DP-fragments is not occurring. Interestingly, DP-SR3-SR9-Venus (region 180-1056) showed an intermediate behaviour with some cells where this fragment was recruited to the nucleus and co-localized with PKP1a and cells where it did not (see red arrows).

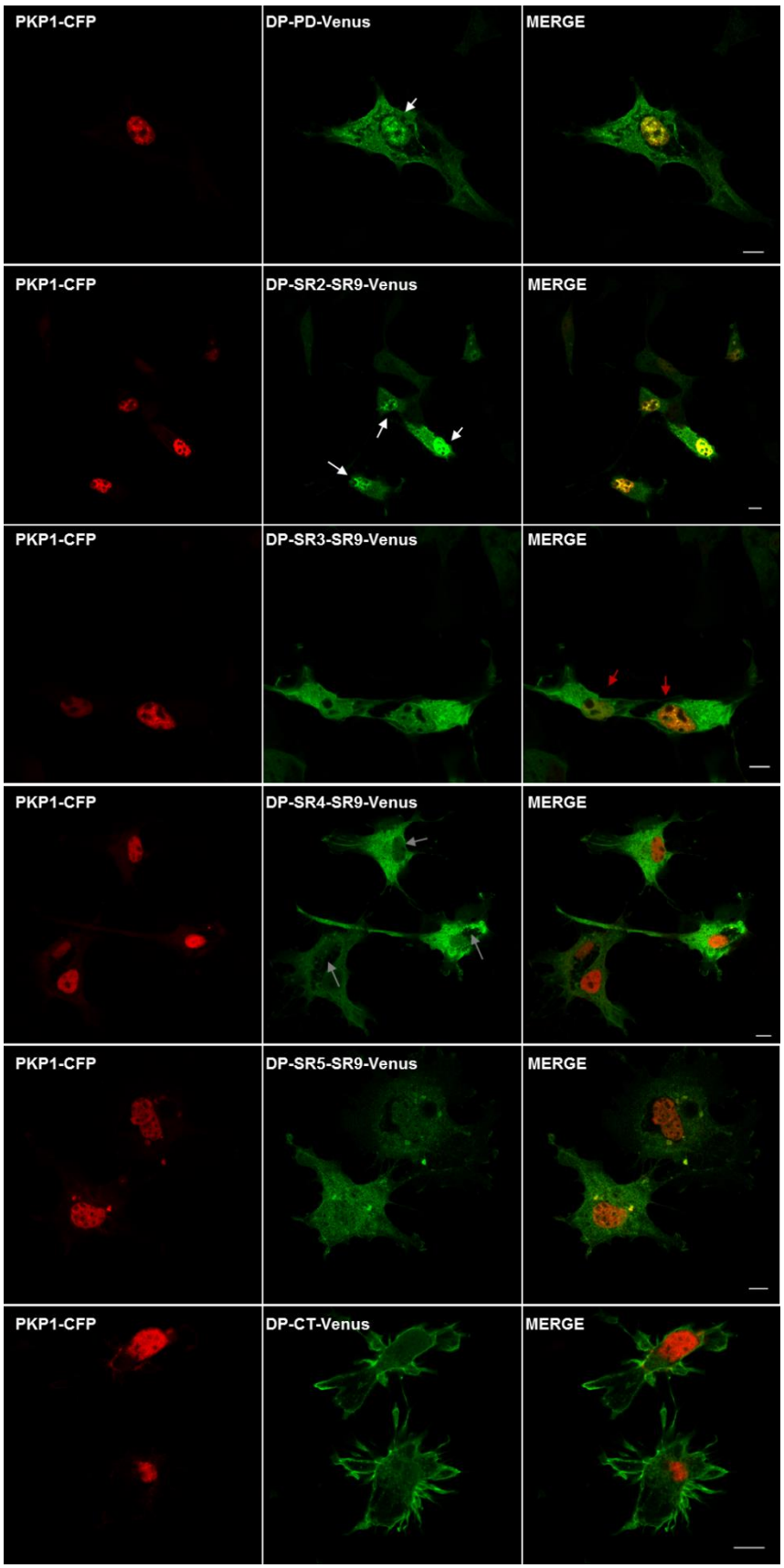

Figure R19. Sub-cellular distribution of PKP1-CFP and amino-terminal deletion mutants of the plakin domain of DP co-transfected in COS-7 cells. CFP-tagged PKP1a and Venus-tagged DP-deletion mutants were co-transfected in COS-7 cells and studied by confocal microscopy. PKP1a full length (PKP1-CFP, region 1-726) was detected upon excitation of CFP (442 nm) and is represented in red. Venus-tagged DP-PD fragments were detected by using an Argon laser line at 514 nm. DP distribution is shown in green. Merge images (right column) show the co-localization of PKP1-CFP and DP-fragments-Venus in yellow. Bar, 10 µm. The displayed images are representative of the subcellular distribution of the studied fusion proteins.

Taking together, these results illustrate that the interaction between PKP1a and DP is primarily mediated by the SR2-like of DP. Yet, the adjacent SR3 domain might also

participate in the interaction but to a lesser extent, establishing secondary interactions with PKP1a, which are not sufficient to support the efficient association in the absence of the SR2.

2. Mapping of the DP-binding site in PKP1a

Once that we knew the specific region of DP that interacts with PKP1a, we investigated the regions of PKP1a that are important for the interaction with DP. Our goal was to obtain a detailed picture of the interaction domain mapping of the DP-PKP1a complex.

DP interacts with the head domain of PKP1a

Previous studies had shown that the N-terminal head domain of PKP1a (region 1-243), interacts with DP (Hofmann et al., 2000; Kowalczyk, 1999; Sobolik-Delmaire, Katafiasz, & Wahl, 2006). We wanted to test our experimental approximation that includes co-IP, FLIM, and co-localization analysis to prove the interaction between DP and the head domain of PKP1a.

Initially, the interaction between DP and PKP1a was analysed by co-IP in COS-1 cells transiently co-transfected with DP-HA and PKP1-FLAG constructs. We used DP-PD-HA (region 1-1056) and DP-NT-HA (region 1-545) that we confronted with PKP1-FLAG (1-726), PKP1-head-FLAG (region 1-243), and PKP1-ARM-FLAG (region 244-726) or the pCEFLAG empty vector as negative control (Figure R20).

Both DP-PD and DP-NT interacted with PKP1a full length and the head domain but they did not interact with the armadillo domain of PKP1a.

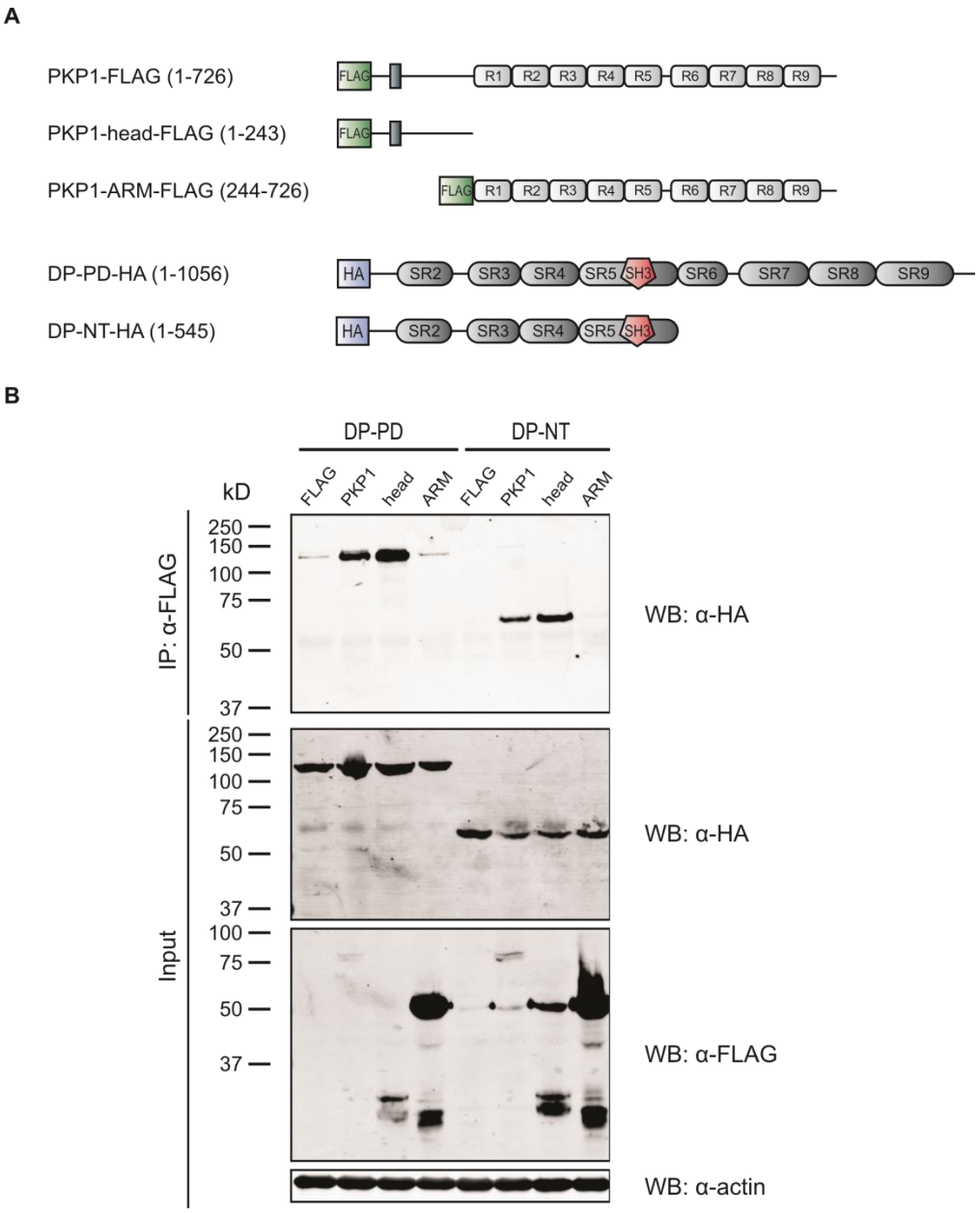

Figure R20. Analysis of the DP-binding site in PKP1a by co-IP. A) Schematic domain representation of FLAG-tagged PKP1a and HA-tagged DP fragments used in co-IP assays. **B)** HA-tagged DP fragments were co-transfected with FLAG-tagged constructs (PKP1a full length, PKP1-head domain, or PKP1-armadillo domain) or with the empty pCEFLAG vector (negative control). Samples were immunoprecipitated using anti-FLAG agarose beads. Co-IP results were investigated by western blotting with a polyclonal antibody anti-HA. DP fragments did not co-immunoprecipitated when the empty pCEFLAG vector was used. Expression of PKP1-FLAG and DP-HA fragments in the input samples (total lysates) was detected by western blotting, using monoclonal antibodies anti-FLAG and anti-HA, respectively. β-actin detection was used as a loading control.

We also wanted to analyse the interaction of the head domain of PKP1a with DP by using FLIM. To do so, we co-transfected COS-7 cells with DP-PD or DP-NT and one PKP1-fragment (PKP1, PKP1-head or PKP1-ARM) tagged with the FRET pair

CFP/Venus and we measured the fluorescence lifetime of CFP (Figure R21 and Table R6).

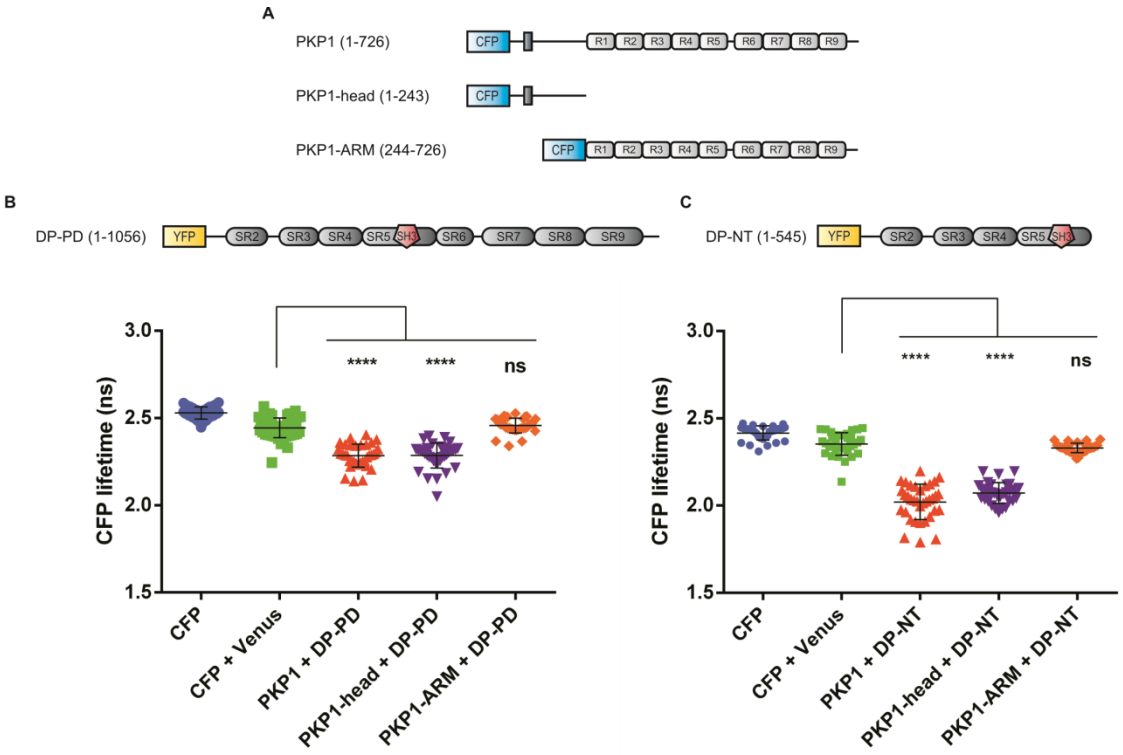

Figure R21. Analysis of the interaction between DP-PD or DP-NT and PKP1a by FLIM. A) Schematic domain representation of CFP-tagged PKP1a fragments used in FLIM experiments. DP-PD-Venus **(B)** and DP-NT-Venus **(C)** were used to analyse the interaction with PKP1a by FLIM. Results of one representative experiment using each DP-fragment are represented in scatter dot plots of the CFP lifetime with the mean and the standard deviation. Statistically significant differences (unpaired unequal variance t-test) are indicated by **** ($p \leq 0.0001$); ns, not significant ($p > 0.05$).

First, we performed the experiments by using the complete plakin domain of DP (DP-PD, region 1-1056). The CFP lifetime was significantly decreased from ~2.44 ns in the control (isolated CFP and Venus) to ~2.28 ns or ~2.29 ns when DP-PD-Venus was co-transfected with PKP1-CFP or PKP1-head-CFP, respectively ($p \leq 0.0001$). On the contrary, CFP lifetime was not significantly altered, with respect to the control, when DP-PD-Venus was co-transfected with PKP1-ARM-CFP ($p > 0.05$).

Similar results were obtained when we used the N-terminal half of DP (DP-NT, region 1-545). When DP-NT was co-transfected with PKP1a or PKP1-head the CFP lifetime was decreased by ~0.3 ns with respect to the control ($p \leq 0.0001$). This drop was not observed when DP-NT was co-transfected with PKP1-ARM-CFP ($p > 0.05$).

Table R6. Descriptive statistics of the data shown in figure R21

Figure	Donor	Acceptor	n	Mean lifetime (ns)	SD	SEM
R21-B	CFP	-	38	2.529	0.035	0.006
	CFP	Venus	48	2.443	0.057	0.008
	PKP1-CFP	DP-PD-Venus	35	2.284	0.066	0.011
	PKP1-head-CFP	DP-PD-Venus	35	2.292	0.061	0.010
	PKP1-ARM-CFP	DP-PD-Venus	35	2.457	0.042	0.007
R21-C	CFP	-	32	2.416	0.041	0.007
	CFP	Venus	34	2.353	0.065	0.011
	PKP1-CFP	DP-NT-Venus	35	2.021	0.102	0.017
	PKP1-head-CFP	DP-NT-Venus	32	2.072	0.060	0.011
	PKP1-ARM-CFP	DP-NT-Venus	33	2.330	0.028	0.005

n, number of values; SD, standard deviation; SEM, standard error of the mean.

To complete the picture, we also looked at the subcellular distribution of PKP1a and DP-fragments when they are co-transfected in COS-7 cells. We have previously demonstrated that DP is recruited to the nucleus by means of its interaction with PKP1a. Here we looked at how the subcellular distribution of DP-NT was affected by different PKP1a fragments. COS-7 cells were transiently transfected with DP-NT and each of the PKP1a constructs (PKP1 full length, head domain or ARM-domain) and the subcellular distribution of each fragment was analysed by using confocal microscopy (Figure R22).

When DP-NT was transfected alone in COS-7 cells, it mainly showed a cytoplasmic distribution with slight presence at the plasma membrane (see Figure R5). However, when it was co-transfected with PKP1a full length (region 1-726) or PKP1-head domain (region 1-243), DP-NT was markedly recruited to the nucleus suggesting that an interaction between DP-NT and PKP1/PKP1-head was taking place. This DP-recruitment is in agreement with the conclusions of co-IP and FLIM experiments regarding that the interaction of DP and PKP1 needs of the PKP1a head domain.

On the other hand, PKP1-ARM-CFP was distributed throughout the cytoplasm and was not present at the nucleus (we will deepen over this in the next section). Therefore, the recruitment of DP fragments to the nucleus could not be used as an indication of interaction with PKP1-ARM.

PKP1-ARM-CFP and DP-NT-Venus co-localized when they were co-expressed. Nonetheless, these two constructs were already present at the cytoplasm when they were independently expressed, suggesting that the overlap between PKP1-ARM-CFP and DP-NT-Venus is most likely fortuitous, due to the sharing of the same subcellular compartment, rather than due to a real interaction between these two proteins. In this respect, the random localization of two proteins in the same compartment does not

imply actual co-localization because their spatial distributions are independent of each other (Costes et al. 2004).

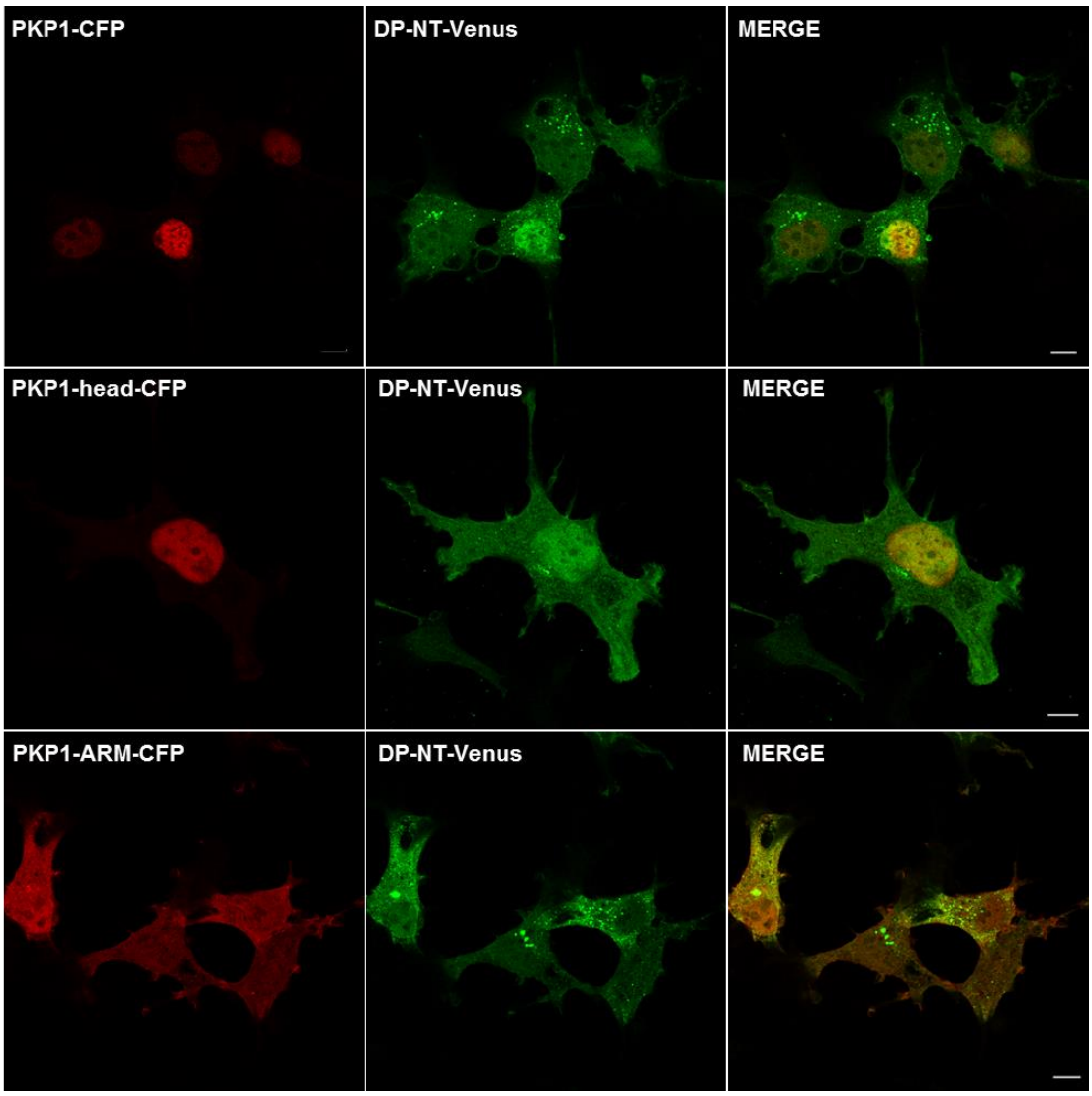

Figure R22. Subcellular localization of DP-NT and PKP1a fragments co-transfected in COS-7 cells. Confocal microscopy images of COS-7 cells ectopically expressing DP-NT and one PKP1a fragment tagged with Venus or CFP, respectively. PKP1a-fragments overexpression was detected upon excitation of CFP (442 nm) and is represented in red. DP-NT was detected by using an Argon laser line at 514 nm and is represented in green. The overlay images (merge) show the co-localization of DP-NT-Venus and the PKP1a-fragments in yellow. Bar, 10 µm. Images are representative of the overall subcellular distribution of the studied fragments.

In summary, we have shown that combination of co-IP, FLIM, and subcellular distribution analysis is a valid approach to analyse the interaction between DP and the head domain of PKP1a.

Mapping of the DP-binding site within the head domain of PKP1a

We wanted to go one step further to more closely delimit the DP-interacting region in PKP1a. With this purpose, we made several FLAG-tagged fragments of the head domain of PKP1. We designed two fragments that halve the head domain in two segments of similar size, regions 1-120 and 121-243. We also created a shorter N-terminal fragment 1-51 (PKP1-1-51) that contains the HR2 motif and has also been implicated in the recruitment of DP to the plasma membrane (Sobolik-Delmaire et al. 2006). In addition, we created the complementary 52-243 fragment (PKP1-52-243). We assayed the interaction of these PKP1 fragments with DP-NT-HA by co-IP (Figure R23).

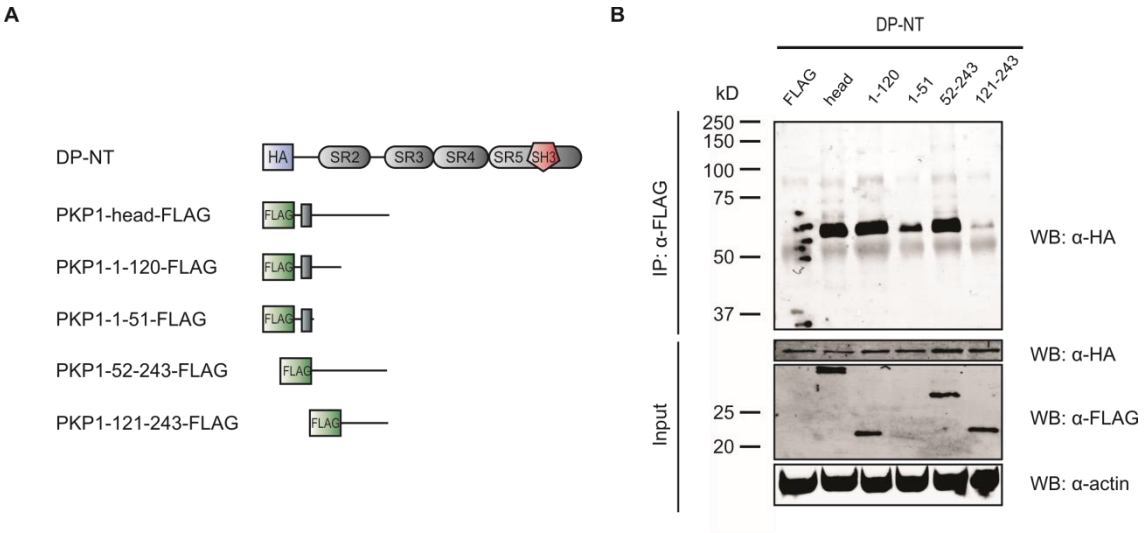

Figure R23. Mapping of the interaction site of DP in the head domain of PKP1 by co-IP. A) Schematic domain representation of HA-tagged DP-NT and FLAG-tagged PKP1-head fragments used in co-IP assays. **B)** The DP interaction site in PKP1-head was analysed by co-IP of DP-NT-HA by five constructs of the head domain of PKP1a (head, 1-120, 1-51, 52-243, and 121-243) using anti-FLAG agarose beads. As a control (lane: FLAG), cells were co-transfected with DP-NT-HA and the empty pCEFLAG vector. The presence of DP-NT-HA in the immunoprecipitated samples was investigated by western blotting using a polyclonal antibody anti-HA. The expression of PKP1-FLAG and DP-HA fragments in the total cell lysates used for the co-IP (input) was proved using monoclonal antibodies anti-FLAG and anti-HA, respectively. β-actin detection was used as a loading control. Notice that it was not possible to see PKP1-1-51 (residues 1-51) in the western blot because of its small molecular weight (~6 kD).

DP-NT interacted with PKP1-1-120 to a similar extent than with the complete PKP1 head domain. On the other hand, the complementary fragment PKP1-121-243 did not interact with DP. DP-NT interacted with the PKP1-1-51 and PKP1-52-243 fragments, but the intensity of the band in the co-IP was significantly weaker for the shorter fragment compared with the band observed for PKP1-52-243, which was

undistinguishable from the band of the complete head domain of PKP1. Taken together, these results suggest that DP-NT interacts with the N-terminal half of the head domain of PKP1, and that while the first 51 residues of PKP1 associate with DP-NT, the major DP-interaction occurs through a region comprehended between residues 52-120.

We wanted to verify the proposed DP-binding region in PKP1 (residues 52-120) by using FLIM. With this purpose we designed PKP1 fragments tagged with CFP and co-transfected them with DP-NT-Venus in COS-7 cells. In this case, taking into account the potential inaccuracies observed in FLIM assays when using small fragments (see Figure R14), we decided to make the fragments as N-terminal deletion mutants of PKP1 full length.

The co-transfection of DP-NT-Venus with PKP1-CFP (region 1-726), PKP1-head-CFP (region 1-243), or PKP1-52-CFP (region 52-726) produced a similar and statistically significant decrement of the CFP lifetime with respect to the control sample. Specifically, the CFP lifetime dropped from ~2.3 to ~2.2 ns ($p \leq 0.0001$) (Table R7 and Figure R24). On the contrary, when DP-NT-Venus was co-transfected with PKP1-121-CFP (region 121-726) or PKP1a-ARM-CFP (region 244-726) the CFP lifetime remained similar to that of the control ~2.3 ns (ns, $p > 0.5$).

Table R7. Descriptive statistics of the data shown in figure R24

Donor	Acceptor	n	Mean lifetime (ns)	SD	SEM
CFP	-	31	2.424	0.028	0.005
CFP	Venus	32	2.344	0.055	0.010
PKP1-CFP	DP-NT-Venus	30	2.246	0.055	0.010
PKP1-head-CFP	DP-NT-Venus	31	2.225	0.086	0.015
PKP1-52-CFP	DP-NT-Venus	31	2.220	0.087	0.016
PKP1-121-CFP	DP-NT-Venus	29	2.333	0.040	0.007
PKP1-ARM-CFP	DP-NT-Venus	30	2.385	0.056	0.010

n, number of values; SD, standard deviation; SEM, standard error of the mean

Our analysis by FLIM supports that the N-terminal 51 residues of PKP1 are dispensable for the interaction with DP, which is mediated by the region 52-120 of the head domain. These results are in agreement with those observed by co-IP.

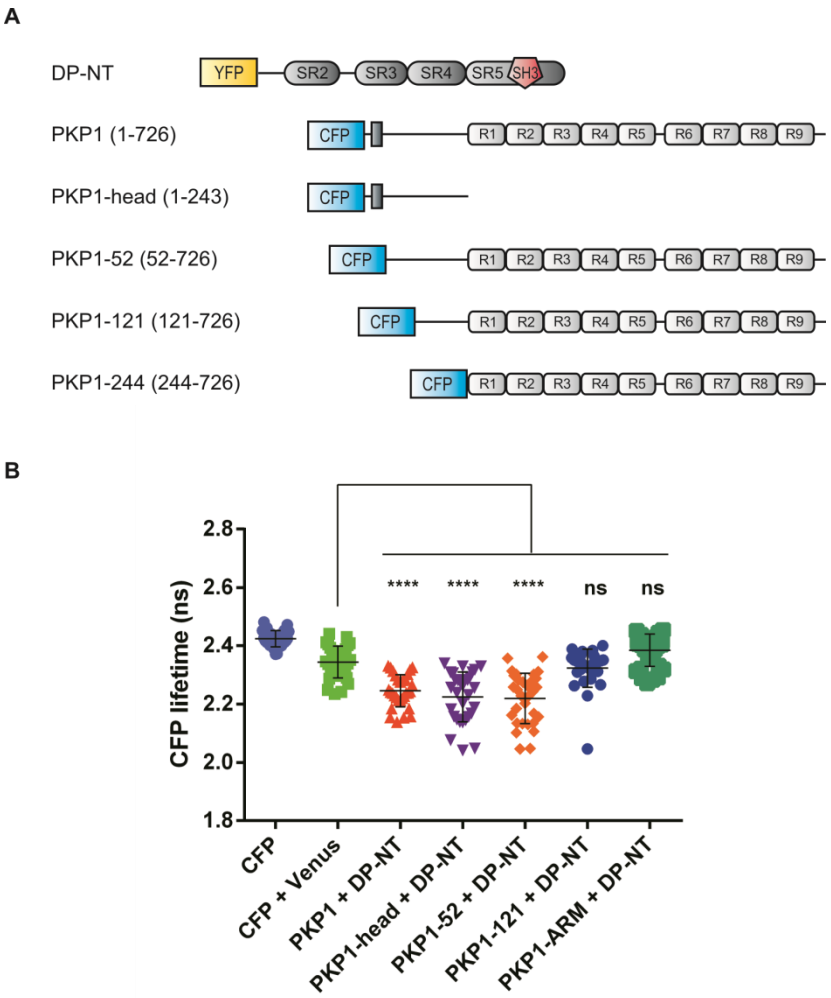

Figure R24. Mapping of the DP-interaction site within the head domain of PKP1a by FLIM. A) Schematic domain representation of the CFP-tagged PKP1a fragments and the Venus-tagged DP-NT fragment used in FLIM experiments. Venus is represented by the acronym YFP. **B)** The interaction between DP-NT and PKP1a fragments was assessed by analysing the fluorescent lifetime of CFP using FLIM. Results of one representative experiment are represented in scatter dot plots of the CFP lifetime with the mean and the standard deviation. Statistically significant differences (unpaired unequal variance t-test) are indicated by **** ($p \leq 0.0001$); ns, not significant ($p > 0.05$).

Co-IP and FLIM experiments showed that the region 52-121 of the head domain of PKP1a was crucial to enable the association with DP. To complete this analysis we analysed the co-localization of PKP1a and DP fragments by confocal microscopy. We co-transfected COS-7 cells with Venus-tagged DP-NT and the CFP-tagged PKP1-fragments: PKP1-head (region 1-243), PKP1-52 (region 52-726), and PKP1-121 (region 121-726) and analysed their subcellular localization (Figure R25).

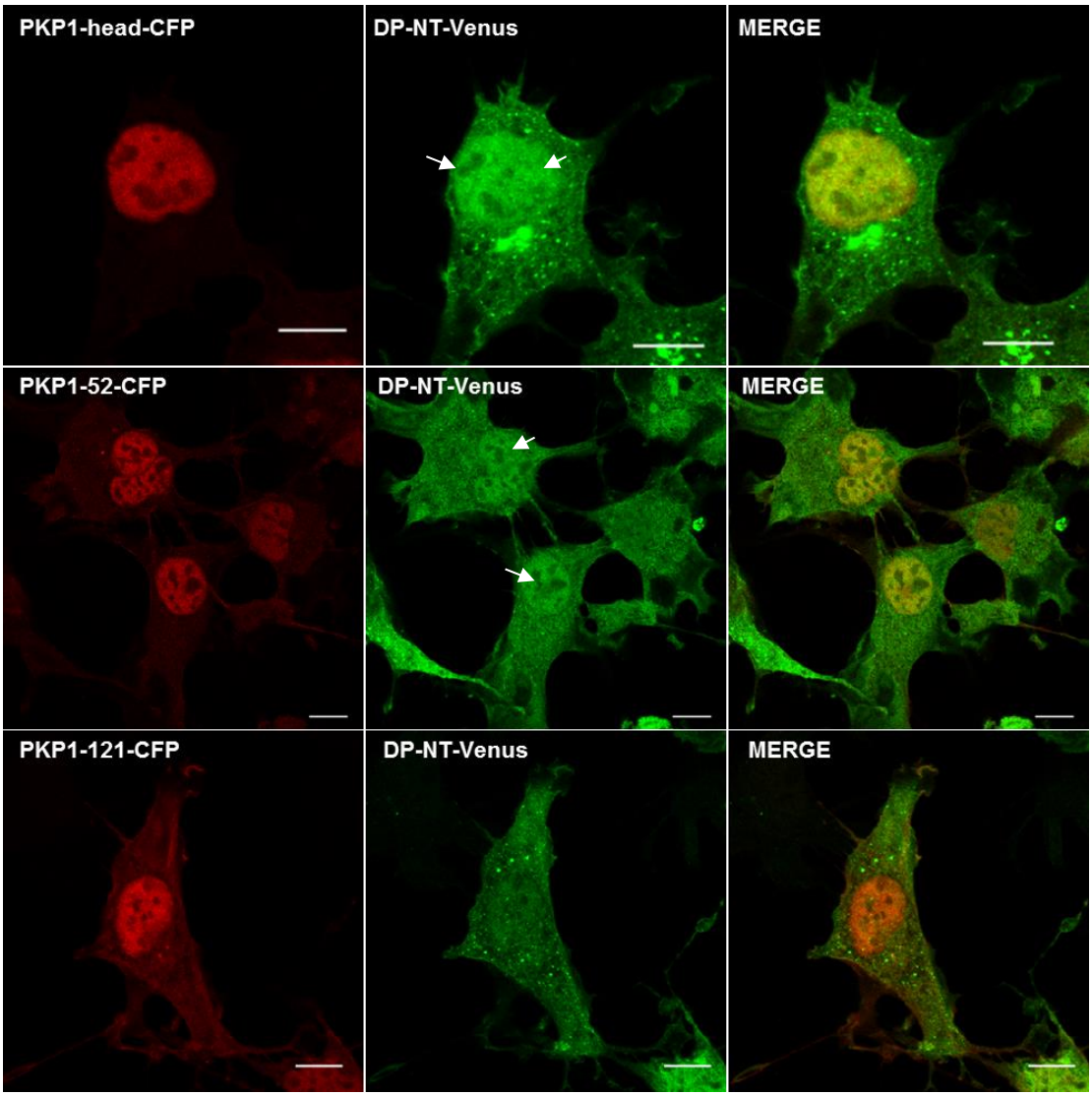

Figure R25. Subcellular localization of DP-NT and PKP1a fragments co-transfected in COS-7 cells. Confocal microscopy images of COS-7 cells ectopically expressing DP-NT and one PKP1a fragment tagged with Venus or CFP, respectively. PKP1a-fragments overexpression was detected upon excitation of CFP (442 nm) and is represented in red. DP-NT-Venus was detected by using an Argon laser line at 514 nm and is represented in green. The overlay images (merge) show the co-localization of DP-NT and PKP1a-fragments in yellow. Bar, 10 µm. Images are representative of the overall subcellular distribution of the studied fragments.

As we had seen before, when DP-NT was co-expressed with the head domain of PKP1a in COS-7 cells, it was recruited to the nucleus by PKP1a exhibiting a marked co-localization. Co-expression of DP-NT with PKP1-52 (52-726) resulted in a similar co-localization of both proteins at the nucleus. However, although PKP1-121 (121-726) also showed certain nuclear localization, it was not able to efficiently recruit DP-NT to the nucleus and the two proteins did not co-localized, neither at the nucleus nor in another cellular compartment.

In summary, co-localization assays are in agreement with co-IP and FLIM results and suggest that residues 52-120 of PKP1a mediate the formation of the DP-PKP1a complex.

Precise mapping of the DP-interaction site within the region 52-120 of PKP1a

Once we identified the region of PKP1a that is critical for the interaction with DP, we tackled the mapping of shorter segments in PKP1 required for the formation of the DP-PKP1a complex. To address this objective we combined co-expression of PKP1a and DP fragments with fluorescent tags with FLIM.

We created several additional constructs of PKP1a tagged with CFP that carried varying deletions from the N-terminus, we confronted them with DP-PD tagged with Venus and analysed comparatively the lifetime of CFP. The design and analysis of these new PKP1a deletion mutants was an iterative process, where results contributed by the earliest mutants directed the design of the upcoming ones.

Initially, we created two constructs PKP1-75 (region 75-726) and PKP1-98 (region 98-726) that together with the previous fragments 52-726 and 121-726 allowed us to trim the region 52-120 in three segments of equal length (23 residues). In addition, we created three shorter fragments: 133-726, 151-726, and 181-726 (Figure R26-A). When DP-PD was co-transfected with PKP1a N-terminal deletion mutants trimmed up to residue 98 (51-726, 75-726, and 98-726), the CFP lifetime was significantly reduced compared to the control sample ($p \leq 0.0001$) (Figure R26-B and Table R8). Moreover, the CFP lifetime of these deletion mutants in the presence of DP-PD-Venus was similar to that observed for the full length PKP1a. On the contrary, the CFP lifetime of shorter PKP1a deletion mutants (121-726, 133-726, 151-726, and 181-726) was not reduced by DP-PD-Venus, suggesting that they did not interact with ($p > 0.5$).

Our previous results suggested that the region 98-120 of PKP1a was important for the interaction with DP. To further narrow down the interaction site within this region we created three more deletion mutants of PKP1a-CFP. Each new fragment starts 6 residues downstream of the previous one (104-726, 110-726, and 116-726). In addition, we created the PKP1a mutant 127-726 (Figure R26-C). We analysed the CFP lifetime of this set of PKP1-CFP constructs using DP-PD-Venus. When DP-PD-Venus was co-expressed with the PKP1a fragments 75-726, 98-726, and 104-726, the CFP lifetime was again significantly reduced compared to the control ($p \leq 0.0001$) (Figure R26-D and Table R8). However, DP-PD-Venus did not cause a significant reduction of the CFP lifetime of the shorter PKP1a fragments: 116-726, 121-726, 127-726, and 151-

726 (p > 0.5). The fragment PKP1-110 showed an intermediate behaviour with a significant result but not as accused as with the larger fragments (p ≤ 0.05).

To summarize, the analysis of CFP lifetimes by FLIM suggested that the region 104-116 of the head domain of PKP1a is a major determinant of the interaction with DP.

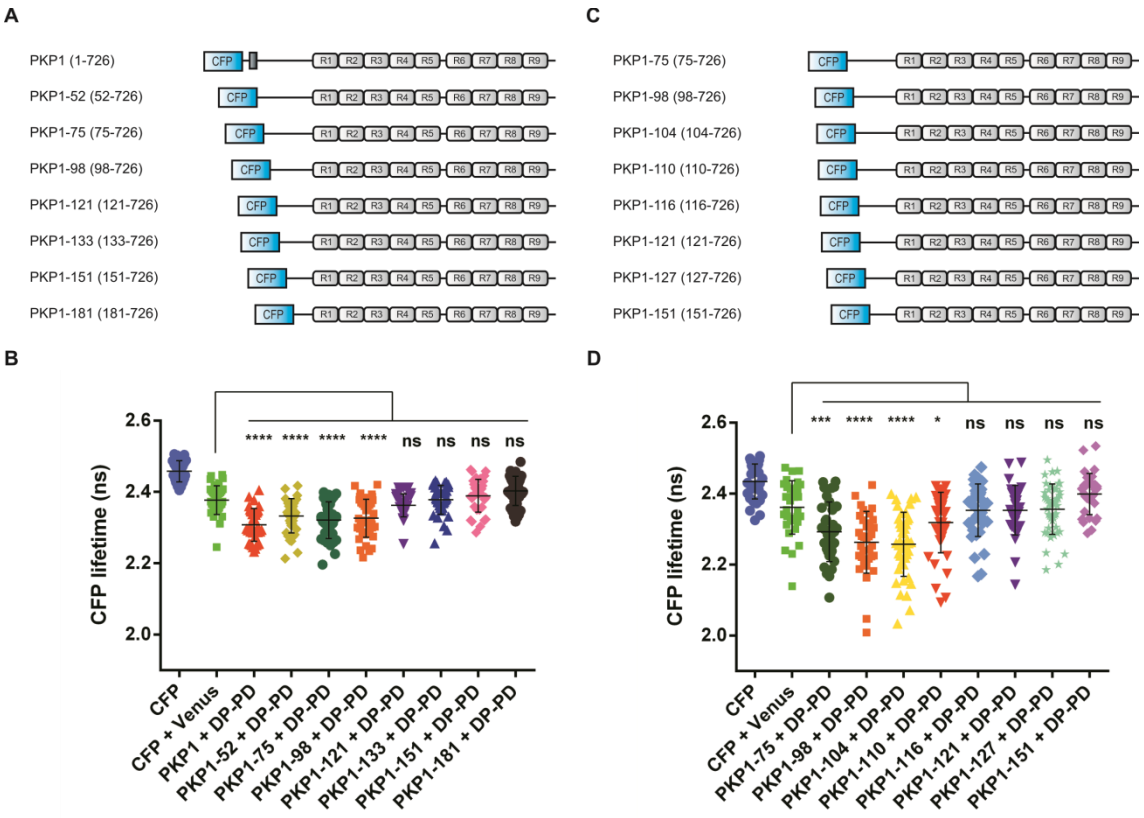

Figure R26. Precise mapping of the DP-interaction site within the region 52-120 of PKP1a by FLIM. A, C) Schematic domain representations of the CFP-tagged PKP1a N-terminal deletion mutants used in FLIM experiments. **B, D)** The DP-PKP1a interaction was analysed by studying the effect of the DP fragments on the fluorescence lifetime of CFP in COS-7 cells using FLIM. Results of representative experiments are represented in scatter dot plots of the CFP lifetime with the mean and the standard deviation. Statistically significant differences (unpaired unequal variance t-test) are indicated by **** (p ≤ 0.0001); *** (p ≤ 0.001); * (p ≤ 0.05); ns, not significant (p > 0.05).

Table R8. Descriptive statistics of the data shown in figure R26

Figure	Donor	Acceptor	n	Mean lifetime (ns)	SD	SEM
R26-B	CFP	-	26	2.296	0.028	0.006
	CFP	Venus	27	2.222	0.082	0.016
	PKP1-CFP	DP-PD-Venus	25	2.159	0.084	0.017
	PKP1-62-CFP	DP-PD-Venus	25	2.146	0.077	0.015
	PKP1-75-CFP	DP-PD-Venus	25	2.119	0.084	0.017
	PKP1-98-CFP	DP-PD-Venus	26	2.132	0.010	0.020
	PKP1-121-CFP	DP-PD-Venus	25	2.225	0.042	0.008
	PKP1-151-CFP	DP-PD-Venus	25	2.247	0.041	0.008
	PKP1-181-CFP	DP-PD-Venus	25	2.253	0.030	0.006
	PKP1-ARM-CFP	DP-PD-Venus	25	2.226	0.056	0.011
R26-D	CFP	-	32	2.434	0.049	0.009
	CFP	Venus	33	2.361	0.075	0.013
	PKP1-75-CFP	DP-PD-Venus	33	2.156	0.082	0.014
	PKP1-98-CFP	DP-PD-Venus	34	2.292	0.084	0.014
	PKP1-104-CFP	DP-PD-Venus	34	2.263	0.087	0.015
	PKP1-110-CFP	DP-PD-Venus	41	2.257	0.090	0.014
	PKP1-116-CFP	DP-PD-Venus	41	2.318	0.085	0.013
	PKP1-121-CFP	DP-PD-Venus	37	2.353	0.074	0.012
	PKP1-127-CFP	DP-PD-Venus	33	2.353	0.070	0.012
	PKP1-151-CFP	DP-PD-Venus	44	2.356	0.071	0.011

n, number of values; SD, standard deviation; SEM, standard error of the mean.

To complement the analysis by FLIM, we looked at the subcellular distribution of CFP- and Venus-tagged constructs by confocal microscopy to study the capability of PKP1a fragments to recruit DP to its localization, as an indication of the formation of a PKP1a-DP complex.

Based in our previous data, we focused the study on the PKP1-deletion mutants that start within the region 52-121. Thus, we co-transfected COS-7 cells with Venus-tagged DP-PD and CFP-tagged PKP1-98 (98-726), PKP1-104 (104-726) or PKP1-116 (116-726) (Figure R27). Additionally, we included PKP1-151 (151-726) in our analysis as a negative control, because we have already shown that deletion of the first 120 N-terminal residues, as in the construct PKP1-121, prevented the co-localization with DP (see Figure R25). When DP-PD-Venus is expressed alone it shows a diffuse cytoplasmic distribution (see Figure R5). Confocal microscopy images of the co-transfections showed that PKP1-98 and PKP1-104 co-localized with, and apparently enriched, DP-PD at the nucleus (see the overlay images). PKP1-116 and PKP1-151 showed a less marked co-localization with DP-PD at the nucleus, suggesting that this shorter fragment interacts less efficiently or do not interact with DP-PD.

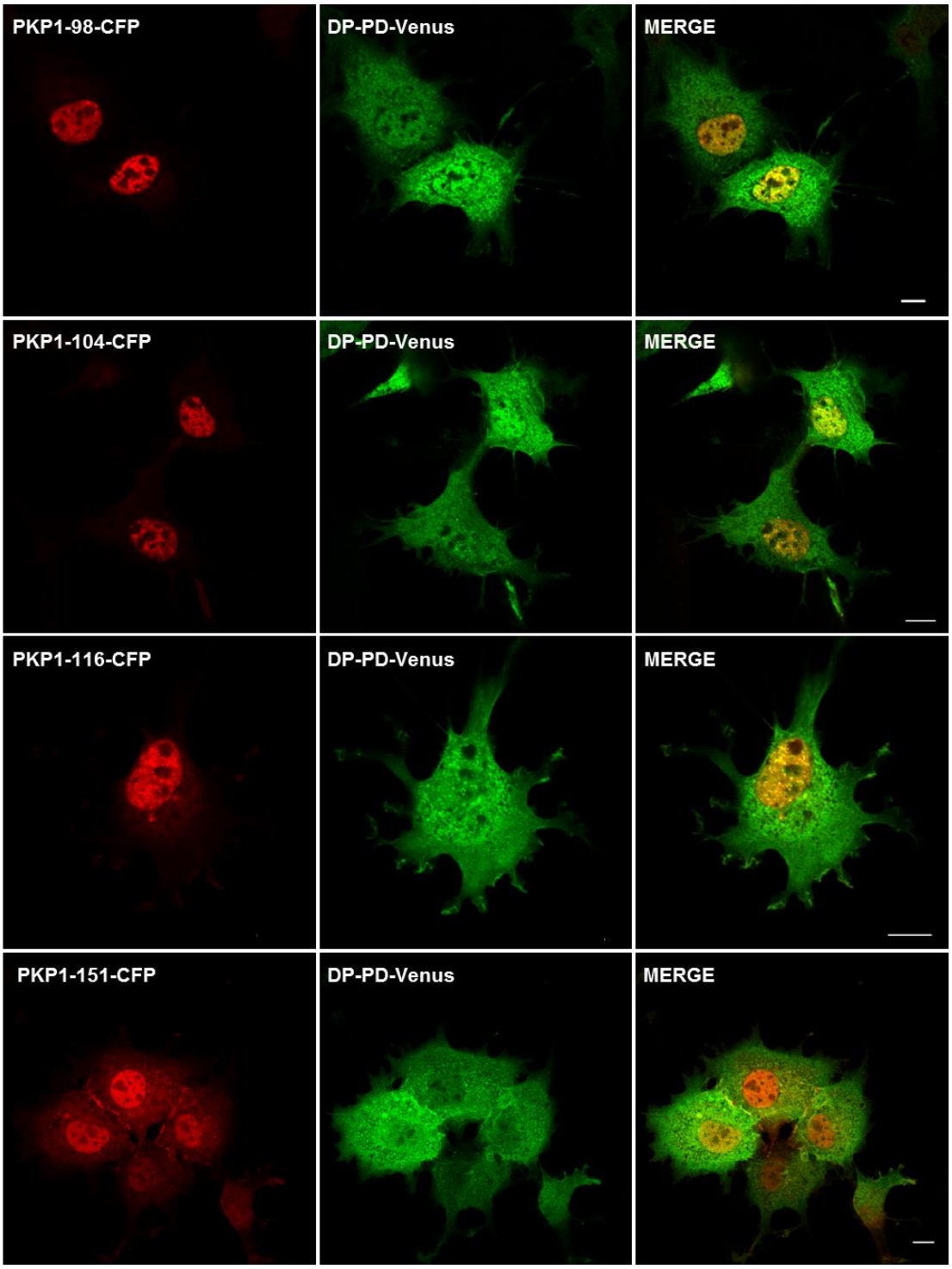

Figure R27. Subcellular localization of DP-PD and PKP1a fragments co-transfected in COS-7 cells. Confocal microscopy images of COS-7 cells ectopically expressing DP-PD and one PKP1a fragment tagged with Venus or CFP, respectively. PKP1a fragments were detected upon excitation of CFP at 442 nm and are represented in red. DP-PD-Venus was detected by using an Argon laser line at 514 nm and is represented in green. The overlay images (merge) show the co-localization of DP-PD and PKP1a-fragments in yellow. Bar, 10 µm. Images are representative of the overall subcellular distribution of the studied fragments.

In summary, by applying three complementary methodologies (co-IP, FLIM, and confocal microscopy) we have precisely identified that the region 98-116 of the head domain of PKP1a is critical for the interaction with DP. Moreover, analysis of the interaction using FLIM suggests that the crucial segment for the formation of the DP-PKP1 complex is even narrower, being composed by the residues 104-116.

Section B

Analysis of the PKP1a-nuclear localization determinants

Subcellular distribution of CFP-tagged PKP1a, PKP2a, and PKG in DMs-bearing and non-bearing cell lines

In addition to their role in the assembly and maintenance of the DMs, endogenous and overexpressed PKPs, prominently localise to the nucleus (Bonné et al. 1999; Mertens et al. 1996; Schmidt et al. 1997). To date, the specific DMs-independent functions of PKPs at the nucleus remain largely unknown.

To better understand the nuclear-localization of PKP1a, we analysed the subcellular distribution of PKP1a in various cell lines. On the one hand, we examined COS-7 cells, which do not form prominent DMs and, on the other hand, we studied normal human keratinocytes (NHK) as a model of a DM-bearing cell line. Cells were transiently transfected with PKP1a full length tagged with CFP and the fluorescence distribution was monitored by confocal microscopy (Figure R28).

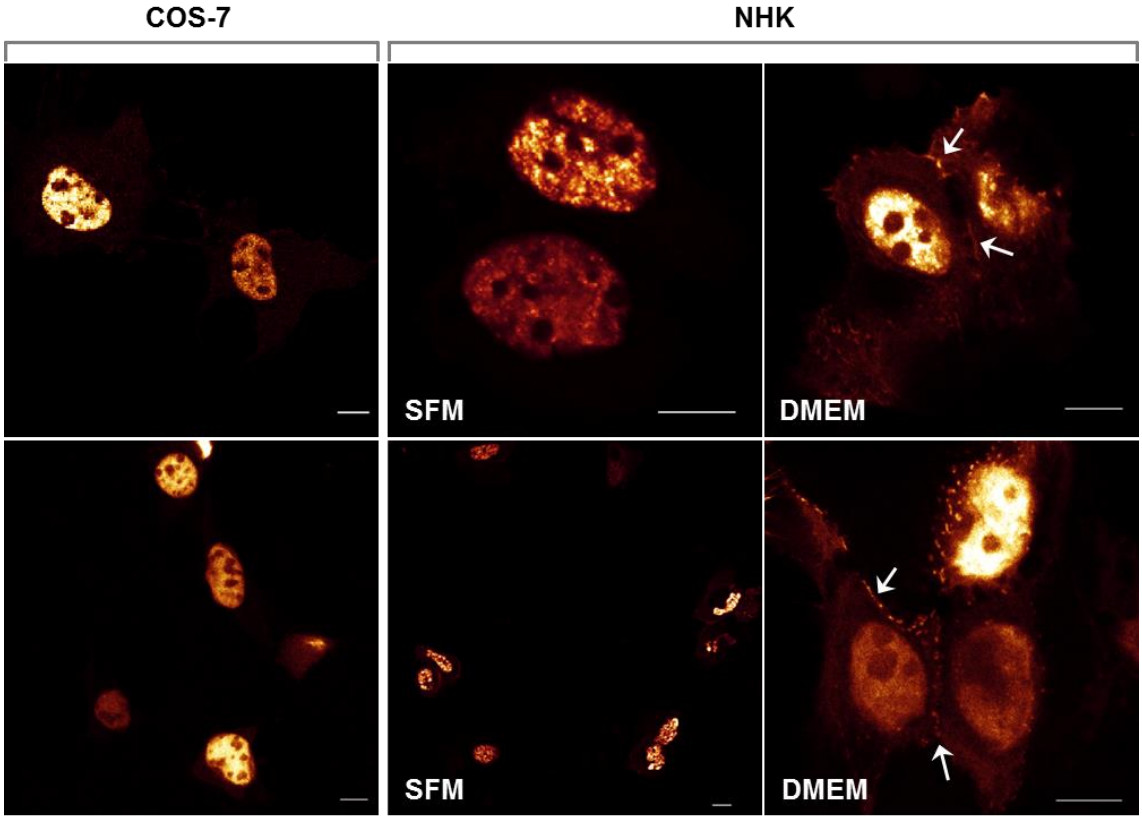

Figure R28. Subcellular distribution of PKP1-CFP in different cell lines. The subcellular localization of ectopically expressed CFP-tagged PKP1a full length was investigated in DMs-bearing (NHK) and non-bearing (COS-7) cell lines by confocal microscopy. This PKP1a construct was created in the pcDNA3-CFP-C4 vector that adds CFP to the N-terminus of the coded protein. PKP1-CFP was detected upon excitation of CFP (442 nm). NHK were analysed in two different growing conditions: undifferentiated NHK growing in low-calcium medium (SFM, 0.09 mM calcium concentration) and differentiated NHK after 24 hours growing at high calcium concentration conditions (DMEM, 1.2 mM calcium concentration). Bar, 10 µm.

PKP1-CFP transiently expressed in COS-7 cells showed an exclusively nuclear staining. This nuclear distribution was observed in all the cells expressing PKP1-CFP. In the close up images (upper row) is it possible to appreciate that PKP1a full length was localised to the nuclear karyoplasm and mostly excluded from nucleoli. This subcellular distribution has been previously reported in various cell types (Hatzfeld et al. 2000; Schmidt et al. 1997; Sobolik-Delmaire et al. 2010) being the expected in cell types not containing prominent DMs, such as COS-7 cells.

Undifferentiated NHKs growing at low-calcium concentration (SFM), which do not assemble DMs, showed the same exclusively nuclear localization of PKP1-CFP observed in COS-7 cells. However, after 24 hours growing in DMEM (1.2 mM calcium concentration), PKP1-CFP localised both to the nucleus and to the plasma membrane where it concentrated in punctuated structures. Probably, the latter is caused by the incorporation of PKP1-CFP into DMs that are assembled in keratinocytes when they grow at high-calcium concentration or at high-density (Bikle et al. 2013; Kimura et al. 2007). The PKP1-CFP relocation observed upon NHKs differentiation demonstrated that CFP does not prevent PKP1a from incorporating into DMs.

Collectively, these results suggest that PKP1-CFP localises to the nucleus of DM-bearing and non-bearing cells lines. Moreover, PKP1-CFP is functional in the sense that its subcellular distribution is the expected on both cells that assemble DMs and cells that do not. In addition, PKP1-CFP takes part of DM-like structures when they are formed.

Since the nuclear targeting of PKP1a appears to be DM-independent we wondered whether COS-7 cells would be a valid model to study the nuclear localization determinants of PKP1a. To further analyse this question, we investigated the distribution of other desmosomal proteins in this cell line and in keratinocytes.

First, we transiently transfected COS-7 cells with un-linked CFP or with CFP-tagged PKP1a, PKP2a, or PKG full length and studied their subcellular localization by confocal microscopy (Figure R29). Each of the analysed proteins showed a specific subcellular distribution. COS-7 cells transiently transfected with an empty vector coding only for CFP showed a diffuse cytoplasmic localization. CFP was also present in the nucleus but to a lesser extent than in the cytoplasm. PKP1-CFP was strictly restricted to the nucleus, as we have shown before. The localization of PKP1-CFP strongly contrasted with the distribution of PKP2-CFP that was excluded from the nucleus and mainly accumulated at the plasma membrane. This is in agreement with previous observations in which the extent of nuclear localization of PKPs is very different between the three variants, being PKP1 the most nuclear-prominent (see an example with A431 and UM-

SCC-38 cells in Sobolik-Delmaire et al. 2010). Overexpressed CFP-tagged PKG showed a dual localization being present at both nucleus and cytoplasm.

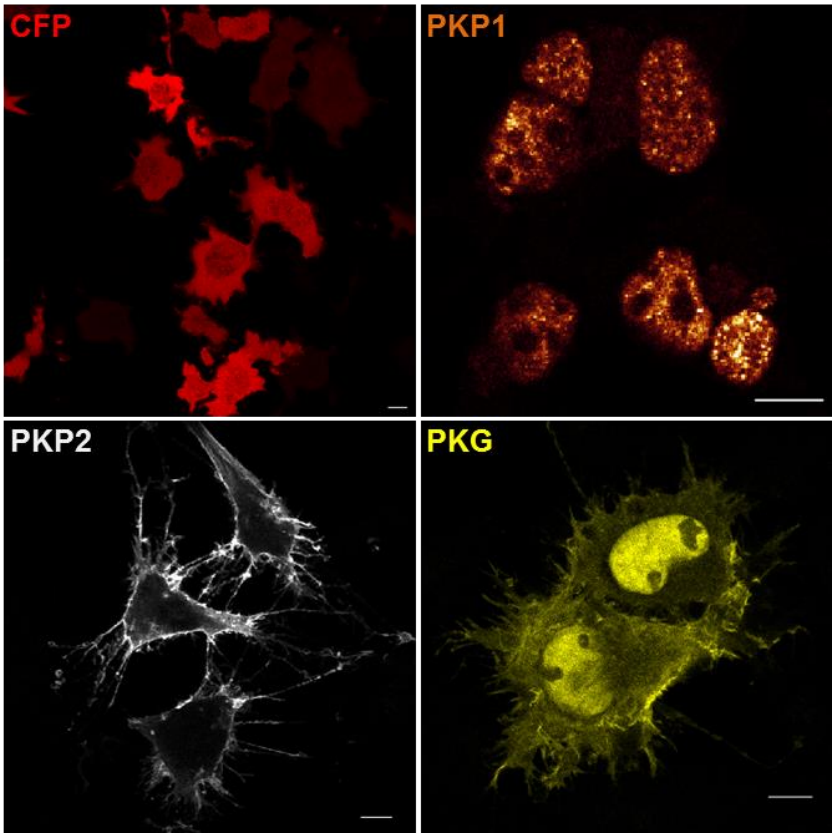

Figure R29. Subcellular distribution of un-linked CFP and CFP-tagged PKP1a, PKP2a, and PKG in COS-7 cells. COS-7 cells were transfected with constructs coding for free CFP or CFP-tagged full length PKP1a, PKP2a, or PKG (vector pcDNA3-CFP-C4). The subcellular localization of the individually expressed proteins was analysed by confocal microscopy. CFP fluorescence was detected upon excitation of CFP at 442 nm and is represented in different colours in each case: un-linked CFP, red; PKP1a, orange; PKP2a, grey; PKG, yellow. Bar, 10 µm.

The fact that several proteins tagged with the same fluorophore showed different and specific subcellular distributions highlighted that the CFP tag was not having a significant effect on the behaviour of the recombinant proteins and suggested that the combination of CFP-fusion proteins and COS-7 cells is a valid model to analyse the nuclear-localization determinants of PKP1a.

Next, we analysed the subcellular localization of the same desmosomal proteins in keratinocytes growing in SFM. For this purpose, keratinocytes were transfected with CFP-tagged PKP1a, PKP2a, or PKG full length and the subcellular distribution of the fusion proteins was analysed by using confocal microscopy upon excitation of CFP (Figure R30).

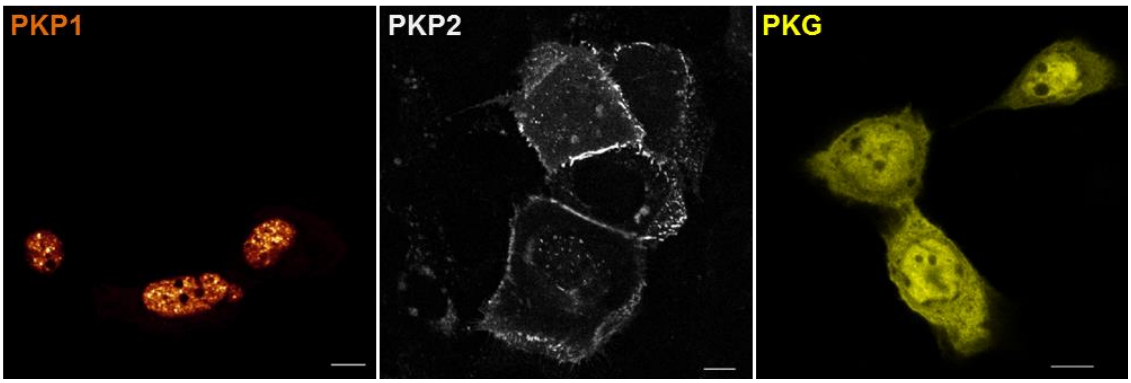

Figure R30. Subcellular distribution of CFP-tagged PKP1a, PKP2a, and PKG in keratinocytes. NHK were transiently transfected with constructs coding for CFP-tagged full length PKP1a, PKP2a, or PKG (vector pcDNA3-CFP-C4) and the subcellular localization of the fusion proteins was investigated by confocal microscopy. Keratinocytes were grown in low calcium SFM. CFP fluorescence was detected upon excitation of CFP at 442 nm and is represented in different colours for each fusion protein: PKP1a, orange; PKP2a, grey; PKG, yellow. Bar, 10 μm.

The subcellular distribution of overexpressed PKP1a, PKP2a, and PKG in keratinocytes growing in SFM (low calcium) was almost equal to those observed in COS-7 cells. Again, PKP1a and PKP2a showed a clear different localization; PKP1a was restricted to the nucleus, whereas PKP2a was mostly at the plasma membrane. PKG showed a broader distribution and was present at both nucleus and cytoplasm.

In summary, PKP1-CFP localised to the nucleus both in COS-7 cells and in NHKs. Similarly, PKP2a and PKG showed resembling and specific subcellular distribution in both cell lines. In addition, PKP1-CFP was recruited to cell-cell contact sites in NHKs in conditions that promote DM assembly, indicating that CFP-tagged PKP1a is functional and capable of incorporating to junctional complexes. Therefore, the study of the PKP1a-nuclear determinants can be undertaken in the transfection-friendly COS-7 cells by using CFP-tagged proteins.

Subcellular distribution of endogenous desmosomal proteins in keratinocytes

We also wanted to know whether the distribution of the transfected fusion proteins was similar to the distribution of the endogenous proteins or, by the contrary, it was influenced by the higher expression levels of the ectopic proteins. For this purpose we studied the main desmosomal proteins by immunofluorescence in both COS-7 cells and keratinocytes.

Immunofluorescence analysis of COS-7 cells did not provide useful results (data not shown), most likely due to the low expression levels of the desmosomal proteins in this cell line. Since the expression levels of desmosomal proteins in keratinocytes are higher compared with those in COS-7 cells, we were able to obtain good

immunofluorescence images from keratinocytes. The subcellular localization of endogenous desmosomal proteins was analysed in NHKs growing in low-calcium SFM and under differentiation conditions to promote the establishment of cell-cell contacts (DMEM, high-calcium medium).

First, we studied the subcellular distribution of E-cadherin and the desmosomal proteins DSGs (DSG-1 and DSG-2), DP and PKG in NHKs (Figure R31). E-cadherin, which is the major transmembrane protein of the AJs (Hartsock & Nelson 2009), showed a membrane lining pattern in low and high calcium. Additionally, it was also observed in discrete cytoplasmic particles distributed throughout all the cytoplasm in low-calcium conditions and closer to the membrane when keratinocyte differentiation was promoted (high-calcium conditions). In contrast, DSGs and DP showed a diffuse distribution in low calcium and were translocated to the plasma membrane upon stimulation of DM-assembly. PKG showed a peripheral staining in low calcium media that was enriched when cells were grown in the presence of high calcium concentration.

Next, we studied the subcellular distribution of endogenous PKP1 and PKP2 in keratinocytes (Figure R32). In this case, two different immunolocalization procedures were used (see materials and methods). On the one hand, we used a standard immunostaining procedure where keratinocytes growing in glass coverslips were fixed before Triton X-100 membrane permeabilization. With this protocol we were not able to appreciate any nuclear signal, either for PKP1 or for PKP2. Both proteins showed cytoplasmic and diffuse peripheral staining in undifferentiated keratinocytes growing in SFM. PKP1 was also enriched in areas of cell-cell contact and was present in discrete cytoplasmic particles (see arrows) that are similar to those described for other desmosomal proteins (Godsel et al. 2005; Jones & Goldman 1985). In keratinocytes grown for 24 hours in the presence of high calcium concentration (DMEM), PKP1 and PKP2 showed a more prominent staining of the plasma membrane and were particularly enriched at cell-cell contact sites, most likely due to their incorporation into DMs (Figure R32-A).

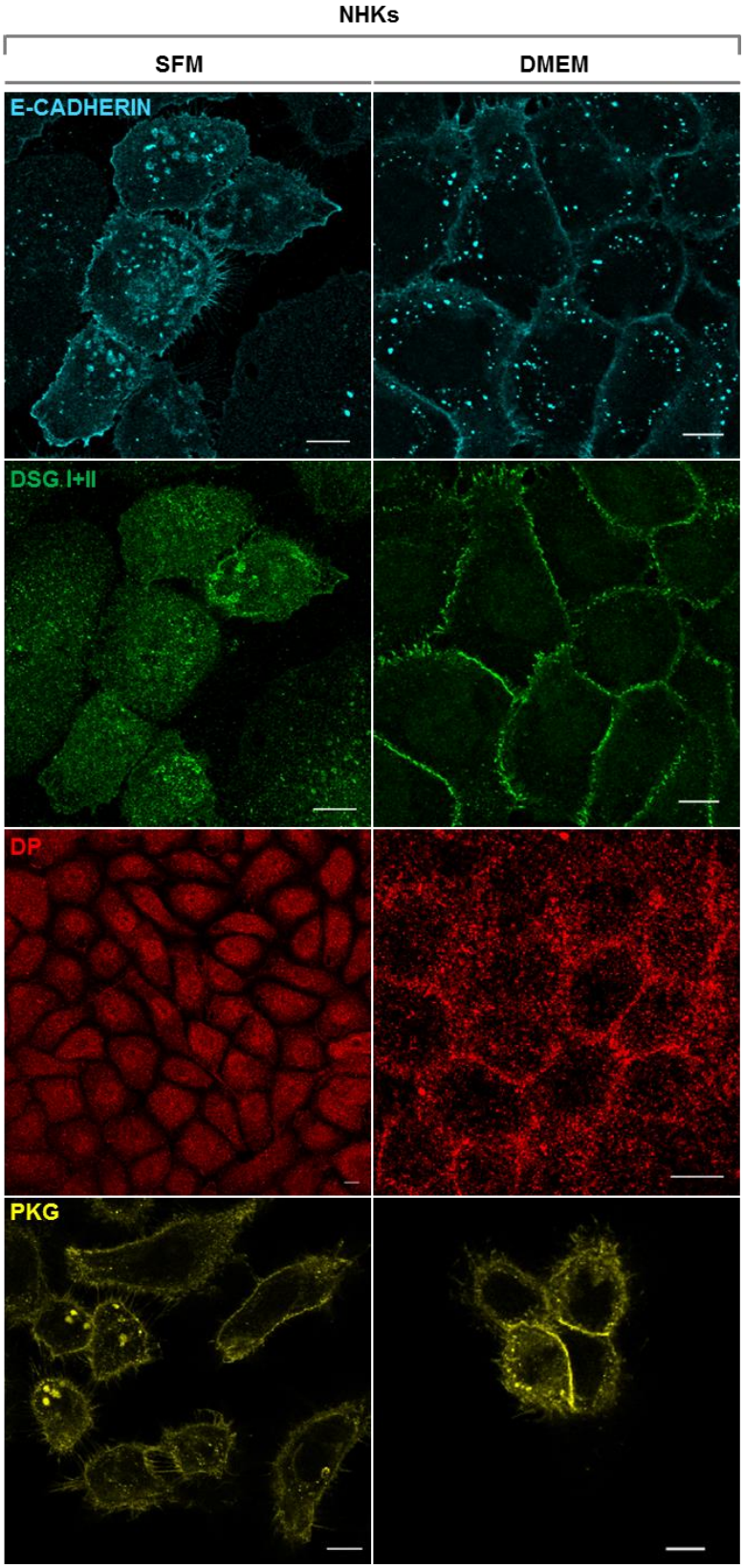

Figure R31. Subcellular distribution of endogenous E-cadherin, DSGs, DP, and PKG in keratinocytes. Confocal microscopy images of the subcellular distribution of endogenous E-cadherin and the desmosomal proteins: DSGs (DSG-1 and DSG-2), DP, and PKG. Protein distributions were investigated in keratinocytes growing in SFM (low-calcium) and DMEM (high-calcium) by immuno-fluorescence using a standard procedure. Endogenous E-cadherin was detected using a monoclonal antibody against the C-terminal region of the human E-cadherin (610182, BD Biosciences), blue; desmosomal cadherins were detected using a monoclonal antibody anti-DSGs (isoforms DSG-1 and DSG-2) (DG3.10, Acris Antibodies), green; endogenous DP was detected with a polyclonal antibody against the C-terminal region of the plakin domain of DP (sc-18086, Santa Cruz), red; and endogenous PKG was detected using a polyclonal antibody raised against a peptide mapping the C-terminus of the human PKG (sc-1497, Santa Cruz), yellow. Bar, 10 μm.

Since neither endogenous PKP1 nor PKP2 were detected at the nucleus in any growing condition (Figure R32-A), we were warned about the possibility that the PKP nuclear localization was being affected by technical issues with the standard indirect

immunofluorescence procedure used. Detecting nuclear staining of PKPs is greatly dependent on the processing of cell samples for immunofluorescence. Therefore, we further investigated about different immunostaining procedures proposed to detect PKPs in the nucleus, at the plasma membrane or to obtain an optimal dual localization (see examples in Mertens et al., 1996; Rickelt, 2012; Schmidt et al., 1997). In brief, most of them are based on treating the cells with a permeabilization agent before fixation. Thus, using a protocol in which cells were permeabilized with 0.2% Triton X-100 in PBS for five minutes before fixation with 2-4% PFA, endogenous PKP1 was detected in the nucleus and at the plasma membrane, but PKP2 was still only detected at cell-cell contact sites (Figure R32-B). These results are in agreement with the previously reported varying degree of nuclear localization showed by the PKPs in several cell lines, being PKP1 the most nuclear-prominent.

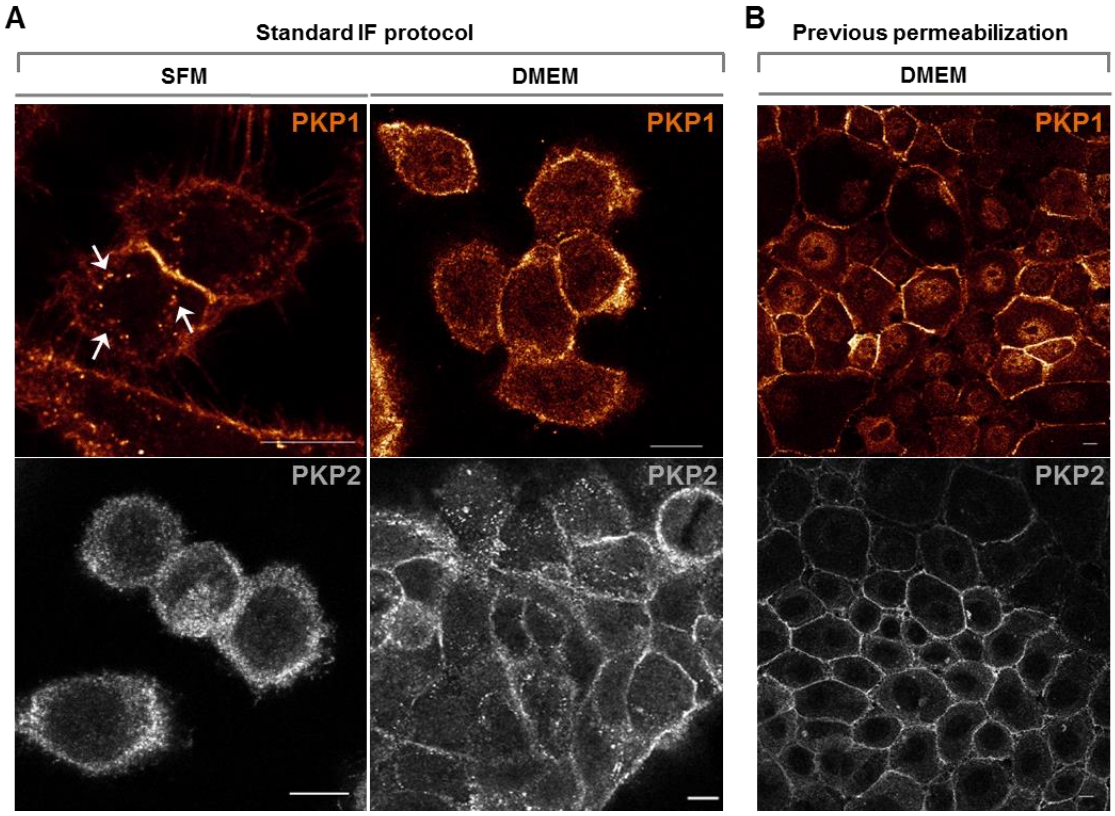

Figure R32. Subcellular distribution of endogenous PKP1 and PKP2 in keratinocytes. The subcellular localization of endogenous PKP1 and PKP2 was investigated in keratinocytes growing in SFM (low calcium) and DMEM (high calcium) by immunostaining and confocal microscopy. Two different immunofluorescence procedures were used: **A)** Standard indirect immunofluorescence protocol: cells growing in glass coverslips were fixed before Triton X-100 membrane permeabilization; **B)** Cells were treated with 0.2% Triton X-100 in PBS for five minutes before PFA fixation. Notice that only the second immunostaining procedure (B) revealed the dual localization of PKP1 at the nucleus and plasma membrane. Bar, 10 μm.

To summarize, in NHKs growing in desmosome-promoting conditions, endogenous PKP1 and PKP2 were located at the plasma membrane, similarly to other desmosomal proteins. In addition, PKP1 was also present in the nucleus despite the formation of DMs, whereas PKP2 was not significantly detected at the nucleus. Finally, transiently expressed PKP1-CFP and PKP2-CFP showed similar subcellular distribution compared to the endogenous proteins.

The region 116-132 of the head domain of PKP1a is important for the nuclear targeting in COS-7 cells

Sequence analysis of PKP1a did not reveal any obvious NLS, either canonical or bipartite. Moreover, none of the known PKP1 interacting partners contain NLS that could indirectly target PKP1a to the nucleus. Thus, the processes that target and transport PKP1a to the nucleus together with its nuclear role remain largely uncharacterized.

It has been shown that the head domain of PKP1a is required for the nuclear localization of PKP1a in COS (Kowalcyk et al. 1999), HaCaT, and HeLa cells (Hatzfeld et al. 2000). Within the head domain, the amino acids 55-125 are important for the nuclear localization in A431 cells (Sobolik-Delmaire et al. 2010). Yet, the amino-acid sequences directly responsible for the nuclear localization are poorly understood.

To better understand the nuclear localization of PKP1a and to identify the amino acids responsible for PKP1a nucleus-cytoplasm shuttling; we performed an exhaustive analysis using an extensive repertory of PKP1a N-terminal deletion mutants. As we demonstrated before, COS-7 cells are an appropriate model to tackle these studies. Thus, we transiently transfected these cells with CFP-tagged PKP1 mutants that carried varying deletions from the N-terminus (made in pcDNA3-CFP-C4) (Figure R33), and studied their subcellular distribution by confocal microscopy (Figure R34).

Fragments trimmed up to residue 110 were localized only to the nucleus, showing a distribution indistinguishable from that of PKP1a full length and PKP1-head. The fragment starting in the residue 116 showed a prominent nuclear localization, although it was also weakly detected in the cytoplasm of some cells. The cytoplasmic-nuclear distribution ratio further increased in fragments with larger deletions up to the construct 133-726, which was almost equally distributed between cytoplasm and nucleus in most of the cells, not showing a predominant nuclear localization. This pattern was even clearer in the 151-726 fragment that showed a homogeneous cytoplasmic-nuclear distribution with no single cells with a predominant nuclear presence of PKP1. Fragments carrying additional N-terminal deletions such as the fragment 181-726 or

the fragment completely ablated of the head domain (region 244-726) showed the same dual localization as the 151-726 fragment, not being enriched in the nucleus albeit present. The observed nuclear localization of the ARM-domain is in agreement with previous reports (Sobolik-Delmaire et al. 2010).

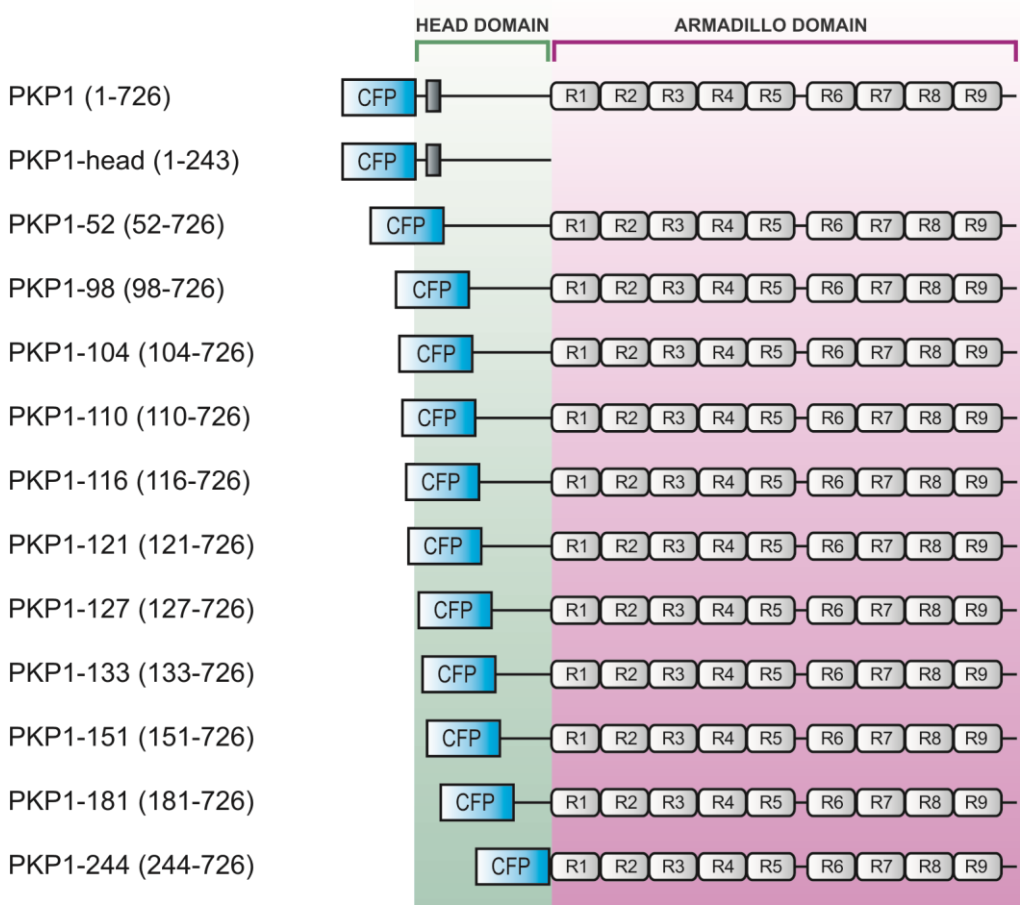

Figure R33. CFP-tagged N-terminal deletion mutants of PKP1a. Schematic domain representation of the PKP1a N-terminal deletion mutants generated to analyse the nuclear localization determinants in PKP1a. The constructs coding for these fragments were created in the pcDNA3-CFP-C4 vector that adds a CFP-tag to the N-terminus. The HR2 motif within the head domain is shown as a grey box (residues 21-45). The design and analysis of the PKP1a-deletion mutants was an iterative process, where results contributed by the earliest mutants directed the design of the upcoming ones.

Collectively, these results prove that the head-domain of PKP1a is necessary for maintaining the nuclear targeting of PKP1a. Within the head-domain of PKP1a, the first 109 residues are dispensable for the nuclear localization because fragments lacking the region 1-109 showed an indistinguishable distribution from that of the PKP1a full length and the head-domain. In contrast, fragments starting at the position 151 and beyond lose their exclusively nuclear localization, being equally distributed throughout the cytoplasm and nucleus. This result suggests that the segment 110-132, and

probably the region 133-150, play an important role in the nuclear-to-cytoplasmic redistribution of PKP1a.

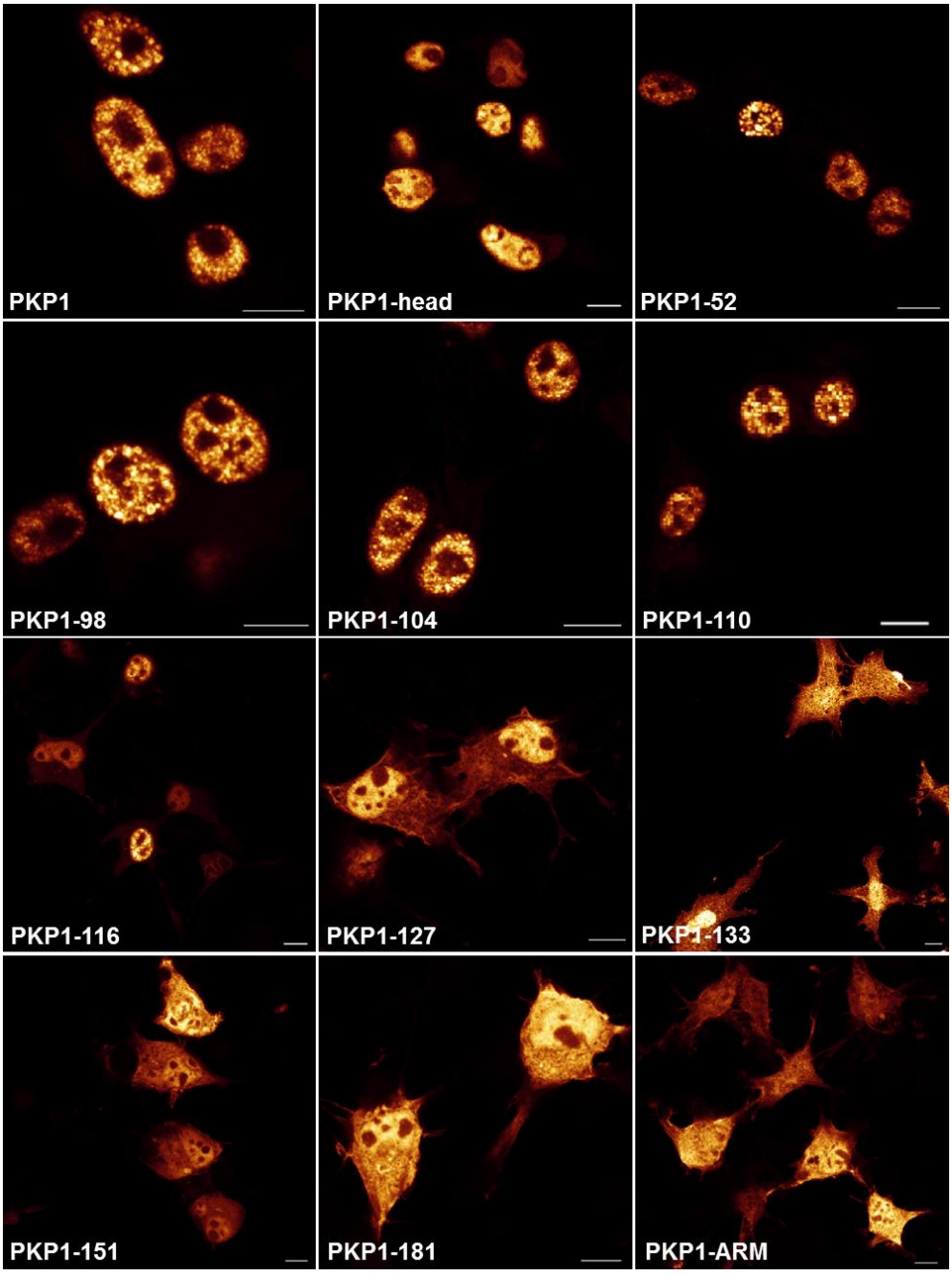

Figure R34. Subcellular distribution of CFP-tagged PKP1a N-terminal deletion mutants in COS-7 cells. Confocal microscopy images of COS-7 cells transfected with each of the PKP1a N-terminal deletion mutants. The localization of the PKP1 fragments was detected upon excitation of CFP at 442 nm. Bar, 10 μm.

The region 116-132 of PKP1a is not sufficient to target PKP1a to the nucleus

Once we precisely delimited that the sequence 116-132 was a key region for maintaining PKP1a in the nucleus, we wondered whether this small segment would be

also sufficient to target PKP1a to this compartment. To address this question we studied by confocal microscopy the subcellular localization of the CFP-tagged fragments PKP1-1-115 (region 1-115), PKP1-1-132 (region 1-132), and PKP1-116-132 (region 116-132). All of them are made in pcDNA3-CFP-C4 (Figure R35).

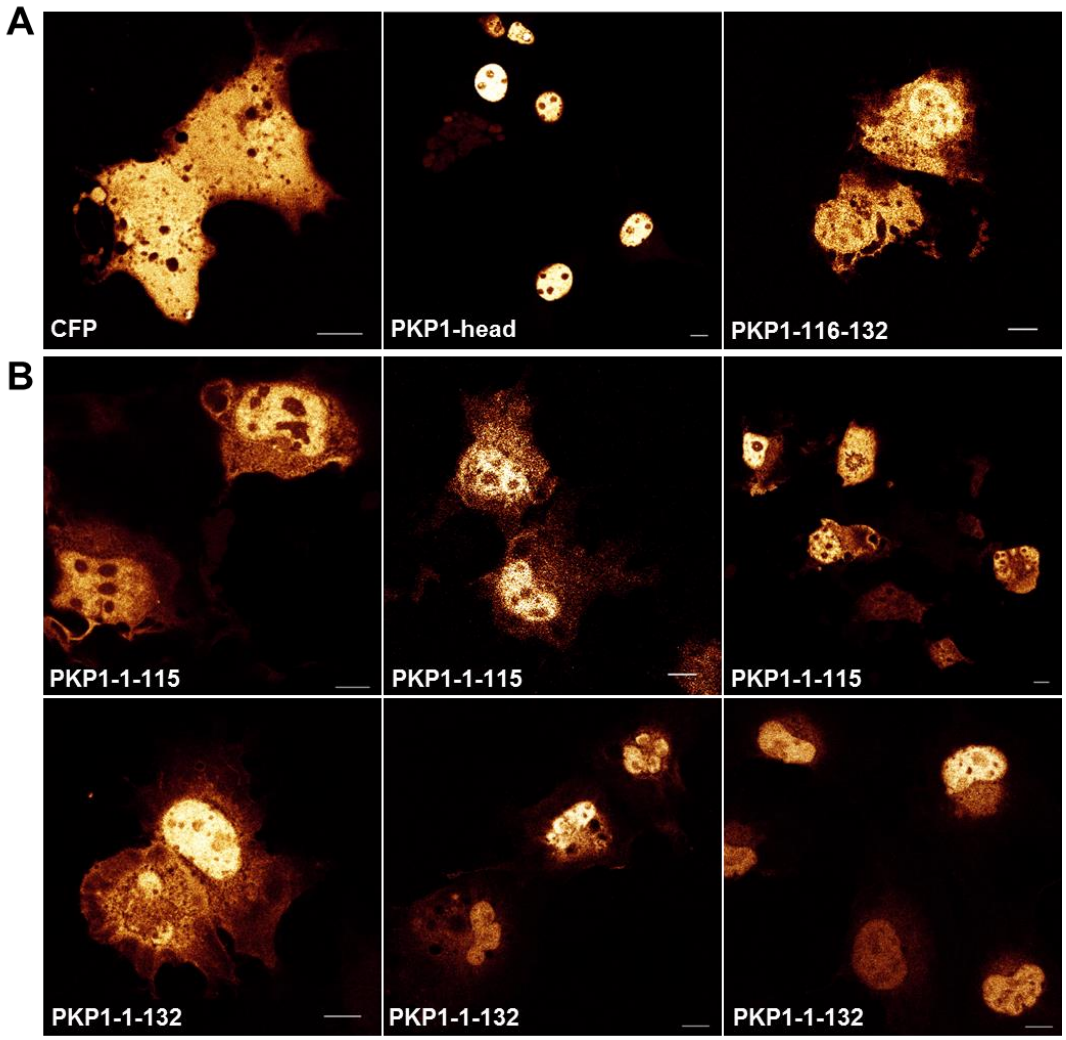

Figure R35. Subcellular distribution of CFP-tagged PKP1a N-terminal fragments in COS-1 cells. A) Confocal microscopy images of free-CFP, PKP1-head, and PKP1-116-132 ectopically expressed in COS-1 cells. **B)** Subcellular distribution of CFP-tagged PKP1-1-115 and PKP1-1-132. Three representative images of the distribution of each of these constructs are shown. CFP fluorescence was detected upon excitation of CFP (442 nm). Bar, 10 µm.

The region 116-132 of the head domain of PKP1a was not sufficient to drive nuclear accumulation of the protein. This fragment showed a diffuse subcellular distribution similar to that observed with the isolated CFP (Figure R35-A). Thus, it might be possible that the localization of this very small sequence of PKP1 (18-residue long) was dominated by the unspecific distribution of the CFP tag.

In order to avoid potential problems due to the small size of the 116-132 fragment, we analysed the subcellular distribution of two longer fragments: PKP1-1-115 and PKP1-1-132 (Figure R35-B). Both fragments were present at the nucleus and cytoplasm. Nonetheless, they were enriched in the nucleus and apparently the PKP1-1-132 nuclear signal was more prominent than that of the shorter fragment. In summary, the region 116-132 of PKP1a is not sufficient for nuclear targeting, which requires the contribution of additional segments of the head domain.

The region 110-150 of PKP1a is dispensable for targeting PKP1a to the nucleus in the presence of other regions of the head domain

Given the cooperative behaviour of the 116-132 segment with other parts of the head domain for targeting PKP1a to the nucleus, we questioned whether the residues 116-132 were required for nuclear localization when segments up- and downstream of this motif were present. Thus, we generated internal deletion mutants that lack the 116-132 sequence and analysed its subcellular distribution (Figure R36). This deletion was introduced in CFP-tagged constructs of the full length protein (PKP1-Δ116-132) and of the head domain (PKP1-head-Δ116-132) cloned into pcDNA3-CFP-C4. Both deletion mutants showed exclusive nuclear staining similar to that of the WT PKP1a full length and PKP1-head.

During the analysis of the N-terminal deletion mutants, the segment 116-132 was the most important region for the nuclear-to-cytoplasm balance of PKP1a (see before). Nonetheless, we had observed that residues preceding and succeeding this region also contributed to the subcellular distribution. Thus, we generated and analysed the localization of two additional internal deletion mutants that lack the segment 110-150. In the context of the full length PKP1a, deletion of the 110-150 segment did not affect the exclusive nuclear localization. On the contrary, the head domain mutant PKP1-head-Δ110-150 was detected in the cytoplasm in some cells, despite a predominant nuclear staining. Collectively, our results indicate that the nuclear targeting of PKP1 involves the contribution of multiple segments of the head domain.

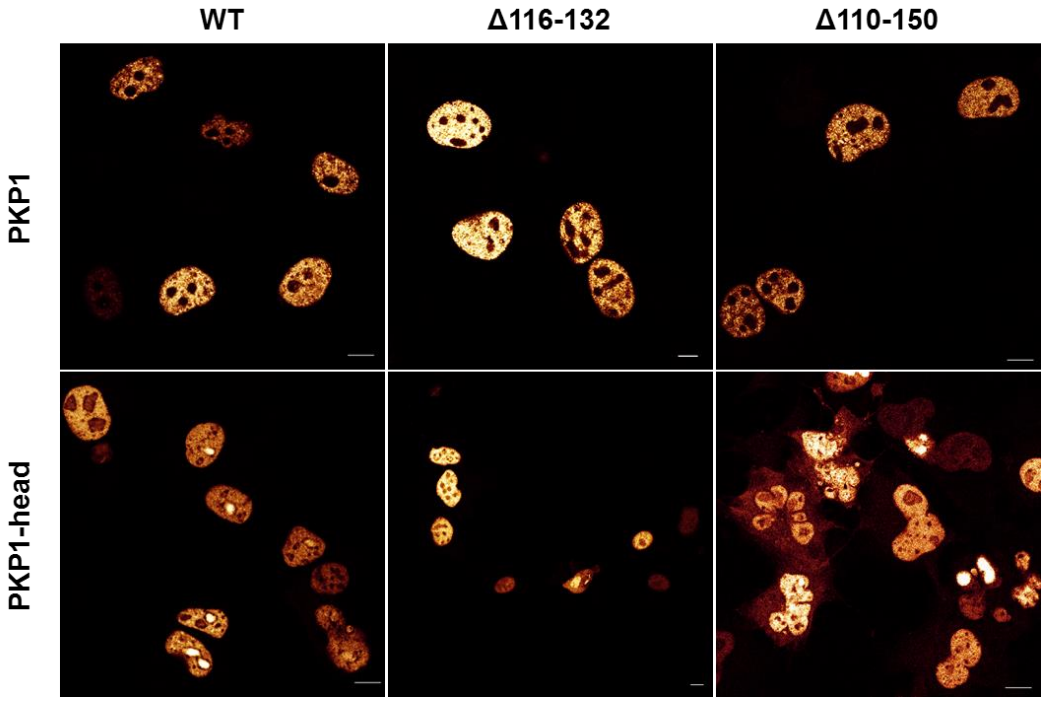

Figure R36. Subcellular distribution of CFP-tagged PKP1a internal deletion mutants in COS-1 cells. Confocal images of CFP-tagged PKP1a, PKP1a-Δ116-132, PKP1a-Δ110-150, PKP1-head, PKP1-head-Δ116-132, and PKP1-head-Δ110-150 ectopically expressed in COS-1 cells. The localization of the PKP1 fragments was detected upon excitation of CFP at 442 nm. Bar, 10 µm.

PKP1a-deletion mutants lacking the N-terminal nuclear determinant do not enter to the nucleus by association with endogenous PKP1

We have shown that fragments lacking the first 116 to 132 residues of PKP1a lost their restricted nuclear localization and appeared equally distributed throughout the cytoplasm and nucleus. Those results suggested that the region 116-132 was a major determinant for targeting PKP1a to the nucleus (see above). However, the remaining nuclear staining observed in the constructs lacking the 116-132 region was intriguing. Previous reports have suggested that PKP1 might have at least two NLS (Sobolik-Delmaire et al. 2010). However, we considered other possibilities, for example, PKP1a deletion mutants might be entering into the nucleus via homo-association with endogenous PKP1 present in the cells, or even via hetero-association with PKP2 or PKP3 (Hofmann, Mücke, et al. 2000).

To study the possibility that PKP1a-deletion mutants were recruited to the nucleus via dimerization with endogenous PKP1, we compared the subcellular distribution of the mutants in two cell lines, one expressing endogenous PKP1 and another lacking PKP1 expression. We used NHK as model cell line that expresses endogenous PKP1, and PKP1-null keratinocytes, which are established from a patient with skin fragility-

ectodermal dysplasia syndrome whit total ablation of PKP1 (South et al. 2003). Both cell lines were transfected with selected CFP-tagged PKP1 N-terminal mutants and their subcellular localization was evaluated by confocal microscopy (Figure R37).

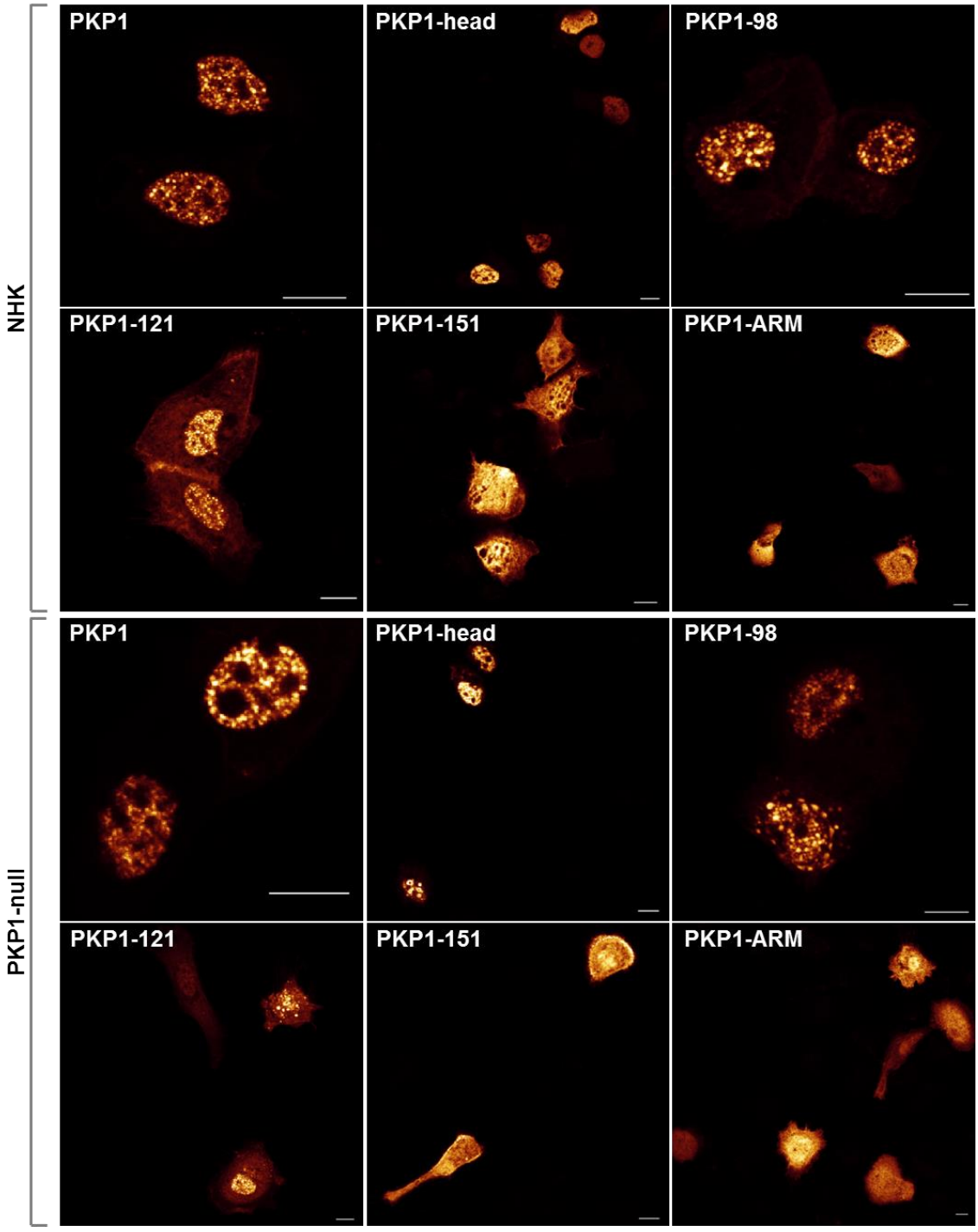

Figure R37. Subcellular distribution of CFP-tagged PKP1a N-terminal deletion mutants in keratinocytes. The subcellular distribution of ectopically expressed CFP-tagged PKP1a N-terminal deletion mutants was investigated in NHKs and PKP1-null keratinocytes by confocal microscopy. The subcellular localization of the PKP1 fragments was detected upon excitation of CFP (442 nm). Bar, 10 µm.

The subcellular distribution of the PKP1a deletion mutants was comparable in both cell lines. Moreover, this distribution was also similar to the localization previously observed in COS-7 cells. PKP1a full length (region 1-726), PKP1-head domain (region 1-243), and PKP1-98 (region 98-726) showed restricted nuclear localization. PKP1-121 (region 121-726) was detected in the cytoplasm but still conserved the predominant nuclear staining. However, PKP1-151 (region 151-726) and PKP1-ARM (region 244-726) lost the predominant nuclear localization, being equally distributed throughout cell.

The fact that the PKP1a-deletion mutants showed the same distribution in cells that express PKP1 and cells that do not, indicates that the dimerization with endogenous PKP1 is not the reason why the mutants lacking the residues implicated in the nuclear targeting of PKP1a were entering to the nucleus.

Effect of fusion tags on the localization of the armadillo domain of PKP1a

Since we were as yet unsure about why the CFP-PKP1a deletion constructs that lack the first 116 to132 residues (i.e. 133-726, 151-726, 181-726, and ARM-domain) were entering to the nucleus. We looked again to a possible effect of the fusion tag. We had observed that our CFP-tagged constructs of PKP2a, PKG, and DP showed a specific subcellular distribution; including PKP2a, which did not exhibit any nuclear signal (see Figures R29, R30, and R32). So, it was very unlikely that the same CFP-tag was recruiting to the nucleus the CFP-PKP1a deletion constructs that lack the first 116 to132 residues (i.e. 133-726, 151-726, 181-726, and ARM-domain). We had previously tested the effect of the tag on the subcellular distribution of PKP1a and DP (see Figure R8). However, in this case we used PKP1 full length that intrinsically shows restricted nuclear localization. Thus, to further analyse the influence of the fusion tag on the presence in the nucleus of PKP1-ARM and similar deletion fragments, we created equivalent PKP1a constructs (PKP1 full length and PKP1-ARM) tagged with HA or FLAG at the N-terminus. The FLAG-tagged constructs were created using the pCEFLAG vector, while the HA-tagged ones were done in the vectors pCEFLHA and pcDNA3-HA. These constructs were transiently expressed in COS-1 cells and their subcellular localization was investigated by immunofluorescence and confocal microscopy (Figure R38).

Full length PKP1a (amino acids 1-726) with FLAG or HA tags showed nuclear-restricted distribution, as observed with the CFP-labelled construct. Similarly, the ARM domain (PKP1-ARM) tagged with HA in the pcDNA3-HA vector showed the same distribution as the CFP-tagged version, that is, equal distribution of the signal between nucleus and cytoplasm (see above). However, PKP1-ARM was excluded from the

nucleus when the PKP1-ARM was tagged with FLAG or with HA using the pCEFLAG or the pCEFLHA vectors, respectively, being only present at the cytoplasm.

Since the armadillo domain was not present in the nucleus when expressed using the pCEFLHA vector, we re-created several representative N-terminal deletion mutants of PKP1a in this vector and analysed their subcellular distribution by immunofluorescence (Figure R39). The HA-tagged constructs PKP1-75 (75-726) and PKP1-116 (116-726) showed an almost exclusive nuclear staining, while the PKP1-121 (121-726) construct had a dual localization in the nucleus and cytoplasm. On the other hand, the shorter constructs PKP1-151 (151-726) and PKP1-181 (181-726) showed diffuse staining in the cytoplasm and were excluded from the nucleus. Collectively, these results are analogous to those observed with similar constructs tagged with CFP (see Figure R34), and highlight the role of the 116-151 region of the head domain of PKP1a in the nuclear targeting of this protein.

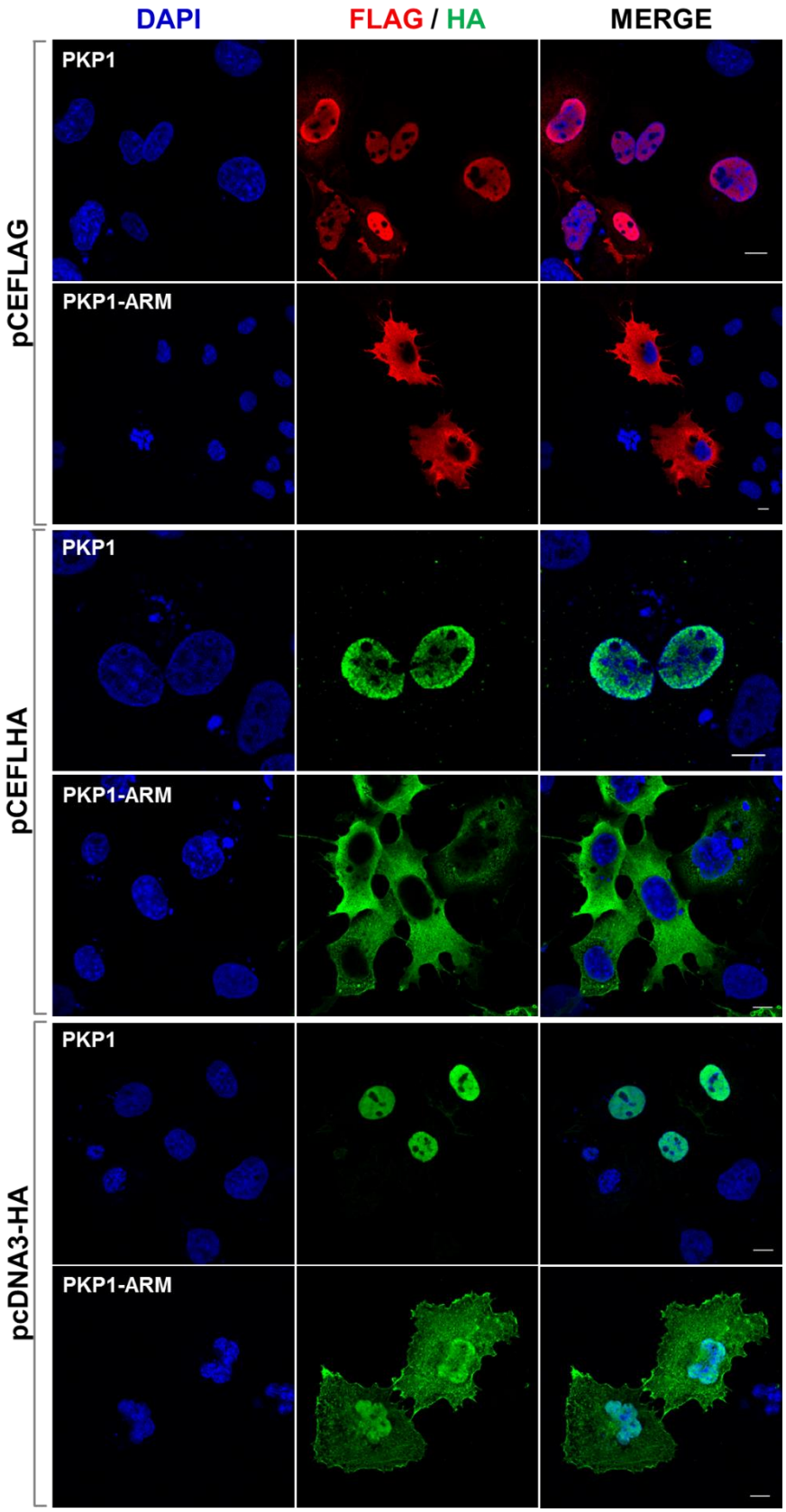

Figure R38. Sub-cellular localization of FLAG- and HA-tagged PKP1a and PKP1a-ARM in COS-1 cells. Immunofluorescence images of PKP1a full length (1-726) and PKP1-ARM (244-726) with two different tags. In red is shown the subcellular distribution of the constructs tagged with FLAG expressed

using the vector pCEFLAG. FLAG-fusion proteins were detected with a monoclonal antibody anti-FLAG (Clone M2, Sigma). In green are shown these same constructs but tagged with HA instead of FLAG, using the vectors pCEFLHA (middle panel) or pcDNA3-HA (bottom panel). HA-tagged fragments were detected by using a monoclonal antibody anti-HA (16B12, Covance). DAPI nuclear counterstain is shown in blue. Bar, 10 µm.

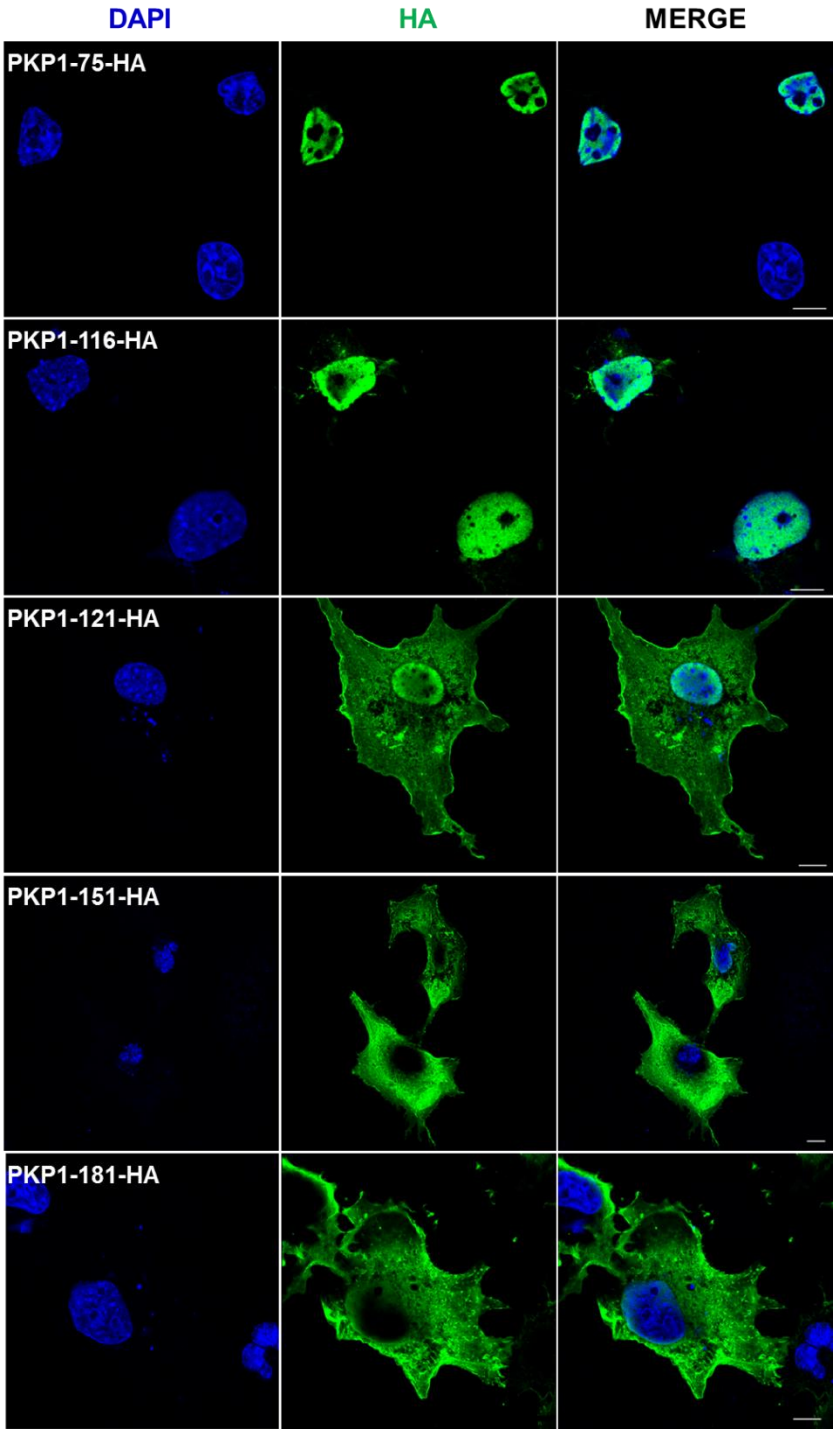

Figure R39. Sub-cellular localization of FLAG-tagged PKP1a fragments cloned in pCEFLHA. Immunofluorescence images of PKP1a N-terminal deletion mutants cloned in pCEFLHA (HA-tag). PKP1a fragments were detected with a monoclonal antibody anti-HA (16B12, Covance). DAPI nuclear counterstain is shown in blue. Bar, 10 µm.

The subcellular distribution of PKP2a is determined by specific residues in the head domain

Given that the subcellular localization of PKP1a is controlled by its head domain, we analysed whether this was also the case for PKP2a. With this purpose, we generated a construct coding for full length PKP2a and several N-terminal deletion mutants tagged with CFP (Figure R40) and looked at their subcellular distribution in COS-7 cells by using confocal microscopy (Figure R41).

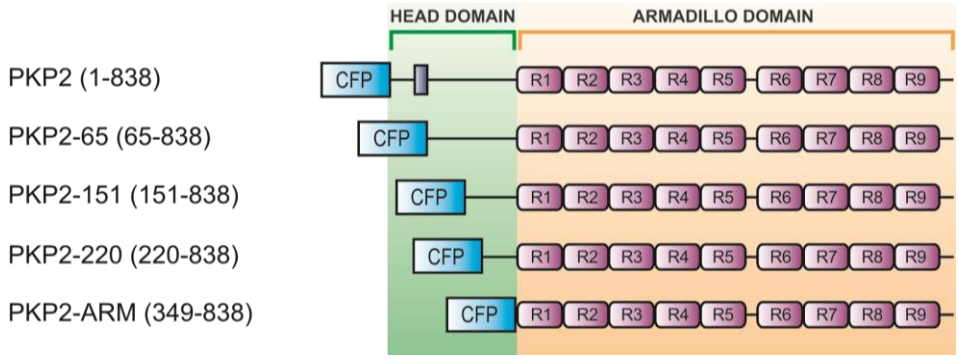

Figure R40. CFP-tagged N-terminal deletion mutants of PKP2a. Schematic domain representation of the PKP2a fragments generated to look for localization determinants in the head domain of PKP2a. The constructs coding for these fragments were created in the pcDNA3-CFP-C4 vector that adds a CFP-tag to the N-terminus. The HR2 motif within the head domain is shown as a grey box in the scheme.

PKP2a mutants lacking the N-terminal half of the head domain, that is, fragments PKP2-65 (region 65-838) and PKP2-151 (region 151-838), showed predominant localization at the plasma membrane, similar to that of the full length PKP2a. However, further N-terminal deletions, as in the fragment PKP2-220 (region 220-838) and the isolated armadillo domain (PKP2-ARM, region 349-838) resulted in the loss of the specific localization at the plasma membrane. These fragments appeared diffusely distributed throughout the cell. Interestingly, the armadillo domain of PKP2a showed prominent nuclear presence (see arrows), similar to that observed for the CFP-tagged armadillo domain of PKP1a.

In summary, similarly to PKP1a and in spite of the different subcellular distribution of these two proteins, the localization of PKP2a is also determined by sequences in the head domain. In PKP2a, the central segment (151-220) of the head domain is required for the peripheral localization of PKP2a. Finally, the nuclear distribution of CFP-tagged constructs of PKP2a that lack the functional targeting sequences, probably does not correspond to a native function.

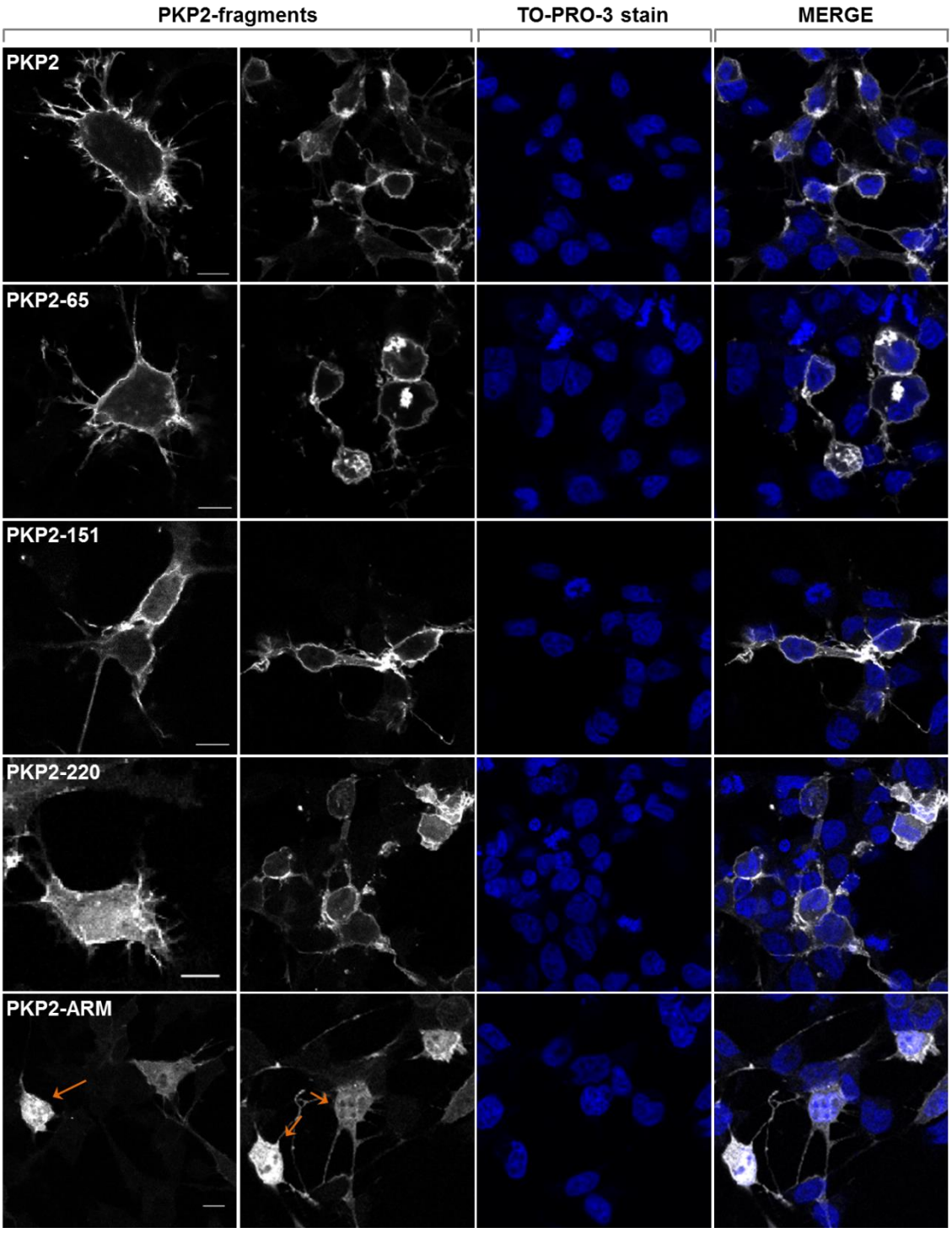

Figure R41. Subcellular distribution of CFP-tagged PKP2a N-terminal deletion mutants in COS-7 cells. The subcellular distribution of ectopically expressed PKP2a and its N-terminal deletion mutants tagged with CFP was investigated in COS-7 cells by confocal microscopy. CFP fluorescence was detected upon excitation of CFP at 442 nm and is represented in grey. Nuclear counterstaining was made by using TO-PRO-3 stain and is represented in blue. Bar, 10 µm.

Section C

Structure of the PD of DP

1. Structural analysis of the N-terminal region of the PD of DP

Sequence analysis of the N-terminal region of the PD of DP suggests the presence of a SR-like domain

Mammalian plakins share a similar multi-modular structural organization that bears in its N-terminal region the so-called plakin domain (PD) (Sonnenberg & Liem 2007; Jefferson et al. 2007). The PD consists of several SRs arranged in tandem that vary in number depending on the plakin-protein, but seven SRs (SR3-SR9) are present in all mammalian plakins. Upstream the SR3, plectin and the BPAG1 variants a, b, and n, have two additional SRs (SR1-SR2), whereas BPAG1e only harbours the SR2. Recent studies have suggested that the N-terminal region of DP that precedes the SR3 (residues 1–179) is unstructured (Al-Jassar et al. 2011).

In order to investigate the possible presence of a SR or SR-like structure in DP upstream of the SR3, we studied several PD sequences by using profile hidden Markov models (HMM profiles). First, we created a multiple sequence alignment of the SR2 domain of plectin, BPAG1, MACF1, periplakin, and envoplakin, which contain bona fide SR2 domains, we constructed the HMM profile and searched for homology against the human proteome and against the DP sequence. These strategies did not identify any canonical SR2 domain in DP. Next, we generated a more general HMM profile using all the sequences of all the SR domains of mammalian plakins, with the exception of the SR6s because of their divergent structure (Sonnenberg et al. 2007; Choi & Weis 2011). Results obtained by searching for homology in the human DP sequence using this HMM profile are summarized in table R9.

Table R9. HMM-based search for SR in human DP-PD [a]

Domain	Score	E-value	Alignment region	Envelope region [b]
SR2	-4.1	1	106-147	65-157
SR3	38.7	6.80E-14	192-272	182-273
SR4	56.7	1.80E-19	270-375	269-376
SR5	45	7.70E-16	377-547	377-549
SR7	35	9.90E-13	664-729	664-741
SR8	56.1	2.80E-19	770-884	769-885
SR9	68.8	3.30E-23	887-1017	887-1028

a, the HMM-based search was done with the program HMMER.
b, an envelope is a subsequence of the target sequence that appears to contain alignment probability mass for a likely domain.

The six canonical SR domains of DP (SR3-SR5, SR7-SR9) were identified by the HMM-based search; this was expected as their sequences were represented in the

HMM profile. In addition, the HMM-based search suggested the presence of an additional SR-like domain upstream of the SR3. Hence, we refer to it as SR2. Despite the lower score and statistical significance (the lower the E-value, the more significant the hit) of the SR2, the HMM-based search suggested that residues 65-157 (envelope region) have, at least, a SR signature, being unlikely to correspond to a disordered region. The envelope region represents the sequence that includes most of the posterior probability for a given homologous domain being the region where the domain's alignment most probably lies.

The presence of a SR-like domain in the N-terminal segment of the DP-PD might have not been noticed in previous reports because by default inclusion thresholds usually require E-values of 0.01 or less; therefore this hit would go unnoticed in an unsupervised sequence analysis. In addition, the use of a HMM profile specific for the plakin domain might have increased the amount of information necessary to identify potential SR homology in DP.

Since the statistical significance of the SR hit in the N-terminal segment of DP fell in a twilight zone, we further characterised its presence. First, we used secondary structure prediction methods based on sequence analysis to identify putative structural elements in the DP region upstream of the SR3 (residues 1-180).

The PredictProtein and the Jpred 3 servers (Yachdav et al. 2014; Cole et al. 2008) indicated the presence of three helices in the DP region 65-156 (Figure R42-A) that coincides with the limits of the SR2-like domain suggested by the search using HMM-profiles. Outside of this region only another short helix is predicted around residues 11-18. When the sequence of the SR2 of plectin was aligned to that of the N-terminal region of DP, the three α-helices of plectin match the position of the helices predicted in DP (Figure R42-B). Nonetheless, the sequence similarity between DP, plectin, and BPAG1e is lower towards the end of the SR2, e.g. beyond residue 153 in DP, where helix C of plectin extends longer than the predicted helix of DP.

In order to illustrate the α-helical properties of the putative helices in the DP region 65-156, we represented their sequences by using helical wheels diagrams (Figure R42-C). In such diagrams the secondary structure is plotted in a swivel manner where the angle of rotation between consecutive amino acids is 100°, obtaining a final representation that looks down the helical axis. This revealed an asymmetric distribution of polar and nonpolar residues. Most of the hydrophobic residues are concentrated on one side of the helix and occupy the *a* and *d* positions of the helical heptad repeat. This is characteristic of amphipathic helices as those that form canonical SRs, where the helices pack with the hydrophobic sides oriented towards the centre of the bundle.

Notably, residues conserved among DP, plectin, and BPAG1e mainly occupy the *a* and *d* positions of the heptads.

Collectively, the analysis of the DP sequence suggests that the region ~65-156 consists of three amphipathic α-helices that likely adopt a SR fold, and supports the hypothesis that the N-terminal region of DP-PD harbours a SR2-like domain.

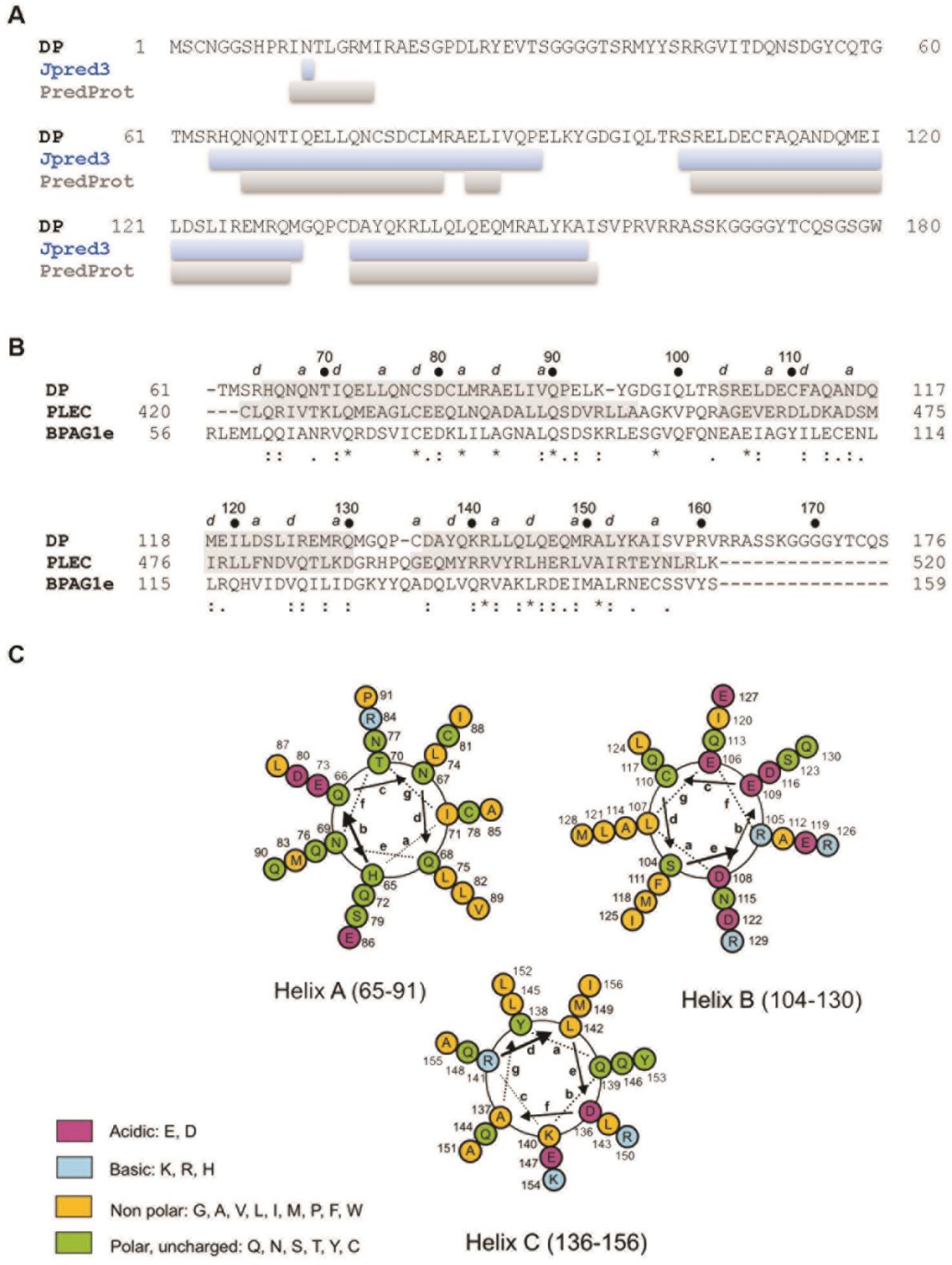

Figure R42. Sequence analysis of the SR2-like domain of DP. A) Amino acid sequence of the region 1-180 of the DP-PD. Below the sequence are represented by coloured boxes the secondary structure predictions made by using Jpred 3 (blue) and PredicProtein (grey). B) Multiple sequence alignment of the

SR2 of plectin (Uniprot entry Q15149-2), BPAG1e (Q03001-3) and DP (P15924). Symbols below the alignment represent the conservation among the sequences. Specifically, asterisks (*) indicate positions which are fully conserved, colons (:) indicate conservation between groups of strongly similar properties and periods (.) conservation between groups of weakly similar properties. The DP sequence expected to be a SR2-like domain is mostly conserved with groups of similar properties among the three sequences. Alpha-helices predicted in DP by the PredictProtein server and α-helices of the crystal structure of plectin (PDB code 2ODU) are represented as grey-shaded regions. The positions *a* and *d* of the heptad repeat in the structure of plectin are indicated on the top of the sequences. C) Helical wheels diagrams showing the distribution of the amino acids in the α-helices predicted in DP. Amino acid properties are represented by using a colour code for non-polar (yellow), polar uncharged (green), acidic (pink) and basic (light-blue) amino acids. Helices A and C are represented with the C-terminus towards the back of the page, while helix B is plotted with the C-terminus towards the reader; this corresponds to the orientations of the helices in canonical SRs. Hydrophobic residues occupy mainly the positions *a* and *d* of the heptad and have been oriented towards the centre of the helical bundle; while polar residues predominate on the outside of the bundle.

Taking into account all the previous evidences based on sequence analysis we created two different constructs of the putative SR2 of DP in the bacterial expression vector pETEV15b:

i) A short construct, DP-SR2-S-pET (residues 64-155), that corresponds approximately to the domain limits indicated by the HMM-based search.
ii) A long construct, DP-SR2-L-pET (residues 64-164), in which the C-terminal limit was extended to account for a possible larger extension of the third α-helix.

The two DP-SR2 constructs were expressed soluble in *E. coli* as His-tagged fusion proteins, were purified by affinity chromatography, and the His-tag was removed by proteolysis.

Biophysical analysis of the SR2-like domain of DP

In order to analyse the secondary structure of the recombinant fragments of the SR2 of DP we measured the far-UV circular dichroism (CD) spectra of DP-SR2-L and DP-SR2-S (Figure R43).

The shape of the far-UV CD spectra allows to qualitatively determining the secondary structure content of proteins. Both spectra are characterized by a double negative minima at ~208 and ~224 nm and a maximum at ~193 that are characteristic of α-helices (Ranjbar & Gill 2009). The spectra of the two constructs are almost identical with only minor differences in the amplitude of the maxima at ~193, suggesting that they have almost equal secondary structure content with a major presence of α-helices.

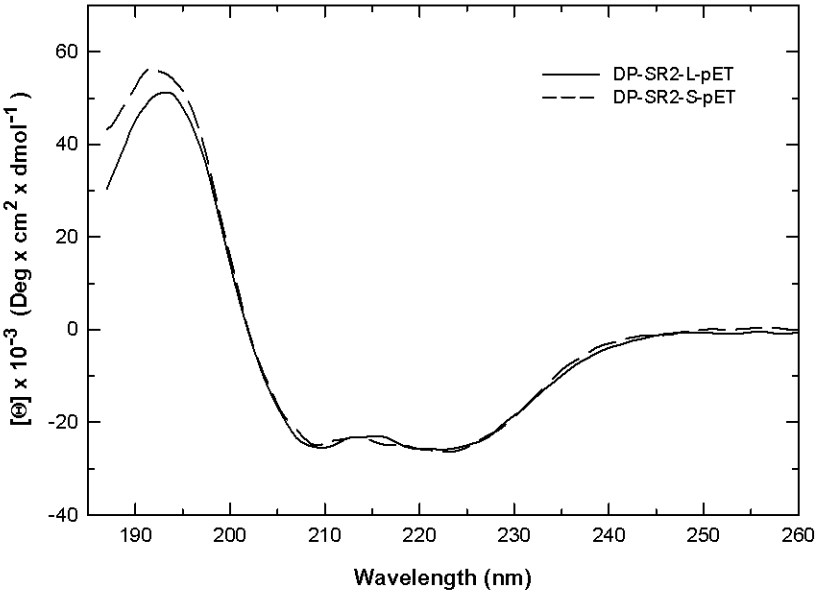

Figure R43. Far-UV CD spectra of purified DP-SR2 fragments. Far-UV CD spectra of the fragments DP-SR2-L (residues 64-164, solid line) and DP-SR2-S (residues 64-155, dashed line) represented in terms of mean residue molar ellipticity ([θ]). Each spectrum is a combination of spectra acquired using cells with optical paths of 1.0 mm and 0.1 mm using protein samples at two different concentrations in 20 mM NaPi (pH 7.5), 150 mM NaCl, 0.3 mM TCEP. DP-SR2-L samples at 0.83 mg/mL and 2.49 mg/mL were measured in the 1.0 mm and 0.1 mm cells, respectively. Similarly, DP-SR2-S samples at 0.66 mg/mL and 2.65 mg/mL were measured in the 1.0 mm and 0.1 mm cells, respectively. Spectra were measured at 20 °C.

The secondary structure content of DP-SR2-L and DP-SR2-S was estimated from their far-UV CD spectra using four methods implemented in the programs K2D3, SELCON, CONTIN, and CDSSTR (Table R10). All methods predicted a major presence of α-helical structure, ranging between ~70 and 85 %, and only a negligible presence of β-sheet that is likely to be not significant. The contents in α-helix estimated from the CD spectra were similar to the α-helical fractions predicted from the sequence (71 % for DP-SR2-L and 78 % for DP-SR2-S according to PredictProtein) and they were compatible with a SR fold.

Table R10. Estimation of the secondary structure content from the far-UV CD spectra

		Fraction of secondary structures (%) [a]				
Fragment	Method	α-helix	β-sheet	turns	random	rmsd [b]
DP-SR2-L	K2D3 [c]	68.4	1.6	-	30.0	-
(64-164)	SELCON	76.4	0.1	9.3	14.2	0.035
	CONTIN	77.3	1.1	9.0	12.6	0.028
	CDSSTR	83.0	2.0	6.0	7.0	0.009
DP-SR2-S	K2D3	68.6	0.9		30.5	-
(64-155)	SELCON	80.5	2.9	4.6	17.8	0.058
	CONTIN	77.0	1.1	6.6	15.2	0.014
	CDSSTR	79.0	1.0	6.0	13.0	0.007

a, data from 190 nm to 240 nm were used for all estimations
b, root mean square deviation
c, K2D3 only estimates the α-helix and β-sheet content and it does not distinguishes between turns and random coil

Temperature induced denaturation provide useful and reliable information about conformational stability of a folded protein. To shed light on the structural organization of the putative SR2, we analysed the thermal stability of the DP-SR2-L and DP-SR2-S fragments by CD and with a thermal shift assay (also known as differential scanning fluorimetry or Thermofluor).

For the CD thermal denaturation we measured the molar ellipticity of the samples at 222 nm, which is proportional to the α-helical content, during a temperature ramp from 20 to 90 ºC (Figure R44). Both proteins showed similar molar ellipticity at 20 ºC and presented a comparable linear increase in the signal in the initial segment of the ramp. At higher temperatures we observed rapid increases in the molar ellipticity that revealed highly cooperative reactions, characteristic of compact and well-ordered structures. After a first denaturation ramp the DP-SR2-L sample was cooled down and a second heating cycle yielded the same denaturation profile, indicating that the unfolding reaction was reversible. The denaturation curves were analysed assuming a two-state transition from a folded to an unfolded state, which allowed for the determination of the Tm of the fragments, equivalent to the midpoint of the transition. The Tm of DP-SR2-L (64-164) was 74.2 ± 0.3 °C, whereas that of the shorter construct DP-SR2-S (64-155) was 61.1 ± 0.1 °C.

The large difference (~13 °C) in the Tm of the two fragments indicates that the segment 156-164 greatly contributes to the conformational stability of the SR2 of DP, and suggests that it is part of the structure of this domain.

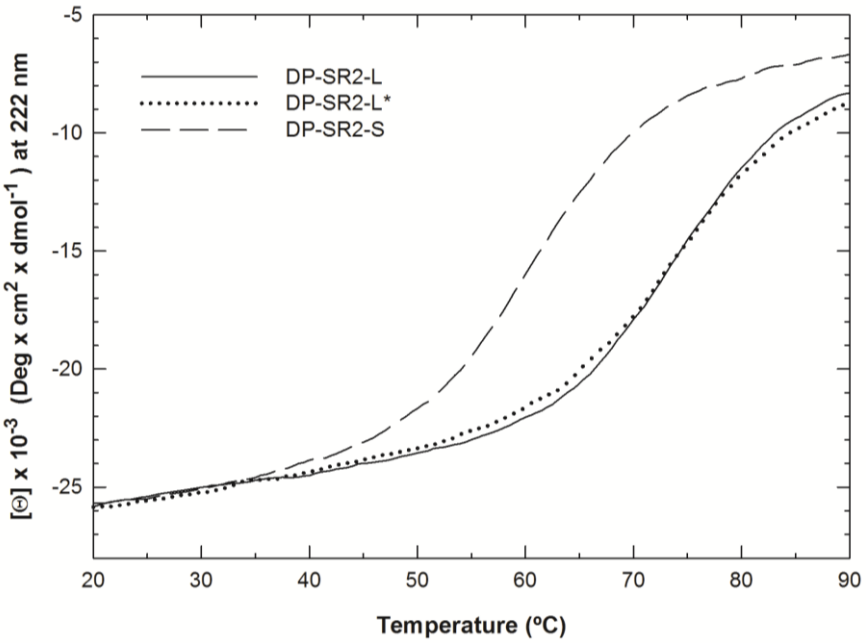

Figure R44. Denaturation profiles of DP-SR2 fragments. The denaturation profiles of DP-SR2-L (64-164, solid line) and DP-SR2-S (64-155, dashed line) were determined by measuring the mean residue molar ellipticity at 222 nm while the temperature was increased from 20 to 90 ºC with a heating rate of 40 ºC/hour. After the first denaturation cycle, the DP-SR2-L sample was cooled down and a second denaturation profile was recorded (DP-SR2-L*, dotted line). This second denaturation profile was almost identical to the first cycle indicating that the denaturation of DP-SR2-L is a reversible process that can be understood as a balance between the folded and unfolded states.

To further characterize the thermal stability of the DP-SR2 constructs we used a thermal shift assay (Thermofluor) that is based on changes in the fluorescence of the probe Sypro Orange upon binding to hydrophobic regions of the proteins that become accessible upon denaturation. The melting curves of the DP-SR2 fragments are characterized by a rapid increase in the fluorescence of the probe followed by a sharp decrease that is probably related to dissociation of the dye or aggregation of the protein. The Tm of the DP-SR2-L and DP-SR2-S at neutral pH were ~ 66 °C and ~ 55 °C, respectively. This confirmed the higher thermal stability of the 64-164 fragment with respect to the 64-155 one (Figure R45-A). We also analysed the effect of the pH in the stability of the two DP-SR2 constructs, yet we did not observed noticeable changes in the thermal stability between pH 6.0 and 8.0 (Figure R45-B, C).

The melting temperatures determined in the thermal shift assays were lower than those observed by CD. These differences likely reflect that each method provides information of different steps of the unfolding process. The far-UV CD assay is sensitive to the stability of the helices, whereas the Thermofluor assay responds to the exposure of hydrophobic patches, such as opening of the SR helical bundle, which might occur at lower temperatures than those required to unfold the α-helices.

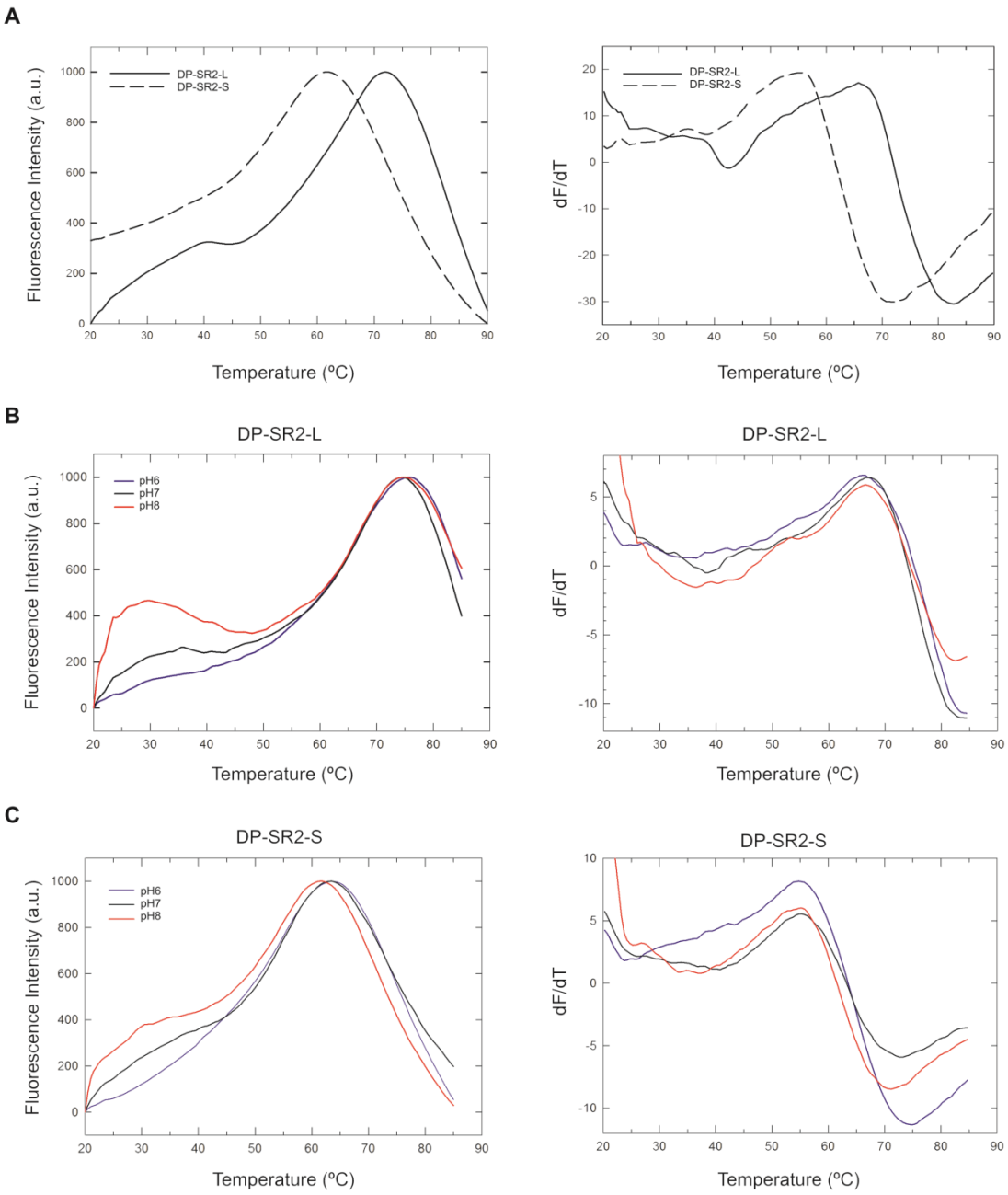

Figure R45. Thermofluor analysis of the stability of DP-SR2 fragments. A) Denaturation profiles of DP-SR2-L (64-164, solid line) and DP-SR2-S (64-155, dashed line) in 50 mM HEPES pH 7.5, 150 mM NaCl in the presence of Sypro Orange (10 arbitrary units, as defined by the manufacturer). The temperature of the samples was increased at a rate of 60 °C/hour. The fluorescence of the probe was measured using 480 nm excitation and 530 nm emission filters (left panel). The Tm was estimated from the maximum of the first derivative of the fluorescence (F) with respect to the temperature (T) (dF/dT) (right panel). **B)** Denaturation curves of DP-SR2-L at pH 6.0 (blue), 7.0 (black) and 8.0 (red). **C)** Denaturation curves of DP-SR2-S at pH 6.0 (blue), 7.0 (black) and 8.0 (red).

Summarizing, our results indicate that the region 64-164 of DP forms a well ordered and stable structural domain with high α-helical content likely to consist of three

amphipathic α-helices and with sequence similarity to the SR domains. Hence, our data is compatible with the presence of a non-canonical SR2 in this region of DP.

Structure of the N-terminal region of the PD of DP: analysis by small angle X-ray scattering (SAXS)

Attempts to crystallize the N-terminal region of the PD of DP (region 1-630) were unsuccessful. Thus, the structure of this region was investigated by SAXS. Analysis of SAXS data provides low-resolution structural information of biomolecules in solution in a straightforward manner including accurate shape and size information.

Scattering profiles of DP-1-SR6 were measured at five different concentrations between 29.2 and 1.825 mg/mL. Preliminary analysis detected radiation damage, strong interparticle attraction, and possible aggregation at high concentration. Therefore, subsequent analyses were performed using only the most diluted curve at 1.825 mg/mL, which did not suffer from radiation damage. The resultant scattering profile after buffer subtraction and normalization is shown in Figure R46-A. This curve was used to calculate the radius of gyration (Rg) and the forward scattering intensity (I_0) using the Guinier approximation (Figure R46-B). Other informative parameters, such as the Porod Volume (Vp), the pair-distribution probability function ($P(r)$), and the maximum particle size (Dmax) were also calculated from the scattering data.

The apparent molecular weight of DP-1-SR6 calculated from the Vp (Vp/1.6; Petoukhov et al., 2012; Rambo & Tainer, 2011) was 77.4 kDa, which is in agreement with the molecular mass calculated from its sequence (73641 Da) and confirms that this fragment of DP is a monomer in solution. Guinier analysis of the scattering data revealed that DP-1-SR6 has a Rg of 62 ± 3 Å (Figure R46-B), which is consonant with the Rg of 64.9 ± 0.3 Å determined in the calculation of the P(r) using data covering a range of the scattering vector from 0.0075 to 0.2970 $Å^{-1}$. The P(r) presented a maximum at small distances with a tail extending up to a Dmax of ~220 Å. This shape is characteristic of elongated molecules (Figure R46-C). The dimensionless Kratky representation of the scattering data showed a maximum of ~2.2 at q*Rg ~6.5, which is displaced from the expected maximum for globular compact particles (~1.1 at q*Rg ~1.73). This deviation may reflect that DP-1-SR6 is a high anisometric structure. This is in agreement with the shape of the P(r) function (Figure R46-D).

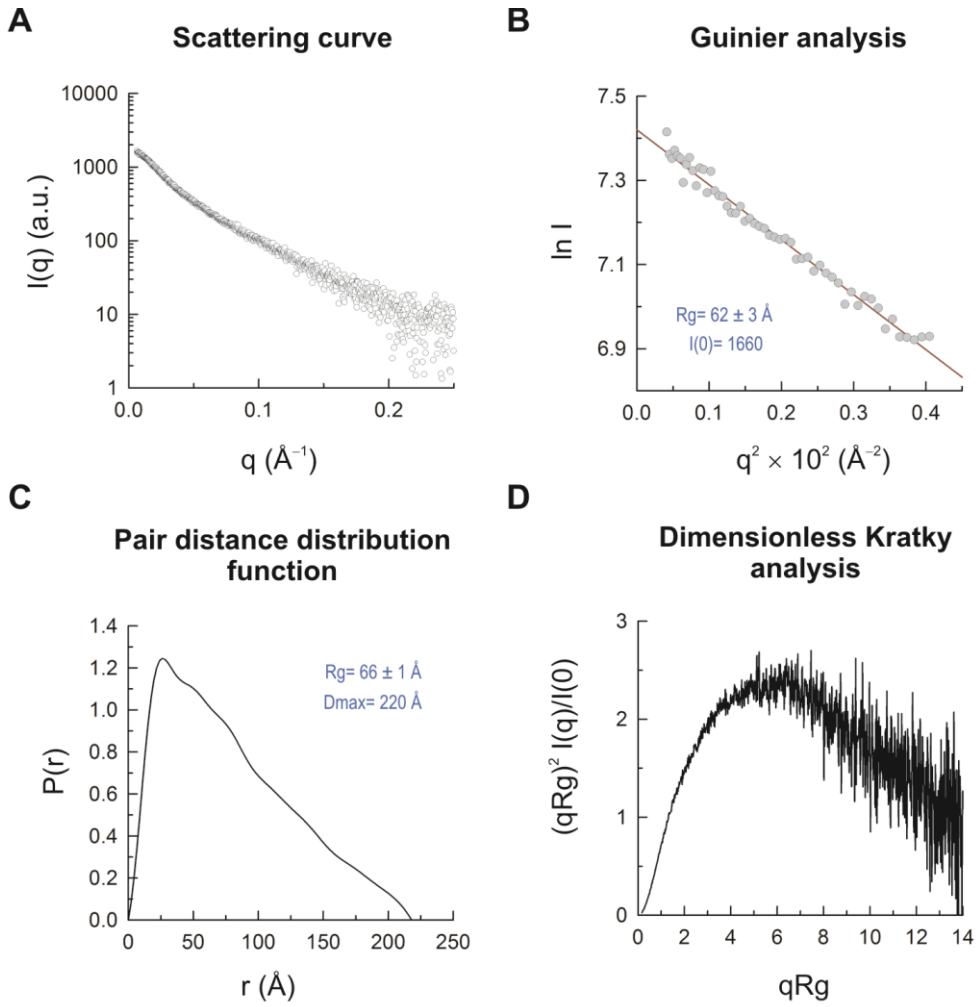

Figure R46. SAXS analysis of the N-terminal region of DP-PD. A) Scattering profile of DP-1-SR6, region 1-630, at 1.825 mg/mL. **B)** Guinier analysis of the scattering curve shown in A. The Rg and I_0 calculated by the Guinier analysis are 62 ± 3 Å and 1660, respectively. **C)** Pair-distance distribution curve estimated from the SAXS data using the program GNOM. **D)** Dimensionless Kratky analysis of the DP-1-SR6 scattering data showing a displacement of the maximum of the plot towards higher levels of q*Rg than that predicted for compact globular particles.

From the scattering data of the DP-1-SR6 fragment we calculated low-resolution shape reconstructions using an *ab initio* method implemented in the program DALAI_GA. We made ten independent reconstructions. After superimposition of the ten models, the normalized spatial discrepancy (NSD, a parameter that measures the similarity of 3D structures, being zero for identical structures and >1 for objects different from one another) was 0.91 ± 0.03, which indicates that the method yields repetitively similar reconstructions. The resulting average model, which is the volumetric representation of the most probable envelope, has a slightly bent rod-like shape (Figure R47).

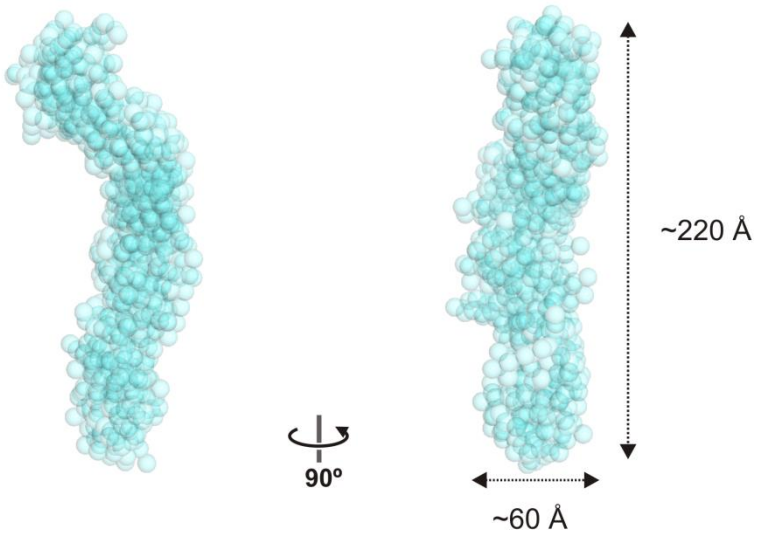

Figure R47. SAXS reconstruction of the N-terminal region of DP-PD. Spheres representation of the low resolution structures of the fragment 1-630 of DP obtained by *ab initio* methods with the program DALAI_GA. Two orthogonal views are shown. Ten models, which were superimposed, are shown in semi-transparent representation. The areas with darker colour correspond to parts of the structure more frequently present in the set of models.

In addition, the structure of DP-1-SR6 was modelled by rigid body fitting against the SAXS data using two different methods implemented in the programs CORAL and BUNCH. On the one hand, we used CORAL to obtain a mixed composite model comprising the atomic model of the SR2 (built by homology modelling using the SR2 of BPAG1e as template) and the crystal structure of DP-SR3-SR6 (PDB entry 3R6N). CORAL starts from arbitrary initial positions and orientations of the rigid domains to build a final model in which the linkers that connect the rigid bodies are modelled using a library of self-avoiding random loops. In all the models obtained with CORAL the SR2 domain is placed on one side of the SR3, whereas the N-terminal tail (residues 1-63) is built in an extended conformation that project away from other parts of the structure (Figure R48-A). It should be noted that the specific relative position of the SR2 with respect to the SR3 cannot be inferred in the absence of additional restraints; yet, the repetitive positioning of the SR2 adjacent to the SR3 suggests that these two domains could establish lateral interactions and adopt a compact arrangement. The composite models obtained with CORAL match the shape estimated by *ab initio* modelling against the SAXS data (Figure R48-B). The theoretical scattering profile of the rigid body model fits the experimental data (Figure R48-C). Similarly, the P(r) and kratky dimensionless plots of the CORAL model also reproduce approximately those obtained from the experimental data (Figure R48-D, E).

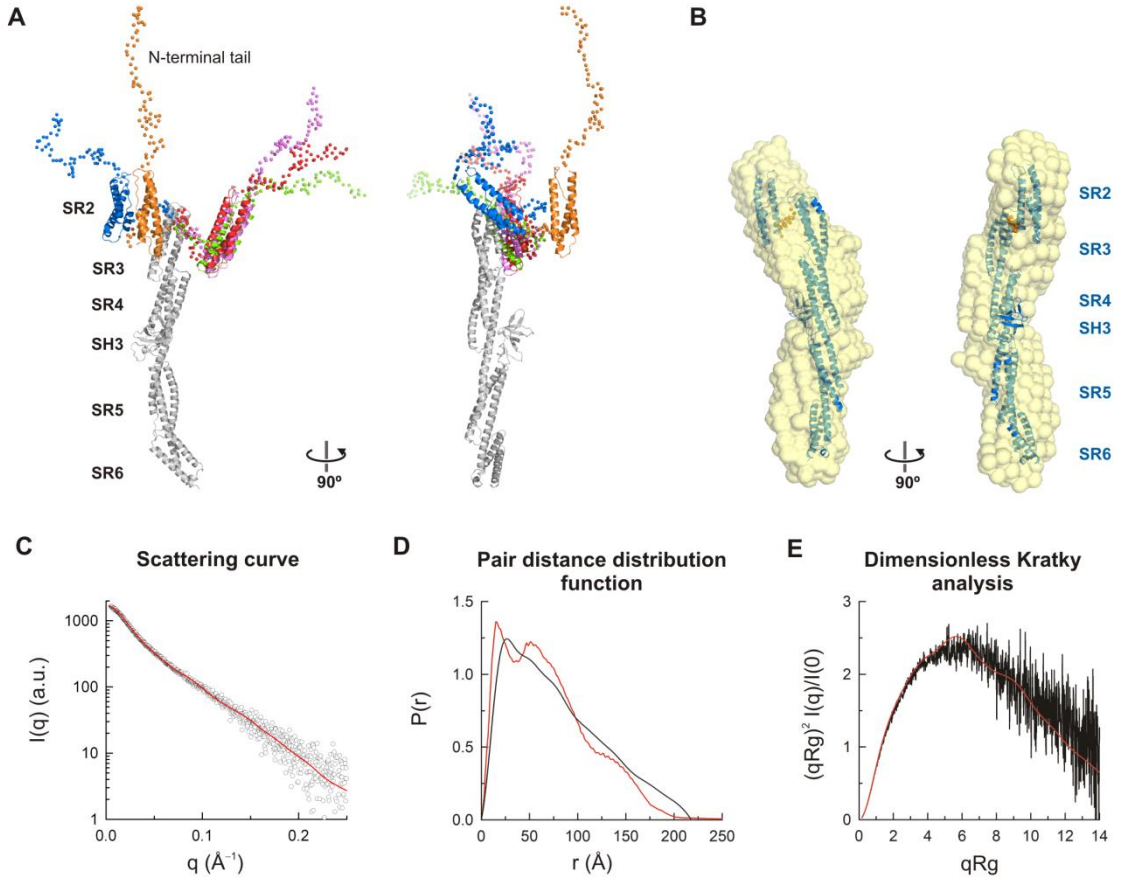

Figure R48. Composite model of the region 1-630 of DP obtained by rigid body fitting with the program CORAL. A) Representation of five rigid body models of DP-1-630. The segment SR3-SR6, which is identical in all models, is shown in grey. The SR2 in each model is shown in a different colour. The N-terminal tail and the linker between the SR2 and SR3 domains were modelled as dummy residues whose Cα atoms are shown as spheres of the same colour as the corresponding SR2 domain. **B)** Superimposition of a representative model of A onto the average molecular envelope calculated from the reconstructions obtained with DALAI_GA. For clarity, the N-terminal tail is not shown. **C)** Experimental SAXS profile of DP-1-SR6 (circles) and fit of the theoretical scattering of a representative model obtained with CORAL (red line). **B)** P(r) function calculated from the SAXS data (black line) and theoretical P(r) calculated from the CORAL model (red line). **C)** Dimensionless Kratky plot of the experimental scattering data (black line) and of the scattering data calculated for the model (red).

Alternatively, we used the program BUNCH, which performs modelling of multi-domain proteins against SAXS data using a combined rigid body and *ab initio* modelling approach in which inter-domain linkers are represented by dummy residues (Figure R48-D). Similarly to the rigid body model obtained with CORAL, in the models produced by BUNCH the SR2 lies adjacent to the SR3 (Figure R49-A). The models match the shape obtained by *ab initio* modelling and the theoretical scattering of the models fit the experimental curves (Figure R49-B-C). Similarly, the P(r) reproduces the experimentally determined function and the kratky dimensionless plot is very similar to

that of the experimental data (Figure R49-D-E). The position of the SR2 in the different models obtained with BUNCH has lower variability than in the models generated with CORAL. This probably reflects that BUNCH explores a more limited conformational space than CORAL, which examines much more possible inter-domain organizations that fit the experimental SAXS data.

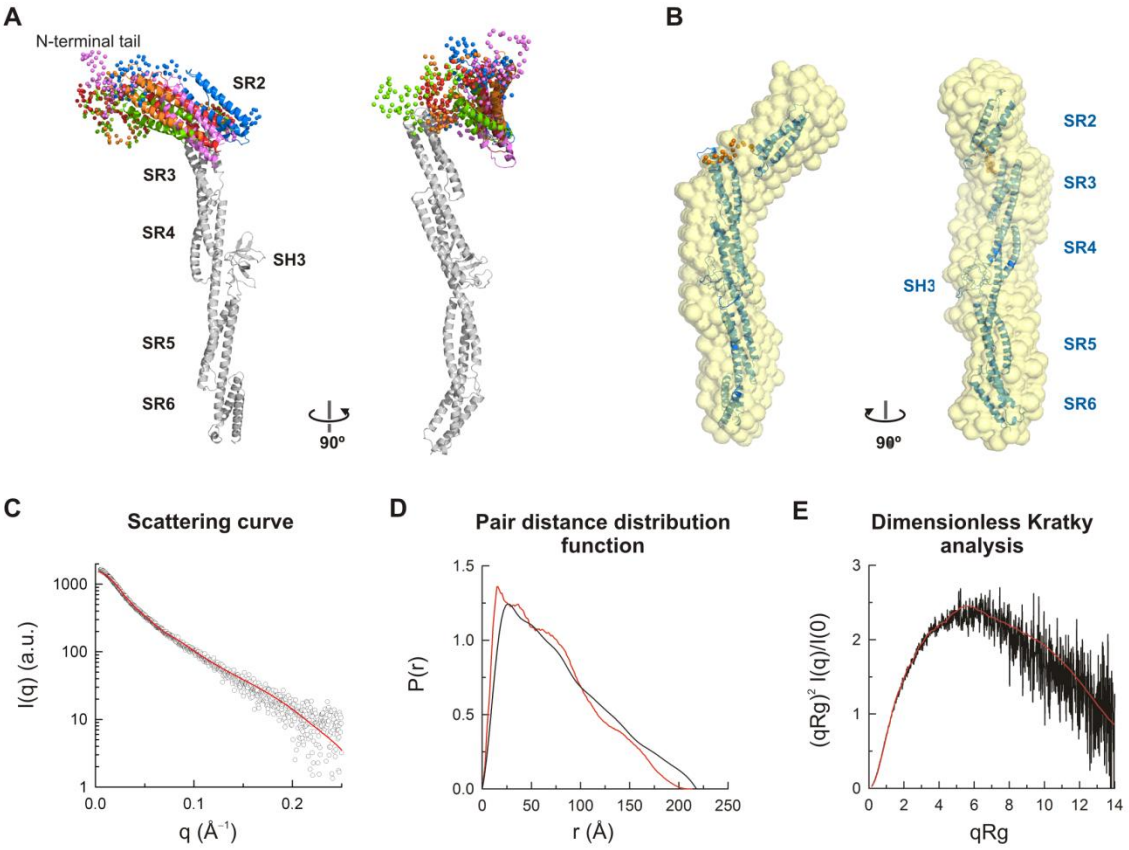

Figure R49. Composite model of the region 1-630 of DP obtained by rigid body fitting with the program BUNCH. A) Representation of five models obtained with BUNCH. The segment SR3-SR6, which is identical in all models, is shown in grey. The SR2 in each model is shown in a different colour. The N-terminal tail and the SR2-SR3 linker were modelled as dummy residues whose Cα atoms are shown as spheres of the same colour as the corresponding SR2 domain. **B)** Superimposition of a representative model of A onto the average molecular envelope calculated from the reconstructions obtained with DALAI_GA. For clarity, the N-terminal tail is not shown. **C)** Experimental SAXS profile of DP-1-SR6 (circles) and theoretical scattering of a representative model obtained with BUNCH (red line). **D)** P(r) function calculated from the SAXS data (black line) and theoretical P(r) calculated from the BUNCH model (red line). **E)** Dimensionless Kratky plot of the experimental scattering data (black line) and of the scattering data calculated for the model (red).

Collectively, the analysis of the SAXS data suggests that the N-terminal region of the DP-PD (residues 1-630) has an elongated shape in which the SR2 could be folded back onto the SR3.

2. Structure of the C-terminal region of the PD of DP

Homo-association of the C-terminal region of the PD of DP in cell culture

Downstream the PD, plakins contain a rod domain thought to form homo-dimers by means of coiled-coil interactions (Green, Virata, et al. 1992; O´Keefe et al. 1989). Our DP-CT construct (region 544-1056) includes the SR6-SR9 region (544-1025) and the initial segment of the rod domain (1026-1056). We wondered whether this N-terminal part of the rod domain would be sufficient to mediate the dimerization of the PD. To test this hypothesis, the ability of DP to self-associate was investigated by co-IP. COS1 cells were transiently co-transfected with constructs coding DP fragments with HA or FLAG tags. FLAG-precipitates were subsequently analysed for the presence of HA-tagged fragments (Figure R50).

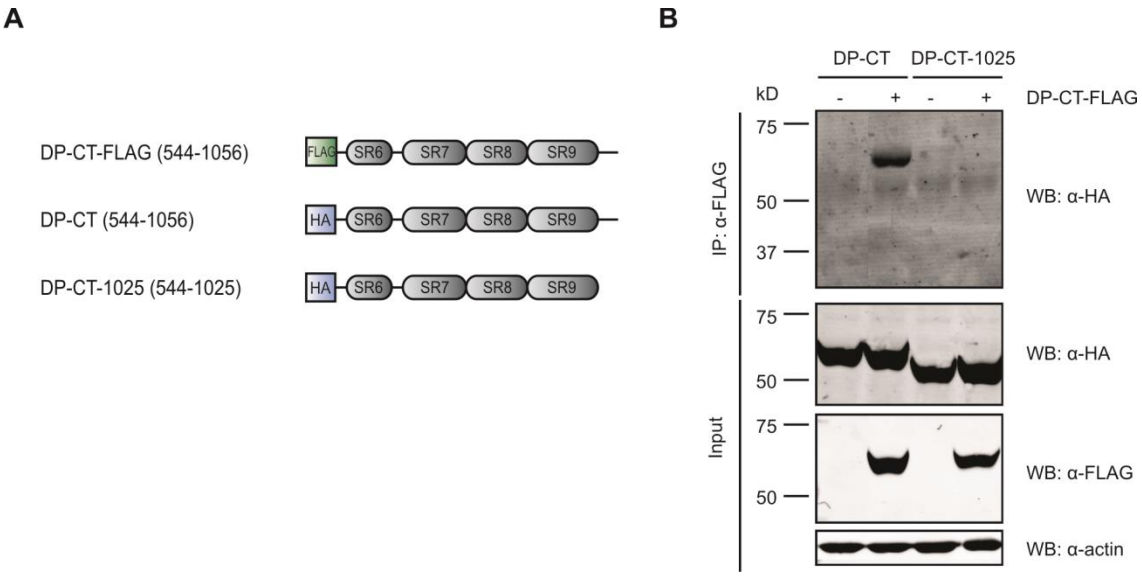

Figure R50. Analysis of the homo-association of the C-terminal region of the PD of DP by co-IP. A) Schematic domain representation of two fragments of the C-terminal half of the PD of DP. The longer construct DP-CT (544-1056) was tagged either with FLAG or HA, the shorter construct DP-CT-1025 was cloned only with a HA tag. **B)** The homo-association of DP-CT was analysed by co-transfection of COS-1 cells with DP-CT tagged with FLAG (or the empty pCEFLAG vector in the control samples) and either the same construct or DP-CT-1025 tagged with HA. Twenty-four hours after transfection total lysates were incubated with anti-FLAG agarose beads (DP lanes). Immunoprecipitated proteins were investigated by western blotting with a polyclonal anti-HA antibody. DP-CT (544-1056) interacts with itself but does not immunoprecipitate the 544-1025 fragment. Expression of DP-fragments in the input total lysates was detected by western blotting using anti-FLAG (Sigma) and anti-HA antibodies (Santa Cruz). β-actin detection was used as a loading control.

Analysis of FLAG-immunoprecipitates showed self-association of the larger DP fragment, residues 544-1056, that includes the initial part of the rod domain (~1026-1056). However, the shorter fragment 545-1025, that completely lacks the rod domain,

did not co-precipitate with DP-CT. pCEFLAG empty vector did not show any unspecific association with HA-tagged constructs, serving as a valid negative control. These results suggest that the initial ~30 residues of the rod domain are sufficient to mediate self-association of DP in cultured cells.

Structure of the SR7-SR9 region of DP-PD, monomeric state

Next, we decided to further study the structure of C-terminal fragments of the DP-PD by using biophysical techniques. With this purpose, we created a construct in the vector pETEV15b that codes for the fragment DP-CT (region 660-1056). This fragment includes the SR7-SR9 domains of the PD and approximately the first 30 residues of the rod domain. This recombinant protein was synthesised soluble in *E. coli* and was purified by using affinity chromatography (see materials and methods for details). Attempts to crystalize this fragment were not successful enough and we only got microcrystals, not suitable to obtain useful diffraction data (data not shown). To overcome this limitation, we applied SAXS to obtain the low-resolution structure of this C-terminal region of the PD of DP.

SAXS profiles of DP-CT (660-1056) were measured at the EMBL BioSAXS beamline P12 (Hamburg, Germany) at four different concentrations between 3.61 and 0.90 mg/mL. Initial analysis of the scattering curves revealed the absence of radiation damage. After buffer subtraction and normalization by the concentration, the resultant scattering profile was extrapolated to infinite dilution (Figure R51-A).

Guinier analysis of the scattering data extrapolated to infinite dilution revealed a Rg of 45 ± 0.8 Å (Figure R51-B). The Rg did not show dependence on the concentration and only with the most concentrated curve is it possible to appreciate a slight increase of the Rg. The Rg value calculated by Guinier was very similar to the Rg of 49 ± 1 Å determined in the calculation of the P(r) using data covering a range of the scattering vector from 0.012 to 0.222 $Å^{-1}$. The P(r) presented a maximum at small distances with a tail extending up to a Dmax of ~165 Å. This shape is characteristic of elongated molecules (Figure R51-C). The dimensionless Kratky representation of the scattering data showed a maximum of ~2.2 at q*Rg ~5 (Figure R51-D), which is displaced from the expected maximum for globular compact particles (~1.1 at q*Rg ~1.73). This deviation suggested a high anisometric structure, in agreement with the shape of the P(r) function.

The apparent molecular weight of this fragment calculated from the Porod volume (Vp/1.6; Petoukhov et al., 2012; Rambo & Tainer, 2011) was 42.3 kDa, which is similar to the molecular mass calculated from its sequence (46772 Da). Thus, the region SR7-

SR9 of DP in solution is a monomer and does not oligomerize. This result contrasts with the results obtained by co-IP experiments and suggests that N-terminal segment of the rod domain, region 1025-1056, is not sufficient to promote DP homo-association *in vitro*.

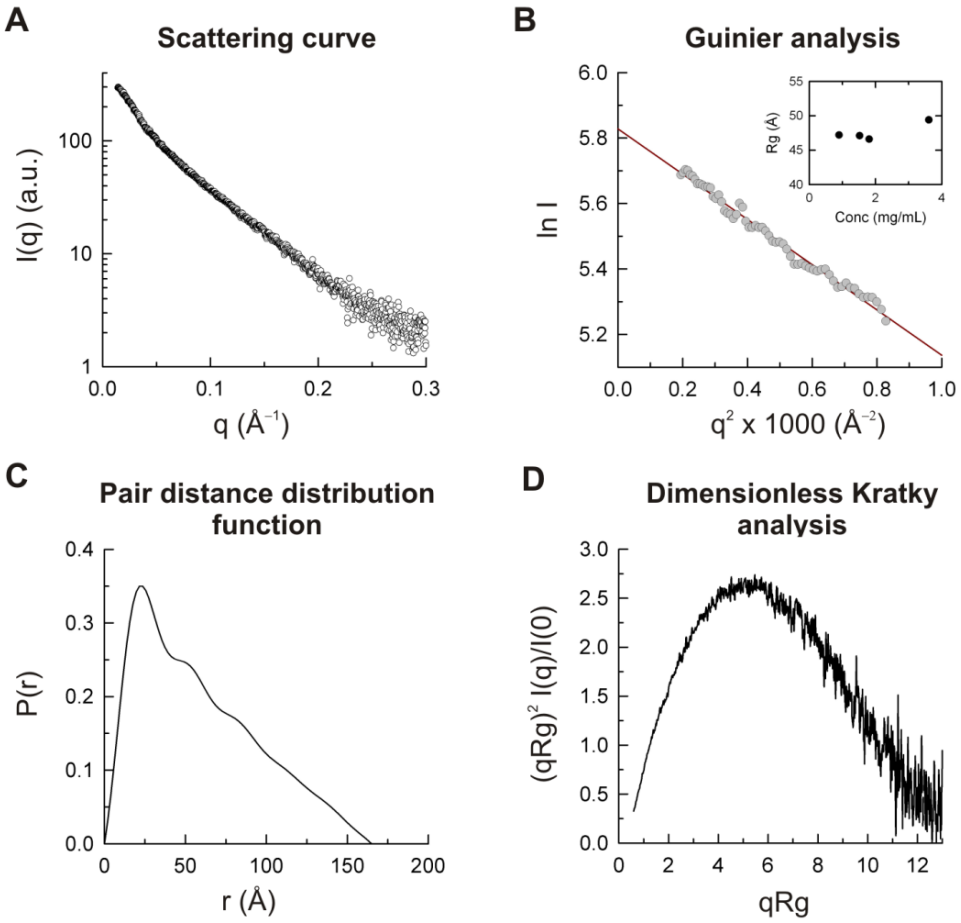

Figure R51. SAXS analysis of the C-terminal region of DP-PD. A) Scattering profile of the SR7-SR9 region, residues 660-1056. **B)** Guinier analysis of the scattering curve shown in A. In the insert is represented the Rg determined by Guinier´s analysis at every concentration. The Rg and I_0 calculated by the Guinier analysis are 45 ± 0.8 Å and 338, respectively. **C)** Pair-distance distribution curve estimated from the SAXS data using the program GNOM. The Rg and Dmax calculated by the GNOM analysis are 48.7 ± 0.3 Å and 165, respectively. **D)** Dimensionless Kratky plot of the DP-SR7-SR9 scattering data showing a displacement of the maximum of the plot towards high levels of q*Rg.

By similarity with the crystal structure of the SR7-SR9 of plectin, this region of DP forms a continuous tandem array of SRs, where the C-terminal helix of the SR9 is predicted to be fused to the helix of the rod domain. Therefore, this fragment is expected to have only very small conformational variability. Thus, we calculated low-resolution structures from the scattering data using *ab initio* methods implemented in DAMMIF. We made 14 independent reconstructions that were very similar to each other (Figure R52-A), having a NSD of 0.78 ± 0.03. After averaging the 14 models, the

resulting envelope, which represents the most probable volume occupied by the model, resembles a slightly bent rod-like shape. An atomic model of the SR7-SR9 of DP was built by homology modelling using the crystal structure of the equivalent region of plectin as template. The atomic model fitted inside the SAXS average envelope with the exception of the final part of the C-terminal helix (Figure R52-B). The theoretical scattering profile calculated from the atomic model showed a good fit to the experimental data (Figure R52-C) and, similarly, the P(r) calculated from the 3D coordinates reproduced the SAXS-derived P(r) pair distance distribution function (Figure R52-D). Finally, the dimensionless Kratky representation of the calculated scattering data matched the experimental curve (Figure R52-E), suggesting that the deviation in the position of the maximum with respect to compact and spherical particles was due to the elongated shape of the SR7-SR9 and probably was not caused by flexibility in this fragment. In summary, the analysis of SAXS data of the SR7-SR9 (660-1056) of DP indicates that *in vitro* this region is a monomeric rod-like structure.

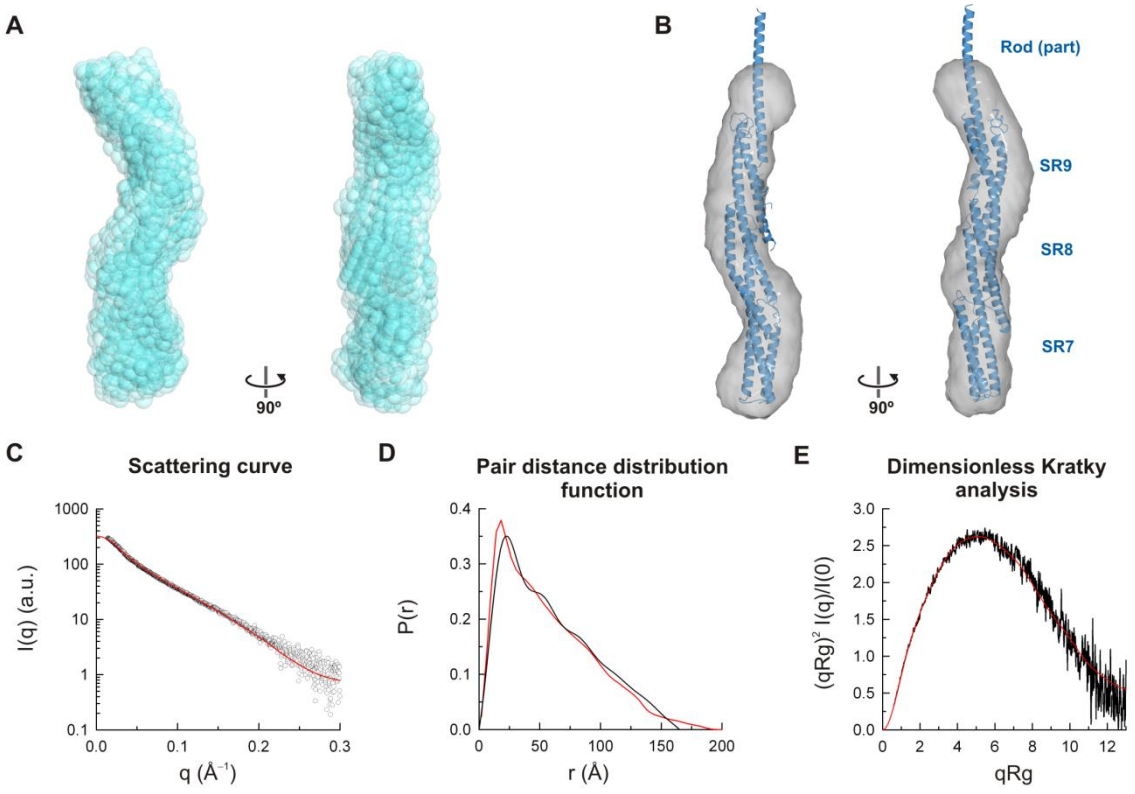

Figure R52. Low-resolution models of the SR7-SR9 region of DP-PD. A) *Ab initio* reconstructions of the structure of the 660-1056 fragment of DP from the SAXS data with the program DAMMIF. Fourteen models are shown after superimposition. The models consist of dummy atoms that are shown as semi-transparent spheres. **B)** Homology model of the atomic structure of this region (shown in ribbon representation) docked into the molecular envelope calculated as the average of the fourteen DAMMIF models (grey surface). **C)** Experimental scattering profile of the SR7-SR9 region (circles) and fit of the

theoretical profile calculated for the atomic model (red line) **D)** Comparison of the P(r) distribution functions estimated from the experimental data (black line) and that determined for the atomic model (red line). **D)** Dimensionless Kratky plot of the experimental (black line) and theoretical (red line) scattering data.

Structure of the SR7-SR9 region of DP-PD, dimeric state

Since the DP-CT (region 660-1056) did not dimerize in solution but it is well established that DP and other plakins form dimers via coiled-coil interactions of the rod domain, we stabilized the homo-dimerization by adding a leucine zipper of the yeast transcriptional activator GCN4 at the C-terminus. The segment 249-281 of GCN4 (hereafter referred as GCN4) forms an extensively characterized homo-dimeric parallel coiled coil (O'Shea et al. 1991). Similarly to other amphipathic helices, the coiled coil sequences show a 7-residues repetition, termed heptads, in which the positions *a* and *d* are most frequently occupied by hydrophobic residues that mediate inter-chain contacts. A DP-CT-GCN4 fusion protein was design in such a way that the predicted heptad repeats of the DP sequence were in frame with the GCN4 heptad (Figure R53).

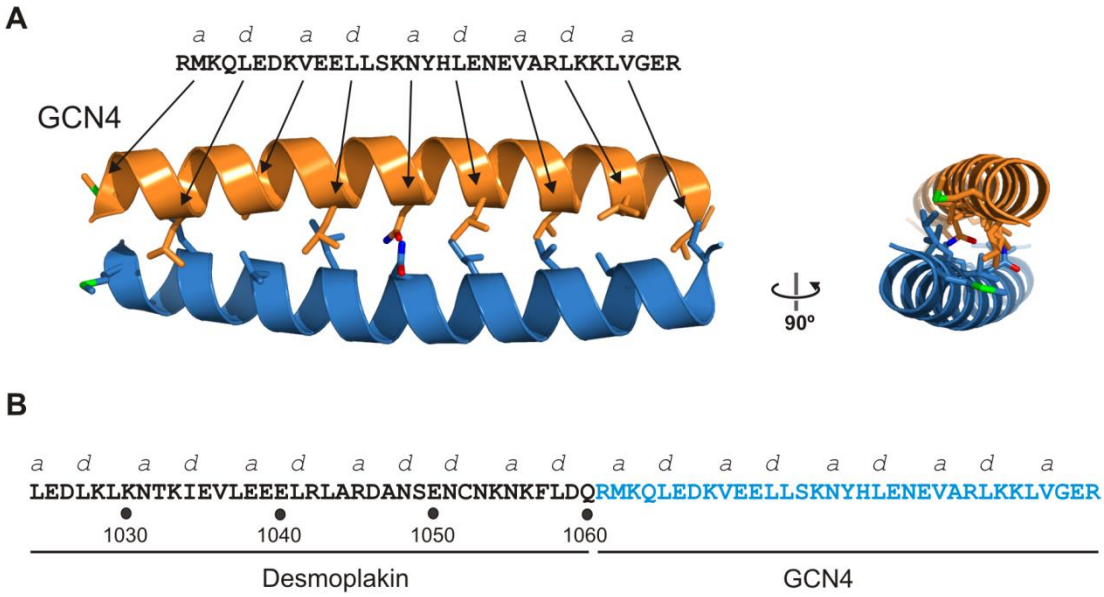

Figure R53. Design of the DP-GCN4 fusion protein. A) Ribbon representation of the crystallographic structure of the GCN4 homo-dimer (PDB entry 2ZTA). The side chains of the residues that occupy the *a* and *d* positions of the heptad repeats are shown as sticks. The GCN4 sequence is shown on top. **B)** Region where the DP and the GCN4 sequences are fused in the DP-CT-GCN4 construct. The *a* and *d* positions of the heptads are labelled on top. For the DP sequence the heptads were assigned with the program PAIRCOIL2 (McDonnell et al. 2006).

The structure of DP-CT-GCN4 (DP region 660-1060) was analysed by SAXS. Scattering profiles were measured at three different concentrations between 3.56 and 0.89 mg/mL. No radiation damage was observed. After buffer subtraction and

normalization by the concentration, the resultant scattering profile was extrapolated to infinite dilution (Figure R54-A). The molecular mass estimated from the Porod volume (Vp ~190000 Å^3) was ~119 kD, which is approximately twice the theoretical molecular weight of DP-CT-GCN4 (51.2 kD) indicating that the GCN4 effectively stabilizes the homo-dimer. Guinier analysis of the scattering curves at different concentrations showed a slight dependence at high concentration. The Rg calculated by Guinier analysis of the data extrapolated at infinite dilution was 61 ± 1 Å (Figure R54-B). The calculation of the P(r) yielded a similar Rg of 66 Å and a Dmax of ~245 Å (Figure R54-C). The dimensionless Kratky representation of the scattering data showed a maximum at ~5 qRg that is in agreement with the position of the maxima observed for other elongated DP fragments (Figure R54-D).

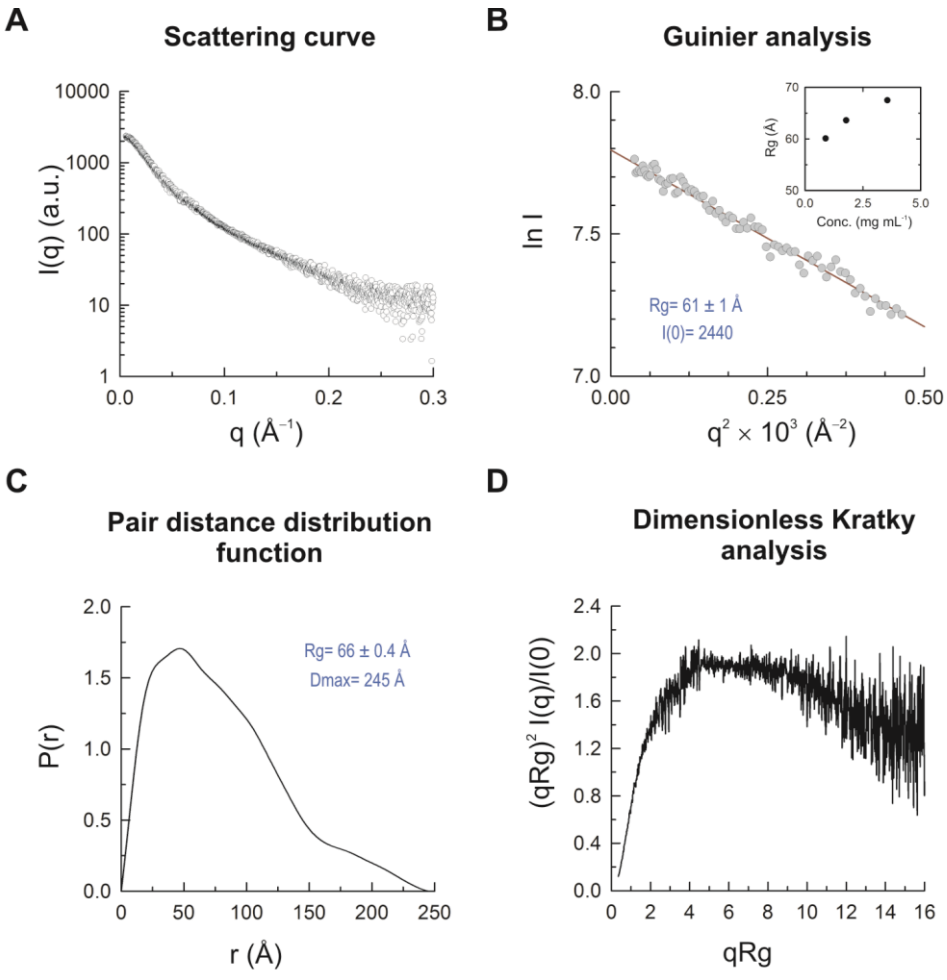

Figure R54. SAXS analysis of a dimeric fragment of the C-terminal region of DP-PD. A) Scattering profile extrapolated to infinite dilution of the dimeric SR7-SR9-GCN4 region, residues 660-1060 fused to GCN4. **B)** Guinier analysis of the scattering curve shown in A. The Rg and I_0 calculated by the Guinier analysis are 61 ± 1 Å and 2440, respectively. The Rg determined by Guinier´s analysis at each individual concentration is shown in the insert. **C)** Pair-distance distribution function, P(r), estimated from the SAXS

data using the program GNOM. The Rg and Dmax calculated by the GNOM analysis are 66 ± 0.4 Å and 245, respectively. **D)** Dimensionless Kratky analysis of the dimeric DP-SR7-SR9-GCN4 scattering data.

Next, we calculated low-resolution structures from the scattering data using *ab initio* methods implemented in DAMMIF. Since the coiled coil was expected to induce a two-fold symmetric arrangement of the protomers, P2 symmetry was imposed for the generation of the *ab initio* reconstructions. Ten independent reconstructions were made and the most probable volume was calculated by averaging all these structures (Figure R55-A). The structure has an overall elongated and flat structure being narrow towards one of the longitudinal ends with an overall dimensions of approximately 240 Å x 105 Å x 45 Å.

In addition, we created a composite atomic model of DP-CT-GCN4 as follows. The SR7-SR9 region was modelled by homology using the structure of the equivalent region of plectin as template. The arrangement of the two protomers in the dimer was taken from the organization of the plectin dimer in the crystal lattice, in which the two copies of the SR7-SR9 lay parallel possibly establishing lateral contacts along the three SR sub-domains. The segment of the rod domain was modelled using a crystal structure of a tropomyosin dimeric fragment (PDB entry 1IC2) (Brown et al. 2001). The GCN4 dimer was modelled using its crystal structure (PDB code 2ZTA). There is a good overall agreement between the composite atomic model and the *ab initio* envelope (Figure R55-B). Despite the P(r) of the atomic model reproduces the features of the experimental P(r), comparison of the theoretical scattering profile with the experimental SAXS data revealed differences (also observed in the dimensionless Kratky representation of the data) (Figure R55-D-E). In summary, the analysis of the SAXS data from DP-CT-GCN4 is compatible with a close arrangement of the DP dimer in which inter-protomer contacts extend through the last three SR of the plakin domain. Nonetheless, the specific arrangement of the two DP molecules might be slightly different from that observed in the plectin crystal structure.

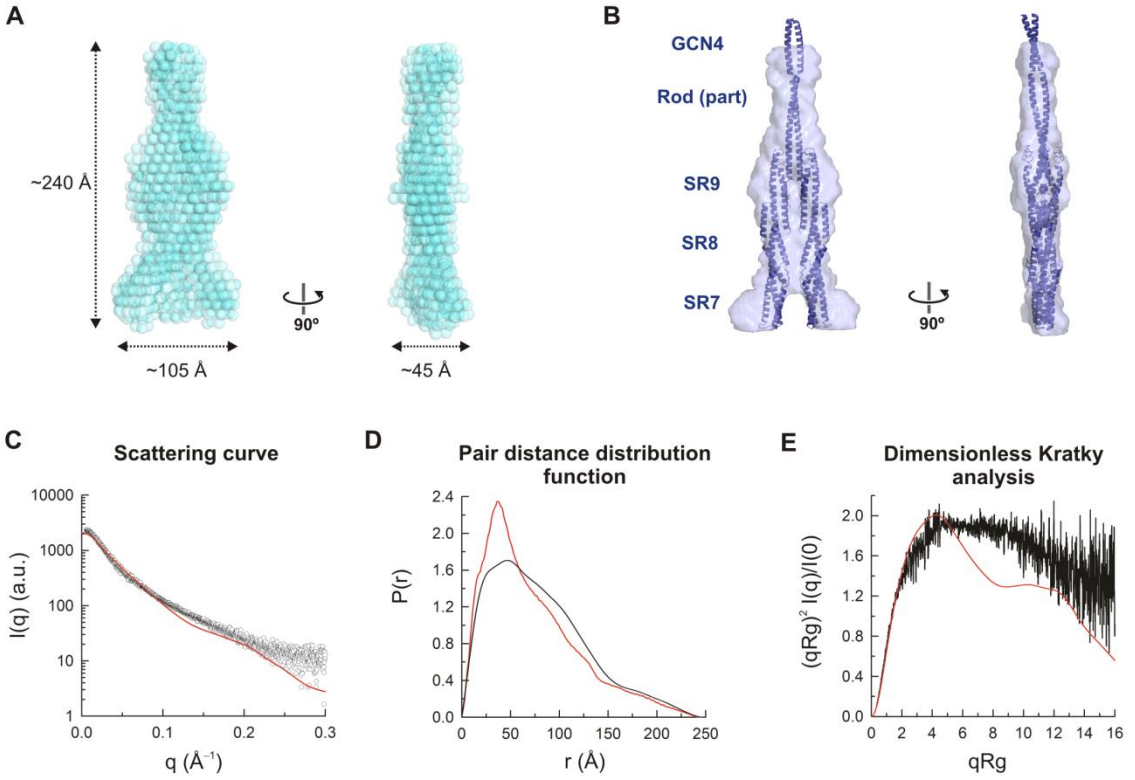

Figure R55. Low-resolution models of the SR7-SR9 region of DP-PD. A) A*b initio* reconstructions of the structure from the SAXS data of DP-CT-GCN4 generated with the program DAMMIF, shown after superimposition. The models consist of dummy atoms that are shown as semi-transparent spheres. **B)** Surface representation of the *ab initio* molecular envelope that corresponds to the average of ten reconstructions. The composite atomic model is shown in ribbon representation after docking into the low resolution structure. **C)** Scattering profile of the dimeric SR7-SR9 region, residues 660-1060 and GNC4, (circles) and fit of the theoretical curve calculated from the atomic model (red line). **D)** Pair-distance distribution function, P(r), estimated from the experimental SAXS data (black line) and that calculated from the 3D structure of the atomic model (red line). **E)** Dimensionless Kratky representation of the experimental and theoretical scattering data shown in B.

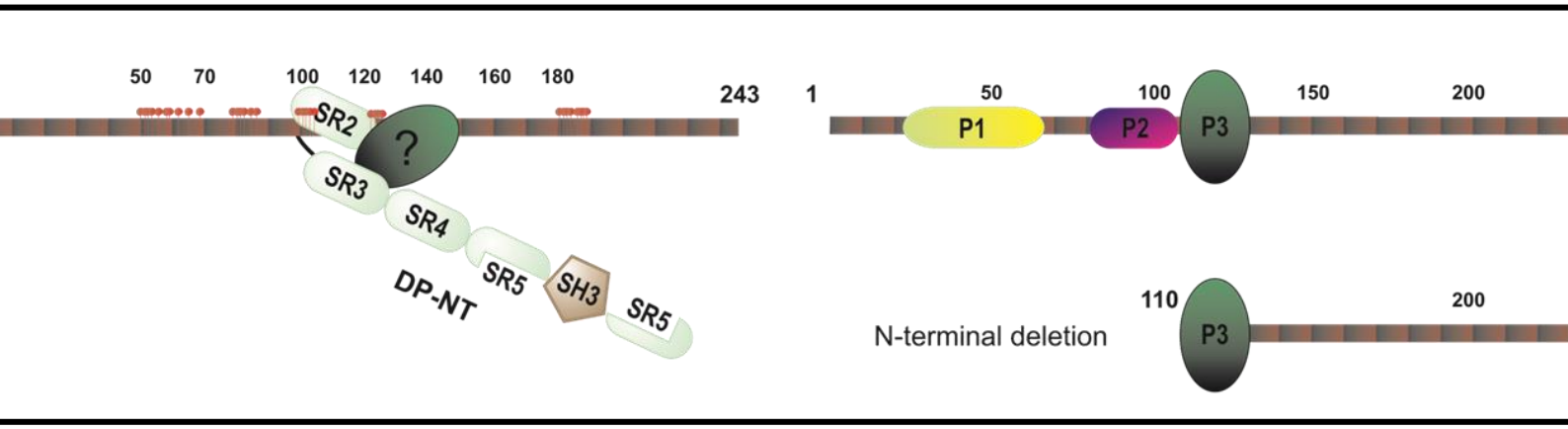

Chapter 5

DISCUSSION

Mapping of the interacting domains in the DP-PKP1a complex

Despite the study of the desmosomal architecture extends back beyond a century and there is a conventional understanding of the intra-desmosomal protein interactions, the precise protein-protein relationships that orchestrate fully functional DMs are still not completely understood. Knowing how desmosomal proteins are connected is fundamental to understanding how cells maintain their shape and polarity, regulate movement, adhesive potential, and strength, or mechanotransduce signals originated at junctional complexes.

Previous studies had established four types of interactions between desmosomal proteins: i) desmosomal cadherins binding their peers on adjacent cells, ii) plaque proteins binding the cytosolic tails of cadherins at the inner dense plaque, iii) plaque proteins binging other plaque proteins, and iv) plaque proteins binding intermediate filaments (IFs) at the outer dense plaque. In this study, we focused on the DP-PKP1a interaction, which takes place between these two plaque proteins at the inner dense plaque. We report a precise mapping of the interacting domains in the DP-PKP1a complex. By using a multi-methodological approach, we have narrowed the molecular definition of the DP-PKP1a recognition sites in both molecules.

Unravelling the PKP1-binding site in DP

The interaction between endogenous DP and PKP1 had been demonstrated in keratinocytes by immunoprecipitation (IP) and sucrose gradient centrifugation (Hofmann, Mertens, et al. 2000). IP experiments in different cells lines and yeast two hybrid assays working with fusion proteins limited the PKP1-binding site to the N-terminal half of the plakin domain of DP (region 1-584) (Hatzfeld et al. 2000; Kowalczyk et al. 1999; Bornslaeger et al. 2001). Most of the studies that, directly or indirectly, analysed the association of DP with PKP1 or other desmosomal proteins, such as co-localization and recruitment assays or DMs assembly experiments, considered the N-terminal region of DP as a functional unit (Kowalczyk et al. 1997; Kowalczyk et al. 1998; Godsel et al. 2005; Chen et al. 2002). Yet, a precise mapping of the domains of DP that mediate the interaction with other desmosomal proteins, and particularly with PKP1, was still missing. The recent elucidation of the 3D structure of fragments of the PD of DP and other plakins paved the way for a more precise analysis of the interaction sites.

PKP1a interacts with the N-terminal half of the PD of DP

We created an extensive collection of fragments of the PD of DP and assayed their interaction with PKP1a by using three complementary approaches. First, we looked for biochemical data by doing co-immunoprecitations (co-IP) of HA-tagged DP fragments using PKP1-FLAG as bait with agarose anti-FLAG beads. Second, we used fluorescence lifetime imaging microscopy (FLIM) to analyse the interaction. Finally, we compared the subcellular distribution and behaviour of PKP1a and DP fragments in DM-bearing and non-bearing cell lines.

Initially, we assayed the interaction between PKP1a and both halves of the DP-PD. Based on the crystal structure of the SR3-SR6 domain of DP (Choi & Weis 2011), we modified the boundaries of the previously reported DP N-terminal fragment (residues 1-584) and chose the limits 1-545 to match the end of the SR5. Thus, our DP-NT fragment comprises the N-terminal tail and the SR2-SR5 domains. The complementary DP-CT fragment (544-1056) comprises the SR6-SR9 domains and includes an initial segment of the rod domain (~1026-1056).

Surprisingly, our co-IP results showed that, in addition to the complete N-terminal half of DP (SR2-SR5 domains), the non-overlapping C-terminal fragment corresponding to the SR6-SR9 domains (DP-CT) also interacted with PKP1a, suggesting the existence of two PKP1-binding sites within the DP-PD, each located on one half of the plakin domain (Figure R1). Nonetheless, when we analysed the interaction between PKP1a and DP-fragments by using constructs tagged with fluorescent proteins in combination with FLIM, we did not observe association between the C-terminal half of DP-PD and PKP1a (Figures R2 and R3).

Trying to understand such discrepancy, we moved the Venus-tag from the N- to the C-terminus of the DP fragments to rule out the possibility that the lack of FRET observed between DP-CT and PKP1a may have been due to a distance between the CFP-Venus pair in the putative complex larger than the Förster distance. Yet, independently of the position of the Venus tag, we did not detect interaction of DP-CT-Venus with PKP1a-CFP (Figure R4).

The reason for the observed co-immunoprecipitation of DP-CT-HA with PKP1-FLAG is unclear. We can exclude an unspecific interaction with the anti-FLAG M2-resin, since DP-CT-FLAG did not co-immunoprecipitate in the control samples without PKP1-FLAG. It has been described that nucleic acids present in the input cell lysates can mediate indirect binding in co-IP experiments, resulting in false positives (Nguyen & Goodrich 2006). This hypothesis is interesting because PKP1a has been described to interact

with single stranded DNA (Sobolik-Delmaire et al. 2010). Nonetheless, DP-CP is unlikely to associate to PKP1a via nucleic acids; the DP-CT is a slightly acidic protein (the theoretical isoelectric point, pI, is ~6.5, similar to the pI ~6.1 of the DP-NT fragment), and it has not been described its association with nucleic acids.

During FLIM experiments we noticed that Venus-tagged DP-NT (region 1-545) and DP-CT (region 544-1056) fragments showed clearly different subcellular localizations in COS-7 cells. To further study this differential behaviour we looked at the subcellular localization of these fragments by confocal microscopy (Figures R5 and R6).

In COS-7 cells the complete plakin domain of DP (DP-PD, region 1-1056) appeared diffusely distributed throughout the cytoplasm, but also decorated the plasma membrane. It is known that DP-PD targets DP to the plasma membrane where, when DP is incorporated into DMs, typically shows a fine and regularly spaced punctate pattern (Bornslaeger et al. 1996; Smith & Fuchs 1998; Godsel et al. 2005). However, our DP-PD fragment was present in extensive stretches at cell-cell borders as if dots were stitched together. This kind of pattern had been reported before in non-bearing DMs cell lines (Kowalczyk et al. 1997) or in cells with high expression of the fusion fragments (Bornslaeger et al. 2001; Hatzfeld et al. 2000).

DP-NT (region 1-545) showed two different distributions in transfected cells. In some cells, DP-NT showed a similar distribution with respect to the full plakin domain (DP-PD). On the contrary, other cells showed an aberrant distribution with DP-NT located only in prominent cytoplasmic aggregates. We hypothesized whether it could be newly synthesized protein that is in the endoplasmic reticulum and Golgi complex and is in the process of being transported to the plasma membrane. Yet, these aggregates were not positive for markers of lysosomes or the Golgi complex, nor co-localize with the recycling endosome marker Rab11 (data not shown). Thus, although the nature of these clusters is unclear we thought that most likely they are a drawback of the overexpression and we ruled out cells with this characteristic expression pattern for subsequent experiments.

DP-CT (region 544-1056) was clearly distributed over the plasma membrane, being excluded from the cytoplasm and nucleus.

Taken together, our results show a clear domain dependence in the subcellular distribution of the PD of DP. Based on the differences in the subcellular distribution of these fragments, it seems that the C-terminal half of the PD of DP is needed to retain the fully functional properties of the plakin domain. On the one hand, the N-terminal half of the PD harbours binding sites for the association with other desmosomal

proteins. Yet, the isolated DP-NT region apparently lacks some regulatory or stabilizing elements that presumably lie on the C-terminal half of the PD, resulting in an aberrant subcellular distribution in some cells when it is ectopically expressed. On the other hand, the membrane-targeting observed with the isolated C-terminal half apparently reflects a non-physiological behaviour, because this region does not recruit the complete PD to the plasma membrane to a similar extent. The PD of DP adopts a mostly extended structure in which the two halves do not make contact (Al-Jassar et al. 2011); therefore, it is unlikely that, in the complete PD, the N-terminal half could be masking a putative membrane targeting site in the C-terminal half. In addition, no membrane targeting motif has been described in the C-terminal half of the PD. Finally, the plasma membrane decoration of the DP-CT does not imply that this fragment was assembling new DMs or participating from DMs previously established.

As a third method to evaluate the interaction between DP and PKP1a, we analysed the ability of PKP1a to relocate DP fragments. Assays where ectopically expressed proteins are targeted to specific cellular organelles to study the relocation of binding partners have been extensively used to demonstrate protein-protein interactions. A recent example with a close related protein is shown by Munoz et al. (2014), who targeted PKP3 to the mitochondrial outer membrane (MOM) and showed that it recruits the transcription factor ETV1.

In COS-7 cells, ectopically expressed PKP1a-CFP showed an exclusively nuclear staining. This subcellular distribution had been previously reported in various cell types (Hatzfeld et al. 2000; Schmidt et al. 1997; Sobolik-Delmaire et al. 2010) being the expected in cell types not containing prominent DMs, such as COS cells. Interestingly, when DP-fragments were co-expressed with PKP1a, DP-PD and DP-NT were recruited to the nucleus, independently of the tag (Figures R7 and R8). This phenomenon was also reported by others (Hatzfeld et al. 2000) and strongly supports a bona fide interaction between PKP1a and the N-terminal half of the DP-PD observed with the others methods. On the other hand, PKP1a failed to recruit DP-CT to the nucleus, further supporting the lack of specific interaction between them.

We wondered whether these results would be reproducible in DM-bearing cell lines. Thus, we performed similar experiments in keratinocytes cell lines (Figures R9 and R10). The main difference in the subcellular distribution of the analysed proteins between COS and keratinocytes was observed for PKP1a. In keratinocytes growing in differentiation conditions (high calcium concentration), in addition to the nucleus, PKP1a was enriched laterally at cell-cell contact sites, as expected due to the formation of DMs. When the complete plakin domain (DP-PD) or the N-terminal half

(DP-NT) were co-expressed with PKP1a, both were co-imported to the nucleus and plasma membrane. Again, DP-CT did not change its distribution after PKP1a co-expression.

In summary, we have established a multi-methodological experimental approach that combines co-IP, FLIM, and co-localization analysis in COS cells and keratinocytes to study the interaction between DP and PKP1a. Collectively, our data confirmed that DP interacts with PKP1a through the N-terminal half of the plakin domain. Our results also revealed that DP and PKP1a are closer than 10 nm when they interact with each other, suggesting a direct binding. Furthermore, such interaction does not require the formation of DMs.

Mapping of the PKP1a-binding site in DP-NT, role of the SR2-like domain

Once the interaction between PKP1a and the N-terminal half of the DP-PD was confirmed, we applied our experimental approach to further map the PKP1a-binding site within this region of DP. For this purpose, we made several constructs of DP and assayed their interaction with PKP1a. By co-IP, we dismissed the need for the SR6 and the SR5(SH3) regions of DP to associate with PKP1a. The N-terminal first 63 residues that precede the SR2 are not required for the interaction with PKP1a, either. However, removing the SR2 compromised the association with PKP1 in co-IP assays. These results indicate that the SR2-like domain of DP-PD is necessary for the interaction with PKP1a. Moreover, a HA-tagged construct containing the SR2-like domain and the preceding N-terminal sequence, region 1-170 (DP-SR2), interacted with PKP1-FLAG to a similar extent than the DP-NT fragment. This supports that the SR2-like domain of DP is sufficient to mediate the interaction with PKP1a, and constitutes a major interaction site (Figures R11 and R12).

The important role of the SR2 in the interaction with PKP1a was further validated by using FLIM (Figure R13). FLIM results were in complete accordance with the biochemical data of the co-IP assays. Summarizing, Venus-tagged DP-PD and DP-NT produced a severely decrease in the CFP lifetime of PKP1-CFP, due to the proximity of the two fluorescent proteins. The effect of DP-Venus over the CFP lifetime of PKP1-CFP was abolished or highly reduced when we eliminated the SR2 segment, suggesting that this region directly participates in the interaction DP-PKP1a. Lastly, the SR2-like domain of DP was sufficient to interact with PKP1a in our FLIM assays, similarly as observed in co-IP experiments. Interestingly, both methods suggested that the region SR3-SR5 might have an accessory contribution to the interaction with PKP1a.

To complement the analysis of the DP-PKP1a interaction, we investigated by confocal microscopy the subcellular distribution of fragments of the N-terminal half of the plakin domain of DP and their co-localization with PKP1a. We used the nuclear recruitment or enrichment of DP fragments as an indication of the interaction with PKP1a. In single transfections, N-terminal fragments of DP showed a diffuse distribution throughout the cell. In addition, likely due to the high level of expression of these small fragments, it was also possible to appreciate some nuclear staining in specific cases. In the presence of PKP1a, a nuclear enrichment of the DP fragments DP-SR2 (1-170) and DP-1-SR4 (1-376) was observed compared to the distribution showed when they were expressed alone. Interestingly, the construct DP-SR3-SR5 showed a dual pattern when co-expressed with PKP1-CFP. In some cells, DP-SR3-SR5 was not recruited to the nucleus by PKP1a. Yet, in other cells DP-SR3-SR5 was clearly enriched in the nucleus where it co-localized with PKP1a. This dual behaviour could be explained if the interaction between DP-SR3-SR5 and PKP1a had only moderate or weak affinity, so that small differences in the expression levels could result in large differences in the association, not always being possible to detect it (Figures R15 and R16).

A preceding study had also tried to narrow the PKP1-binding site in DP (Smith & Fuchs 1998). These authors had identified the first 176 residues of the DP-PD as a region containing a desmosome-recognition site. They addressed the ability of this segment of DP to associate with other desmosomal components by using overlay assays. They concluded that the first 176 residues of DP interact with the DSC1a cytoplasmic tail, DP itself, PKP1, as well as PKG, though weakly. Mapping the PKP1a interaction site in DP was not the scope of these authors, so they did not make an exhaustive analysis and did not prove the interaction of PKP1 with more fragments of DP-PD. Nevertheless, our results are in agreement with those findings. Interestingly, Smith and Fuchs located the desmosomal recognition site in the segment 86-176 of DP, which roughly corresponds to the SR2-like domain (residues 64-164) that we have shown to be a key element of the interaction with PKP1a.

The location of the PKP1a-interaction region near the N-terminus of DP is reminiscent of the location of protein-binding sites in other plakins. For example, the N-terminal actin binding domain of plectin binds to multiple proteins including the integrin α6β4, nesptin-3α, actin, and calmodulin (reviewed in Castañón et al. 2013). Furthermore, the integrin β4 binding site in the epithelial variant of BPAG1 (BPAG1e) has been mapped to the first 92 residues (Koster et al. 2002). Despite internal regions of the plakin domain also mediate protein interactions, the frequent location of binding sites near the N-terminus suggest that these regions might have evolved to support specific

functions, while the SR3-SR9 region of the plakin domain, which shown a lower modular variability, might have a predominant structural role.

Interestingly, the binding site for p0071 had also been mapped within the plakin domain of DP (Setzer et al. 2004). Like PKPs, p0071 is a member of the p120-catenin subfamily. p0071 normally localises to AJs but it is also able to associate with DMs through interactions with the PD of DP (Keil et al. 2013; Calkins et al. 2003). The dual localization of p0071 in actin- and IF-attached junctions raises the possibility that p0071 plays a role in the mutual regulation of DMs and AJs. In fact, it has been shown that overexpression of p0071 affects the balance between desmosomal and AJs adhesion. Interestingly, this function is specific for p0071 and it is not shared with close related proteins (Setzer et al. 2004).

The mechanisms by which p0071 promotes AJs formation at the expense of DMs assembly are not understood. Previous reports had shown that p0071 interacts with classical cadherins by means of its ARM-domain, whereas its head domain is able to interact with desmosomal proteins such as DP or PKG (Calkins et al. 2003; Hatzfeld 2003). Using yeast two-hybrid assays, Calkin et al found that a small N-terminal fragment of DP, residues 1-160, was sufficient to interact with p0071, whereas the region 160-584 did not interact (Calkins et al. 2003).

When p0071 associates with DMs it binds to the first 160 residues of DP, exactly the same region that we have identified as the main PKP1a-binding site in DP. Taking into account that the function of p0071 is in striking contrast to the role of PKP1; it might be possible that p0071 and PKP1a bind to DP in a mutually exclusive manner. This would shift the balance between the formation of DMs and AJs depending on p0071 interactions. Thus, the overlapping of binding regions might be considered as a regulatory mechanism that contributes to the cross-talking between junctions.

Our model combines three different sources of information: i) preceding observations that demonstrated that p0071 has a key role in regulation the balance between DMs and AJs, ii) previous work on the interactions between p120-catenin family proteins and cadherins, and iii) our mapping of the interaction between DP and PKP1a. We hypothesize that when the DMs formation is somehow negatively regulated, p0071 binds the N-terminal region of DP displacing or preventing the formation of the PKP1a-DP complex. In such scenario, the balance between junctions would favour the AJs, where p120-catenin would be attached to classical cadherins. However, since PKP1a is a key determinant in the assembly of DMs, and it recruits DP to cell-cell contacts sites and promotes lateral associations between desmosomal cadherins and desmosomal plaque proteins; when DMs assembly is required, PKP1a-DP complex

formation would be favoured at expense of the DP-p0071 binding. The release of p0071 from the complex with DP might also regulate the p120-catening/cadherins interactions at the AJs. Data currently available are compatible with this model but further investigation is required to assess whether p0071 and PKP1 actually compete for the binding to DP and to fully understand the role of the simultaneous stabilization of some interactions and inhibition of others in the interplay and cross-talking between DMs and AJs.

Regarding to the possible regulation of junctions by mutually exclusive binding sites, the different interaction of DP mutants with PKP1 and PKG is of interest. Mutations in DP, among other desmosomal proteins, cause ARVC, a complex myocardial disorder associated with right-sided cardiomyopathy and arrhythmia, and characterized by gradual loss of myocytes and replacement by fatty and fibrous tissue (Corrado et al. 1997). The ARVC-linked mutation Q90R lies in the region that we have identified as the main PKP1a-binding site in DP. Yet, this mutation does not compromise the interaction between PKP1a and DP (data not shown). On the other hand, the mutation Q90R affects the interaction of DP with PKG (Yang et al. 2006). Similarly, the DP mutation V30M also abolishes the interaction between DP and PKG, but has not effect over the PKP1-DP interaction (Yang et al. 2006). In addition, Calkins et al. (2003) had showed that PKG is able to interac with different fragments of the N-terminal region of DP, such as, DP-1-160 (residues 1-160) and DP-160-584 (residues 160-584). These results suggest that, contrary to the case of p0071 and PKP1, PKG and PKP1 do not interact with DP by the same region or at least not in an exclusive manner. Apparently, the PKG-binding site in DP involves a more extended region than that of PKP1a. This might be related with the fact that PKG interacts with DP by means of its ARM-domain, whereas PKP1a does by means of its N-terminal head domain. Finally, the fact that both ARM-proteins may interact simultaneously with DP is in agreement with their function at the DMs, since PKG and PKP1 have an additive effect in cellular adhesion strengthen.

Structure of the SR2-like domain of DP

Ironically, from a structural point of view the existence of the SR2 domain of DP, which apparently mediates important functions in the interaction with ARM-proteins, had been controversial to date. Based on sequence conservation the plakin domain of DP had been predicted to have seven spectrin repeats (SR3-SR9) and a SH3 (Al-Jassar et al. 2011; Sonnenberg et al. 2007). The organization of the SR3-SR6 region was unveiled by the crystal structure (Choi & Weis 2011). On the other hand, the sequence upstream

of the SR3 (region 1-179) has been proposed to be unstructured (Al-Jassar et al. 2011; Choi & Weis 2011).

In order to investigate the possible presence of a SR or SR-like domain in DP upstream of the SR3, we analysed several PD sequences by using profile hidden Markov models (HMM profiles). Using as template the bona fide SR2 domains of plectin, BPAG1, MACF1, periplakin, and envoplakin our profile-based search did not identify any canonical SR2 domain in DP. However, HMM profiles generated by using the sequences of all the SR domains of mammalian plakins, with the exception of the SR6s because of their divergent structure (Sonnenberg et al. 2007; Choi & Weis 2011), identified a region upstream of the SR3 (residues 65-157), which have at least a weak SR signature. It should be noted that the level of sequence identity and similarity between different repeats is rather low and, apparently, the structural homology between them is sustained by few conserved residues (Choi & Weis 2011). Furthermore, the SR2 domain of other plakins, such as plectin, lacks some of the structural features of the canonical SRs (Sonnenberg et al. 2007).

In any case, since the statistical significance of the SR2-like fell in a doubtful zone, we further scrutinized this region in search for other SR-like signatures. First, sequence-based secondary structure predictions made with two independent methods suggested the presence of three helices in the region 65-156 (Figure R42-A). Moreover, the limits of the three predicted helices in DP match the position of the three α-helices of the SR2 of plectin in sequence alignments (Figure R42-B). These predicted helices have amphipathic character. Hydrophobic residues cluster on one side of the helix and occupy the first and fourth positions in the helical heptad repeat (positions *a* and *d*), while polar groups are more frequent in the opposite side. The predicted short loops that connect the helices suggest that the helices in the region 65-156 of DP pack in a helical bundle, compatible with a SR like fold.

Next, we synthesised in *E. coli*, purified, and characterized by biophysical methods two constructs of the putative SR2 of DP with different lengths: DP-SR2-S-pET (region 64-155) and DP-SR2-L-pET (region 64-164). Far-UV CD analysis revealed that both fragments have almost equal secondary structure. Based on the CD spectra they have a major content of α-helical structure, estimated between 68 and 83 %, with marginal presence of β-sheet content. This high α-helical content is compatible with a SR fold (Figure R43).

To shed light on the structural organization of the SR2-like domain, we analysed the thermal stability of the DP-SR2-L and DP-SR2-S fragments by using CD and Thermofluor. By CD both proteins showed sigmoidal denaturation profiles that revealed

cooperative transitions similar to those observed during the denaturation of folded and well-ordered structures (Figure R44). In fact, the denaturation curves could be analysed using a two-state transition from a folded to an unfolded state, which fitted the experimental data. The Tm of the short (64-155) and the long (64-164) constructs were ~61 °C and ~74 °C, respectively. These fragments are more thermostable than the fragments SR4-SR6, SR7-SR8, and SR8-CT of DP, that have reported Tm of 50, 60, and 52 °C, respectively (Al-Jassar et al. 2011). The higher thermal stability of the 64-164 fragment with respect to the 64-155 was confirmed using Thermofluor assays, in which the Tm of the DP-SR2-L and DP-SR2-S at neutral pH were ~66 °C and ~55 °C, respectively.

The large difference between the Tm of the short and long constructs of the putative SR2-like domain was striking (~13 °C in the CD melting curves), and revealed that the 156-164 greatly contributes to the stability of the SR2. The secondary structure predictions suggest that this final stretch is not helical; yet, it could be possible that the 156-164 segment would stabilize the final turns of helix C. Alternatively, the 156-164 could act as a cap that tights the helical bundle via electrostatic interactions. This segment contains a patch of three basic residues R160, R162, and R163, which could interact with an electronegative area that includes acidic residues at the C-terminus of helix A (E86 and E92) and the N-terminus of helix B (E106 and E109). Interestingly, we did not observed changes in the Tm of this fragment in a range of pH between 6.0 and 8.0. This is compatible with a predicted stable protonation state of Glu and Arg within this range of pH.

We have obtained evidences supporting that the region 64-164 of DP forms a helical bundle, probably very similar to other SRs. The very low similarity with the SR2 domains of other plakins suggests that this region of DP might have a different origin than other SR2 domains or that it has evolved in a divergent way from them. In summary, we consider the DP-PD having eight SRs (SR2-SR9). The SR2-SR3 domains are separated by a linker of ~20 residues, whereas the rest of the SRs are connected by fussing the helix C from one repeat to the helix A of the following.

Secondary PKP1a-interactions in the DP-PD

Our data suggested that the region SR3-SR5 of DP has an accessory contribution to the interaction with PKP1a. Similar to how proteins in a complex cooperatively bind to each other to achieve specific functions, there is also such cooperation among domains in the same protein. When the interaction between DP-Venus and PKP1a-CFP was analysed by FLIM, the complete DP-PD, and the regions DP-SR2-SR9 and

DP-SR3-SR9 caused significant reductions of the CFP lifetime with respect to the control samples, indicating that these fragments of DP interact with PKP1a. Yet, shorter fragments starting at the SR4, SR5, or SR6 did not interact noticeably (Figure R17). Similar results were obtained by looking at the subcellular distribution and co-localization of PKP1a and DP fragments ectopically expressed in COS-7 cells, although in this analysis the fragment DP-SR3-SR9 showed a mixed behaviour, it co-localized with PKP1a in some cells but not in others (Figure R19). Thus, it seems that in addition to the primary site located in the SR2-like domain, the SR3 sub-domain possibly cooperates in the association providing secondary sites for the interaction with PKP1a. These secondary interactions are not sufficient to drive the proper association of DP and PKP1 by their own, as it was highlighted by the co-localization analysis, but are likely to reinforce the binding mediated for the SR2-like domain.

We tried to understand the structural basis of the cooperation between the SR2 and the SR3. The SR3 is part of an apparently rigid structural unit formed by the repeats SR3-SR6. Unfortunately, attempts to crystallize the N-terminal region of the PD of DP (region 1-630) were unsuccessful. Thus, the structure of this region was investigated by SAXS. This region has an overall elongated shape, as indicated by the form of the P(r) function, the dimensionless Kratky representation of the scattering data, and the rigid body modelling. The presence of two putative non-helical segments in the N-terminal half of the plakin domain of DP, one upstream the SR2-like and a second connecting the SR2-like and the SR3, suggested that *a priori* there could be significant conformational variability in this region. Yet, multiple rounds of rigid body refinement against SAXS data of the region 1-630 of DP using two independent modelling methods (implemented in the programs CORAL and BUNCH) yielded models with repetitive features. The refinement was done using two rigid bodies (the SR2 and the SR3-SR6 region) and two flexible segments (the 63 residues long N-terminal tail and the ~20 residues long linker between the SR2-SR3 domains). In all the models obtained with both programmes, the SR2 domain is placed on one side of the SR3, whereas the N-terminal tail (residues 1-63) is built in an extended conformation that project away from other parts of the structure (Figures R48-A and R49-A). The repetitive positioning of the SR2 adjacent to the SR3 suggests that these two domains could establish lateral interactions and adopt a compact arrangement. Notably, the *ab initio* reconstructions of the 1-630 structure from the SAXS data yielded low resolution envelopes with a slightly bent rod-like shape (Figure R47) that are in good agreement with the atomic models obtained by rigid body fitting.

The role of the linker connecting the SR2 and SR3 domains and the structural organization of this region of DP are unknown. In this respect, the crystal structure of the SR3-SR4 of BPAG1e (PDB entry 2IAK) includes 16 residues upstream of the SR3, which adopt an extended conformation and pack alongside against the SR3 in between helices A and B (Jefferson et al. 2007). By analogy, the SR2-SR3 linker in DP may also adopt a relatively ordered structure. Nonetheless, this linker is sensitive to proteolytic digestion with trypsin and chymotrypsin, which cleave DP after K167 and Y172, respectively (Choi & Weis 2011). This suggests that the linker has a loose structure, at least in part.

The folded-back organization of the SR2 onto the SR3 has implications for the interaction of this region with PKP1a. This closed arrangement could generate a binding site for PKP1a or it could favour the correct display of two sub-sites in each domain. In addition, binding of PKP1a to DP could induce a change in the arrangement of the SR2-SR3 region which could be linked to the modulation of DP function, for example exposing cryptic binding sites. Conversely, changes in the organization of the SR2-SR3 arrangement could modulate the affinity for PKP1a or other ligands that bind to the N-terminal region of the plakin domain. For example, stretching of DP would alter the organization of the SR2-SR3 region, which in turn could modify the way this region interacts with other proteins, suggesting that DP might act as a mechanosensor in a similar form as focal adhesion proteins (Ciobanasu et al. 2013).

Unravelling the DP-binding site in PKP1a

It had been shown that the head domain of PKP1a mediates the interaction with DP (Hofmann et al., 2000; Kowalczyk, 1999; Sobolik-Delmaire, Katafiasz, & Wahl, 2006). Initially, we used this well-established interaction to assess the effectiveness of our multi-methodological approach, which includes Co-IP, FLIM, and co-localization analysis, to map the DP-interaction site in PKP1a. Association of the head domain of PKP1a with DP-PD and DP-NT was observed in Co-IP and FLIM assays, whereas the ARM domain of PKP1 did not interact with this DP fragments (Figures R20 and R21). Furthermore, DP-NT was markedly recruited to the nucleus when co-transfected with PKP1a full length or head domain. PKP1-ARM-CFP was diffusely distributed throughout the cytoplasm and was not markedly present at the nucleus. This precluded the use of the co-localization with DP-NT as an indication of interaction, since both proteins were already located at the same subcellular compartment.

The head domain of the three PKPs is considered mainly disordered with only a small fragment near the N-terminus (HR2) believed to form an α-helix. Interestingly, the head

domain is much larger in PKPs than in the rest of the ARM-proteins. PKG, for instance, has a merely 79 amino acids head domain, also predicted to be intrinsically disordered (Choi et al. 2009). Accordingly, the function of the head domain in PKPs is opposed to that of this same domain in the rest of the ARM-proteins. Typically, ARM-proteins interact with their binding partners by means of their ARM-domains, which form an elongated superhelical structure that facilitates protein associations as shown by the crystallographic structures of several ARM-domains (Liu et al. 2009; Huber et al. 1997; Choi & Weis 2005). PKPs, however, use the amino-terminal head domain to drive all their known interactions.

In recent years, it has been recognized that PKPs are multifunctional proteins that promote cell adhesion at the DMs but also participate in several signalling-related functions in the cytoplasm and nucleus (reviewed in Hatzfeld et al. 2014; see examples in Godsel et al. 2010; Hatzfeld et al. 2000; Hofmann et al. 2006; Koetsier et al. 2014; Mertens et al. 2001; Sklyarova et al. 2008; Wolf et al. 2010). During this time, the study of the function and structure of inherently disordered proteins has also come to the fore. These proteins are characterised for their remarkable capacity to interact with many molecular species, participating in numerous processes within cells (Zhuang et al. 2011). Thus, PKPs might be stretching this plasticity by adopting suitable conformations upon interaction with their different binding partners, resulting in distinct structures and promiscuity in functions. Another tool for achieving the required flexibility needed by PKPs to cover their different functions may be related with post-translational modifications (PTMs). The head domain of the three PKPs possesses a very high number of phosphorylable residues. Specifically for PKP1, they have been reported ~60 phosphorylation-sites in its head domain (http://www.phosphosite.org; Hornbeck et al. 2004) distributed in hot-spots of phosphorylation around residues ~50-70, ~78-85, ~98-110, ~118-121, and ~180-190. The high number of phosphorylation-sites in the head domain of PKPs suggests that this PTM may play an important role in the structure-to-function acquisition (Hatzfeld et al. 2014). Recently, Wolf et al. (2013) have reported an interesting example of how phosphorylation induced by insulin signalling switches PKP1 function from stabilizing cell adhesion to promoting cell proliferation. In this case, phosphorylation in S118 by Akt2 results in the delayed degradation of PKP1. The higher protection of p-PKP1 (phosphorylated PKP1) against degradation might be correlated with the secondary structure acquisition, although much further investigation is required in this field.

Precise mapping of the DP-binding site within the head domain of PKP1a

Non-structured proteins are often involved in molecular interactions mediated by localized binding sites, sometimes as narrow as 10 amino acid residues or less (Dunker et al. 2008). We wondered whether the DP-recognition site in PKP1a would also be a short sequence. Thus, we used our multi-methodological approach with N-terminal deletion mutants of PKP1a to identify the minimal region that supports the interaction with DP. This was narrowed down in several stages.

First, we delimited the major DP-interaction determinant in PKP1a to a region comprehended between residues 52-120. A previous report had proposed that the PKP1 region 1-34 was essential to mediate the interaction with DP (Sobolik-Delmaire et al. 2006). In contrast, our data revealed that the N-terminal 51 residues, which contain the HR2 motif, were dispensable for the interaction, albeit this segment 1-51 was sufficient to moderately pull-down DP-NT in Co-IP assays (Figure R23).

Next, we narrowed the DP-interaction site within the 52-120 region of PKP1a. Using FLIM we mapped the DP-recognition site to the region 98-120 of PKP1a. Further analysis within this segment suggested that the major determinant of the interaction with DP is located in the region 104-116 of the head domain of PKP1a (Figure R26). Co-localization assays did not allow such precise mapping but agreed with FLIM results identifying the region 98-116 of the head domain of PKP1a as critical for the interaction with DP (Figure 27).

Interestingly, this minimal DP-recognition site in PKP1a appears to require only ~10 residues, which are sufficient to mediate this interaction. We do not exclude that other segments of the head domain of PKP1 upstream of this site might additionally contribute to the interaction. Our approach was directed to the identification of a minimal site. More quantitative analysis will be required to assess whether DP engages with multiple sites in PKP1a other than the 104-116 segment, and if so, whether DP binds simultaneously to these multiple sites in PKP1a.

In DMs PKP1a functions as a multi-linker protein, interacting concurrently with several proteins to promote lateral associations. Thus, it is plausible a model where small and localized interaction sites for different proteins are arranged along the head domain of PKP1a. This arrangement would provide a multiple-interaction surface favouring the formation of multi-protein complexes. Yet, the precise interacting-regions for other PKP1-binding partners have not been identified to date.

Identification of one nuclear-targeting sequence in PKP1-head

It had been extensively reported that endogenous and overexpressed PKPs, in addition to DMs, also localise to the nucleus (Bonné et al. 1999; Mertens et al. 1996; Schmidt et al. 1997). This localization is independent of DMs formation, occurring in DM-bearing and non-bearing cells lines (Hatzfeld et al. 2014).

To date, the specific nuclear functions of PKPs remain largely speculative. Only recently they have been reported interactions between PKP2 and the RNA polymerase III, between PKP3 and the ETV1/ER81 transcription factor, as well as between PKP1 and ssDNA (Mertens et al. 2001; Sobolik-Delmaire et al. 2010; Munoz et al. 2014).

Out of the three PKPs, PKP1 is the most nuclear-prominent. The PKP1a isoform is present at both nucleus and DMs, whereas PKP1b is only detected in the nucleus (Schmidt et al. 1997). The sequences of both PKP1 isoforms do not contain any obvious NLS (nuclear localization signal), nor any canonical NES (nuclear exporting signal). PKP1b only differs from PKP1a in an additional exon, which adds 21 amino acids after the residue 411 in the ARM-domain. Considering that the rest of the sequence is identical in both isoforms and all PKP1-interaction partners reported so far bind PKP1 within his head domain, the processes that target, transport, and maintain one of the isoforms in the nucleus remain completely uncharacterized.

An initial cue to understand the prominent nuclear localization of PKP1a derives from the differential behaviour of PKP1a in DM-bearing and non-bearing cell lines (Figure R28). In cells that do not form DMs, PKP1a is completely localized to the nucleus. That is the case also for keratinocytes growing in serum-free medium, which remain in an undifferentiated state where DMs are not formed. However, when keratinocytes are stimulated to differentiation, PKP1a is relocated into cell-cell junctions, yet still present at the nucleus. Thus, although PKPs had been proposed as desmosomal proteins since the beginning and the non-desmosomal functions of these proteins just arose during the last years; now, it seems plausible that the primary location of PKP1a is the nucleus, and therefore, they have a prominent nuclear function. In fact, a recent study has suggested that the Wnt-signaling related functions of catenin proteins might have arisen earlier in evolution than their roles in adhesion (Dickinson et al. 2011).

To shed light on the processes that govern the relocation of PKP1a in the cell and the cytoplasm/nucleus shuttling, we aimed to identify the region of PKP1a that mediates the nuclear targeting. We studied the nuclear determinants of PKP1a in COS-7 cells, which do not form prominent DMs. In addition, we used normal human keratinocytes (NHK) as a model of DM-bearing cell line. In COS-7 and undifferentiated NHKs

(growing at low-calcium concentration), PKP1-CFP showed an exclusively staining of the nuclear karyoplasm, being mostly excluded from nucleoli, in agreement with previous reports (Hatzfeld et al. 2000; Schmidt et al. 1997; Sobolik-Delmaire et al. 2010). When keratinocytes were induced to differentiate by rising calcium concentration in the growth medium, PKP1-CFP localised both to the nucleus and to the plasma membrane where it concentrated in punctuated structures, characteristic of DMs (Figure R28). The relocation of PKP1-CFP at cell-cell contact sites upon differentiation demonstrated that CFP does not prevent PKP1a normal subcellular trafficking and that PKP1a nuclear localization is DM-independent. This also revealed that the study of the nuclear determinants in PKP1a can be done by using CFP-tagged constructs transiently transfected in COS-7 cells.

It had been shown that the head domain of PKP1a is required for the nuclear localization of PKP1a in COS (Kowalcyk et al. 1999), HaCaT, and HeLa cells (Hatzfeld et al. 2000). Sobolik-Delmaire et al. (2010) had identified the segment 55-125 as an important region for the nuclear targeting in A431 cells. We have further enlarged the mapping of the regions important for the nuclear localization of PKP1a (Figure R34). The first 109 residues of the head domain of PKP1a were dispensable for the nuclear localization. Shorter deletion mutants starting on positions 116 to 151 showed a progressive increase in the cytoplasmic fraction of PKP1a. Fragments with further deletions or complete ablation of the head domain showed an equal distribution between nucleus and cytoplasm. Our results suggest that the segment 110-132, and probably the region 133-150, play an important role in the nuclear-to-cytoplasmic relocation of PKP1a.

Since PKP1 lacks defined NLSs, it is possible that an unidentified nuclear protein assists PKP1a with the nuclear import. However, efforts to identify PKP1-binding partners have been mostly unproductive so far. Only recently, some putative nuclear PKP1-interacting partners have been suggested, but the biological significance of the reported interactions is still pending (Reddy 2013). Interestingly, the nuclear determinant that we have identified is downstream of the DP-binding site (residues ~98-116). The recruitment of DP to the nucleus by PKP1a suggests that PKP1a probably interacts simultaneously with DP and a putative nuclear binding partner (Figure D1).

It is also possible that the nuclear localization of PKP1a relies on some PTM, rather than on binding to a nuclear protein. It is well established that some modifications, such as phosphorylation, palmitoylation, ubiquitination, etc. regulate diverse protein features including protein localization, activity, and stability (Deribe et al. 2010; Hunter 2010).

Accordingly, the nuclear determinant that we have identified (residues ~116-132) matches one of the hot-spots of phosphorylation mentioned before (region ~118-121) (Figure D1). Notably, Akt2-dependent phosphorylation of PKP1a at S118 regulates the subcellular distribution of PKP1, although it apparently has a minor effect on its nuclear localization (Wolf et al. 2013). In addition, it has been recently reported that palmitoylation of a conserved cysteine residue present in the three PKPs ARM-domains regulates PKP incorporation into assembled DMs, and prevents PKP-dependent DM formation (Roberts et al. 2014). Yet, further investigation on the effects of PTMs in PKPs, is still needed.

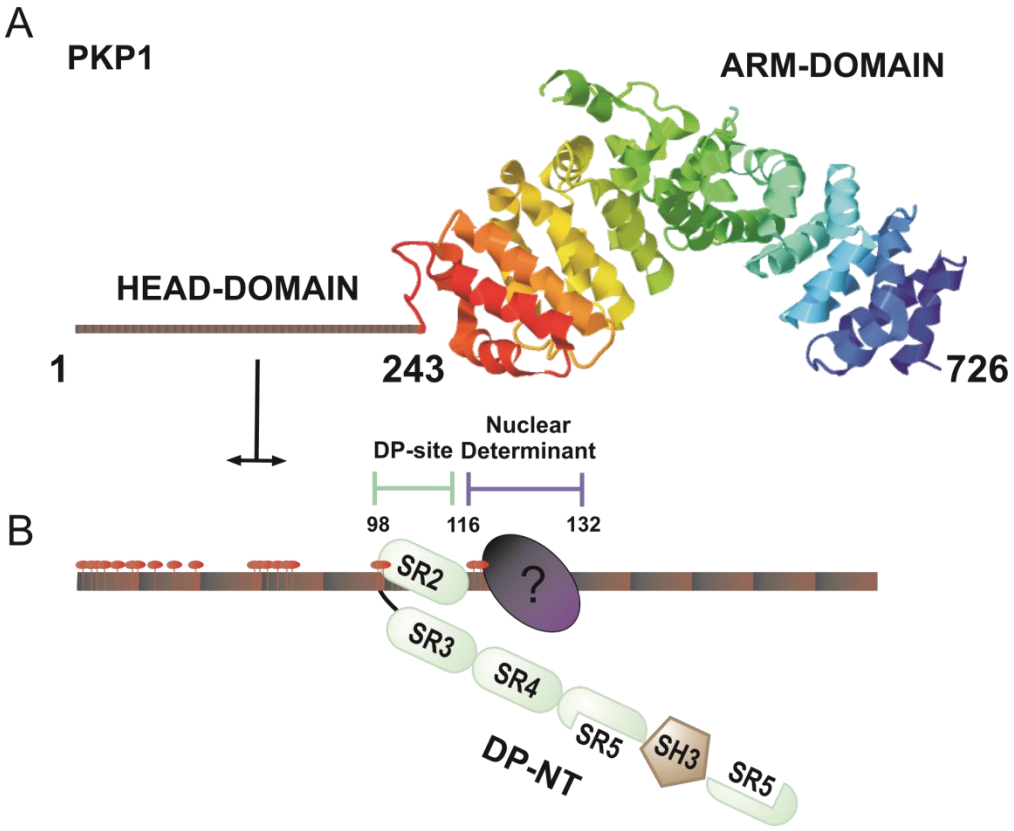

Figure D1. PKP1-head domain functional sites. A) Schematic representation of PKP1a. The head domain of PKP1a is represented by a line divided in 24 segments of 10 residues. The ARM-domain is represented by its atomic structure (PDB entry 1xm9). **B)** Detail of the PKP1-head domain. Numbers above the sequence identify the functional domains of PKP1-head: i) DP-binding site (DP-site), DP is represented by the DP-NT fragment (region 1-545), which interacts with PKP1a in the region ~98-116; ii) Nuclear determinant identified in this work (Nuclear determinant), corresponding to the region ~116-132. In the figure it is also represented the uncharacterized nuclear protein that might participate in the PKP1 nuclear-targeting (?) by interacting with this region of the PKP1-head domain (residues ~116-132). Notice that both sites are not mutually exclusive, but also are located one next to the other; iii) Predicted phosphorylation sites are marked by red dots (http://www.phosphosite.org). Notice that one of the hot-spot of phosphorylation matches the DP-binding site (~98-110), whereas the next is inside the nuclear determinant (~118-121).

The analysis of N-terminal deletion mutants revealed an important role of the region 116-132 in the nuclear localization of PKP1a. Yet, this segment is not sufficient by itself to mediate nuclear targeting, suggesting that this process may involve multiple sites at the head domain. In fact, the N-terminal segment 1-132 was enriched in the nucleus in the absence of other regions, despite it was dispensable for nuclear targeting in the initial N-terminal deletion analysis. The contribution of multiple sites to the nuclear localization of PKP1a was further supported by the efficient nuclear localization of PKP1a internal deletion mutants in which the regions 116-132 or 110-150 had been removed. Collectively, our results suggest that the head domain of PKP1a may contain at least three regions involved in its nuclear accumulation: the 116-132 motif, and two additional regions up- and downstream of this segment (sites P1, P2, and P3).

Our results could be explained if PKP1a interacts with several nuclear partners via several putative sites (Figure D2 shows an explanation with three putative sites). In this model, the nuclear targeting of PKP1a would require the combined contribution of several regions; therefore, it would be lost only when more than one nuclear localization site is deleted. In the N-terminal deletion mutants, fragments trimmed down to ~110 would lose the P1 site, but they could still be targeted to the nucleus through the P2 and P3 sites (Figure D2-B). Shorter N-terminal deletion fragments, in which the region 116-132 was removed, would have lost the P1 and P2 sites. The remaining P3 site would be insufficient to maintain PKP1a in the nucleus (Figure D2-C). Internal deletion mutants that lack the 110-150 region (site P2) would be recruited to the nucleus via the P1 and P3 sites (Figure D2-D). Finally, the N-terminal fragment 1-132, which lacks the putative P3 site, would be targeted to the nucleus by the P1 and P2 sites (Figure D2-E).

The existence of multiple regions that contribute to the nuclear targeting of proteins has been previously reported (Guo et al. 2013; Mavinakere et al. 2012; Shaulsky et al. 1990). For instance, the C-terminal region of p53 contains a cluster of three NLSs that mediate nuclear import; where NLS-I and -II cooperate to target p53 to the nucleus (Shaulsky et al. 1990). In the case of PKP1, it also seems that the nuclear determinants do not participate equally in the nuclear targeting of PKP1. For instance, the fragment PKP1-1-132 (region 1-132) that in our hypothetical model has two putative binding-sites for nuclear proteins does not show a restricted nuclear localization. Conversely, the internal deletion mutants and the N-terminal deletion fragments trimmed up to residue 109, which also harbour two putative interaction-sites, show this confined localization.

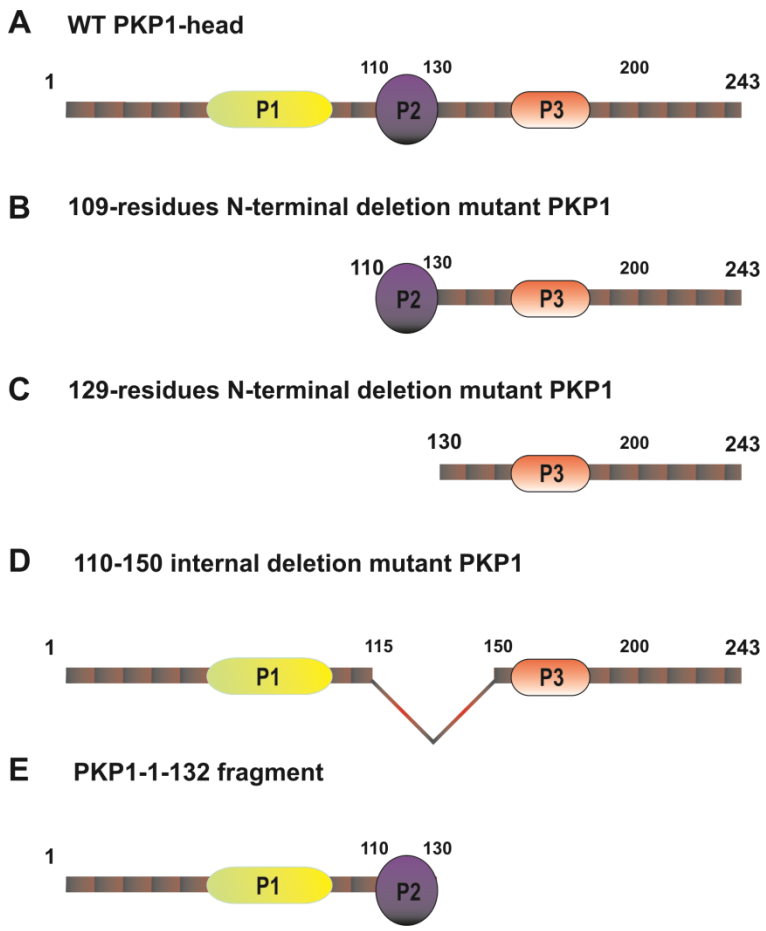

Figure D2. Multiple regions of the PKP1-head contribute to the PKP1-nuclear localization. Hypothetical models to explain how multiple regions of the PKP1-head domain contribute to the PKP1-nuclear localization. **A)** Schematic representation of WT PKP1a-head with three nuclear interacting partners (P1, P2, and P3). In this scenario, PKP1a would localise to the nucleus. **B-C)**, N-terminal deletion mutants of the PKP1-head domain compromise the interaction of putative PKP1-nuclear binding partners. Depending on the depth of the deletion one or more sites would be removed. In this scenario, PKP1a would preserve the nuclear localization when at least two nuclear determinants were present (B). **D)** The internal deletion of the 116-132 or 110-150 segments only would remove one of the nuclear localization sites. Thus, the nuclear localization of PKP1a would not be affected. **E)** The N-terminal fragment 1-132, which lacks the putative P3 site, would be targeted to the nucleus by the P1 and P2 sites.

Finally, NLSs are characterized by short sequences of positively charged amino acids (Kalderon et al. 1984). The very basic condition of the head domain of PKP1a, with an pI ~9.5, might favour that multiple sequences within this domain act as non-canonical NLSs that cooperate to retain PKP1a in the nucleus.

During all these experiments we realised that independent of how much we trimmed PKP1a and, even working only with the PKP1-ARM domain, a remaining nuclear staining was repeatedly observed. Previous reports had suggested that PKP1 might have at least two NLS (Sobolik-Delmaire et al. 2010). However, we considered other possibilities, such as the nuclear recruitment of PKP1a-fragments by means of the

homo-association with endogenous PKP1 (Hofmann, Mücke, et al. 2000). Yet, this option was ruled out because the subcellular distribution of PKP1 mutants was similar in NHK (that expresses endogenous PKP1) and in PKP1-null keratinocytes established from a patient with skin fragility-ectodermal dysplasia syndrome whit total ablation of PKP1 (South et al. 2003) (Figure R37). These subcellular distributions were also similar to those previously observed in COS-7 cells.

At this point we thought again in a possible effect of the CFP tag. We had previously observed that our CFP-tagged constructs of PKP2a, PKG, and DP showed specific subcellular distributions; including PKP2a, which did not exhibit any nuclear signal (see Figures R29, R30, and R32). So, it was very unlikely that the same CFP-tag was recruiting to the nucleus the CFP-tagged PKP1a deletion constructs that lack the first 116 to132 residues (i.e. 133-726, 151-726, 181-726, and ARM-domain). Yet, we analysed the localization of constructs fused to an N-terminal HA tag (using two vectors: pCEFLHA and pcDNA3-HA) or FLAG tag (pCEFLAG vector) (Figure R38). Full length PKP1a showed a similar distribution in the CFP-, HA-, and FLAG-tagged constructs. The ARM domain showed an equal nuclear and cytoplasmic distribution when expressed with a CFP-tag or with a HA-tag using the pcDNA3-HA vector. Strikingly, the ARM domain was excluded from the nucleus when the PKP1-ARM was tagged with FLAG or with HA using the pCEFLAG or the pCEFLHA vectors, respectively. The contrasting results observed for the HA-tagged ARM domain with the pcDNA3-HA and pCEFLHA vectors suggested that it might be a dependence of the promoter used (EF1 promoter in pCEFL-vectors or CMV in pcDNA3-based vectors). This is in agreement with the nuclear localization of the CFP-tagged ARM construct, which was also made using the pcDNA3 vector.

Despite these unexpected vector-dependent results, altogether they reveal that the nuclear localization of PKP1a is determined by the head domain, without participation of secondary NLSs located in the ARM-protein. This was confirmed by analysing the subcellular distribution of several HA-tagged PKP1a N-terminal deletion mutants (made in the pCEFLHA vector), which highlighted the role of the 116-151 region of the head domain of PKP1a for its nuclear targeting. Constructs starting at residue 151 or 181 did not show nuclear localization. Collectively, these results agreed with those observed with similar constructs tagged with CFP (compare Figures R34 and R39).

Finally, we also analysed whether the subcellular distribution of PKP2a was also determined by sequences in its head domain (region 1-348). In COS-7 cells, PKP2a is predominantly located at the plasma membrane. This distribution was also observed in the N-terminal deletion mutants 65-838 (PKP2-65) and 151-838 (PKP2-151). However,

further N-terminal deletions, as in the fragment 220-838 (PKP2-220) and the isolated armadillo domain (PKP2-ARM, region 349-838), resulted in the loss of the specific localization at the plasma membrane. PKP2-220 and PKP2-ARM appeared distributed throughout the whole cell. Interestingly, the armadillo domain of PKP2a showed a prominent nuclear presence, similar to that observed for the CFP-tagged armadillo domain of PKP1a.

Altogether, these results suggest that PKP1a and PKP2a harbour specific regions within their head domains that dictate the functional subcellular localization of these proteins. Interestingly, each protein is specifically targeted to different subcellular compartments but, in the absence of the functional-targeting sequences in the head domain, both are equally misallocated showing a diffuse distribution throughout the cell, including nuclear staining. This is particularly striking for PKP2 that is absent from the nucleus in the full length form. Therefore, the nuclear localization of CFP-tagged constructs of PKP1a and PKP2a that lack the relevant targeting sequences most likely does not correspond to a native function.

Structure of the C-terminal half of the PD of DP

While the N-terminal half of the PD of DP harbours the PKP1a-interaction site, the C-terminal half (repeats SR7-SR9) contributes indirectly to the function of the PD. Therefore, we have analysed the structure of this region of DP.

The constructs of DP used in the functional assays contain the C-terminal half extended to residue 1056, including the initial part (residues ~1026-1056) of the rod domain. The rod domain is thought to mediate homo-dimerization by means of coiled-coil interactions (Green, Virata, et al. 1992; O´Keefe et al. 1989). By using Co-IP assays we have shown that the short segment 1026-1056 of the rod domain mediates self-association of the C-terminal part of the PD.

To further study the structure of the C-terminal region of the PD of DP, we expressed in bacteria and purified the fragment 660-1056 that includes the SR7-SR9 and beginning of the rod domain. Attempts to crystallize this fragment were not sufficient successful and we only obtain microcrystals, not suitable for crystallographic analysis (data not shown). To overcome this limitation, we applied SAXS to analyse the structure at low-resolution of this region of DP.

Surprisingly, analysis of the SAXS profiles revealed that the apparent molecular weight of this fragment (42.3 kDa) correspond to the theoretical molecular mass of the monomer (46.8 kDa). Thus, in contrast to the association detected by Co-IP, the short

N-terminal segment of the rod domain was insufficient to mediate self-association *in vitro* using purified protein. The differences between the Co-IP results that revealed dimerization and the monomeric state observed *in vitro* suggest that the homo-association might be stabilized by adaptor molecules present in the COS-1 cell lysates. It would also be possible that in mammalian cells the DP fragment undergoes PTMs that favour self-association. Finally, the association observed by Co-IP might represent only a minor fraction of the total protein levels in the lysates.

The monomeric SR7-SR9 has an elongated shape with a maximum dimension of ~165 Å, as revealed by the SAXS-derived P(r) distance distribution function and the *ab initio* reconstructions of the structure. This elongated shape is consistent with three concatenated tandem SRs. In fact, a homology 3D model of this region built using the structure of the SR7-SR9 region of plectin reproduced the scattering data. It had been suggested that the region 883-1022 of DP would not form a SR, but it would constitute a flexible region instead (Al-Jassar et al. 2011). Yet, the DP region 885-1025 shares a ~38% sequence identity with the SR9 of plectin, supporting that DP has a well ordered and bona fide SR9. Moreover, our SAXS data indicates that the SR7-SR9 region is an apparently rigid structure.

Since the DP-CT fragment (region 660-1056) did not dimerize in solution but it is well stablished that DP and other plakins form dimers via coiled-coil interactions of the rod domain, we stabilized the homo-dimerization by adding a leucine zipper of the yeast transcriptional activator GCN4 at the C-terminus. GCN4 forms a stable homo-dimeric parallel coiled coil that has been extensively characterized and is frequently used as a model homo-dimerization motif (O'Shea et al. 1991). The structure of the DP-CT-GCN4 protein (DP region 660-1060) was analysed by SAXS. The molecular mass of this fragment in solution estimated from the SAXS data (~119 kDa) was approximately twice the molecular weight calculated from the sequence (51.2 kDa) indicating that the GCN4 effectively stabilizes the homo-dimer. Low resolution reconstructions of the DP-CT-GCN4 structure using the scattering data and *ab initio* methods revealed an elongated and flat structure being narrow towards one of the longitudinal ends, with overall dimensions of approximately 240 Å x 105 Å x 45 Å . This shape suggested that the two protomers run parallel and possibly establish contacts along the SR7-SR9 modules. Interestingly, the crystal structure of the SR7-SR9 of plectin contains two plectin molecules in the asymmetric unit of the crystal. A composite atomic model of the DP-CT-GCN4 based on the crystallographic dimer of plectin matched the *ab initio* low resolution structure of DP and approximately reproduced the scattering data, suggesting that the model reproduces the overall features of the DP dimeric structure.

This suggests that the observed parallel arrangement of the SR7-SR9 might also occur in plectin and other plakins. Nonetheless, the specific arrangement of the two DP molecules might be slightly different from that observed in the plectin crystal structure.

Collectively, the PD of DP resembles a tripartite articulated structure consisting of three apparently rigid modules: the SR2-like domain, the SR3-SR6 region, and the SR7-SR9, that are connected by flexible linkers.

Dimerization of DP via the rod domain would favour the interaction with other proteins by exposing bivalent biding sites. The parallel and proximal arrangement of the SR7-SR9 module probably restricts the maximum distance between binding sites located in the N-terminal half of the PD. This is likely to impose a limit in the maximum separation of the ligands to achieve efficient binding, and suggests that efficient binding of DP to other proteins, such as PKPs, requires a minimum ligand density.

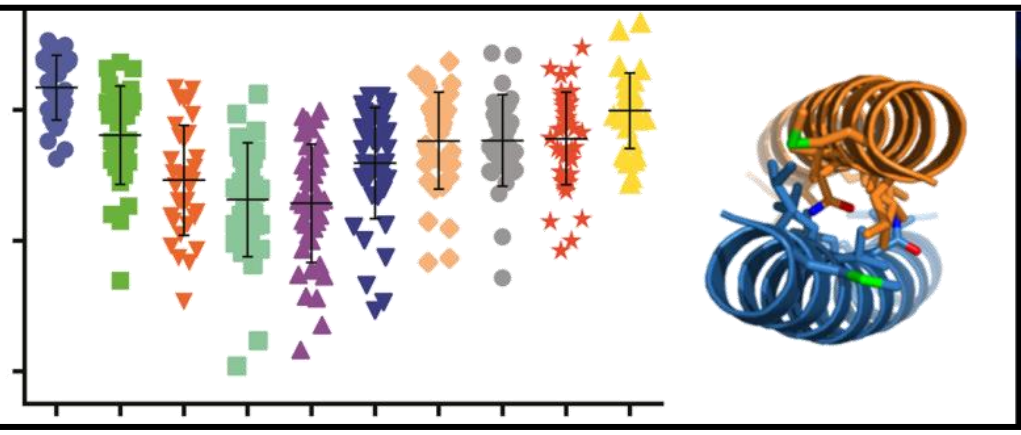

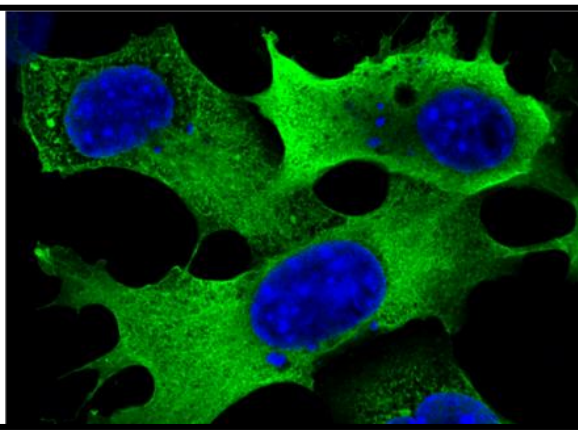

Chapter 6

CONCLUSIONS

1. The N-terminal half of the plakin domain of desmoplakin interacts with the head domain of plakophilin 1a. This association is independent of the assembly of desmosomes.

2. The SR2-like domain of desmoplakin is necessary and sufficient for the interaction with plakophilin 1a. The SR3 domain contributes secondarily to this interaction.

3. The central region of the head domain of plakophilin 1a, residues 98-116, is critical for the interaction with desmoplakin. Within this region, the residues 104-116 form a crucial motif of interaction.

4. The head domain of plakophilins 1a and 2a is the main determinant of their subcellular localization.

5. Plakophilin 1a localizes predominantly to the nucleus in desmosome-bearing and non-bearing cells lines. The segment 116-132 acts as a nuclear localization signal. Yet, these residues are not sufficient to maintain plakophilin 1a in the nucleus.

6. The nuclear localization of PKP1a requires the combined contribution of several regions of the head domain. In the presence of sequences either up- or down-stream of the region 110-150, this segment is dispensable for nuclear targeting.

7. The N-terminal region of desmoplakin, residues 64-164, has very high content of α-helical structure that is likely to consist of three helices that form a non-canonical SR2-like domain.

8. The SR2-like domain of desmoplakin is apparently located on one side of the SR3-SR6 segment, and possibly makes lateral contacts with the SR3.

9. The C-terminal half of the plakin domain, residues 660-1056, forms a monomeric rigid rod-like structure in solution that is compatible with a structure consisting of an array of three SR (SR7-SR9).

10. Dimerization of the C-terminal half of the plakin domain of desmoplakin by a coiled-coil that mimics the rod domain results in a parallel arrangement with possible inter-protomer contacts along the SR7-SR9 domains.

References

Aktary, Z. et al., 2010. Plakoglobin interacts with and increases the protein levels of metastasis suppressor Nm23-H2 and regulates the expression of Nm23-H1. *Oncogene*, 29(14), pp.2118–29.

Aktary, Z. et al., 2013. Plakoglobin interacts with the transcription factor p53 and regulates the expression of 14-3-3σ. *J Cell Sci*, 126(Pt 14), pp.3031–42.

Aktary, Z. & Pasdar, M., 2012. Plakoglobin: role in tumorigenesis and metastasis. *Int J Cell Biol*, 2012(189521).

Al-Amoudi, A. et al., 2011. The three-dimensional molecular structure of the desmosomal plaque. *Proc Natl Acad Sci U S A*, 108(16), pp.6480–5.

Al-Jassar, C. et al., 2013. Mechanistic basis of desmosome-targeted diseases. *J Mol Biol*, 425(21), pp.4006–22.

Al-Jassar, C. et al., 2011. The nonlinear structure of the desmoplakin plakin domain and the effects of cardiomyopathy-linked mutations. *J Mol Biol*, 411(5), pp.1049–61.

Alonso-García, N. et al., 2009. Structure of the Calx-beta domain of the integrin beta4 subunit: insights into function and cation-independent stability. *Acta Crystallogr D Biol Crystallogr*, 65(Pt 8), pp.858–71.

Andl, C.D. & Stanley, J.R., 2001. Central role of the plakoglobin-binding domain for desmoglein 3 incorporation into desmosomes. *J Invest Dermatol*, 117(5), pp.1068–74.

Angst, B.D., Nilles, L.A. & Green, K.J., 1990. Desmoplakin II expression is not restricted to stratified epithelia. *J Cell Sci*, 97(Pt 2), pp.247–257.

Aoyama, Y. et al., 2009. Low to high Ca2+-switch causes phosphorylation and association of desmocollin 3 with plakoglobin and desmoglein 3 in cultured keratinocytes. *Exp Dermatol*, 18(4), pp.404–408.

Argos, P., 1990. An investigation of oligopeptides linking domains in protein tertiary structures and possible candidates for general gene fusion. *J Mol Biol*, 211(4), pp.943–58.

Von Arnim, C. a F. et al., 2004. Demonstration of BACE (beta-secretase) phosphorylation and its interaction with GGA1 in cells by fluorescence-lifetime imaging microscopy. *J Cell Sci*, 117(Pt 22), pp.5437–45.

Bikle, D.D., Xie, Z. & Lu, C.-L., 2013. Calcium regulation of keratinocyte differentiation. *Expert Rev Endocrinol Metab*, 7(4), pp.461–472.

Bonné, S. et al., 2003. Defining desmosomal plakophilin-3 interactions. *J Cell Biol*, 161(2), pp.403–16.

Bonné, S. et al., 1999. Plakophilin-3, a novel armadillo-like protein present in nuclei and desmosomes of epithelial cells. *J Cell Sci*, 112(Pt 1), pp.2265–76.

Bornslaeger, E.A. et al., 1996. Breaking the connection: displacement of the desmosomal plaque protein desmoplakin from cell-cell interfaces disrupts anchorage of intermediate filament bundles and alters intercellular junction assembly. *J Cell Biol*, 134(4), pp.985–1001.

Bornslaeger, E.A. et al., 2001. Plakophilin 1 interferes with plakoglobin binding to desmoplakin , yet together with plakoglobin promotes clustering of desmosomal plaque complexes at cell-cell borders. *J Cell Sci*, 114(4), pp.727–738.

Bouameur, J.-E., Favre, B. & Borradori, L., 2014. Plakins, a Versatile Family of Cytolinkers: Roles in Skin Integrity and in Human Diseases. *J Invest Dermatol*, 134, pp.885–894.

Boukamp, P. et al., 1988. Normal Keratinization in a Spontaneously Immortalized aneuploid human keratinocyte cell line. *J Cell Biol*, 106(3), pp.761–771.

Brown, J.H. et al., 2001. Deciphering the design of the tropomyosin molecule. *Proc Natl Acad Sci U S A*, 98(15), pp.8496–501.

Cabral, R.M. et al., 2010. Identification and characterization of DSPIa, a novel isoform of human desmoplakin. *Cell Tissue Res*, 341(1), pp.121–9.

Calkins, C.C. et al., 2003. The Armadillo family protein p0071 is a VE-cadherin- and desmoplakin-binding protein. *J Biol Chem*, 278(3), pp.1774–83.

Carnahan, R.H. et al., 2010. The molecular evolution of the p120-catenin subfamily and its functional associations. *PloS one*, 5(12), p.e15747.

Castañón, M.J. et al., 2013. Plectin-intermediate filament partnership in skin, skeletal muscle, and peripheral nerve. *Histochem Cell Biol*, 140(1), pp.33–53.

Chacón, P. et al., 2000. Reconstruction of protein form with X-ray solution scattering and a genetic algorithm. *J Mol Biol*, 299(5), pp.1289–302.

Chen, J. et al., 2012. The C-terminal unique region of desmoglein 2 inhibits its internalization via tail-tail interactions. *J Cell Biol*, 199(4), pp.699–711.

Chen, X. et al., 2002. Protein binding and functional characterization of plakophilin 2. Evidence for its diverse roles in desmosomes and beta-catenin signaling. *J Biol Chem*, 277(12), pp.10512–22.

Chiariello, M., Marinissen, M.J. & Gutkind, J.S., 2000. Multiple Mitogen-Activated Protein Kinase Signaling Pathways Connect the Cot Oncoprotein to the c-jun Promoter and to Cellular Transformation. *Mol Cell Biol*, 20(5), pp.1747–1758.

Chitaev, N.A. & Troyanovsky, S.M., 1997. Direct Ca+2-dependent Heterophilic Interaction between Desmosomal Cadherins, Desmoglein and Desmocollin, Contributes to Cell–Cell Adhesion. *J Cell Biol*, 138(1), pp.193–201.

Choi, H.-J. et al., 2009. Interactions of plakoglobin and beta-catenin with desmosomal cadherins: basis of selective exclusion of alpha- and beta-catenin from desmosomes. *J Biol Chem*, 284(46), pp.31776–88.

Choi, H.-J. & Weis, W.I., 2011. Crystal structure of a rigid four-spectrin-repeat fragment of the human desmoplakin plakin domain. *J Mol Biol*, 409(5), pp.800–12.

Choi, H.-J. & Weis, W.I., 2005. Structure of the armadillo repeat domain of plakophilin 1. *J Mol Biol*, 346(1), pp.367–76.

Ciobanasu, C., Faivre, B. & Le Clainche, C., 2013. Integrating actin dynamics, mechanotransduction and integrin activation: the multiple functions of actin binding proteins in focal adhesions. *European journal of cell biology*, 92(10-11), pp.339–48.

Cole, C., Barber, J.D. & Barton, G.J., 2008. The Jpred 3 secondary structure prediction server. *Nucleic Acids Res*, 36(Web Server issue), pp.W197–201.

Corrado, D. et al., 1997. Spectrum of Clinicopathologic Manifestations of Arrhythmogenic Right Ventricular Cardiomyopathy/Dysplasia: A Multicenter Study. *J Am Coll Cardiol*, 30(6), pp.1512–1520.

Costes, S. V et al., 2004. Automatic and quantitative measurement of protein-protein colocalization in live cells. *Biophys J*, 86(6), pp.3993–4003.

Danquah, J.O. et al., 2012. Direct interaction of baculovirus capsid proteins VP39 and EXON0 with kinesin-1 in insect cells determined by fluorescence resonance energy transfer-fluorescence lifetime imaging microscopy. *J Virol*, 86(2), pp.844–53.

Delmar, M. & McKenna, W.J., 2010. The cardiac desmosome and arrhythmogenic cardiomyopathies: from gene to disease. *Circ Res*, 107(6), pp.700–14.

Deribe, Y.L., Pawson, T. & Dikic, I., 2010. Post-translational modifications in signal integration. *Nat Struct Mol Biol*, 17(6), pp.666–72.

Dickinson, D., Nelson, W. & Weis, W., 2011. A Polarized Epithelium Organized by β- and α-Catenin Predates Cadherin and Metazoan Origins. *Science*, 331(6022), pp.1336–1339.

DuBridge, R.B. et al., 1987. Analysis of mutation in human cells by using an Epstein-Barr virus shuttle system. *Mol Cell Biol*, 7(1), pp.379–87.

Dunker, A.K. et al., 2008. Function and structure of inherently disordered proteins. *Curr Opin Struct Biol*, 18(6), pp.756–64.

Fasman, G.D. ed., 1996. *Circular Dichroism and the Conformational Analysis of Biomolecules*, New York: Springer.

Finn, R.D. et al., 2014. Pfam: the protein families database. *Nucleic Acids Res*, 42(Database issue), pp.D222–30.

Finn, R.D., Clements, J. & Eddy, S.R., 2011. HMMER web server: interactive sequence similarity searching. *Nucleic Acids Res*, 39(Web Server issue), pp.W29–37.

Franke, D. & Svergun, D.I., 2009. DAMMIF, a program for rapid ab-initio shape determination in small-angle scattering. *J Appl Crystallogr*, 42(2), pp.342–346.

Franke, W.W. et al., 2006. The area composita of adhering junctions connecting heart muscle cells of vertebrates. I. Molecular definition in intercalated disks of cardiomyocytes by immunoelectron microscopy of desmosomal proteins. *Eur J Cell Biol*, 85(2), pp.69–82.

Gaigalas, A.K. et al., 2001. The development of fluorescence intensity standards. *J Res Natl Inst Stand Technol*, 106(2), pp.381–389.

Gallicano, G.I. et al., 2009. Desmoplakin Is Required Early in Development for Assembly of Desmosomes and Cytoskeletal Linkage. *J Cell Biol*, 143(7), pp.2009–2022.

Gallicano, G.I., Bauer, C. & Fuchs, E., 2001. Rescuing desmoplakin function in extra-embryonic ectoderm reveals the importance of this protein in embryonic heart, neuroepithelium, skin and vasculature. *Development*, 128(6), pp.929–941.

Garrod, D. & Chidgey, M., 2008. Desmosome structure, composition and function. *Biochim Biophys Acta*, 1778(3), pp.572–87.

Garrod, D. & Kimura, T.E., 2008. Hyper-adhesion: a new concept in cell-cell adhesion. *Biochem Soc Trans*, 36(Pt 2), pp.195–201.

Garrod, D.R. et al., 2005. Hyper-adhesion in desmosomes: its regulation in wound healing and possible relationship to cadherin crystal structure. *J Cell Sci*, 118(Pt 24), pp.5743–54.

Gluzman, Y., 1981. SV40-transformed simian cells support the replication of early SV40 mutants. *Cell*, 23(1), pp.175–82.

Godsel, L.M. et al., 2005. Desmoplakin assembly dynamics in four dimensions: multiple phases differentially regulated by intermediate filaments and actin. *J Cell Biol*, 171(6), pp.1045–59.

Grailhe, R. et al., 2006. Monitoring protein interactions in the living cell through the fluorescence decays of the cyan fluorescent protein. *Chemphyschem*, 7(7), pp.1442–54.

Green, K., Virata, M., et al., 1992. Comparative structural analysis of desmoplakin, bullous pemphigoid antigen and plectin: members of a new gene family involved in organization of intermediate filaments. *Int J Biol Macromol*, 14(3), pp.145–53.

Green, K., Stappenbeck, T., et al., 1992. Structure of desmoplakin and its association with intermediate filaments. *J Dermatol*, 19(11), pp.765–769.

Greenfield, N.J., 2007. Using circular dichroism collected as a function of temperature to determine the thermodynamics of protein unfolding and binding interactions. *Nat Protoc*, 1(6), pp.2527–35.

Groot, K.R. et al., 2004. Kazrin, a novel periplakin-interacting protein associated with desmosomes and the keratinocyte plasma membrane. *J Cell Biol*, 166(5), pp.653–9.

Grossmann, K.S. et al., 2004. Requirement of plakophilin 2 for heart morphogenesis and cardiac junction formation. *J Cell Biol*, 167(1), pp.149–60.

Guinier, A. & Fournet, G., 1955. *Small-Angle Scattering of X-Rays*, London: Chapman & Hall, Ltd.

Guo, H. et al., 2013. Identification of critical regions in human SAMHD1 required for nuclear localization and Vpx-mediated degradation. *PloS one*, 8(7), p.e66201.

Harmon, R. & Green, K., 2013. Structural and functional diversity of desmosomes. *Cell Commun Adhes*, 20(6), pp.171–187.

Hartsock, A. & Nelson, W.J., 2009. Adherens and Tight Junctions: Structure, Function and Connections to the Actin Cytoskeleton. *Biochim Biophys Acta*, 1778(3), pp.660–669.

Hatsell, S. & Cowin, P., 2001. Deconstructing desmoplakin. *Nat Cell Biol*, 3(12), pp.270–272.

Hatzfeld, M. et al., 1994. Band 6 protein, a major constituent of desmosomes from stratified epithelia, is a novel member of the armadillo multigene family. *J Cell Sci*, 107(Pt 8), pp.2259–70.

Hatzfeld, M., 2003. Targeting of p0071 to desmosomes and adherens junctions is mediated by different protein domains. *J Cell Sci*, 116(7), pp.1219–1233.

Hatzfeld, M., 1999. The armadillo family of structural proteins. *Int Rev Cytol*, 186, pp.179–224.

Hatzfeld, M. et al., 2000. The function of plakophilin 1 in desmosome assembly and actin filament organization. *J Cell Biol*, 149(1), pp.209–222.

Hatzfeld, M., 2005. The p120 family of cell adhesion molecules. *Eur J Cell Biol*, 84(2-3), pp.205–14.

Hatzfeld, M. & Nachtsheim, C., 1996. Cloning and characterization of a new armadillo family member, p0071, associated with the junctional plaque: evidence for a subfamily of closely related proteins. *J Cell Sci*, 109(Pt 11), pp.2767–78.

Hatzfeld, M., Wolf, A. & Keil, R., 2014. Plakophilins in desmosomal adhesion and signaling. *Cell Commun Adhes*, 21(1), pp.25–42.

Heim, R. & Tsien, R.Y., 1996. Engineering green fluorescent protein for improved brightness, longer wavelengths and fluorescence resonance energy transfer. *Curr Biol*, 6(2), pp.178–82.

Hofmann, I. et al., 2006. Identification of the Junctional Plaque Protein Plakophilin 3 in Cytoplasmic Particles Containing RNA-binding Proteins and the Recruitment of Plakophilins 1 and 3 to Stress Granules. *Mol Biol Cell*, 17(3), pp.1388–1398.

Hofmann, I., Mertens, C., et al., 2000. Interaction of plakophilins with desmoplakin and intermediate filament proteins: an in vitro analysis. *J Cell Sci*, 113(Pt 1), pp.2471–83.

Hofmann, I., Mücke, N., et al., 2000. Physical characterization of plakophilin 1 reconstituted with and without zinc. *Eur J Biochem*, 267(14), pp.4381–9.

Hopp, T.P. et al., 1988. A Short Polypeptide Marker Sequence Useful for Recombinant Protein Identification and Purification. *Nat Biotechnol*, 6, pp.1204 – 10.

Hornbeck, P. V. et al., 2004. PhosphoSite: A bioinformatics resource dedicated to physiological protein phosphorylation. *Proteomics*, 4(6), pp.1551–61.

Huber, A.H., Nelson, W.J. & Weis, W.I., 1997. Three-Dimensional Structure of the Armadillo Repeat Region of beta-Catenin. *Cell*, 90(5), pp.871–882.

Hunter, T., 2010. Tyrosine phosphorylation : thirty years and counting. *Curr Opin Cell Biol*, 21(2), pp.140–146.

Ishida-Yamamoto, A. & Igawa, S., 2014. Genetic skin diseases related to desmosomes and corneodesmosomes. *J Dermatol Sci*, 74(2), pp.99–105.

Janes, R., 2009. Reference Datasets Circular Dichroism and Synchrotron Radiation Circular Dichroism Spectroscopy of Proteins. In B. A. Wallace & R. W. Janes, eds. *Modern Techniques in Circular Dichroism and Synchrotron Radiation Circular Dichroism Spectroscopy*. IOS Press.

Jaroszewski, L. et al., 2005. FFAS03: a server for profile--profile sequence alignments. *Nucleic Acids Res*, 33(Web Server issue), pp.W284–8.

Jefferson, J.J. et al., 2007. Structural Analysis of the Plakin Domain of Bullous Pemphigoid Antigen1 (BPAG1) Suggests that Plakins are Members of the Spectrin Superfamily. *J Mol Biol*, 366(1), pp.244–57.

Jones, J.C. & Goldman, R.D., 1985. Intermediate filaments and the initiation of desmosome assembly. *J Cell Biol*, 101(2), pp.506–17.

Kalderon, D. et al., 1984. A Short Amino Acid Sequence Able to Specify Nuclear Location. *Cell*, 39(Pt 2), pp.499–509.

Kami, K. et al., 2009. The desmoglein-specific cytoplasmic region is intrinsically disordered in solution and interacts with multiple desmosomal protein partners. *J Mol Biol*, 386(2), pp.531–43.

Kapprell, H.P., 1988. Identification of a basic protein of Mr 75,000 as an accessory desmosomal plaque protein in stratified and complex epithelia. *J Cell Biol*, 106(5), pp.1679–91.

Keil, R., Schulz, J. & Hatzfeld, M., 2013. p0071/PKP4, a multifunctional protein coordinating cell adhesion with cytoskeletal organization. *Biol Chem*, 394(8), pp.1005–17.

Kelly, S.M., Jess, T.J. & Price, N.C., 2005. How to study proteins by circular dichroism. *Biochim Biophys Acta*, 1751(2), pp.119–39.

Kimura, T.E., Merritt, A.J. & Garrod, D.R., 2007. Calcium-independent desmosomes of keratinocytes are hyper-adhesive. *J Invest Dermatol*, 127(4), pp.775–81.

Kimutai, L.K. et al., 2002. Modulations in epidermal calcium regulate the expression of differentiation-specific markers. *J Invest Dermatol*, 119(5), pp.1128–36.

Kleywegt, G.J. et al., 2004. The Uppsala Electron-Density Server. *Acta Crystallogr D Biol Crystallogr*, 60(Pt 12 Pt 1), pp.2240–9.

Knudsen, K.A. & Wheelock, M.J., 1992. Plakoglobin, or an 83-kD Homologue Distinct from beta-catenin, Interacts with E-cadherin and N-cadherin. *J Cell Biol*, 118(3), pp.671–9.

Koch, M.H.J., Vachette, P. & Svergun, D.I., 2003. Small-angle scattering: a view on the properties, structures and structural changes of biological macromolecules in solution. *Q Rev Biophys*, 36(2), pp.147–227.

Koepf, E. et al., 1999. WW: An isolated three-stranded antiparallel beta-sheet domain that unfolds and refolds reversibly; evidence for a structured hydrophobic cluster in urea and GdnHCl and a disordered thermal unfolded state. *Protein Sci*, 8(4), pp.841–53.

Konarev, P. V. et al., 2003. PRIMUS: a Windows PC-based system for small-angle scattering data analysis. *J Appl Crystallogr*, 36, pp.1277–82.

Koster, J. et al., 2002. Analysis of the interactions between BP180, BP230, plectin and the integrin alpha6beta4 important for hemidesmosome assembly. *J Cell Sci*, 116(2), pp.387–399.

Kouklis, P., Hutton, E. & Fuchs, E., 1994. Making a Connection: Direct Binding between Keratin Intermediate Filaments and Desmosomal Proteins. *J Cell Biol*, 127(4), pp.1049–60.

Kowalczyk, A., Borgwardt, J. & Green, K., 1996. Analysis of desmosomal cadherin-adhesive function and stoichiometry of desmosomal cadherin-plakoglobin complexes. *J Invest Dermatol*, 107(3), pp.293–300.

Kowalczyk, A.P. et al., 1997. The amino-terminal domain of desmoplakin binds to plakoglobin and clusters desmosomal cadherin-plakoglobin complexes. *J Cell Biol*, 139(3), pp.773–784.

Kowalczyk, A.P. et al., 1999. The Head Domain of Plakophilin-1 Binds to Desmoplakin and Enhances Its Recruitment to Desmosomes. Implications for Cutaneous Disease. *J Biol Chem*, 274(26), pp.18145–18148.

Kowalczyk, A.P. et al., 1998. VE-cadherin and desmoplakin are assembled into dermal microvascular endothelial intercellular junctions : a pivotal role for plakoglobin in the recruitment of desmoplakin to intercellular junctions. *J Cell Sci*, 111(Pt 20), pp.3045–3057.

Kowalczyk, A.P. & Green, K.J., 2013. Structure, function, and regulation of desmosomes. *Prog Mol Biol Transl Sci.*, 116, pp.95–118.

Kozak, M., 1986. Point mutations define a sequence flanking the AUG initiator codon that modulates translation by eukaryotic ribosomes. *Cell*, 44(2), pp.283–92.

Kozin, M.B. & Svergun, D.I., 2001. Automated matching of high- and low-resolution structural models research papers. *J Appl Crystallogr*, 34, pp.33–41.

Kuwamoto, S., Akiyama, S. & Fujisawa, T., 2004. Radiation damage to a protein solution, detected by synchrotron X-ray small-angle scattering: dose-related considerations and suppression by cryoprotectants. *J Synchrotron Radiat*, 11(Pt 6), pp.462–8.

Lai Cheong, J.E., Wessagowit, V. & McGrath, J. a, 2005. Molecular abnormalities of the desmosomal protein desmoplakin in human disease. *Clin Exp Dermatol*, 30(3), pp.261–6.

Lechler, T. & Fuchs, E., 2007. Desmoplakin: an unexpected regulator of microtubule organization in the epidermis. *J Cell Biol*, 176(2), pp.147–54.

Leinonen, P.T. et al., 2009. Reevaluation of the normal epidermal calcium gradient, and analysis of calcium levels and ATP receptors in Hailey-Hailey and Darier epidermis. *J Invest Dermatol*, 129(6), pp.1379–87.

Leung, C.L. et al., 2001. The BPAG1 locus: Alternative splicing produces multiple isoforms with distinct cytoskeletal linker domains, including predominant isoforms in neurons and muscles. *J Cell Biol*, 154(4), pp.691–7.

Li, S.S., 2005. Specificity and versatility of SH3 and other proline-recognition domains: structural basis and implications for cellular signal transduction. *Biochem J*, 390(Pt 3), pp.641–53.

Liu, J. et al., 2009. The C. elegans SYS-1 protein is a bona fide β-catenin. *Dev Cell*, 14(5), pp.751–761.

Louis-Jeune, C., Andrade-Navarro, M. a & Perez-Iratxeta, C., 2012. Prediction of protein secondary structure from circular dichroism using theoretically derived spectra. *Proteins*, 80(0), pp.374–81.

Mathur, M., Goodwin, L. & Cowin, P., 1994. Interactions of the cytoplasmic domain of the desmosomal cadherin Dsg1 with plakoglobin. *J Biol Chem.*, 269(19), pp.14075–14080.

Mavinakere, M.S. et al., 2012. Multiple novel signals mediate thyroid hormone receptor nuclear import and export. *J Biol Chem*, 287(37), pp.31280–97.

McDonnell, A. V. et al., 2006. Paircoil2: improved prediction of coiled coils from sequence. *Bioinformatics*, 22(3), pp.356–8.

McGrath, J. & Mellerio, J., 2010. Ectodermal dysplasia-skin fragility syndrome. *Dermatol Clin*, 28(1), pp.125–129.

McGrath, J.A. et al., 1997. Mutations in the plakophilin 1 gene result in ectodermal dysplasia/skin fragility syndrome. *Nat Genet*, 15(3), pp.266–8.

Meng, J.-J. et al., 1997. Two-hybrid Analysis Reveals Fundamental Differences in Direct Interactions between Desmoplakin and Cell Type-specific Intermediate Filaments. *J Biol Chem*, 272(34), pp.21495–503.

Mertens, C. et al., 2001. Nuclear particles containing RNA polymerase III complexes associated with the junctional plaque protein plakophilin 2. *Proc Natl Acad Sci U S A*, 98(14), pp.7795–800.

Mertens, C., Kuhn, C. & Franke, W.W., 1996. Plakophilins 2a and 2b: constitutive proteins of dual location in the karyoplasm and the desmosomal plaque. *J Cell Biol*, 135(4), pp.1009–25.

Mertens, H.D.T. & Svergun, D.I., 2010. Structural characterization of proteins and complexes using small-angle X-ray solution scattering. *J Struct Biol*, 172(1), pp.128–41.

Moll, I. et al., 1997. The distribution of the desmosomal protein, plakophilin 1, in human skin and skin tumors. *Invest Dermatol.*, 108(2), pp.139–146.

Mühmer, M. et al., 2014. An alternative promoter of the human plakophilin-3 gene controls the expression of the new isoform PKP3b. *Cell Tissue Res*, 355(1), pp.143–62.

Müller, J. et al., 2003. Functional analysis of C-TAK1 substrate binding and identification of PKP2 as a new C-TAK1 substrate. *EMBO J.*, 22(17), pp.4431–42.

Munoz, W. a et al., 2014. Plakophilin-3 Catenin Associates with the ETV1/ER81 Transcription Factor to Positively Modulate Gene Activity. *PloS one*, 9(1), p.e86784.

Nagai, T. et al., 2002. A variant of yellow fluorescent protein with fast and efficient maturation for cell-biological applications. *Nat Biotechnol*, 20(1), pp.87–90.

Nekrasova, O. & Green, K.J., 2013. Desmosome assembly and dynamics. *Trends Cell Biol*, 23(11), pp.537–46.

Newman, J. et al., 2005. Towards rationalization of crystallization screening for small- to medium-sized academic laboratories: the PACT/JCSG+ strategy. *Acta Crystallogr D Biol Crystallogr*, 61(Pt 10), pp.1426–31.

Nguyen, T.N. & Goodrich, J.A., 2006. Protein-protein interaction assays: eliminating false positive interactions. *Nat methods*, 3(2), pp.135–9.

Nie, Z. et al., 2011. Membrane-impermeable cross-linking provides evidence for homophilic, isoform-specific binding of desmosomal cadherins in epithelial cells. *J Biol Chem*, 286(3), pp.2143–54.

Niessen, C.M. et al., 1996. Deficiency of the integrin beta 4 subunit in junctional epidermolysis bullosa with pyloric atresia: consequences for hemidesmosome formation and adhesion properties. *J Cell Sci*, 109(Pt 7), pp.1695–706.

North, A.J. et al., 1999. Molecular map of the desmosomal plaque. *J Cell Sci*, 112(Pt 23), pp.4325–36.

O´Keefe, E.J., Ericksonb, H.P. & Bennett, V., 1989. Desmoplakin I and desmoplakin II. Purification and characterization. *J Biol Chem*, 264(14), pp.8310–8.

O'Shea, E. et al., 1991. X-ray structure of the GCN4 leucine zipper, a two-stranded, parallel coiled coil. *Science*, 254(5031), pp.539–544.

Ortega, E. et al., 2011. The structure of the plakin domain of plectin reveals a non-canonical SH3 domain interacting with its fourth spectrin repeat. *J Biol Chem*, 286(14), pp.12429–38.

Pace, C.N. et al., 1995. How to measure and predict the molar absorption coefficient of a protein. *Protein Sci*, 4(11), pp.2411–23.

Palka, H.L. & Green, K.J., 1997. Roles of plakoglobin end domains in desmosome assembly. *J Cell Sci*, 110(Pt 19), pp.2359–71.

Pantoliano, M.W. et al., 2001. High-Density Miniaturized Thermal Shift Assays as a General Strategy for Drug Discovery. *J Biomol Screen*, 6(6), pp.429–40.

Petoukhov, M. V & Svergun, D.I., 2005. Global rigid body modeling of macromolecular complexes against small-angle scattering data. *Biophys J*, 89(2), pp.1237–50.

Petoukhov, M. V. et al., 2012. New developments in the ATSAS program package for small-angle scattering data analysis. *J Appl Crystallogr*, 45(2), pp.342–50.

Rambo, R.P. & Tainer, J. a, 2011. Characterizing flexible and intrinsically unstructured biological macromolecules by SAS using the Porod-Debye law. *Biopolymers*, 95(8), pp.559–71.

Rampazzo, A. et al., 2002. Mutation in human desmoplakin domain binding to plakoglobin causes a dominant form of arrhythmogenic right ventricular cardiomyopathy. *Am J Hum Genet*, 71(5), pp.1200–6.

Ranjbar, B. & Gill, P., 2009. Circular dichroism techniques: biomolecular and nanostructural analyses- a review. *Chem Biol Drug Des*, 74(2), pp.101–20.

Reddy, R., 2013. Elucidating the non-junctional role of plakophilin-1 and its significance in regulating desmosomal cell adhesion. *PhD Thesis, University of Nebraska Medical Center*.

Rickelt, S., 2012. Plakophilin-2: a cell-cell adhesion plaque molecule of selective and fundamental importance in cardiac functions and tumor cell growth. *Cell Tissue Res*, 348(2), pp.281–94.

Roberts, B.J. et al., 2014. Palmitoylation of plakophilin is required for desmosome assembly. *Journal of cell science*, 127(Pt 17), pp.3782–93.

Roberts, B.J., Reddy, R. & Wahl, J.K., 2013. Stratifin (14-3-3 σ) limits plakophilin-3 exchange with the desmosomal plaque. *PloS one*, 8(10), p.e77012.

Roh, J. & Stanley, J., 1995. Plakoglobin binding by human Dsg3 (pemphigus vulgaris antigen) in keratinocytes requires the cadherin-like intracytoplasmic segment. *J Invest Dermatol*, 104(5), pp.720–724.

Ruxton, G.D., 2006. The unequal variance t-test is an underused alternative to Student's t-test and the Mann-Whitney U test. *Behav Ecol*, 17(4), pp.688–690.

Saito, M. et al., 2012. Classical and desmosomal cadherins at a glance. *J Cell Sci*, 125(Pt 11), pp.2547–52.

Schmidt, A. et al., 1997. Plakophilins 1a and 1b : widespread nuclear proteins recruited in specific epithelial cells as desmosomal plaque components. *Cell Tissue Res*, 290(3), pp.481–499.

Setzer, S. V. et al., 2004. Comparative Analysis of Armadillo Family Proteins in the Regulation of A431 Epithelial Cell Junction Assembly, Adhesion and Migration. *J Invest Dermatol*, 123(3), pp.426–433.

Sevilla, L.M. et al., 2008. Kazrin regulates keratinocyte cytoskeletal networks, intercellular junctions and differentiation. *J Cell Sci*, 121(Pt 21), pp.3561–9.

Shaulsky, G. et al., 1990. Nuclear Accumulation of p53 Protein Is Mediated by Several Nuclear Localization Signals and Plays a Role in Tumorigenesis. *Mol Cell Biol*, 10(12), pp.6565–6577.

Sievers, F. & Higgins, D.G., 2014. Clustal Omega, accurate alignment of very large numbers of sequences. *Methods Mol Biol*, 1079, pp.105–16.

Sklyarova, T. et al., 2008. Plakophilin-3-deficient mice develop hair coat abnormalities and are prone to cutaneous inflammation. *J Invest Dermatol*, 128(6), pp.1375–85.

Smith, E.A. & Fuchs, E., 1998. Defining the interactions between intermediate filaments and desmosomes. *J Cell Biol*, 141(5), pp.1229–41.

Sobolik-Delmaire, T. et al., 2010. Plakophilin-1 localizes to the nucleus and interacts with single-stranded DNA. *J Invest Dermatol*, 130(11), pp.2638–46.

Sobolik-Delmaire, T., Katafiasz, D. & Wahl, J.K., 2006. Carboxyl terminus of Plakophilin-1 recruits it to plasma membrane, whereas amino terminus recruits desmoplakin and promotes desmosome assembly. *J Biol Chem*, 281(25), pp.16962–70.

Sonnenberg, A. & Liem, R.K.H., 2007. Plakins in development and disease. *Exp Cell Res*, 313(10), pp.2189–203.

Sonnenberg, A., Rojas, A.M. & de Pereda, J.M., 2007. The structure of a tandem pair of spectrin repeats of plectin reveals a modular organization of the plakin domain. *J Mol Biol*, 368(5), pp.1379–91.

South, a. P., 2004. Plakophilin 1: an important stabilizer of desmosomes. *Clin Exp Dermatol*, 29(2), pp.161–7.

South, A.P. et al., 2003. Lack of plakophilin 1 increases keratinocyte migration and reduces desmosome stability. *J Cell Sci*, 116(Pt 16), pp.3303–14.

Sreerama, N., Venyaminov, S.Y.U. & Woody, R.W., 1999. Estimation of the number of alpha-helical and beta-strand segments in proteins using circular dichroism spectroscopy. *Protein Sci*, 8(2), pp.370–80.

Sreerama, N. & Woody, R.W., 2000. Estimation of protein secondary structure from circular dichroism spectra: comparison of CONTIN, SELCON, and CDSSTR methods with an expanded reference set. *Anal Biochem*, 287(2), pp.252–60.

Stadler, C. et al., 2013. Immunofluorescence and fluorescent-protein tagging show high correlation for protein localization in mammalian cells. *Nat methods*, 10(4), pp.315–23.

Stappenbeck, T.S. & Green, K.J., 1992. The Desmoplakin Carboxyl Terminus Coaligns with and Specifically Disrupts Intermediate Filament Networks When Expressed in Cultured Cells. *J Cell Biol*, 116(5), pp.1197–209.

Sterk, L.M.T. et al., 2000. The Tetraspan Molecule CD151, a Novel Constituent of Hemidesmosomes, Associates with the Integrin alpha6beta4 and May Regulate the Spatial Organization of Hemidesmosomes. *J Cell Biol*, 149(4), pp.969–82.

Von Stetten, D. et al., 2012. Structure of a fluorescent protein from Aequorea victoria bearing the obligate-monomer mutation A206K. *Acta Crystallogr Sect F Struct Biol Cryst Commun*, 68(Pt 8), pp.878–82.

Van Stokkum, I.H.M. et al., 1990. Estimation of protein secondary structure and error analysis from circular dichroism spectra. *Anal Biochem*, 191(1), pp.110–118.

Studier, F.W. & Moffatt, B. a, 1986. Use of bacteriophage T7 RNA polymerase to direct selective high-level expression of cloned genes. *J Mol Biol*, 189(1), pp.113–30.

Sumigray, K.D. & Lechler, T., 2012. Desmoplakin controls microvilli length but not cell adhesion or keratin organization in the intestinal epithelium. *Mol Biol Cell*, 23(5), pp.792–9.

Svergun, D., Barberato, C. & Koch, M.H.J., 1995. CRYSOL – a Program to Evaluate X-ray Solution Scattering of Biological Macromolecules from Atomic Coordinates. *J Appl Crystallogr*, 28, pp.768–73.

Svergun, D.I., 1992. Determination of the regularization parameter in indirect-transform methods using perceptual criteria. *J Appl Crystallogr*, 25, pp.495–503.

Syed, S. et al., 2002. Molecular interactions between desmosomal cadherins. *Biochem J*, 362(Pt 2), pp.317–27.

Tartof, K.D. & Hobbs, C.A., 1987. Improved Media for Growing Plasmid and Cosmid Clones. *Bethesda Res Lab Focus*, 9, p.12.

Tewari, R. et al., 2010. Armadillo-repeat protein functions: questions for little creatures. *Trends Cell Biol*, 20(8), pp.470–81.

Thomas, A. V et al., 2006. Interaction between presenilin 1 and ubiquilin 1 as detected by fluorescence lifetime imaging microscopy and a high-throughput fluorescent plate reader. *J Biol Chem*, 281(36), pp.26400–7.

Todorović, V. et al., 2010. Plakoglobin regulates cell motility through Rho- and fibronectin-dependent Src signaling. *J Cell Sci*, 123(Pt 20), pp.3576–86.

Troyanovsky, S.M., Troyanovsky, R.B., Eshkind, L., et al., 1994. Identification of amino acid sequence motifs in desmocollin , a desmosomal glycoprotein , that are required for plakoglobin binding and plaque formation. *Proc Natl Acad Sci U S A*, 91(23), pp.10790–4.

Troyanovsky, S.M., Troyanovsky, R.B., Eshkind, L.G., et al., 1994. Identification of the Plakoglobin-binding Domain in Desmoglein and Its Role in Plaque Assembly and Intermediate Filament Anchorage. *J Cell Biol*, 127(1), pp.151–60.

Tucker, D.K., Stahley, S.N. & Kowalczyk, A.P., 2014. Plakophilin-1 protects keratinocytes from pemphigus vulgaris IgG by forming calcium-independent desmosomes. *J Invest Dermatol*, 134(4), pp.1033–1043.

Uzumcu, A. et al., 2006. Loss of desmoplakin isoform I causes early onset cardiomyopathy and heart failure in a Naxos-like syndrome. *J Med Genet*, 43(2), p.e5.

Vasioukhin, V. et al., 2001. Desmoplakin is essential in epidermal sheet formation. *Nat Cell Biol*, 3(12), pp.1076–85.

Volkov, V. V & Svergun, D.I., 2003. Uniqueness of ab initio shape determination in small-angle scattering. *J Appl Crystallogr*, 36, p.4.

Waschke, J. et al., 2007. Imaging and force spectroscopy on desmoglein 1 using atomic force microscopy reveal multivalent Ca(2+)-dependent, low-affinity trans-interaction. *J Membr Biol*, 216(2-3), pp.83–92.

Whitmore, L. & Wallace, B. a, 2004. DICHROWEB, an online server for protein secondary structure analyses from circular dichroism spectroscopic data. *Nucleic Acids Res*, 32(Web Server issue), pp.W668–73.

Wilkins, M.R. et al., 1999. Protein identification and analysis tools in the ExPASy server. *Methods Mol Biol*, 112, pp.531–52.

Wilson, I.A. et al., 1984. The structure of an antigenic determinant in a protein. *Cell*, 37(3), pp.767–78.

Witcher, L. et al., 1996. Desmosomal Cadherin Binding Domains of Plakoglobin. *J Biol Chem*, 271(18), pp.10904–9.

Wolf, A. et al., 2013. Insulin signaling via Akt2 switches plakophilin 1 function from stabilizing cell adhesion to promoting cell proliferation. *J Cell Sci*, 126(Pt 8), pp.1832–44.

Wolf, A. et al., 2010. Plakophilin 1 stimulates translation by promoting eIF4A1 activity. *J Cell Biol*, 188(4), pp.463–71.

Wriggers, W., 2010. Using Situs for the integration of multi-resolution structures. *Biophys Rev*, 2(1), pp.21–27.

Yachdav, G. et al., 2014. PredictProtein-an open resource for online prediction of protein structural and functional features. *Nucleic Acids Res*, 42(Web Server issue), pp.W337–43.

Yang, Z. et al., 2006. Desmosomal dysfunction due to mutations in desmoplakin causes arrhythmogenic right ventricular dysplasia/cardiomyopathy. *Circ Res*, 99(6), pp.646–55.

Zhao, Q. et al., 2012. Modulated electron-multiplied fluorescence lifetime imaging microscope: all-solid-state camera for fluorescence lifetime imaging. *J Biomed Opt*, 17(12), p.126020.

Zhao, Q., Young, I.T. & de Jong, J.G.S., 2011. Photon budget analysis for fluorescence lifetime imaging microscopy. *J Biomed Opt*, 16(8), p.086007.

Zhou, X. et al., 2004. Desmoplakin is required for microvascular tube formation in culture. *J Cell Sci*, 117(Pt 15), pp.3129–40.

Zhuang, Z. et al., 2011. Assisted peptide folding by surface pattern recognition. *Biophys J*, 100(5), pp.1306–15.

List of Figures

Section C. Structure of the PD of DP

Chapter 5. Discussion

List of Tables

Chapter 1. Introduction

Chapter 3. Materials & Methods

Chapter 4. Results

Section A. Mapping of the interacting domains in the DP-PKP1a complex

Section C. Structure of the PD of DP